
**Dynamic Density-Matrix Renormalization
for the Symmetric Single Impurity Anderson Model**

Inaugural-Dissertation
zur
Erlangung des Doktorgrades
der Mathematisch-Naturwissenschaftlichen Fakultät
der Universität zu Köln

vorgelegt von

Carsten Raas

aus Trier

Köln 2005

Berichterstatter: Prof. Dr. G. S. Uhrig
Prof. Dr. A. Rosch

Vorsitzender der Prüfungskommission: Prof. Dr. L. H. Tjeng

Tag der mündlichen Prüfung: 11. Juli 2005

Contents

0	Introduction	1
1	Single impurity Anderson model	5
1.1	Historical remarks	5
1.2	Impurities in host metals	6
1.3	Single impurity Anderson model	8
1.4	Linear chain version of the SIAM	11
1.5	Single-particle dynamics of the symmetric SIAM	15
1.6	Density-matrix renormalization for SIAMs	22
1.6.1	Introduction	22
1.6.2	Jordan-Wigner transformation for the SIAM	23
1.6.3	Green function of the SIAM	27
1.6.4	Self-energy of the SIAM via the Q -function	28
1.7	Effective impurity models in the framework of dynamic mean-field theory	35
2	Dynamic density-matrix renormalization	37
2.1	Conventional DMRG	38
2.1.1	Standard real-space blocking scheme	38
2.1.2	Boundary conditions	39
2.1.3	Density-matrix projection	40
2.1.4	Optimization of expectation values	41
2.1.5	Optimization of the wave function	44
2.1.6	Multiple target states	45
2.1.7	Infinite size algorithm	46
2.1.8	Finite size algorithm	51
2.1.9	Checks via conventional DMRG	54
2.2	Dynamic DMRG	64
2.2.1	Introduction	64
2.2.2	Lanczos method	65
2.2.3	Correction vector method	70

2.2.4	Inversion performance	75
2.2.5	Projective D-DMRG	79
3	Deconvolution	85
3.1	Introduction	85
3.2	Linear Extraction Schemes	87
3.2.1	FFT	87
3.2.2	Matrix inversion	90
3.3	Non-Linear Extraction Schemes	94
3.3.1	Basic Algorithm	94
3.3.2	Robustness towards inaccuracies	98
3.4	Summary	101
4	Results for the SIAM	103
4.1	Introduction	103
4.2	Overview	104
4.3	Non-interacting case	106
4.4	Kondo resonance	107
4.5	Hubbard satellites	110
4.5.1	Broadened data	110
4.5.2	Deconvolved data	114
5	Results for the $d = \infty$ Hubbard model on a Bethe lattice	121
5.1	Introduction	121
5.2	D-DMRG as impurity solver in a DMFT framework	123
5.3	Results	124
6	Summary	131
	Bibliography	135
	Appendix	153
	Kurze Zusammenfassung	155
	Abstract	157
	Danksagung	159
	Erklärung	161
	Teilpublikationen	161
	Lebenslauf	163

0 Introduction

The behavior of magnetic impurities in metals has been an enduring challenge in condensed matter theory over the past forty years. The essential physics of this problem is captured in *single impurity models* where a single magnetic impurity is coupled to a fermionic host. Single impurity models are—despite their formal simplicity—difficult many-body problems at the very basis of the description of strong correlation phenomena. Landmarks in this field of research are the Kondo problem and the single impurity Anderson model.

Single impurity Anderson model

The essential physics of a single magnetic impurity coupled to a fermionic host is embodied at its simplest in the single impurity Anderson model (SIAM): a correlated, non-degenerate impurity with local interaction, hybridized with a non-interacting host band. In the conventional case of a metallic host, the SIAM serves as a basic model for understanding magnetic impurities in metals. It has become highly topical again in the context of quantum dots for instance or surface atoms probed by scanning tunneling microscopy (STM).

The dynamic mean-field theory (DMFT) represents another broad and very active field where the SIAM occurs. In this approach, as in all mean-field approaches, the lattice problem of strongly interacting fermions is mapped onto an effective single-site problem, namely a SIAM. This SIAM is linked to the original lattice problem by a self-consistency condition. The clue is that the mean-field, the Green function of the bath, is a dynamic quantity depending on frequency. Thus, the quantitative determination of the dynamic correlations of single impurity models is essential for the solution of the DMFT equations. The numerical method of our choice to solve the dynamics of the SIAM is the *dynamic density-matrix renormalization*.

Dynamic density-matrix renormalization

The density-matrix renormalization group (DMRG) is a numerical technique for the efficient truncation of the Hilbert space of one and quasi-one-dimensional strongly correlated quantum systems. Since its was introduced more than ten years ago the DMRG

has been successfully applied to both fermionic and bosonic low-dimensional quantum lattice systems. Originally designed as a real-space scheme for finding accurate approximations to the ground state and the low-lying excited states of one-dimensional quantum lattice systems at zero temperature the field of application has been extended in 1995 to the calculation of dynamic quantities. We use the dynamic density-matrix renormalization (D-DMRG) in a correction vector scheme with optimized direct matrix inversion. This allows us to calculate the local propagator of a fermionic impurity in a bath at constant energy resolution. The approach is particularly useful for energetically higher-lying excitations.

Objective of this Thesis

The objective of this thesis is to develop and optimize a D-DMRG program which calculates the local dynamics of a SIAM with arbitrary (but non-interacting) fermionic bath with constant (or at least adaptive) energy resolution over the full frequency range accurately and within a reasonable amount of time. A well-controlled numerical approach to impurity problems will be a useful tool in the field of the dynamic mean-field theory as well as for more complex impurities like quantum dots, molecules, or for the effective problems of extended DMFT schemes. It will complement the numerical methods which theorists have been using for solving models like the SIAM in the past, e.g. the quantum Monte Carlo (standard QMC, accurate for high temperatures but difficult to extrapolate to zero temperature; or projective QMC at $T = 0$, difficult to extrapolate from complex to real frequencies) or the numerical renormalization group (NRG, works very accurately for low energies but resolving high energy features is difficult).

In this thesis the algorithm is gauged and optimized by applying it to the SIAM with a semi-elliptic hybridization function $\Gamma(\omega)$. The hybridization V (which couples the bath to the impurity) and the local Coulomb interaction U on the impurity are varied and the corresponding local dynamics on the impurity is calculated. We check that the Kondo energy scale can be resolved and we analyze the lineshape of the Hubbard satellites. Furthermore, we report briefly on the application of the DMRG program developed in this thesis as “impurity solver” in the framework of the DMFT. The investigated model is the $d = \infty$ Hubbard model on a Bethe lattice. The focus is the Mott-Hubbard metal-insulator transition and the electron spectra close to the transition.

Thesis Outline

- **Chapter 1: Single impurity Anderson model**

In this chapter the SIAM is introduced. The model's origin and some basic properties are discussed.

The SIAM is mapped onto a semi-infinite chain in a first step. In a second step the fermionic model is mapped by Jordan-Wigner transformations onto a spin chain which is an advantageous representation for the DMRG. The single-particle dynamics of the symmetric SIAM is discussed. An alternative approach to calculate spectral functions is presented: The computation of the irreducible self-energy $\Sigma(z)$ via the reducible self-energy $Q(z)$ increases the accuracy in comparison to the direct calculation of the local propagator $G(z)$.

- **Chapter 2: Dynamic density-matrix renormalization**

The conventional DMRG and the D-DMRG are explained and presented in the way they are implemented in the C++ program. Special emphasis is put on the most time consuming step in a correction vector scheme: the calculation of the frequency dependent correction vector $|\xi\rangle$ itself. It turns out that inversion of the linear equation $[\omega + i\eta - (\mathcal{H} - E_0)]|\xi\rangle = d^\dagger|0\rangle$ for the calculation of the correction vector is very efficient for low and intermediate frequencies when using a special iterative solver, i. e. the quasi-minimal residuum method (QMR).

- **Chapter 3: Deconvolution**

The DMRG provides the density of states convolved with a Lorentzian of width η . Choosing η is a trade-off between run-time and energy resolution. Thus, accurate deconvolution strategies are essential. We analyze several linear deconvolution methods to calculate continuous spectral densities and propose a novel non-linear algorithm, the least-bias algorithm (LB). The LB deconvolution provides a continuous and positive-definite spectral density (opposed to linear deconvolution schemes). The positive-definiteness of the LB scheme is essential in the robust implementation of the DMFT self-consistency condition as non-causal artefacts in the Green function would pose a severe problem when closing the self-consistency cycle of the DMFT.

- **Chapter 4: Results for the SIAM**

The central peak at $\omega = 0$, i. e. the Abrikosov-Suhl resonance or the Kondo peak, is analyzed. This is a first important benchmark for the D-DMRG, as the exponentially small Kondo energy scale has to be resolved. We check that the density at zero energy $\rho(0)$ is pinned to its non-interacting value as required by the sum rules.

In a next step we focus on an analysis of the high energy features of the model, i. e. the upper and lower Hubbard satellites. In contrast to other approaches, sharp dominant resonances at high energies are found. We analyze their line shapes and discuss their origin and importance.

- **Chapter 5: Results for the $d = \infty$ Hubbard model on a Bethe lattice**

A short summary of the findings of Mihał Karski's diploma thesis is presented here. This was the first time the impurity solver developed in this thesis was used in the context of the dynamic mean-field theory. Some modifications of the program had to be done when treating spectral densities with energy gap.

- **Chapter 6: Summary**

The thesis concludes with a brief summary.

1 Single impurity Anderson model

1.1 Historical remarks

When magnetic impurities are embedded in metals a variety of interesting many-body phenomena can arise. This has attracted theory and experiment for many years [Hew93]. Starting in the early 30s of the last century [Haa34] the observation of the resistivity minimum in some metals has posed a severe problem to solid state theory. The resistivity minimum at low temperatures and the increase of the resistivity when further lowering the temperature was in contradiction to the behavior expected for ordinary metals, i. e. the phononic contribution to the resistivity decreases proportional to T^5 (“Bloch T^5 law”) [Ash76]. It was recognized later that the existence of a resistivity minimum is an impurity effect. A significant advance in the theory of magnetic impurities was the explanation of this effect by *J. Kondo* in 1964 [Kon64], nowadays called the *Kondo effect*. The Kondo theory is based on a model where a local magnetic moment with spin S is coupled via an exchange interaction J with the conduction electrons (s-d model, Zener model [Zen51]). Kondo used a third order perturbation theory analysis in the coupling J to show that this interaction leads to singular scattering of electrons near the Fermi level and a $\ln T$ contribution to the resistivity. The logarithmic term increases at low temperatures for an antiferromagnetic coupling. Combined with the phonon contribution to the resistivity this is sufficient to explain the observed resistance minimum. On the other hand it is obvious that Kondo’s perturbational calculations are not valid at low temperatures due to the logarithmic divergence. The difficulties to construct a fully consistent theory for the limit $T \rightarrow 0$ led to a lot of theoretical interest in the late 60s and early 70s and the search for a theory became famous as the “Kondo problem” [Kon64, Kon65]. The puzzle was finally solved in a non-perturbative way by *K. G. Wilson* using the “numerical renormalization group” [Wil75]. Another breakthrough were the exact Bethe-ansatz solutions found independently by *Andrei* [And80] and *Wiegmann* [Wie80] in 1980.¹ The developments and the interest in this field never ceased; for an extensive overview see the monograph Ref. [Hew93]. In recent years the interest in the Kondo effect peaked again—leading to

¹Further early papers on Bethe ansatz techniques applied to the s-d exchange model are Refs. [Wie81a, Wie81b, Tsv82a]. For a detailed review of the Bethe-ansatz approach to the solution of various versions of the Kondo problem see Refs. [And83, Tsv83a, Sch89].

a “revival of the Kondo effect” [Kou01]. The reason for this are new experimental techniques from the rapidly developing field of nanotechnology which gave an unprecedented control over Kondo systems.

The s-d model can be deduced from the *Anderson model* in the appropriate parameter regime [Sch66]². The model was introduced by *P. W. Anderson* in 1961 [And61] as a different formulation of the concept of “virtual bound states”³. The properties of 3d (transition metal) and 4f (rare earth) electrons impurities distributed statistically in a host metal can be accounted for in the framework of the Anderson Hamiltonian. The model contains, in addition to a narrow resonance associated with the impurity states, a short range Coulomb interaction U between the localized electrons.⁴

After some more general remarks on models of impurities in host metals in the [next section 1.2](#), the single impurity Anderson model (SIAM) is introduced in [Sect. 1.3](#). As the dynamics of this model is investigated in this thesis with a numerical approach working especially well for low-dimensional systems (the D-DMRG, see [Chapt. 2](#)) we map the SIAM onto a semi-infinite linear chain in [Sect. 1.4](#). [Sect. 1.5](#) introduces the basics of the single-particle dynamics of the SIAM, i. e. the most important formulas and the expected qualitative behavior. In [Sect. 1.6](#) the fermionic model is mapped via Jordan-Wigner transformations onto a spin $S=1/2$ model. This representation is very convenient when applying the DMRG. In brief, [Sect. 1.7](#) explains where single impurity Anderson models come into play when investigating lattice models in the framework of the dynamic mean-field theory.

1.2 Impurities in host metals

A system of an impurity in a metallic host can be described by a general Hamiltonian incorporating all N_0 electrons and their interactions,

$$\mathcal{H} = \sum_{i=1}^{N_0} \left(\frac{\mathbf{p}_i^2}{2m} + U_{\text{host}}(\mathbf{r}_i) + V_{\text{imp}}(\mathbf{r}_i) \right) + \frac{1}{2} \sum_{i \neq j}^{N_0} \frac{e^2}{|\mathbf{r}_i - \mathbf{r}_j|} + \sum_{i=1}^{N_0} \lambda(\mathbf{r}_i) \mathbf{l}_i \cdot \boldsymbol{\sigma}_i. \quad (1.1)$$

The kinetic energy of the electrons is represented by the first term, the second one represents the periodic potential U_{host} of the host metal due to the nuclei without the impurity. Thus, an *additional* potential V_{imp} due to the nucleus of the impurity has to be added (third

²We will briefly recall the relation between the Anderson and Kondo Hamiltonians pointed out by *J. R. Schrieffer* and *P. A. Wolff* [Sch66] in [Sect. 1.3](#).

³Virtual bound state (VBS): state which is almost localized due to resonant scattering at the impurity site.

⁴For exact results for various versions of the Anderson model obtained via Bethe-ansatz see Refs. [Wie81a, Kaw81, Kaw82, Kaw83, Fil82, Tsv82b, Wie83b, Wie83a, Wie83c, Tsv83b, Ogi83, Tsv84] or the monograph Ref. [Hew93].

term). The Coulomb interactions between the electrons are given by the fourth term and the last term is the spin-orbit interaction, which is a relativistic correction. The strong Coulomb interaction prohibits perturbational calculations starting from the Hamiltonian Eq. (1.1). A possible treatment via the density-functional theory (DFT) [Jon89] would be appropriate as long as the electrons are only weakly correlated. For systems with strong local Coulomb interaction, such as systems with incomplete d or f shells, correlations are expected to be strong. As this is the generic scenario for transition metal and rare earth impurities—though DFT might work for the ground state properties—it will fail to give accurate results for excitations or dynamic properties.

The route we will follow is to use simpler model Hamiltonians which describe the low energy excitations associated with the impurity and ignore features that are not directly relevant to the calculation of impurity effects. The first simplification arises from the fact that in simple metals the conduction bands derived from s and p states are broad. Then the wide band conduction electrons behave approximately as independent particles moving within a periodic potential. Long range Coulomb interactions between the conduction electrons are screened. Thus, they are essentially quasi-particles (electrons together with their screening cloud). Quasi-particle interactions are usually neglected due to the predominant delocalization in the wide conduction bands. This is reasonable as it is known from Landau Fermi liquid theory that the lifetimes of single quasi-particles near the Fermi level ε_F are very long. In this spirit the host metal conduction electrons can be described by a one-electron Hamiltonian,

$$\mathcal{H}_c = \sum_{\mathbf{k}, \sigma} \varepsilon_{\mathbf{k}} c_{\mathbf{k}, \sigma}^\dagger c_{\mathbf{k}, \sigma} , \quad (1.2)$$

where $c_{\mathbf{k}, \sigma}^\dagger$ and $c_{\mathbf{k}, \sigma}$ are the creation and annihilation operators for Bloch states $\phi_{\mathbf{k}, \sigma}(\mathbf{r})$ of wavevector \mathbf{k} and spin component σ corresponding to an energy eigenvalue $\varepsilon_{\mathbf{k}}$. The creation and annihilation operators in second quantization fulfill the standard fermionic anticommutation rules

$$\{c_{\mathbf{k}, \sigma}^\dagger, c_{\mathbf{k}', \sigma'}\} = \delta_{\mathbf{k}, \mathbf{k}'} \delta_{\sigma, \sigma'} \quad \{c_{\mathbf{k}, \sigma}, c_{\mathbf{k}', \sigma'}\} = 0 . \quad (1.3)$$

The conduction states are characterized by a density of states $\rho_0(\varepsilon)$ (DOS) at energy ε ,

$$\rho_0(\varepsilon) = \sum_{\mathbf{k}} \delta(\varepsilon - \varepsilon_{\mathbf{k}}) . \quad (1.4)$$

Using the free particle picture for the conduction electrons we can include the impurity within the same independent particle picture by introducing an effective potential $V_{\text{imp}}^{\text{eff}}(\mathbf{r})$. Expressing the effective potential via the Bloch states of the host metal's conduction elec-

trons the combined Hamilton operator reads

$$\mathcal{H} = \sum_{\mathbf{k}, \sigma} \varepsilon_{\mathbf{k}} c_{\mathbf{k}, \sigma}^{\dagger} c_{\mathbf{k}, \sigma} + \sum_{\mathbf{k}, \mathbf{k}', \sigma} V_{\mathbf{k}, \mathbf{k}'} c_{\mathbf{k}, \sigma}^{\dagger} c_{\mathbf{k}', \sigma} \quad (1.5)$$

where we introduced $V_{\mathbf{k}, \mathbf{k}'} = \langle \mathbf{k} | V_{\text{imp}}^{\text{eff}} | \mathbf{k}' \rangle$ for the matrix elements. This ansatz turns out to yield a bad description for transition metal or rare earth impurities [Hew93]. Nevertheless, it is useful to note it here as an intermediate step. In the next section we will introduce the full interacting Anderson model also starting from a “non-interacting” variant like Eq. (1.5).

1.3 Single impurity Anderson model

If the local impurity potential V_{imp} is sufficiently attractive a local bound state below the conduction band of the host metal is formed. The wave function of an electron in this bound state localized in the vicinity of the impurity falls off exponentially with the distance r from the impurity as $r \rightarrow \infty$. Even if the impurity potential is not sufficiently attractive to produce a “real” bound state it may tend to localize the conduction electrons in the vicinity of the impurity. Such *virtual bound states* (VBS) are observed for transition metal (3d) or rare earth (4f) impurities when the d or f levels lie within the conduction band of the host metal.⁵ The resonant scattering at the impurity induces a narrow peak in the conduction band density of states. Such a scattering process can be viewed as a process in which an electron with momentum k out of the host metal s/p band collides with the impurity atom and resides for an average time Δt at the impurity site in an impurity 3d state. A conduction electron in a virtual bound state spends a relatively long—but finite—time in the impurity region. Then, it continues its path as a free electron with momentum k' through the metallic host. Thus, it is not a real bound state because the electron escapes from the VBS into the continuum of free electron states and the wave function becomes a Bloch state far from the impurity. This concept is known as *virtual bound state resonance* and was the starting point of early interpretations of transition metal impurity effects in metals [Fri58, Bla59].

Let us follow Anderson’s route to explain these resonances [And61]. Using the atomic d functions of the isolated impurity ion Anderson calculated their modification induced by the presence of the neighboring metal ions in the host metal. Let $\Phi_{\mathbf{d}}$ represent the atomic d level, $\Psi_{\mathbf{d}\delta}$ the Wannier wave function of the conduction electrons at site $\mathbf{d}\delta$ and \mathcal{H} the full Hamiltonian Eq. (1.1). Then the overlap or hybridization matrix element $V_{\mathbf{k}}$

⁵We drop the repetitive phrases like “d or f states” and let the term “d state” stand for the impurity state, “ $\varepsilon_{\mathbf{d}}$ ” for the impurity energy level, etc.

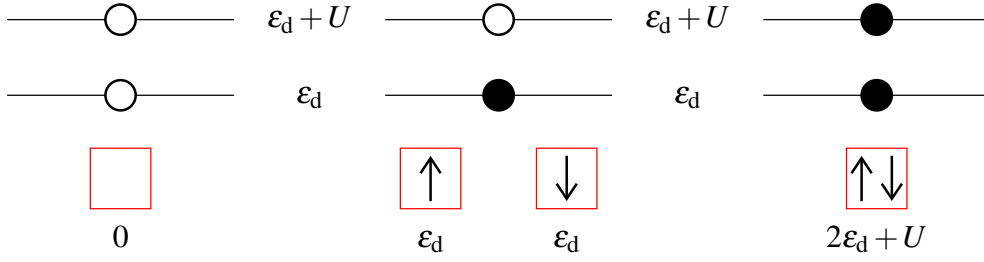


Figure 1.1: Configurations for the impurity state (a non-degenerate d level) assuming the hybridization to the conduction band vanishes, $V_{\mathbf{k}} = 0$. *Left:* empty ($E = 0$). *Middle:* single occupancy ($E = \varepsilon_d$). *Right:* double occupancy ($E = 2\varepsilon_d + U$).

of an impurity state with the conduction electron Bloch states is given by

$$V_{\mathbf{k}} = \sum_{\delta} e^{i\mathbf{k}\cdot\mathbf{d}\delta} \langle \Phi_{\mathbf{d}} | \mathcal{H} | \Psi_{\mathbf{d}\delta} \rangle. \quad (1.6)$$

In this mixed representation the Hamiltonian can be expressed in the form

$$\mathcal{H} = \sum_{\sigma} \varepsilon_d d_{\sigma}^{\dagger} d_{\sigma} + \sum_{\mathbf{k}, \sigma} \varepsilon_{\mathbf{k}} c_{\mathbf{k}, \sigma}^{\dagger} c_{\mathbf{k}, \sigma} + \sum_{\mathbf{k}, \sigma} \left(V_{\mathbf{k}} d_{\sigma}^{\dagger} c_{\mathbf{k}, \sigma} + V_{\mathbf{k}}^* c_{\mathbf{k}, \sigma}^{\dagger} d_{\sigma} \right) \quad (1.7)$$

where ε_d is the energy of the d level of the impurity ion and d_{σ}^{\dagger} and d_{σ} are creation and annihilation operators for an electron in this state. Note, that we ignored any orbital degeneracy⁶ of this state and treat it as a state with spin degeneracy only.

The Hamiltonian Eq. (1.7) (without any explicit inter-electron interactions) is usually referred to as the *non-interacting Anderson model*. If a local magnetic moment shall be described within the framework of the Anderson model the Coulomb interaction U between the electrons in the impurity ion d states has to be included,

$$U = \int \Phi_{\mathbf{d}}^*(\mathbf{r}) \Phi_{\mathbf{d}}^*(\mathbf{r}') \frac{e^2}{|\mathbf{r} - \mathbf{r}'|} \Phi_{\mathbf{d}}(\mathbf{r}') \Phi_{\mathbf{d}}(\mathbf{r}) d\mathbf{r} d\mathbf{r}'. \quad (1.8)$$

Adding the Coulomb interaction to Eq. (1.7) we get the Hamiltonian of the *interacting Anderson model*

$$\mathcal{H} = \sum_{\sigma} \varepsilon_d n_{d, \sigma} + U n_{d, \uparrow} n_{d, \downarrow} + \sum_{\mathbf{k}, \sigma} \varepsilon_{\mathbf{k}} c_{\mathbf{k}, \sigma}^{\dagger} c_{\mathbf{k}, \sigma} + \sum_{\mathbf{k}, \sigma} \left(V_{\mathbf{k}} d_{\sigma}^{\dagger} c_{\mathbf{k}, \sigma} + V_{\mathbf{k}}^* c_{\mathbf{k}, \sigma}^{\dagger} d_{\sigma} \right) \quad (1.9)$$

where we introduced the particle number operator $n_{d, \sigma} = d_{\sigma}^{\dagger} d_{\sigma}$ for the d electron and

⁶Anderson treats the case of a two-fold degenerate d level in Appendix A of Ref. [And61].

again only the simplest case of a non-degenerate d orbital has been used. Thus it has at most a double occupancy with a spin \uparrow and a spin \downarrow electron. In the trivial case where the localized impurity d states are decoupled from the conduction electrons, i. e. the hybridization $V_{\mathbf{k}}$ vanishes, there are three different energy configurations for the d states (cf. [Fig. 1.1](#)): (i) zero occupation with vanishing energy contribution $E_0 = 0$; (ii) single occupation by a spin σ with a total energy $E_{1,\sigma} = \varepsilon_d$ where $\sigma = \uparrow, \downarrow$; (iii) double occupation with a spin \uparrow and a spin \downarrow with a total energy $E_2 = 2\varepsilon_d + U$, as the Coulomb contribution has to be added to the binding energies of the impurity electrons. In this ‘‘atomic limit’’ of an isolated impurity the condition for a ‘‘local moment’’ to exist is that the singly occupied configuration lies lowest, which requires $\varepsilon_d < \varepsilon_F$, so that it is favorable to add one electron, and $\varepsilon_d + U > \varepsilon_F$ so that it is unfavorable to add a second electron.

In the regime for sufficiently small hybridizations $V_{\mathbf{k}}$ the Anderson model can be mapped onto the s-d model (Kondo model) [[Sch66](#)]. Applying a canonical transformation to the Anderson Hamiltonian (1.9), Schrieffer and Wolff derived an effective model with an s-d Heisenberg exchange interaction between a local moment with spin S_d and the conduction electrons

$$\mathcal{H}_{s-d} = \sum_{\mathbf{k}, \mathbf{k}'} J_{\mathbf{k}, \mathbf{k}'} \left[\mathbf{S}_d^+ c_{\mathbf{k}, \downarrow}^\dagger c_{\mathbf{k}', \uparrow} + \mathbf{S}_d^- c_{\mathbf{k}, \uparrow}^\dagger c_{\mathbf{k}', \downarrow} + \mathbf{S}_d^z \left(c_{\mathbf{k}, \uparrow}^\dagger c_{\mathbf{k}', \uparrow} - c_{\mathbf{k}, \downarrow}^\dagger c_{\mathbf{k}', \downarrow} \right) \right] \quad (1.10)$$

with a coupling constant (Eq. (1.73) in Ref. [[Hew93](#)]⁷)

$$J_{\mathbf{k}, \mathbf{k}'} = V_{\mathbf{k}}^* V_{\mathbf{k}'} \left[\frac{1}{(U + \varepsilon_d - \varepsilon_{\mathbf{k}'})} + \frac{1}{(\varepsilon_{\mathbf{k}} - \varepsilon_d)} \right]. \quad (1.11)$$

The complete Hamiltonian is given by the sum of \mathcal{H}_{s-d} and the potential scattering term (1.5). For conduction electrons in the region of the Fermi level, $\mathbf{k} \simeq k_F$ and $\mathbf{k}' \simeq k_F$, $J_{\mathbf{k}, \mathbf{k}'}$ is given by (see Eq. (13) in Ref. [[Sch66](#)]⁸)

$$J_{k_F, k_F} := -|V_{k_F}|^2 \frac{U}{\varepsilon_d(\varepsilon_d + U)} > 0 \quad (1.12)$$

where we set $\varepsilon_F = 0$. This coupling is antiferromagnetic provided the above-described conditions for the existence of a local moment are fulfilled, i. e. $\varepsilon_d < \varepsilon_F$ and $\varepsilon_d + U > \varepsilon_F$. The exchange interaction is inversely proportional to U . Therefore the limit of strong Coulomb interaction corresponds to the weak coupling limit of the Kondo model and conversely the weak Coulomb interaction corresponds to the Kondo model with strong coupling. It is important to keep in mind that for small U , the Anderson model is no longer

⁷See also Eq. (9b) in Ref. [[Sch66](#)]. Note that the conventions for $J_{\mathbf{k}, \mathbf{k}'}$ differ by a factor of -2 .

⁸Again a factor of -2 is different here.

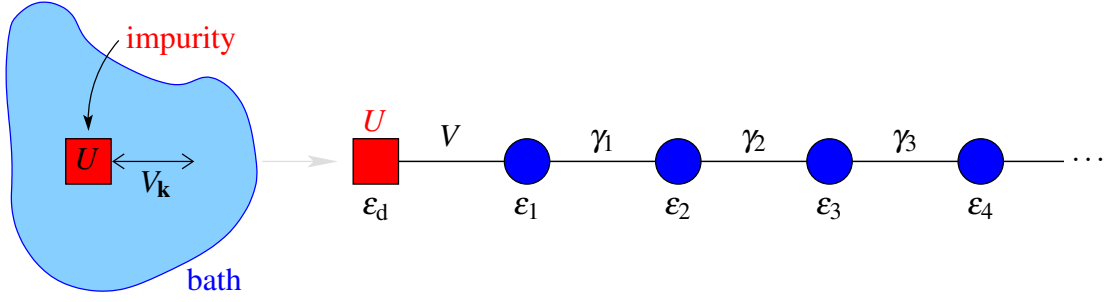


Figure 1.2: *Left:* Cartoon of the single impurity model before the mapping onto a linear chain. *Right:* Single impurity model with the bath as half-infinite chain.

in the local moment regime and the Schrieffer-Wolff transformation is not applicable. In the Kondo model the d electron is fixed at its lattice site.

We are interested in the intermediate range for the hybridization and the Coulomb interaction. Thus we treat the more general Anderson model where double or zero occupancies of the impurity site are allowed. This gives rise to interesting high energy features in the one-particle dynamics of the SIAM which are not present in s-d models.

1.4 Linear chain version of the SIAM

For a theoretical investigation of the Anderson model (1.9) with a method designed for the treatment of low-dimensional quantum systems it is very efficient to map the Hamiltonian onto a linear chain (see Fig. 1.2). The result of this mapping is a representation of the single impurity Anderson model as a semi-infinite tight-binding chain with the impurity at the head of the chain and nearest-neighbor hopping only. The bath of conduction electrons is characterized by a continued fraction representation [Vis94] of the hybridization function.

The creation operators $c_{\mathbf{k},\sigma}^\dagger$ of the N_c conduction electrons directly coupled to the impurity via the hybridization $V_{\mathbf{k}}$ are superposed to a new operator $c_{1,\sigma}^\dagger$,

$$c_{1,\sigma}^\dagger = \frac{1}{V} \sum_{\mathbf{k}} V_{\mathbf{k}} c_{\mathbf{k},\sigma}^\dagger \quad \text{with} \quad V^2 := \sum_{\mathbf{k}} |V_{\mathbf{k}}|^2. \quad (1.13)$$

The operator $c_{1,\sigma}^\dagger$ is the creation operator for a localized one-electron state $|1\rangle$ on the first

⁹Note that the hybridization matrix elements $V_{\mathbf{k}}$ decay like $1/\sqrt{N_c}$ which makes the sum defining V^2 in Eq. (1.13) finite.

site of the conduction electron chain,

$$|1\rangle = c_{1,\sigma}^\dagger |0\rangle, \quad (1.14)$$

where $|0\rangle$ denotes the Fock vacuum. With $c_{1,\sigma}^\dagger$ and $c_{1,\sigma}$ the hybridization part of (1.9) can be written as

$$\sum_{\mathbf{k},\sigma} \left(V_{\mathbf{k}} d_{\sigma}^\dagger c_{\mathbf{k},\sigma} + V_{\mathbf{k}}^* c_{\mathbf{k},\sigma}^\dagger d_{\sigma} \right) = \sum_{\sigma} V \left(d_{\sigma}^\dagger c_{1,\sigma} + c_{1,\sigma}^\dagger d_{\sigma} \right). \quad (1.15)$$

We introduced the hybridization V as a real positive definite number here. Assume, $V \rightarrow Ve^{i\phi}$ is complex. Then we can gauge away this additional phase by applying a unitary transformation to the operators $c_{1,\sigma}^\dagger \rightarrow c_{1,\sigma}^\dagger e^{-i\phi}$. Thus, to keep things as simple as possible, we restrict ourselves to the case of real ‘‘hopping amplitudes’’ V and γ_i . The latter ones are introduced in the next step.

The contribution \mathcal{H}_c from the free conduction electrons [cf. Eq. (1.2)],

$$\mathcal{H}_c = \sum_{\mathbf{k},\sigma} \varepsilon_{\mathbf{k}} c_{\mathbf{k},\sigma}^\dagger c_{\mathbf{k},\sigma},$$

to the full Hamiltonian (1.9) is transformed using a Lanczos tridiagonalization [Lan50]. A new single-particle basis for the conduction electron states starting the state $|1\rangle$ is constructed. We get a sequence of new basis states for the conduction electrons by applying a Schmidt orthogonalization to $|1\rangle, \mathcal{H}_c|1\rangle, \mathcal{H}_c^2|1\rangle, \dots, \mathcal{H}_c^{N_c-1}|1\rangle$. Given the state $|1\rangle$, the next basis state $|2\rangle$ can be constructed from $|1\rangle$ and $\mathcal{H}_c|1\rangle$,

$$|2\rangle = \frac{1}{\gamma_1} \left(\mathcal{H}_c|1\rangle - |1\rangle \langle 1|\mathcal{H}_c|1\rangle \right), \quad (1.16)$$

where the orthogonality $\langle 2|1\rangle = 0$ is obvious and γ_1 has to be chosen as to normalize $|2\rangle$. The recursive relation to get the $(n+1)$ th state $|n+1\rangle$ for $1 < n < (N_c - 1)$ of the basis set from the two ‘‘precursors’’ reads

$$|n+1\rangle = \frac{1}{\gamma_n} \left(\mathcal{H}_c|n\rangle - |n\rangle \langle n|\mathcal{H}_c|n\rangle - |n-1\rangle \langle n-1|\mathcal{H}_c|n\rangle \right), \quad (1.17)$$

where again γ_n normalizes $|n+1\rangle$. This procedure guarantees orthonormality for all states $|1\rangle, \dots, |N_c\rangle$ of the new conduction electron basis.¹⁰ Multiplying Eq. (1.17) on the left by

¹⁰ A more frequently-used notation is: Choose an initial arbitrary Lanczos vector $|1\rangle$. The second Lanczos vector is given by $|2\rangle = \mathcal{H}_c|1\rangle - a_1|1\rangle$ with $a_1 = \langle 1|\mathcal{H}_c|1\rangle / \langle 1|1\rangle$. The next Lanczos vectors for $n > 1$ are calculated using $|n+1\rangle = \mathcal{H}_c|n\rangle - a_n|n\rangle - b_n^2|n-1\rangle$ with $a_n = \langle n|\mathcal{H}_c|n\rangle / \langle n|n\rangle$ and $b_n^2 = \langle n-1|\mathcal{H}_c|n\rangle / \langle n-1|n-1\rangle$.

a state $\langle m|$ and exploiting the hermiticity of \mathcal{H}_c we find the matrix elements

$$\langle m|\mathcal{H}_c|n\rangle = \begin{cases} \varepsilon_n & \text{if } m = n, \\ \gamma_n & \text{if } m = n + 1, \\ \gamma_{n-1} & \text{if } m = n - 1, \\ 0 & \text{else,} \end{cases} \quad (1.18)$$

where we introduced the ε_n as the diagonal elements of \mathcal{H}_c , i. e. $\langle n|\mathcal{H}_c|n\rangle = \varepsilon_n$. Thus, the Hamiltonian is tridiagonal in the new basis and \mathcal{H}_c acting on a state yields

$$\begin{aligned} \mathcal{H}_c|1\rangle &= \gamma_1|2\rangle + \varepsilon_1|1\rangle \\ \mathcal{H}_c|n\rangle &= \gamma_n|n+1\rangle + \varepsilon_n|n\rangle + \gamma_{n-1}|n-1\rangle \quad (1 < n < N_c) \\ \mathcal{H}_c|N_c\rangle &= \varepsilon_{N_c}|N_c\rangle + \gamma_{N_c-1}|N_c-1\rangle \end{aligned} \quad (1.19)$$

and the conduction electron Hamiltonian in second quantized form becomes a tight binding linear chain

$$\mathcal{H}_c = \sum_{i=1, \sigma}^{N_c} \varepsilon_i c_{i, \sigma}^\dagger c_{i, \sigma} + \sum_{i=1, \sigma}^{N_c-1} \gamma_i \left(c_{i, \sigma}^\dagger c_{i+1, \sigma} + c_{i+1, \sigma}^\dagger c_{i, \sigma} \right), \quad (1.20)$$

with nearest-neighbor hoppings only. In the case of $N_c = \infty$ we get a semi-infinite chain for the representation of the conduction electrons. For the numerical solution of the SIAM we have to restrict ourselves to finite N_c anyway, so it is useful to keep N_c in the formulas. For practical calculations N_c has to be chosen large enough to yield a good approximation for the thermodynamic limit of the conduction electron band. Typical values of N_c in the DMRG calculations will be between 120 and 400 at most.¹¹ Using (1.15) and (1.20) the full interacting single impurity Anderson model Hamiltonian (1.9) can be written as

$$\begin{aligned} \mathcal{H} &= \sum_{\sigma} \varepsilon_d n_{d, \sigma} + \sum_{i=1, \sigma}^{N_c} \varepsilon_i c_{i, \sigma}^\dagger c_{i, \sigma} + U n_{d, \uparrow} n_{d, \downarrow} + \\ &\sum_{\sigma} V \left(d_{\sigma}^\dagger c_{1, \sigma} + c_{1, \sigma}^\dagger d_{\sigma} \right) + \sum_{i=1, \sigma}^{N_c-1} \gamma_i \left(c_{i, \sigma}^\dagger c_{i+1, \sigma} + c_{i+1, \sigma}^\dagger c_{i, \sigma} \right). \end{aligned} \quad (1.21)$$

¹¹Strictly speaking, we should use the numbers 119 and 399 here. The total number of fermions N_f (one impurity plus N_c conduction electrons) will be kept even for calculations in the metallic regime, thus N_c will be odd.

Introducing the impurity site as site “0” using the compact notation

$$\varepsilon_0 := \varepsilon_d \quad \gamma_0 := V \quad c_{0,\sigma}^{(\dagger)} := d_{\sigma}^{(\dagger)} \quad n_{i,\sigma} := c_{i,\sigma}^{\dagger} c_{i,\sigma} \quad (1.22)$$

the SIAM Hamiltonian (1.21) reads

$$\mathcal{H} = \sum_{i=0,\sigma}^{N_c} \varepsilon_i n_{i,\sigma} + U n_{0,\uparrow} n_{0,\downarrow} + \sum_{i=0,\sigma}^{N_c-1} \left(\gamma_i c_{i,\sigma}^{\dagger} c_{i+1,\sigma} + \text{h.c.} \right). \quad (1.23)$$

In this representation the coefficients ε_i and γ_i for $i > 0$ are the continued fraction coefficients of the hybridization function [Pet85, Vis94],

$$\Gamma(z) = V^2 \Delta(z) \quad \text{with} \quad z := \omega + i0^+ \quad (1.24)$$

and

$$\Delta(z) = \langle 1 | \frac{1}{z - \mathcal{H}_c} | 1 \rangle. \quad (1.25)$$

The connection between the tridiagonal Hamiltonian and the continued fraction representation of $\Delta(z)$ can be established recognizing that the resolvent (1.25) is given by the (11)-element of the inverse of the $(N_c \times N_c)$ -matrix $[z - \mathcal{H}_c]$ gained by the Lanczos algorithm,

$$\langle 1 | \frac{1}{z - \mathcal{H}_c} | 1 \rangle = [[z - \mathcal{H}_c]^{-1}]_{11}. \quad (1.26)$$

with

$$[z - \mathcal{H}_c] = \begin{pmatrix} (z - \varepsilon_1) & -\gamma_1 & & & \\ -\gamma_1 & (z - \varepsilon_2) & -\gamma_2 & & \\ & -\gamma_2 & (z - \varepsilon_3) & -\gamma_3 & \\ & & & \ddots & \ddots & \ddots \end{pmatrix}. \quad (1.27)$$

For a tridiagonal matrix $[z - \mathcal{H}_c]$ this matrix element can be expressed as the ratio of two determinants [Vis94],

$$\Delta(z) = \frac{T_2(z)}{T_1(z)}. \quad (1.28)$$

The determinant of the full matrix $[z - \mathcal{H}_c]$ is denoted with $T_1(z)$, whereas $T_i(z)$ ($1 < i \leq N_c$) has the first $(i - 1)$ rows and columns of $[z - \mathcal{H}_c]$ omitted and $T_{N_c+1} := 1$. Using a Laplace expansion for the first column of $T_1(z)$ we find [Kar04b]

$$T_1(z) = (z - \varepsilon_1) T_2(z) - \gamma_1^2 T_3(z). \quad (1.29)$$

The general recursion relation for the determinants $T_i(z)$ is then given by

$$\begin{aligned} T_i(z) &= (z - \varepsilon_i)T_{i+1}(z) + \gamma_i^2 T_{i+2}(z) \quad \text{for } i = 1, \dots, N_c - 2 \\ T_{N_c-1}(z) &= (z - \varepsilon_{N_c-1})T_{N_c}(z) + \gamma_{N_c-1}^2 \\ T_{N_c}(z) &= (z - \varepsilon_{N_c}) . \end{aligned} \quad (1.30)$$

Inserting

$$\frac{T_i(z)}{T_{i+1}(z)} = (z - \varepsilon_i) + \gamma_i^2 \frac{T_{i+2}(z)}{T_{i+1}(z)} \quad (1.31)$$

into Eq. (1.28) recursively yields $\Delta(z)$ in continued fraction representation,

$$\Delta(z) = \frac{T_2(z)}{T_1(z)} = \frac{1}{z - \varepsilon_1 - \gamma_1^2 \frac{T_3(z)}{T_2(z)}} = \frac{1}{z - \varepsilon_1 - \frac{\gamma_1^2}{z - \varepsilon_2 - \gamma_2^2 \frac{T_4(z)}{T_3(z)}}} = \dots . \quad (1.32)$$

Hence, the hybridization function can be written as continued fraction via

$$\Gamma(z) = \frac{V^2}{z - \varepsilon_1 - \frac{\gamma_1^2}{z - \varepsilon_2 - \frac{\gamma_2^2}{z - \varepsilon_3 - \dots}}} . \quad (1.33)$$

or for finite N_c as

$$\Gamma(z) = \frac{V^2}{z - \varepsilon_1 - \frac{\gamma_1^2}{z - \varepsilon_2 - \frac{\dots}{z - \varepsilon_{N_c-1} - \frac{\gamma_{N_c-1}^2}{z - \varepsilon_{N_c}}}}} . \quad (1.34)$$

In this way, the bath of conduction electrons is represented by the coefficients $\gamma_i \geq 0$ and ε_i in (1.21). They are the coefficients of the continued fraction of the hybridization function $\Gamma(z)$.

1.5 Single-particle dynamics of the symmetric SIAM

The model investigated at zero temperature is the fully particle-hole symmetric version of the single impurity Anderson model using the linear chain representation derived in

the [previous section](#). Before we specialize in the symmetric case, let us briefly collect the more general things first. The dynamics we wish to compute is the dynamics of the fermionic single-particle propagator of the d electron representing the impurity which is correlated due to the interaction $U > 0$. Aiming at the properties at $T = 0$, the one-particle Green function reads

$$G^>(\omega + i\eta) = \left\langle 0 \left| d_\sigma \frac{1}{\omega + i\eta - (\mathcal{H} - E_0)} d_\sigma^\dagger \right| 0 \right\rangle \quad (1.35)$$

$$G^<(\omega + i\eta) = \left\langle 0 \left| d_\sigma^\dagger \frac{1}{\omega + i\eta + (\mathcal{H} - E_0)} d_\sigma \right| 0 \right\rangle \quad (1.36)$$

where the superscripts $>$ and $<$ imply that $G^>$ and $G^<$ represent only the part of the usual Green function at positive or negative frequencies, respectively. Here the ground state is denoted by $|0\rangle$ and its energy by E_0 . Since we focus on a spin-disordered solution the propagator has no dependence on the spin index σ . Hence it is not denoted as argument of G . The frequencies ω and η are real. The complete propagator is recovered by

$$G(\omega + i\eta) = G^>(\omega + i\eta) + G^<(\omega + i\eta) \quad (1.37)$$

and the standard retarded Green function is obtained for $\eta \rightarrow 0^+$,

$$\begin{aligned} G_{\text{R}}^>(\omega) &= \lim_{\eta \rightarrow 0^+} G^>(\omega + i\eta) \\ G_{\text{R}}^<(\omega) &= \lim_{\eta \rightarrow 0^+} G^<(\omega + i\eta) \\ G_{\text{R}}(\omega) &= \lim_{\eta \rightarrow 0^+} G(\omega + i\eta) . \end{aligned} \quad (1.38)$$

The quantity we are looking for is the spectral density

$$\rho(\omega) := -\frac{1}{\pi} \Im G_{\text{R}}(\omega) . \quad (1.39)$$

If necessary the real part can be obtained from the Kramers-Kronig relation

$$\Re G(\omega) = -\frac{1}{\pi} \mathcal{P} \int_{-\infty}^{\infty} d\zeta \frac{\Im G(\zeta)}{\omega - \zeta} \quad (1.40)$$

with \mathcal{P} denoting the Cauchy principal value and dropping the subscript R from now on as we only deal with retarded Green functions.

The experimental methods by which the spectra removing ($G^<$) and adding ($G^>$) electrons can be measured, are photoemission spectroscopy (PES) [[Ley79](#)] and inverse pho-

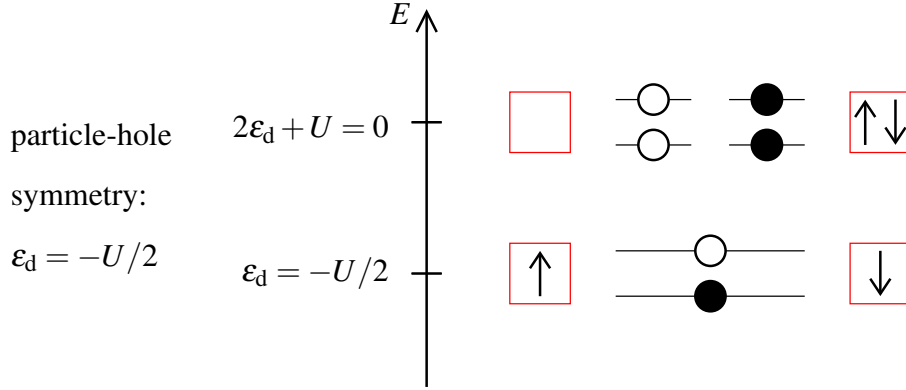


Figure 1.3: Configurations for the impurity state assuming the hybridization vanishes, $V = 0$, and setting $\varepsilon_F = 0$. Compare this scenario with the general case depicted in [Fig. 1.1](#).

toemission spectroscopy (IPES)¹², respectively. In PES photons incident on a sample excite photoelectrons which are detected and analyzed for their kinetic energies, whereas in IPES the reverse experiment is performed (cf. Ref. [\[All05\]](#) and references therein).

In the [previous section 1.4](#) we introduced the SIAM in a linear chain version (1.21) with arbitrary hybridization function $\Gamma(z)$ describing the coupling of the conduction electron bath and the impurity d electron. The one-particle Green function for the non-interacting case $U = 0$ is then given by ($z := \omega + i0^+$)

$$G_0(z) = \frac{1}{z - \varepsilon_d - \Gamma(z)} = \frac{1}{z - \varepsilon_d - V^2 \Delta(z)} = \frac{1}{z - \varepsilon_0 - \frac{\gamma_0^2}{z - \varepsilon_1 - \frac{\gamma_1^2}{z - \varepsilon_2 - \dots}}} \quad (1.41)$$

and the corresponding free density of states (DOS) is

$$\rho_0(\omega) := -\frac{1}{\pi} \Im \lim_{\eta \rightarrow 0^+} G_0(\omega + i\eta). \quad (1.42)$$

As any hybridization function with non-negative DOS can be represented by an appropriate choice of the γ_i and ε_i , the representation of the bath as semi-infinite chain does not restrict the generality of the model. Note that $\Delta(z)$ is by construction the single-particle propagator of the first site of the conduction electron chain, cf. Eqs. (1.14) and (1.25).

If $\varepsilon_d = \varepsilon_0 = \varepsilon_F - U/2$ the model is symmetric in the atomic limit $V = 0$: the impurity levels in the one-particle spectral density are placed symmetrically about the Fermi level

¹²Also known as Bremsstrahlung isochromat spectroscopy (BIS) when performed with X-ray photons [\[Lan79\]](#).

ε_F at (cf. [Fig. 1.3](#) and left plot of [Fig. 1.4](#))

$$\begin{aligned} E_{>} &= E_2 - E_1 = 2\varepsilon_d + U - \varepsilon_d = \varepsilon_F + U/2 & \text{and} \\ E_{<} &= E_1 - E_0 = \varepsilon_d - 0 & = \varepsilon_F - U/2. \end{aligned} \quad (1.43)$$

Choosing also an conduction band which is symmetric about the Fermi level and half filled, the model has complete *particle-hole symmetry* and the impurity state is on average singly occupied, $\langle n_d \rangle = 1$,

$$\varepsilon_d = \varepsilon_0 = -U/2 \quad \text{and} \quad \varepsilon_i = 0 \quad \forall_{i>0} \quad \Rightarrow \quad \text{particle-hole symmetric}, \quad (1.44)$$

where the chemical potential is set to $\mu = \varepsilon_F = 0$. For the particle-hole symmetric case (half-filling and symmetric conduction band) the SIAM Hamiltonian is conveniently written in symmetrized form

$$\mathcal{H} = U (n_{d,\uparrow} - 1/2) (n_{d,\downarrow} - 1/2) + \sum_{\sigma} V (d_{\sigma}^{\dagger} c_{1,\sigma} + \text{h.c.}) + \sum_{i=1, \sigma}^{N_c-1} \gamma_i (c_{i,\sigma}^{\dagger} c_{i+1,\sigma} + \text{h.c.}) \quad (1.45)$$

which differs for the parameter choice (1.44) from [Eq. \(1.21\)](#) only by a constant $U/4$. [Eq. \(1.45\)](#) is invariant under particle-hole transformations. In the particle-hole symmetric case, the Green function and the DOS fulfill the symmetry relations

$$\begin{aligned} \Re G(\omega + i\eta) &= -\Re G(-\omega + i\eta) \\ \Im G(\omega + i\eta) &= \Im G(-\omega + i\eta) \\ \rho(\omega) &= \rho(-\omega) \end{aligned} \quad (1.46)$$

and the reconstruction of the full Green function is much easier because only $G^>(z)$ is needed,

$$G(\omega + i\eta) = G^>(\omega + i\eta) - G^>(-\omega - i\eta) = G^>(\omega + i\eta) + G^>(-\omega + i\eta). \quad (1.47)$$

We will restrict ourselves to this particle hole-symmetric case and look at a generic situation with finite band width $W = 2D$. For simplicity we choose a $\Delta(\omega)$ with semi-elliptic DOS, i. e., $\gamma_i = D/2$ for $i > 0$. The full free Green function G_0 can be easily constructed using the recurrence relations used in the [previous section](#). The partitioning of the matrix $[z - \mathcal{H}_c]$ led to the result

$$\Delta_1(z) := \Delta(z) = \frac{1}{z - \gamma_1^2 \Delta_2(z)} \quad \text{with} \quad \Delta_i(z) = \frac{1}{z - \gamma_i^2 \Delta_{i+1}(z)}. \quad (1.48)$$

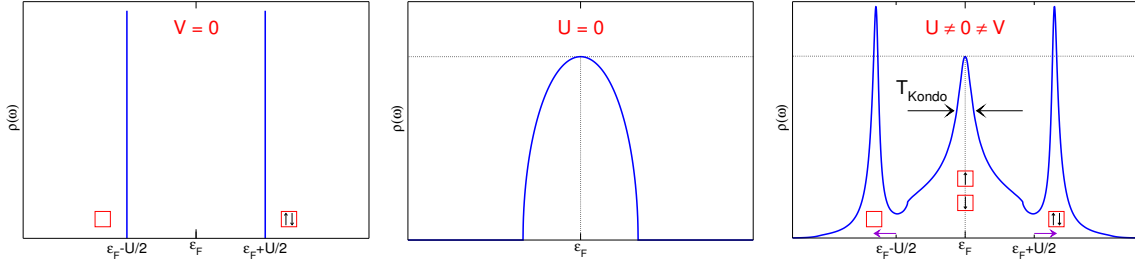


Figure 1.4: Schematic scenarios for the one-particle density of states of the particle-hole symmetric SIAM. *Left:* atomic limit ($V = 0$) with δ -peaks at the impurity levels. *Middle:* non-interacting case ($U = 0$) with semi-elliptic $\rho(\omega) = \rho_0(\omega)$. *Right:* interacting case with non-vanishing hybridization V and finite interaction U yields the typical three-peak structure of upper and lower Hubbard bands/peaks and the Abrikosov-Suhl resonance (ASR).

For the specific parameter choice of a homogeneous conduction electron chain with $N_c = \infty$

$$(\gamma_i := \gamma := D/2 \quad \text{for } i > 0) \quad \Rightarrow \quad \Delta_1(z) = \Delta_2(z), \quad (1.49)$$

so Eq. (1.48) becomes a quadratic equation for $\Delta_1(z)$ with the solution

$$\Delta(z) = \frac{1}{2\gamma^2} \left(z \pm \sqrt{z^2 - (2\gamma)^2} \right) = \frac{2}{D^2} \left(z \pm \sqrt{z^2 - D^2} \right) \quad (1.50)$$

where the signs have to be chosen such that $\Re \epsilon \Delta(z)$ decays like $1/\Re \epsilon(z)$ and that the imaginary part is negative semi-definite, $\Im \Delta(z) \leq 0$. This yields

$$\Delta(\omega + i\eta) = \frac{2}{D^2} \left(z - \text{sgn}(\omega) \sqrt{(\omega + i\eta)^2 - D^2} \right) \quad (1.51)$$

$$\Delta(\omega) = \frac{2}{D^2} \cdot \begin{cases} \left(\omega - \text{sgn}(\omega) \sqrt{\omega^2 - D^2} \right) & \text{for } |\omega| > D \\ \left(\omega - \sqrt{\omega^2 - D^2} \right) & \text{for } |\omega| \leq D. \end{cases} \quad (1.52)$$

Choosing also $V = \gamma_0 = D/2$, the free Green function

$$G_0(z) = \frac{1}{z - V^2 \Delta(z)} \quad (1.53)$$

is (for $N_c = \infty$) equal to $\Delta(z)$ and the free DOS of the d-electron is also semi-elliptic (cf. middle plot of Fig. 1.4),

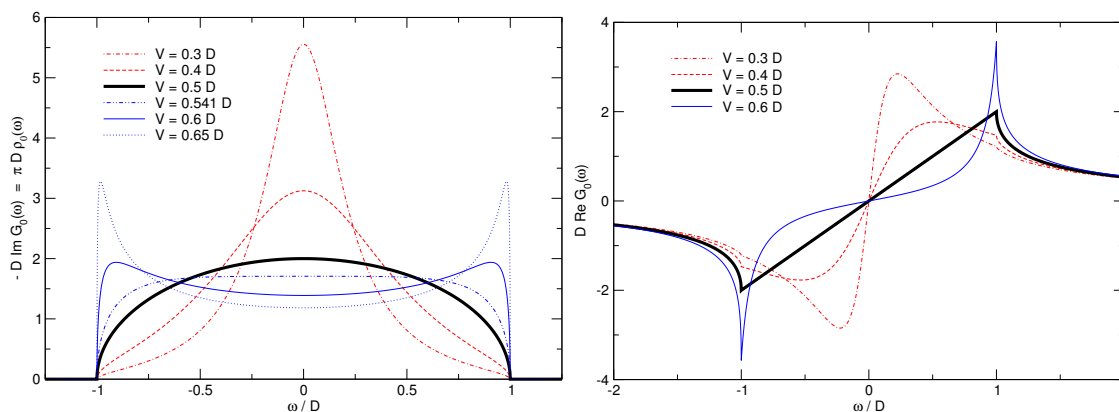


Figure 1.5: Free Green function for $\gamma_i = \gamma = D/2$ ($i > 0$) and various values of V . Choosing $V = \gamma = D/2$, the imaginary part of the Green function is also semi-elliptic. *Left:* imaginary part. *Right:* real part.

$$\rho_0(\omega) = \begin{cases} \frac{2\sqrt{D^2 - \omega^2}}{\pi D^2} & \text{if } |\omega| \leq D \\ 0 & \text{else.} \end{cases} \quad (1.54)$$

Fig. 1.5 shows the imaginary (left) and real (right) parts of the free Green function for various values of V . The imaginary part $\Im m G_0 = -1/\pi \rho_0$ is for most of the calculations chosen to be semi-elliptic, i. e. $V = D/2$. For $V \geq D/\sqrt{2} \approx 0.707D$ bound states at $\omega_b = \pm 2V^2/\sqrt{(2V)^2 - D^2}$ emerge from the bare band with a spectral weight of $I(V) = [2V^2 - D^2]/[(2V)^2 - D^2]$ for each of the peaks according to

$$I^{-1} = \left. \frac{\partial G_0^{-1}(\omega)}{\partial \omega} \right|_{\omega=\omega_b}. \quad (1.55)$$

Note that $I(V = D/\sqrt{2}) = 0$ for $\omega_b(V = D/\sqrt{2}) = D$ and $I(V = \infty) = 1/2$. Another special case is determined by

$$\left. \frac{\partial^2 \Im m G_0(\omega)}{\partial \omega^2} \right|_{\omega=0} \stackrel{!}{=} 0 \quad \Rightarrow \quad V = D \cdot \sqrt{1 \pm 1/\sqrt{2}} \approx \begin{cases} 0.541D \\ 1.307D \end{cases} \quad (1.56)$$

where the smaller value of $V \approx 0.541D$ in regime with no bound states is shown in **Fig. 1.5**. For $V \approx 0.541D$ the free DOS is totally structureless around $\omega \simeq 0$ and is similar to a well-known particular case of the SIAM, the flat-band model [Hew93]. In the case of a real flat-band model, the width of the host band W is much larger than any other energy scales and the hybridization function is assumed to be constant on these scales, $\Gamma(\omega) = \Gamma_0$.

The DOS is chosen such that the overall weight is normalized,

$$\int_{-\infty}^{\infty} \rho_0(\omega) d\omega = 1 = \int_{-D}^D \rho_0(\omega) d\omega \quad (1.57)$$

where the last equals sign only holds for $V \leq D/\sqrt{2}$. The total weight does not change for finite interactions $U > 0$,

$$\int_{-\infty}^{\infty} \rho(\omega) d\omega = \int_{-\infty}^{\infty} \rho_0(\omega) d\omega. \quad (1.58)$$

This can be used as an accuracy benchmark for the numerics.

If the local Coulomb interaction U on the impurity site is switched on a universal three-peak structure emerges which can be understood on a qualitative level from the limiting cases $U = 0$ (non-interactive) and $V = 0$ (atomic limit, isolated impurity). We show a typical scenario in the right plot of [Fig. 1.4](#). The central peak at $\omega = 0$ is the Kondo or Abrikosov-Suhl resonance (ASR). The DOS at $\omega = 0$ is pinned to its non-interacting value

$$\rho_0(\omega = 0) = \frac{D}{2\pi V^2} = \rho(U, \omega = 0) \quad (1.59)$$

$$V := D/2 \quad \Rightarrow \quad \rho_0(\omega = 0) = \frac{2}{\pi D} = \rho(U, \omega = 0) \quad (1.60)$$

independent of U as required by Friedel's sum rule and the density of states rule [[Lut60](#), [Lut61](#), [And91](#), [Hew93](#)]. We take this as check for the reliability of the numerical algorithm. The pinning is visualized in [Fig. 1.4](#) as horizontal line. For larger U (smaller V) the peak's width decreases rapidly so that the ASR is very difficult to resolve [[Nis04b](#)]. The ASR is characterized by the exponentially small Kondo energy scale T_K . This scale can be read off from the spectral densities, for instance as half the width at half the maximum, i. e. at $\pi D \rho(\omega = T_K) = 1$ for $V = D/2$. The analytic formula for the Kondo temperature T_K will be compared with the widths derived from the D-DMRG calculations in [Sect. 4.4](#). This provides a tool to check how and under which conditions very sharp peaks can be resolved systematically with the dynamic density-matrix renormalization group.

An increase in U leads to the formation of Hubbard satellites below and above the free band ([Fig. 1.4](#)). The satellite positions are slightly shifted from the position of the atomic peaks at $\pm U/2$ due to level repulsion. They are situated at energies $\omega_{\text{up/low}} = \pm(U/2 + \delta_{\text{shift}})$, $\delta_{\text{shift}} > 0$ and become more pronounced on increasing U in two ways. They capture more weight and they become sharper. We analyze these features in [Sect. 4.5](#) and compare to results from leading order perturbation theory for the widths and the

shifts of the peaks. The lineshape of the Hubbard satellites is investigated and is found to become asymmetric for large interactions U .

1.6 Density-matrix renormalization for SIAMs

1.6.1 Introduction

So far, the methods applied to the SIAM were designed to capture the low-energy physics, in particular the fixed points and the thermodynamics [Km80a, Sch82]. The numerical renormalization group (NRG) was later extended to calculate also dynamic, i. e., spectral information [Sak89, Cos94]. It provides reliable data on the scale of the Kondo temperatures T_K , see Ref. [Hew93, Bul00a] and references therein. On larger scales, the energy resolution is less well-controlled [Raa04].

But in various applications the behavior at higher energies is important to achieve quantitative accuracy. For instance, the self-consistency cycle of the DMFT mixes modes at all energies. Hence, excellent quantitative control over the dynamics at high energies is indispensable, even if finally only the behavior at low energies matters.

Another application is the optical control of isolated $S=1/2$ impurities or quantum dots coupled to narrow bands [War00, Kar04a]. If the impurities differ so that the energy between the singly occupied ground state and the excited double occupancy differs, they can be switched selectively from the ground state to the double occupancy (and back) by shining light at the resonant frequency onto the sample. The lifetime of the double occupancy, i. e., the inverse line width of the resonance, determines how well the resonance condition has to be met, how selective the switching can be, and how stable the excited state is.

In view of the above, we perform a numerical investigation which aims to describe both the low-energy dynamics and the high-energy dynamics quantitatively. Features at low energies are not as delicately resolved as by NRG, but in return features at high energies are much better under control. We apply the dynamic density-matrix renormalization (D-DMRG) [Hal95, Ram97, Küh99b, Höv00] to compute the one-particle propagator (1.35). The DMRG is a real-space approach [Whi92a, Whi93, Pes99] which works best for open boundary conditions so that it is particularly well-suited to treat impurity problems. In this section we present the representation of the model used in the DMRG program and the observables calculated in this way. A general introduction to DMRG as well as technical and algorithmic details are postponed to [Chapt. 2](#).

1.6.2 Jordan-Wigner transformation for the SIAM

In [Sect. 1.4](#) we derived a linear chain version of the SIAM where the bath of conduction electrons is described by a hybridization function in continued fraction representation, cf. [Fig. 1.2](#). The problem is illustrated in the upper part of [Fig. 1.6](#). The fermionic representation of the model is mapped by two standard Jordan-Wigner transformations [[Jor28](#)] onto two XY spin $1/2$ chains, the S -chain and the T -chain. The S -chain results from the \uparrow fermions, the T -chain from the \downarrow fermions. We map the four possible configurations $\{\uparrow\downarrow\}$, $\{\uparrow-\}$, $\{-\downarrow\}$, $\{-\ -\}$ onto

$$\uparrow = \begin{cases} \text{occupied} \Rightarrow \mathbf{S} \uparrow \\ \text{un-occupied} \Rightarrow \mathbf{S} \downarrow \end{cases} \quad \downarrow = \begin{cases} \text{occupied} \Rightarrow \mathbf{T} \uparrow \\ \text{un-occupied} \Rightarrow \mathbf{T} \downarrow \end{cases}$$

They are coupled at site zero where the density-density coupling is mapped onto the product of z -components. The resulting chain is depicted for the symmetric SIAM in the lower part of [Fig. 1.6](#). The mapping procedure is explained in detail on the following pages. The couplings are given by $\gamma_0 = V$ and γ_i for $i \geq 1$. The mapping from fermions onto spins avoids the fermionic Fock space which would require to keep track of long-range phases. The mapping makes the Hilbert space the direct product of the local Hilbert spaces at each site. The DMRG is a real space blocking scheme where blocks (parts of the full system) are enlarged by one lattice site iteratively. In the spin representation a single site has Hilbert space dimension two, while for a “true” fermionic site the local Hilbert space dimension is four. As the enlarged basis of a block in DMRG is projected onto a reduced basis set, it is clear that the projection error is smallest when the Hilbert space enlargement prior to projection is kept small. Thus, adding a single “Jordan-Wigner site” instead of a “Hubbard site” is advantageous.

In the following we derive the full Jordan-Wigner transformed Hamiltonian in detail. Assume we deal with a spin-up \uparrow for a moment and let us collect some formulas for the \mathbf{S} spins representing the \uparrow fermions of the model. The spin one-half operators $\vec{\mathbf{S}}_i = \{\mathbf{S}_i^x, \mathbf{S}_i^y, \mathbf{S}_i^z\}$ behave in the usual way, i. e.

$$\begin{aligned} [\mathbf{S}_i^a, \mathbf{S}_j^b] &= i\epsilon^{abc} \mathbf{S}_i^c \delta_{i,j} \quad \text{with} \quad \{a, b, c\} = \{x, y, z\} \\ \mathbf{S}_i^\pm &= \mathbf{S}_i^x \pm i\mathbf{S}_i^y \\ [\mathbf{S}_i^-, \mathbf{S}_j^+] &= 2\mathbf{S}_i^z \delta_{i,j} \quad [\mathbf{S}_i^z, \mathbf{S}_j^\pm] = \pm \mathbf{S}_j^\pm \delta_{i,j} \quad (\mathbf{S}_i^-)^2 = (\mathbf{S}_i^+)^2 = 0. \end{aligned}$$

In one dimension, there is a deep connection between the physics of fermions, bosons, and spins that does not hold in higher dimensions [[Sch68](#)]. There are several different hand-waving ways of expressing what is special in one dimension: one way to put it is

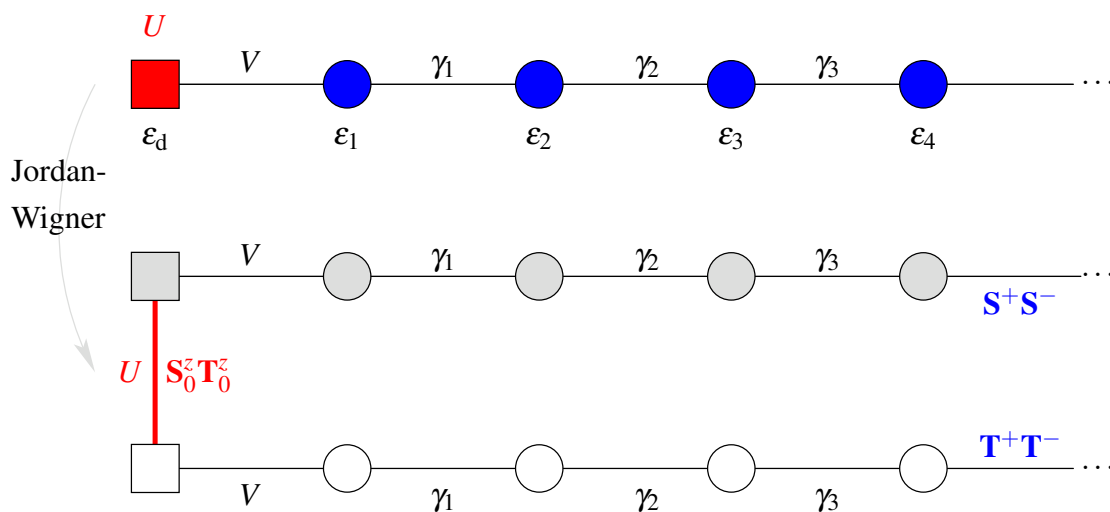


Figure 1.6: *Top:* single impurity model with the bath as half-infinite chain. *Bottom:* equivalent spin model after the Jordan-Wigner transformations: **S**-spins come from \uparrow -fermions, **T**-spins from \downarrow -fermions.

that particle statistics are defined in terms of exchanges of particles. In one dimension any exchange requires that the particles pass through each other (collide), which is not true in higher dimensions. The simplest such transformation that changes the particle statistics in one dimension is the Jordan-Wigner transformation [Jor28]. For a single spin-half, one can try to write it in terms of spinless fermion using

$$c_i^\dagger c_i = \mathbf{S}_i^z + 1/2 \quad c_i^\dagger = \mathbf{S}_i^+ \quad c_i = \mathbf{S}_i^- .$$

However, this will not work for many spins because spins have fermion commutation rules on sites but commute on different sites (i. e. behave like bosons) while fermions anticommute, i. e.

$$\begin{aligned} \{\mathbf{S}_i^-, \mathbf{S}_i^+\} = 1 \quad \text{and} \quad [\mathbf{S}_i^\pm, \mathbf{S}_j^\pm] = 0 \quad (\forall i \neq j) \\ \text{but} \quad \{c_i, c_j^\dagger\} = \delta_{i,j} . \end{aligned}$$

The answer is to add a nonlocal “string” of operators

$$\mathcal{H}_i = \exp \left[i\pi \sum_{j=0}^{i-1} \mathbf{S}_j^+ \mathbf{S}_j^- \right] . \quad (1.61)$$

As

$$\begin{aligned} \exp(\mathbf{S}_i^+ \mathbf{S}_i^-) \exp(\mathbf{S}_j^+ \mathbf{S}_j^-) &= \exp(\mathbf{S}_i^+ \mathbf{S}_i^- + \mathbf{S}_j^+ \mathbf{S}_j^-) \quad \forall i, j \\ \text{because } [\mathbf{S}_i^+ \mathbf{S}_i^-, \mathbf{S}_j^+ \mathbf{S}_j^-] &= 0 \quad \forall i, j \end{aligned}$$

we may use

$$\begin{aligned} \exp[\pm i\pi \mathbf{S}_i^+ \mathbf{S}_i^-] &= \exp(\pm i\pi) \mathbf{S}_i^+ \mathbf{S}_i^- = (-1)^{\mathbf{S}_i^+ \mathbf{S}_i^-} = \begin{cases} +1 & \text{if } \mathbf{S}_i^+ \mathbf{S}_i^- = 0 \\ -1 & \text{if } \mathbf{S}_i^+ \mathbf{S}_i^- = 1 \end{cases} \\ &= 1 - 2\mathbf{S}_i^+ \mathbf{S}_i^- . \end{aligned} \quad (1.62)$$

Using (1.62) in Eq. (1.61) yields a simple expression for \mathcal{H}_i ,

$$\mathcal{H}_i = \prod_{j=0}^{i-1} [1 - 2\mathbf{S}_j^+ \mathbf{S}_j^-] . \quad (1.63)$$

The Jordan-Wigner strings \mathcal{H}_i obey the following identities

$$\begin{aligned} \mathcal{H}_i \mathcal{H}_i^\dagger &= \mathcal{H}_i^\dagger \mathcal{H}_i = \mathcal{H}_i^2 = 1 \\ \mathcal{H}_i \mathcal{H}_j &= \mathcal{H}_j \mathcal{H}_i \\ \mathcal{O}_i \mathcal{H}_j &= \eta \mathcal{H}_j \mathcal{O}_i \end{aligned}$$

for $\mathcal{O}_i \in \{\mathbf{S}_i^\pm\}$, and $\eta = +1$ for $i \geq j$ but $\eta = -1$ if $i < j$. Using (1.63) the explicit transformations for the fermionic operators read

$$c_i = \mathcal{H}_i \mathbf{S}_i^- = \exp \left[i\pi \sum_{j=0}^{i-1} \mathbf{S}_j^+ \mathbf{S}_j^- \right] \mathbf{S}_i^- \quad d = c_0 = \mathbf{S}_0^- \quad (1.64)$$

$$c_i^\dagger = \mathbf{S}_i^+ \mathcal{H}_i^\dagger = \mathbf{S}_i^+ \exp \left[-i\pi \sum_{j=0}^{i-1} \mathbf{S}_j^+ \mathbf{S}_j^- \right] \quad d^\dagger = c_0^\dagger = \mathbf{S}_0^+ . \quad (1.65)$$

One can check that these preserve the ordinary spin [and (for the inverse relations) the fermionic] commutation relations. The reason the Jordan-Wigner transform works is very simple: the string is designed such that so that it changes sign from $+1$ to -1 depending on whether the number of fermions to the left of site i is even or odd.

Now let us transform the operators appearing in the fermionic Hamiltonian. The density

operators read

$$\begin{aligned} n_i = c_i^\dagger c_i &= \mathbf{S}_i^+ \exp[i\pi 0] \mathbf{S}_i^- = \mathbf{S}_i^+ \mathbf{S}_i^- = 1/2 + \mathbf{S}_i^z \quad \Leftrightarrow \quad \mathbf{S}_i^z = n_i - 1/2 \\ c_i c_i^\dagger &= \mathbf{S}_i^- \exp[i\pi 0] \mathbf{S}_i^+ = \mathbf{S}_i^- \mathbf{S}_i^+ = 1/2 - \mathbf{S}_i^z . \end{aligned}$$

The hopping terms are translated via

$$\begin{aligned} c_i^\dagger c_{i+1} &= \mathbf{S}_i^+ \exp[i\pi \mathbf{S}_i^+ \mathbf{S}_i^-] \mathbf{S}_{i+1}^- = \mathbf{S}_i^+ [1 - 2\mathbf{S}_i^+ \mathbf{S}_i^-] \mathbf{S}_{i+1}^- \\ &= [\mathbf{S}_i^+ - \underbrace{2\mathbf{S}_i^+ \mathbf{S}_i^+ \mathbf{S}_i^-}_0] \mathbf{S}_{i+1}^- = \mathbf{S}_i^+ \mathbf{S}_{i+1}^- \\ c_{i+1}^\dagger c_i &= \mathbf{S}_{i+1}^+ \exp[-i\pi \mathbf{S}_{i+1}^+ \mathbf{S}_i^-] \mathbf{S}_i^- = \mathbf{S}_{i+1}^+ [1 - 2\mathbf{S}_i^+ \mathbf{S}_i^-] \mathbf{S}_i^- \\ &= \mathbf{S}_{i+1}^+ [\mathbf{S}_i^- - \underbrace{2\mathbf{S}_i^+ \mathbf{S}_i^- \mathbf{S}_i^-}_0] = \mathbf{S}_{i+1}^+ \mathbf{S}_i^- . \end{aligned}$$

Using the new spin representations \mathbf{S} and \mathbf{T} of the fermionic operators we find for the Jordan-Wigner representation of the SIAM Hamiltonian (1.21)

$$\begin{aligned} \mathcal{H} &= U/4 + \varepsilon_d + \sum_{i=1}^{N_c} \varepsilon_i + (\varepsilon_d + U/2) (\mathbf{S}_0^z + \mathbf{T}_0^z) + \sum_{i=1}^{N_c} \varepsilon_i (\mathbf{S}_i^z + \mathbf{T}_i^z) \\ &\quad + U \mathbf{S}_0^z \mathbf{T}_0^z + \sum_{i=0}^{N_c-1} [\gamma_i (\mathbf{S}_i^+ \mathbf{S}_{i+1}^- + \mathbf{T}_i^+ \mathbf{T}_{i+1}^-) + \text{h.c.}] . \end{aligned} \quad (1.66)$$

For the particle-hole symmetric case, cf. Eq. (1.44),

$$\varepsilon_d = \varepsilon_0 = -U/2 \quad \text{and} \quad \varepsilon_i = 0 \quad \forall_{i>0} ,$$

we find

$$\begin{aligned} \mathcal{H} &= -U/4 + U \mathbf{S}_0^z \mathbf{T}_0^z + \sum_{i=0}^{N_c} [\gamma_i (\mathbf{S}_i^+ \mathbf{S}_{i+1}^- + \mathbf{T}_i^+ \mathbf{T}_{i+1}^-) + \text{h.c.}] \\ &= (V \mathbf{S}_0^+ \mathbf{S}_1^- + \text{h.c.}) + \sum_{i=1}^{N_c} (\gamma_i \mathbf{S}_i^+ \mathbf{S}_{i+1}^- + \text{h.c.}) + U \mathbf{S}_0^z \mathbf{T}_0^z + \text{const.} \\ &\quad + (V \mathbf{T}_0^+ \mathbf{T}_1^- + \text{h.c.}) + \sum_{i=1}^{N_c} (\gamma_i \mathbf{T}_i^+ \mathbf{T}_{i+1}^- + \text{h.c.}) . \end{aligned} \quad (1.67)$$

The constant shift of $-U/4$ drops out if we use the particle-hole symmetric Hamiltonian (1.45). Thus, the constant shift can be safely omitted.

1.6.3 Green function of the SIAM

The DMRG can easily determine the ground state $|0\rangle$ and its energy E_0 for a finite chain. So the chain in the lower part of [Fig. 1.6](#) is truncated such that there are N_f spins in the upper and in the lower part of the chain corresponding originally to a finite bath representation of $N_c = N_f - 1$ fermions plus the impurity. The dynamic quantity we are interested in is the retarded Green function at zero temperature ([1.35](#)). In terms of the spin operators it reads

$$G^>(\omega + i\eta) = \left\langle 0 \left| \mathbf{S}_0^- \frac{1}{\omega + i\eta - (\mathcal{H} - E_0)} \mathbf{S}_0^+ \right| 0 \right\rangle. \quad (1.68)$$

In the symmetric case, the complete Green function $G(\omega + i\eta)$ is recovered via ([1.47](#)), while in the asymmetric case,

$$G^<(\omega + i\eta) = \left\langle 0 \left| \mathbf{S}_0^+ \frac{1}{\omega + i\eta + (\mathcal{H} - E_0)} \mathbf{S}_0^- \right| 0 \right\rangle \quad (1.69)$$

must be determined separately and ([1.37](#)) has to be used. We stress that $G(\omega + i\eta)$ is the fermionic propagator even though it is computed in terms of spins after the Jordan-Wigner mapping, cf. Eqs. ([1.64](#)) and ([1.65](#)). As the fermionic propagator is evaluated for the head of the chain no additional phase factors appear in Eqs. ([1.68](#), [1.69](#)) after the Jordan-Wigner transformation.

The key idea of the dynamic DMRG is to include the real and the imaginary part of a frequency dependent correction vector $|\xi\rangle$ in the target states of a standard DMRG algorithm [[Ram97](#), [Küh99b](#), [Höv00](#)]. The natural choice is

$$|\xi\rangle = \frac{1}{\omega + i\eta - (\mathcal{H} - E_0)} \mathbf{S}_0^+ |0\rangle. \quad (1.70)$$

The computation of $|\xi\rangle$ is numerically the most demanding step due to the inversion of an almost singular non-hermitian matrix. We prefer to stabilize this inversion by optimized algorithms [[Fre92a](#)] instead of using the variational approach proposed by Jeckelmann [[Jec02](#)] which requires a minimization in a high-dimensional Hilbert space. The details of these “correction vector D-DMRG” schemes are postponed to [Sect. 2.2.3](#).

The numerical calculations cannot be performed for $\eta = 0$. Even small values of η are very time consuming. So we compute first $G(\omega + i\eta)$ at finite η . The spectral density ([1.39](#))

$$\rho^{(\eta)}(\omega) := -\frac{1}{\pi} \Im G(\omega + i\eta) \quad (1.71)$$

can be seen as the actual spectral density $\rho(\omega)$ convolved by the Lorentzian

$$\rho_L(\omega) = \frac{\eta}{\pi(\omega^2 + \eta^2)} \quad (1.72)$$

of width η . Hence it is possible to retrieve $\rho(\omega)$ by deconvolution. A standard technique for deconvolution is Fourier transformation, realized best by fast Fourier transforms, division by $\exp(-\eta\tau)$ plus low-pass filtering, and the inverse transform. A flexible alternative with similar properties is the explicit matrix inversion of the convolution procedure [Geb03, Raa04]. A third variant of deconvolution is the non-linear Least Bias (LB) algorithm [Raa04], which belongs to the class of maximum entropy methods. We present these deconvolution schemes in [Chapt. 3](#).

1.6.4 Self-energy of the SIAM via the Q -function

The key problem that must be solved to determine the dynamics of the SIAM is the calculation of the full local Green function $G(z)$ (1.37) or, equivalently, the local self-energy $\Sigma(z)$. In this section a sum rule for the self-energy $\Sigma(z)$ of single impurity models is derived. This sum rule provides a simple check for numerical and analytical impurity solvers.

In a first step we follow Ref. [Bu98] and derive a representation of $\Sigma(z)$ which turned out to be numerically more stable in NRG calculations. We then go one step further following Ref. [Uhr03] and derive the “improper” self-energy $Q(z)$ and the relations between $G(z)$, $\Sigma(z)$, $Q(z)$ and their corresponding sum rules.

A convenient representation of the generic single impurity Anderson model (1.9) to be solved is given by the spin-symmetric Hamiltonian

$$\mathcal{H} = \mathcal{H}_{\text{imp}} + \mathcal{H}_{\text{hyb}} + \mathcal{H}_{\text{bath}} . \quad (1.73)$$

The constituents are given by

$$\mathcal{H}_{\text{imp}} = U (n_{d,\uparrow} - n) (n_{d,\downarrow} - n) - \mu_0 \sum_{\sigma} (n_{d,\sigma} - n) \quad (1.74a)$$

$$\mathcal{H}_{\text{hyb}} = \sum_{\mathbf{k},\sigma} V_{\mathbf{k}} \left(d_{\sigma}^{\dagger} c_{\mathbf{k},\sigma} + \text{h.c.} \right) \quad (1.74b)$$

$$\mathcal{H}_{\text{bath}} = \sum_{\mathbf{k},\sigma} \epsilon_{\mathbf{k}} : c_{\mathbf{k},\sigma}^{\dagger} c_{\mathbf{k},\sigma} : \quad (1.74c)$$

where U is the interaction strength and μ_0 the chemical potential at the impurity site, $V_{\mathbf{k}}$ is the hybridization, $n_{d,\sigma} := d_{\sigma}^{\dagger} d_{\sigma}$ and $n := \langle n_{d,\sigma} \rangle$ are the particle density at the impurity

site and its spin-independent expectation value, \mathbf{k} parameterizes the continuum of bath levels with energy $\varepsilon_{\mathbf{k}}$. Defining the hybridization function (1.24)

$$\Gamma(z) = \sum_{\mathbf{k}} V_{\mathbf{k}}^2 \frac{1}{z - \varepsilon_{\mathbf{k}}} \quad (1.75)$$

the free, i. e. non-interacting, local Green function at the impurity site is given by

$$G_0^{-1}(z) = z + \mu_0 - \Gamma(z) . \quad (1.76)$$

Knowing the self-energy $\Sigma(z)$ at the impurity site allows to express the full Green function by

$$G^{-1}(z) = z + \mu_0 - \Gamma(z) - \Sigma(z) = G_0^{-1}(z) - \Sigma(z) . \quad (1.77)$$

Let us generally define fermionic Green functions [Ric80] by

$$\langle A|B \rangle_z := -i \int_0^{\infty} \langle \{A(t), B(0)\} \rangle e^{izt} dt \quad (1.78)$$

where the brackets $\langle \cdot \rangle$ stand for conventional expectation values whereas the brackets $\langle \cdot | \cdot \rangle_z$ will be used for the above Green functions. By integration by parts we obtain

$$z \langle A|B \rangle_z + \langle \mathcal{L}A|B \rangle_z = \langle \{A(0), B(0)\} \rangle \quad (1.79)$$

where \mathcal{L} is the Liouville operator defined by $\mathcal{L}X = [\mathcal{H}, X]$ [Fu193]. For instance, the time evolution of an operator can be expressed conveniently by $A(t) = \exp(i\mathcal{H}t)A \exp(-i\mathcal{H}t) = \exp(i\mathcal{L}t)A$. The invariance with respect to translation in time $\langle \{A(t), B(0)\} \rangle = \langle \{A(0), B(-t)\} \rangle$ yields

$$z \langle A|B \rangle_z - \langle A|\mathcal{L}B \rangle_z = \langle \{A(0), B(0)\} \rangle . \quad (1.80)$$

In a first step, we apply (1.79) for $A = d_{\sigma}, B = d_{\sigma}^{\dagger}$ in order to learn something on the Green function $G(z) = \langle d_{\sigma}|d_{\sigma}^{\dagger} \rangle_z$

$$(z + \mu_0)G(z) - UF(z) - \sum_{\mathbf{k}} V_{\mathbf{k}} \langle c_{\mathbf{k},\sigma} | d_{\sigma}^{\dagger} \rangle_z = 1 \quad (1.81)$$

where the definition

$$F(z) := \langle d_{\sigma} (n_{d,-\sigma} - n) | d_{\sigma}^{\dagger} \rangle_z \quad (1.82)$$

is employed. Next, we choose $A = c_{\mathbf{k},\sigma}$, $B = d_{\sigma}^{\dagger}$ to obtain

$$(z - \varepsilon_{\mathbf{k}}) \left\langle c_{\mathbf{k},\sigma} \left| d_{\sigma}^{\dagger} \right\rangle_z - V_{\mathbf{k}} G(z) = 0. \quad (1.83)$$

Solving Eq. (1.83) for $\langle c_{\mathbf{k},\sigma} | d_{\sigma}^{\dagger} \rangle_z$ and inserting the result in (1.81) yields

$$[z + \mu_0 - \Gamma(z)] G(z) - U F(z) = 1. \quad (1.84)$$

Comparing this relation to (1.77) leads to

$$\Sigma(z) = U \frac{F(z)}{G(z)} \quad (1.85)$$

which is the relation derived and used in Ref. [Bul98]¹³.

But one does not have to stop here [Uhr03]. In a second step, we apply (1.80) with $A = d_{\sigma}(n_{d,-\sigma} - n)$, $B = d_{\sigma}^{\dagger}$ to arrive at

$$(z + \mu_0) F(z) - U Q(z) - \sum_{\mathbf{k}} V_{\mathbf{k}} \left\langle A \left| c_{\mathbf{k},\sigma}^{\dagger} \right\rangle_z = 0 \quad (1.86)$$

where we introduce the important generalized fermionic Green function

$$Q(z) := \left\langle d_{\sigma}(n_{d,-\sigma} - n) \left| d_{\sigma}^{\dagger}(n_{d,-\sigma} - n) \right\rangle_z. \quad (1.87)$$

Next, we choose $B = c_{\mathbf{k},\sigma}^{\dagger}$ and A as before

$$(z - \varepsilon_{\mathbf{k}}) \left\langle d_{\sigma}(n_{d,-\sigma} - n) \left| c_{\mathbf{k},\sigma}^{\dagger} \right\rangle_z - V_{\mathbf{k}} F(z) = 0. \quad (1.88)$$

Solving Eq. (1.88) for $\langle d_{\sigma}(n_{d,-\sigma} - n) | c_{\mathbf{k},\sigma}^{\dagger} \rangle_z$ and inserting the result into (1.86) yields

$$[z + \mu_0 - \Gamma(z)] F(z) - U Q(z) = 0 \quad (1.89)$$

whence we conclude $F(z) = U Q(z) G_0(z)$. Together with Eq. (1.85) follows

$$\Sigma(z) = U^2 \frac{Q(z) G_0(z)}{G(z)} = U^2 Q(z) [1 - \Sigma(z) G_0(z)]. \quad (1.90)$$

¹³For the advantage of Eq. (1.85) over a direct calculation of the self-energy via (1.77), $\Sigma(z) = G_0^{-1}(z) - G^{-1}(z)$, in NRG calculations see Sect. 2.2 in Ref. [Bul98].

The last identity allows to express the self-energy as

$$\Sigma(z) = \frac{U^2 Q(z)}{1 + U^2 Q(z) G_0(z)} \quad (1.91)$$

which represents the main result of this section. Eq. (1.91) has many interesting implications.

1. Knowledge of a single diagonal response function, namely $Q(z)$, allows to compute the self-energy. The previously used relation (1.85) required two non-trivial response functions of which $F(z)$ is a non-diagonal Green function.
2. The full Green function can be expressed directly by the Q -function

$$G(z) = G_0(z) [1 + U^2 Q(z) G_0(z)] . \quad (1.92)$$

3. Since $Q(z)$ is a straightforward fermionic response function it has the same analytic properties as for instance the single particle Green function [Ric80]. Its positive spectral function $\rho_Q(\omega)$ is given by

$$\rho_Q(\omega) = -\frac{1}{\pi} \Im Q(\omega + i0^+) . \quad (1.93)$$

From the definition (1.87) the asymptotic behavior

$$\begin{aligned} \lim_{z \rightarrow \infty} [z Q(z)] &= \left\langle \left\{ d_\sigma (n_{d,-\sigma} - n), d_\sigma^\dagger (n_{d,-\sigma} - n) \right\} \right\rangle = \left\langle (n_{d,-\sigma} - n)^2 \right\rangle \\ &= n(1 - n) \end{aligned} \quad (1.94)$$

follows directly. From the Hilbert representation we conclude the sum rule for the Q function

$$\int_{-\infty}^{\infty} \rho_Q(\omega) d\omega = n(1 - n) . \quad (1.95)$$

But the identity (1.91) implies also the asymptotic behavior of the self-energy

$$\lim_{z \rightarrow \infty} [z \Sigma(z)] = U^2 n(1 - n) . \quad (1.96)$$

Note that in the way we defined the self-energy the constant Hartree term was excluded since it was explicitly accounted for in the normal-ordered form in which H_{imp} was denoted, cf. Eq. (1.74a). As for the Q -function we conclude that (1.96) implies the sum rule

for the spectral density $\rho_\Sigma(\omega) = -\pi^{-1}\Im\Sigma(\omega + i0^+)$ of the self-energy

$$\int_{-\infty}^{\infty} \rho_\Sigma(\omega) d\omega = U^2 n(1-n). \quad (1.97)$$

The asymptotic form (1.96) was already exploited previously [Kaj96], but the resulting sum rule (1.97) has not been mentioned in the literature before in this form to our knowledge. But similar approaches have been used for the SIAM [Czy96] or for the $d = \infty$ Hubbard model [Pot97]. We advocate to use the sum rules (1.95) or (1.97) to check explicit calculations or $Q(\omega)$ or $\Sigma(\omega)$. We expect these sum rules to be of particular use for numerical calculations like numerical renormalization group, density-matrix renormalization or exact diagonalization where the spectral weights in certain frequency intervals are directly computed.

Second, we suggest to compute in the first place the generalized Green function $Q(z)$ to find the self-energy in a second step via Eq. (1.91). The advantage is that only a diagonal response function has to be found which does not have a pronounced dependence on the interaction, for instance its sum rule (1.95) is interaction independent. This response function is not 1-particle irreducible so that no numerically complicated projection is required. Hence it is directly accessible to numerical techniques like NRG, DMRG or exact diagonalization. In the particle-hole symmetric case, the definition and evaluation of $Q(z)$ (1.87) is straightforward because $n = \langle n_{d,\sigma} \rangle$ stays at its constant value $n = 1/2$ (also for finite temperatures). Nevertheless, it is worthwhile noting that away from half-filling, n has to be determined by the calculation to define the \hat{Q} operator. In this thesis only particle-symmetric problems are treated, so no difficulties arising from the n -dependent definition of \hat{Q} are expected.

In the half-filled case, $n = 1/2$ and $\mu_0 = 0$,

$$\begin{aligned} \hat{Q} &:= d_\uparrow^\dagger (n_{d,\downarrow} - 1/2) \\ Q(z) &:= \left\langle \hat{Q}^\dagger | \hat{Q} \right\rangle_z = \left\langle d_\uparrow (n_{d,\downarrow} - 1/2) \left| d_\uparrow^\dagger (n_{d,\downarrow} - 1/2) \right\rangle_z \end{aligned} \quad (1.98)$$

translates to

$$\begin{aligned} \hat{Q} &:= \mathbf{S}_0^+ \mathbf{T}_0^z \\ Q(z) &:= \left\langle \hat{Q}^\dagger | \hat{Q} \right\rangle_z = \left\langle \mathbf{S}_0^- \mathbf{T}_0^z | \mathbf{S}_0^+ \mathbf{T}_0^z \right\rangle_z \end{aligned} \quad (1.99)$$

in the language of the Jordan-Wigner spins. In the D-DMRG one simply has to replace \mathbf{S}_0^+ by $\mathbf{S}_0^+ \mathbf{T}_0^z$ in Eq. (1.68) (and \mathbf{S}_0^- by $\mathbf{S}_0^- \mathbf{T}_0^z$) and to adjust the definition of the correction vector $|\xi\rangle$ (1.70). The raw data output of the DMRG is then the broadened Q -function

$Q(\omega + i\eta)$. Calculating the Q -function via DMRG and subsequent extraction of the Green function instead of directly calculating G is advantageous. The propagator for a finite chain of length L has a number of poles of the order $\mathcal{O}(L)$. The self-energy and the Q -function have $\mathcal{O}(L^3)$ finite size poles, cf. Ref. [MH89b] or Eq. (1.104). Thus, finite size effects due the rendering of the bath with finite instead of semi-infinite chains are reduced.

The optimum procedure to get the unbroadened Green function from the broadened Q -function is as follows:

$$\text{D-DMRG} \longrightarrow Q(z) \xrightarrow{(1.91)} \Sigma(z) \xrightarrow[\text{cf. Chapt. 3}]{\text{deconvolution}} \Sigma(\omega) \xrightarrow[(1.102)]{(1.101)} \begin{cases} G(\omega) \\ Q(\omega) \end{cases} \quad (1.100)$$

where we used in the last step

$$G(z) = G_0(z) \left[1 + \frac{G_0(z)\Sigma(z)}{1 - G_0(z)\Sigma(z)} \right] = \frac{1}{G_0^{-1}(z) - \Sigma(z)} \quad (1.101)$$

and

$$Q(z) = \frac{\Sigma(z)}{U^2[1 - G_0(z)\Sigma(z)]}. \quad (1.102)$$

A different route is to translate $Q(z)$ into $G(z)$ via (1.92) and to deconvolve $G(\omega + i\eta)$ to $G(\omega)$. The direct deconvolution of $Q(z)$ to $Q(\omega)$ and subsequent translation to $G(\omega)$ via (1.92) turned out to be unstable. The three routes to obtain $G(\omega)$ from $Q(\omega + i\eta)$ have been tested in great detail in Ref. [Fas05] on the basis of DMRG data produced with the impurity solver developed in this thesis.

Note that for the formulas relating a broadened quantity with another broadened one, also the broadened $G_0(z = \omega + i\eta)$ has to be used. If an unbroadened quantity shall be related to another unbroadened one, $G_0(\omega)$ has to be used. This is easy in the case of the semi-elliptic DOS where the analytic formula is known, cf. Eqs. (1.52) and (1.53). If only the continued fraction representation of $G_0(\omega)$ is available an appropriate termination scheme has to be used, cf. Ref. [Vis94].

The self-energy is zero for the non-interacting case $U = 0$. But the generalized Green function $Q(z)$ does not vanish in this case. To obtain an impression what the Q -function looks like, we calculate it for the non-interacting case. We follow Ref. [MH89b]. The first order (Hartree) self-energy $\Sigma_1 = 0$ is trivial. The leading dynamic effects in the weak coupling expansion given in Ref. [MH89b] are contained in the second order self-energy. It is represented by the skeleton diagram shown in Fig. 1 in Ref. [MH89b] and its imaginary part is given by

$$\Im \Sigma_2(\omega - i0^+) = \pi U^2 q(\omega) \quad (1.103)$$

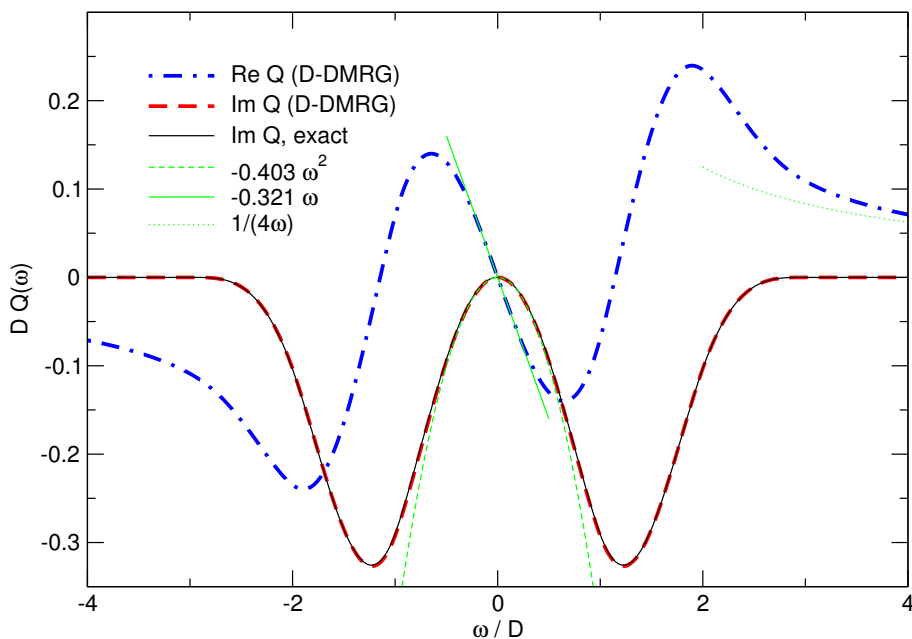


Figure 1.7: Q -function for vanishing interaction $U = 0$ and semi-elliptic free DOS with bandwidth $W = 2D$. The exact result (thin solid line) for the imaginary part is compared to the deconvolved D-DMRG data.

with

$$q(\omega) := \int_0^\omega d\omega_1 \rho(\omega_1 - \omega) \int_0^{\omega_1} d\omega_2 \rho(\omega_2) \rho(\omega_1 - \omega_2). \quad (1.104)$$

Using (1.102) for

$$\lim_{U \rightarrow 0} \Sigma = \lim_{U \rightarrow 0} (\Sigma_1 + \Sigma_2) \quad (1.105)$$

yields

$$\lim_{U \rightarrow 0} \Im Q(z) = \Im \lim_{U \rightarrow 0} \frac{\Sigma(z)}{U^2 [1 - G_0(z) \Sigma(z)]} = \pi q(\omega). \quad (1.106)$$

The complete Q -function is obtained through the Kramers-Kronig relation.¹⁴

Fig. 1.7 shows the real and imaginary parts of the Q -function for the case of vanishing interaction and a semi-elliptic free DOS with bandwidth $W = 2D$. For the D-DMRG calculation we used $m = 256$ states in the projected basis and a chain of $N_f = 200$ fermions. The exact result (for $N_f = \infty$) and the deconvolved DMRG data for the imaginary part are nearly indistinguishable on this scale. The maximum difference between the DMRG data for $\Im Q$ and the exact result is $|\Im(Q_{\text{DMRG}} - Q_{\text{exact}})| \simeq 0.00285D$ reached for $\omega \simeq 1.2D$. The sum rule (1.95) predicting a value of $-\frac{\pi}{4} \simeq -0.7853982$ for the inte-

¹⁴From Eq. (1.104) we can learn why the Q -function has $\mathcal{O}(L^3)$ poles: The two-fold convolution of a function $\rho(\omega)$ with $\mathcal{O}(L)$ poles has $\mathcal{O}(L^3)$ poles.

grated imaginary part of $Q(\omega)$ is fulfilled by the D-DMRG result -0.7853999 with a relative error of $2 \cdot 10^{-4}\%$. The high-frequency limit of the real part $\Re Q(\omega) \rightarrow 1/(4\omega)$ [cf. Eq. (1.94)] and low-frequency fits for the real and the imaginary parts are shown in Fig. 1.7 for comparison. The imaginary part is expected to behave like $\Im Q(\omega) = -4/\pi^2 \omega^2 \simeq -0.405\omega^2$ for $\omega \rightarrow 0$ which agrees nicely with the low-frequency fit on the fit-interval $\omega \in [-0.2D, 0.2D]$ of $-0.403\omega^2$. The value $\Im Q(0) = -0.000101D$ at zero frequency provides a further indication for the accuracy of the DMRG if compared to the expected exact result of $\Im Q(0) = 0$.

1.7 Effective impurity models in the framework of dynamic mean-field theory

The interest in the quantitative analysis of SIAMs has been intensified considerably by the advent of a systematic mapping of strongly correlated lattice models such as the periodic Anderson or Hubbard models onto an effective quantum impurity hybridizing with the surrounding fermionic bath. This is the key point of dynamic mean-field theory (DMFT) [Jar92, Geo92] which is based on an appropriate scaling of the non-local parts of the Hamiltonian [Met89, MH89a], for reviews see Ref. [Pru95, Geo96, Bul04b]. In Chapt. 5 a one-band Hubbard model on the Bethe lattice with infinite coordination number $z \rightarrow \infty$ in the half-filled case with one electron per site, nearest-neighbor hopping t , and Coulomb repulsion U is investigated, cf. also Refs. [Kar04b, Kar05]. In the none-interacting case $U = 0$ we choose as “free” bandwidth $W = 2D$ introducing D as energy scale. Scaling the hopping $t = D/(2\sqrt{z})$ [Met89] leads to the dynamic mean-field theory (DMFT) [MH89a, Jar92, Geo92]. For treating Hubbard models in the framework of the DMFT the lattice problem is mapped onto an effective single impurity Anderson model (SIAM) supplemented by the self-consistency conditions that the interaction U , the full local Green function $G(\omega)$ and the local self-energy $\Sigma(\omega)$ are the same in the lattice and in the SIAM [Geo96].

The DMFT as an approximation to finite dimensional systems is by now a widely employed technique [Kot04]. In recent years, the DMFT is applied very successfully in combination with *ab initio* density-functional theories to include important correlation effects in the description of real materials [Ani97, Lic98]. In this way, the unbiased knowledge about the bands could be enhanced by the inclusion of interaction effects between the excited quasi-particles. It turned out that the combination of density-functional results and DMFT makes the quantitative understanding of spectroscopic data possible [Kot01, Hel01a, Hel01b, Blü02, Hel02, Hel03, Kot04, Geo04, Vol05]. Hence the quanti-

2 Dynamic density-matrix renormalization

The density-matrix renormalization group (DMRG) is a numerical technique for the efficient truncation of the Hilbert space of one and quasi-one-dimensional strongly correlated quantum systems. Since it was introduced in 1992 by *Steven R. White* [Whi92a, Whi93] the DMRG has been applied to both fermionic and bosonic low-dimensional quantum lattice systems. Originally designed as a real-space scheme for finding accurate approximations to the ground state and the low-lying excited states of one-dimensional quantum lattice systems at zero temperature the field of application has been extended remarkably.

Sect. 2.1 of this chapter presents a short introduction to the conventional density-matrix renormalization group. The main part of this chapter describes the concrete DMRG implementation developed in this thesis and the methods used to calculate the zero-temperature dynamics of single impurity Anderson models.

Let us collect some introductory and reviewing literature on DMRG. The proceedings of the workshop “Density-Matrix Renormalization” held in Dresden in 1998 edited by *Peschel et al.* [Pes99] give a pedagogical introduction to real-space DMRG and present some of the most important applications. The DMRG has its origin in the numerical renormalization group (NRG) by *Wilson* [Wil75]. This connection is worked out in Refs. [Whi98, Noa99]. An introductory course to the Lanczos method and to DMRG algorithms can be found in Ref. [Mal03]. For a more complete overview to applications in and beyond condensed matter physics we refer to the review articles from *Hallberg* [Hal99, Hal04] and *Schollwöck* [Sch05a]. These review articles describe apart from the calculation of static, dynamic, and thermodynamic quantities the potential of DMRG in two-dimensional quantum systems, quantum chemistry, three-dimensional small grains, inclusion of phonons and disorder, equilibrium and non-equilibrium statistical physics, nuclear physics, and high energy physics. *Shibata* [Shi03] concentrates on DMRG methods applied to finite temperatures and two-dimensional systems. *Dukelsky and Pittel* [Duk04] give an overview of DMRG for finite Fermi systems such as small grains, small molecules and nuclei (including momentum space DMRG (kDMRG) [Xia96, Nis02], particle-hole DMRG (phDMRG) [Duk99, Duk00], and preservation of symmetries throughout the iterative truncation process [McC01, McC02]). *Nishino*

[Nis99] introduces the DMRG from a variational point of view. *Pati et al.* [Pat03] describe and compare exact and approximate theoretical techniques for quantum magnetism in low dimensions putting special emphasis on DMRG. To finish this summary of the introductory literature we want to hint to the homepage of the workshop on “Recent Progress and Prospects in Density-Matrix Renormalization” held in Leiden in 2004 [Lei04] which gives an up-to-date list of groups working on and with DMRG and their current projects.

2.1 Conventional DMRG

After *Wilson* was so successful applying his numerical renormalization group approach to the single impurity Kondo problem [Wil75] there was great hope that other many-body problems such as the one-dimensional Hubbard model [Hub63a, Hub63b, Hub64] or Heisenberg models [Hei28] might be treated in a similar fashion. But the real-space renormalization group (RG) techniques [Cos99] applied to these models turned out to give rather poor results.

2.1.1 Standard real-space blocking scheme

The key idea of all real-space renormalization group techniques is to enlarge the system iteratively while keeping only a constant number m of basis states. Thus in standard approaches one begins with breaking up the full system into several sublattices (finite parts of the system, “blocks”) B_n and proceeds with building larger blocks out of the smaller ones. Let us denote the Hamilton operator involving the sites contained in block B_n by \mathcal{H}_{B_n} . Usually one starts with a small system B_{\min} that can still be treated exactly. The dimension of the Hilbert space grows exponentially with the system size L ,

$$\dim = f^L, \quad (2.1)$$

assuming we have f degrees of freedom per lattice site (e. g. $f = 2$ for a single $S = 1/2$ site). Thus the number of sites in the small block B_{\min} which can still be represented by m states is

$$L_{\min} = \text{TRUNC}(\log_f m). \quad (2.2)$$

The real-space blocking scheme consists of the following steps:

- ❶ Choose two blocks B and B' of the set $\{B_n\}$. Preferably, these blocks contain L_{\min} sites and can be represented by m basis states.
- ❷ Construct the Hamilton operator $\mathcal{H}_{BB'}$ consisting of \mathcal{H}_B , $\mathcal{H}_{B'}$ and the part containing the *interblock* terms (involving sites of block B and B' .)



Figure 2.1: Joining two sublattices (“blocks”) B and B' .

- ④ If the size of the Hilbert space of the concatenated system $C = BB'$ (see Fig. 2.1) does not exceed m continue with step ① replacing B and B' in $\{B_n\}$ by C .
- ④ Otherwise, diagonalize \mathcal{H}_C obtaining the m eigenvalues lowest in energy and their corresponding eigenvectors.
- ⑤ Perform a base transformation projecting \mathcal{H}_C onto the truncated space spanned by the m lowest-lying eigenstates: Form $\tilde{\mathcal{H}}_C = \mathcal{O}^\dagger \mathcal{H}_C \mathcal{O}$ where the columns of \mathcal{O} are the m lowest eigenvectors of \mathcal{H}_C .
All operators \mathcal{A} of interest (observables which shall be evaluated finally) or operators at the block edges (needed to glue the new block C to another one) have to be transformed also to the new basis: $\tilde{\mathcal{A}} = \mathcal{O}^\dagger \mathcal{A} \mathcal{O}$.
- ⑥ Replace blocks B and B' in $\{B_n\}$ by block C .
- ⑦ Continue with the first step ①.

It is important to keep in mind that the Hamiltonian $\tilde{\mathcal{H}}_C$ is only an approximation for the Hamiltonian of block $C = BB'$ since its projected on the states kept during the iterative procedure. The selection criterion—which states to keep in the reduced basis and which to drop—is based on the energies of the corresponding states in the above-described real-space RG scheme. An important difference to Wilson’s solution of the Kondo model is that this truncation procedure does *not* lead to an effective (“renormalized”) model with exponential decrease of the couplings between adjacent “momentum shells” which is essential for the method to work [Wil75, Km80a, Km80b]. Instead the coupling remains constant. Thus, the selection criterion is not the optimum. Improvements have to be found. This is the topic of Sect. 2.1.3.

2.1.2 Boundary conditions

One of the reasons for the unreliability of the attempts to extend Wilson’s approach to a real-space scheme could be identified by *White and Noack* [Whi92b]. Fig. 2.2 illustrates the ground state wave functions of two blocks B and B' and of the compound block $C = BB'$. The lowest-lying states of B and B' all have nodes at the block ends. Thus, they are a bad choice to describe the ground state of C because all product states of BB' have nodes at the center of the combined block. In this sense the low-lying eigenstates kept in



Figure 2.2: Cartoon of the ground state wave functions of blocks B , B' , and the fusion block $C = BB'$.

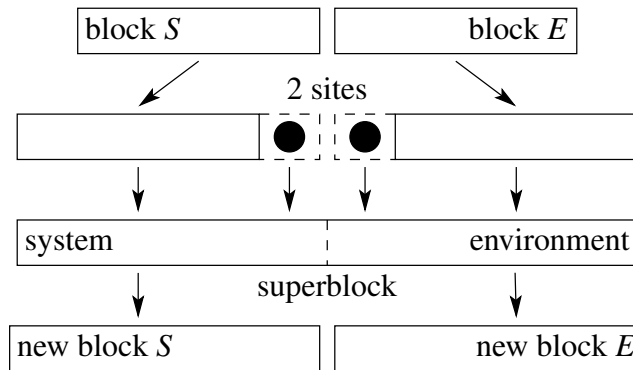


Figure 2.3: Schematic form of a superblock procedure. Open rectangles represent blocks and solid circles are single sites. The system (S) and environment (E) block are enlarged by one site \bullet . Together they form the superblock where the target states are calculated. The new blocks are obtained by a density-matrix projection (cf. Sect. 2.1.3).

standard renormalization group blocking schemes only provide a too incomplete basis set to obtain an accurate eigenstate for a larger lattice size.

By applying a variety of boundary conditions (and combinations of them) to a real-space block in order to simulate the effect of the environmental blocks *White and Noack* obtained excellent results for the toy model investigated (the “particle in a box” problem). A different way to ensure the use of correct boundary conditions is the so-called **superblock procedure**. The key idea is to consider not merely isolated blocks which would impose wrong boundary conditions but to embed the block in a larger system, the superblock. This superblock method seemed to be much better suited for applications to interacting systems, since the general behavior at the boundaries is provided *automatically* by the embedding of the block of interest in a large superblock, mimicking the thermodynamic limit system in which the block is ultimately embedded.

2.1.3 Density-matrix projection

The other key essence of an appropriate real-space renormalization scheme was added by *White* in two subsequent papers [[Whi92a](#), [Whi93](#)]: What is the correct prescription to

select the relevant states of a system? In Wilson’s NRG the systematic thinning out of degrees of freedom—leading to simplified (“renormalized”) effective Hamiltonians—is performed via integrating out contributions from high-lying energy levels. This *truncation* or *projection* scheme was called into question by White. He replaced the tracing out of high energy states (to describe the physics on successively lower energy scale) by a new selection prescription: The optimum states to keep are the most probable eigenstates of the reduced density-matrix of the block. This decimation procedure—the **density-matrix projection**—can be justified following three different routes [Sch05a]:

1. optimization of expectation values [Whi98],
2. optimization of the wave function [Whi92a, Whi93] and
3. optimization of entanglement [Gai01, Gai04, Lat04, Osb02].

All three lines of argument lead to the same truncation prescription based on properties of density-matrices. In the following two sections the basic arguments of White’s lines of arguments is presented.

2.1.4 Optimization of expectation values

Let us consider a finite part of the lattice called the *system block* with a Hilbert space of dimension M . The goal is to derive a truncation procedure from M to $m < M$ states. The rest of the lattice is called *environment block*, which may be finite or infinite. Let $|i\rangle$ denote the entire set of many-body states of the system block and $|j\rangle$ the many-body states of the environment block. If $|\Psi\rangle$ is a pure state of the entire lattice (the *superblock*, sometimes also called “universe” in the DMRG literature), we can write it as

$$|\Psi\rangle = \sum_{i,j} \Psi_{ij} |i\rangle |j\rangle \quad \text{with} \quad \langle \Psi | \Psi \rangle = 1 . \quad (2.3)$$

Then the state of the system block can be described in terms of a reduced density-matrix

$$\hat{\rho} = \text{Tr}_{\text{env}} |\Psi\rangle \langle \Psi| , \quad (2.4)$$

where the states of the environment have been traced out,

$$\rho_{ii'} = \langle i | \hat{\rho} | i' \rangle = \sum_j \Psi_{ij}^* \Psi_{i'j} . \quad (2.5)$$

The density-matrix operator $\hat{\rho}$ is hermitian ($\hat{\rho} = \hat{\rho}^\dagger$) or symmetric ($\hat{\rho} = \hat{\rho}^t$) if $\rho_{ii'}$ is real. Let $\hat{\rho}$ have M eigenvalues w_α and orthonormal eigenstates $|u_\alpha\rangle$,

$$\hat{\rho}|u_\alpha\rangle = w_\alpha|u_\alpha\rangle. \quad (2.6)$$

$\hat{\rho}$ is positive semidefinite, $\hat{\rho} \geq 0$, as $\langle\beta|\hat{\rho}|\beta\rangle = \sum_\alpha w_\alpha |\langle\beta|u_\alpha\rangle|^2 \geq 0$ for every $|\beta\rangle$, and

$$\text{Tr} \hat{\rho} = 1 \quad \sum_{\alpha=1}^M w_\alpha = 1. \quad (2.7)$$

We can write $\hat{\rho}$ as a sum of weighted projection operators $|u_\alpha\rangle\langle u_\alpha|$,

$$\hat{\rho} = \sum_{\alpha=1}^M w_\alpha |u_\alpha\rangle\langle u_\alpha|. \quad (2.8)$$

The $w_\alpha \geq 0$ are the probabilities of the states $|u_\alpha\rangle$. It is intuitively clear that those m states with the largest weights w_α in the reduced density-matrix are the important ones when describing the ground state of the system. Let \hat{A} be an arbitrary operator acting on the system. Its expectation value is, using Eqs. (2.3) and (2.5),

$$\langle\hat{A}\rangle = \frac{\langle\Psi|\hat{A}|\Psi\rangle}{\langle\Psi|\Psi\rangle} = \sum_{i,i'} A_{ii'} \rho_{ii'} = \text{Tr}_{\text{sys}} (\hat{\rho}\hat{A}). \quad (2.9)$$

Expressing Eq. (2.9) in terms of the density-matrix eigenbasis $|u_\alpha\rangle$ (2.8), we find

$$\langle\hat{A}\rangle = \sum_{\alpha=1}^M w_\alpha \langle u_\alpha|\hat{A}|u_\alpha\rangle. \quad (2.10)$$

This equation is the key result of this section: If for a particular α , $w_\alpha \approx 0$, we make (nearly) no error in $\langle\hat{A}\rangle$ if we discard the corresponding state $|u_\alpha\rangle$, for any \hat{A} .

Let us assume the states $|u_\alpha\rangle$ are ordered such that $w_1 \geq w_2 \geq w_3 \geq \dots$ and project the system state space onto the m dominant eigenvectors $|u_\alpha\rangle$ with the largest eigenvalues w_α ,

$$\langle\hat{A}\rangle_{\text{approx}} = \sum_{\alpha=1}^m w_\alpha \langle u_\alpha|\hat{A}|u_\alpha\rangle. \quad (2.11)$$

If \hat{A} is a bounded operator, such as the energy per lattice site,

$$\|\hat{A}\| = \max_{\{\Phi\}} \left| \frac{\langle\Phi|\hat{A}|\Phi\rangle}{\langle\Phi|\Phi\rangle} \right| \equiv c_A, \quad (2.12)$$

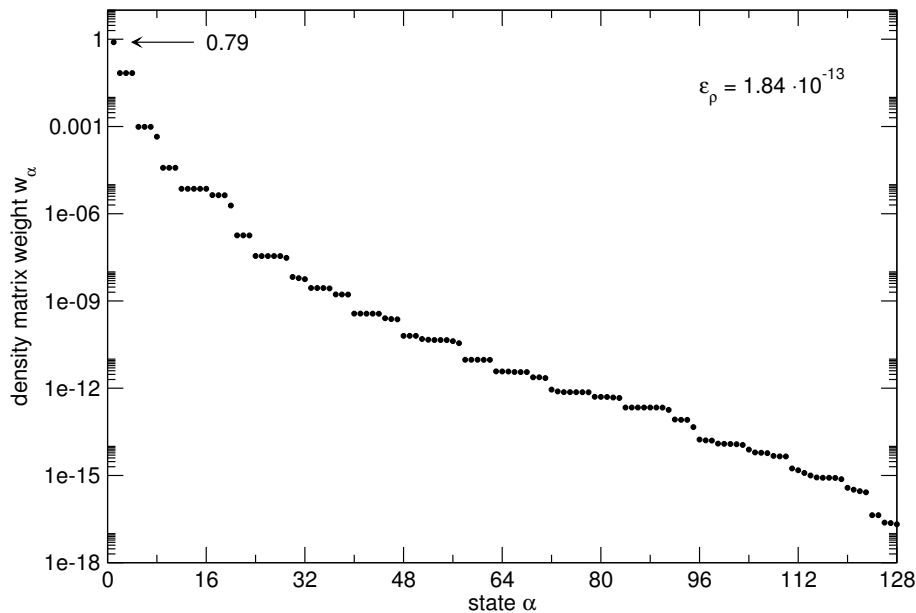


Figure 2.4: Weights in the reduced density-matrix of a $S = 1/2$ Heisenberg chain with 40 sites in the first symmetric block configuration after the build-up (system and environment block with each 20 sites). The first $m = 128$ of $M = 256$ eigenvalues of $\hat{\rho}$ are shown. The truncated weight is $\varepsilon_\rho = 1.38 \cdot 10^{-13}$ for this example.

the error for $\langle \hat{A} \rangle$ is bounded by the *truncation error*

$$|\langle \hat{A} \rangle_{\text{approx}} - \langle \hat{A} \rangle| \leq \left(\sum_{\alpha > m}^M w_\alpha \right) c_A \equiv \varepsilon_\rho c_A. \quad (2.13)$$

The error for local quantities, such as energy, magnetization or density, is of the order of the *truncated weight*

$$\varepsilon_\rho = 1 - \sum_{\alpha=1}^m w_\alpha = \sum_{\alpha > m}^M w_\alpha. \quad (2.14)$$

The discarded $(M - m)$ states contribute with a relative weight of ε_ρ . Thus, a fast decay of density-matrix eigenvalues w_α is essential for this truncation procedure. A typical example for the decay of the weights is given in Fig. 2.4 for the DMRG ground state energy calculation of a $S = 1/2$ Heisenberg chain. The discarded weight of Eq. (2.14) is proportional to the total error in the quantity of interest only in *one* DMRG step assuming the system had been embedded in the final and exactly described environment. In a real calculation, the errors accumulate and additional sources due to the approximate representation of the environment come into play (*environmental error*). After additional steps

to eliminate environmental errors (i. e. a considerable number of finite size sweeps, cf. [Sect. 2.1.8](#)) the error (though often larger than the truncated weight) remains small.

In summary, we have convinced ourselves that if the superblock is in a pure state, the optimum states to keep are the m most significant eigenstates (i. e. the states with the largest eigenvalues) of the reduced density-matrix of the system block, obtained from the wave function of the superblock via [Eq. \(2.5\)](#). The state $|\Psi\rangle$ in [Eq. \(2.5\)](#) is called *target state* as the reduced basis is optimized to represent this specific state. One can also consider the superblock to be in a *mixed state*, which we will address in [Sect. 2.1.6](#).

2.1.5 Optimization of the wave function

In this section we follow White's original way [[Whi92a](#), [Whi93](#)] to justify the truncation scheme we derived in the [previous section](#) via "optimization of expectation values". Let us assume we obtained one particular state $|\Psi\rangle$, typically the ground state. The task is now to find a truncation procedure such that the approximate wave function $|\tilde{\Psi}\rangle$ minimizes the distance in the quadratic norm,

$$\mathcal{S} := \left\| |\Psi\rangle - |\tilde{\Psi}\rangle \right\|. \quad (2.15)$$

Using $|i\rangle$ ($i = 1, \dots, M_S$) for the full basis set of M_S states of the system block S , $|j\rangle$ ($j = 1, \dots, M_E$) for the environment E , and $|u_\alpha\rangle$ ($\alpha = 1, \dots, m$) with $m < M_S$ and $|u_\alpha\rangle = \sum_i u_{\alpha,i} |i\rangle$ for the reduced set of m states of the system, the approximate wave function $|\tilde{\Psi}\rangle$ can be written as

$$|\tilde{\Psi}\rangle = \sum_{\alpha=1}^{m < M_S} \sum_{j=1}^{M_E} a_{\alpha,j} |u_\alpha\rangle |j\rangle \stackrel{!}{\approx} |\Psi\rangle = \sum_{i=1}^{M_S} \sum_{j=1}^{M_E} \Psi_{ij} |i\rangle |j\rangle. \quad (2.16)$$

Given a specified value of m , the minimization of \mathcal{S} has to be achieved by varying over all $a_{\alpha,j}$ and $|u_\alpha\rangle$, subject to $\langle u_\alpha | u_{\alpha'} \rangle = \delta_{\alpha,\alpha'}$. Writing

$$|\tilde{\Psi}\rangle = \sum_{\alpha}^m a_{\alpha} |u_{\alpha}\rangle |v_{\alpha}\rangle \quad (2.17)$$

where $v_{\alpha,j} := \langle j | v_{\alpha} \rangle = N_{\alpha} a_{\alpha,j}$. The constants N_{α} are chosen to normalize $|v_{\alpha}\rangle$, i. e. $\sum_j |v_{\alpha,j}|^2 = 1$. In matrix notation and assuming real coefficients for simplicity, we find

$$\mathcal{S} = \sum_{i,j} \left(\Psi_{ij} - \sum_{\alpha=1}^m a_{\alpha} u_{\alpha,i} v_{\alpha,j} \right)^2, \quad (2.18)$$

and \mathcal{S} has to be minimized over all $u_{\alpha,i}$, $v_{\alpha,j}$, and a_α . The solution of this minimization problem is given by the singular value decomposition (SVD) [Pre92, Gol96] of Ψ ,

$$\Psi = \mathbf{U}\mathbf{D}\mathbf{V}^t. \quad (2.19)$$

$\mathbf{U} \in \mathbb{R}^{M_S \times M_S}$ is orthogonal, $\mathbf{V} \in \mathbb{R}^{M_S \times M_E}$ is column-orthogonal, and $\mathbf{D} \in \mathbb{R}^{M_E \times M_E}$ is diagonal and contains the singular values of Ψ .¹ Let u_α and v_α denote the α th column of the matrices \mathbf{U} and \mathbf{V} , respectively. The u_α , v_α , and a_α which minimize \mathcal{S} are given according to the SVD decomposition: the m largest-magnitude diagonal elements of \mathbf{D} are the a_α and the corresponding columns of \mathbf{U} and \mathbf{V} are the u_α and v_α .

The optimal states $|u_\alpha\rangle$ are the eigenvectors of the reduced density-matrix $\hat{\rho}$ of the system block (2.5),

$$\rho_{ii'} = \langle i | \hat{\rho} | i' \rangle = \sum_{j=1}^{M_E} \Psi_{ij} \Psi_{i'j},$$

where the Ψ_{ij} were assumed to be real. With this definition of ρ we find

$$\rho = \mathbf{U} \underbrace{\mathbf{D}\mathbf{V}^t\mathbf{V}}_{\mathbf{1}} \underbrace{\mathbf{D}^t}_{\mathbf{D}} \mathbf{U}^t = \mathbf{U}\mathbf{D}^2\mathbf{U}^t \quad (2.20)$$

and conclude, that \mathbf{U} diagonalizes ρ . The eigenvalues of the density-matrix ρ are $w_\alpha = a_\alpha^2$ and the optimal states $|u_\alpha\rangle$ are the eigenstates of $\hat{\rho}$ with the *largest eigenvalues*. Again, each w_α represents the probability of the system block being in state $|u_\alpha\rangle$, with $\sum_{\alpha=1}^{M_S} w_\alpha = 1$. The deviation from unity is the truncated weight (2.14)

$$\varepsilon_\rho = 1 - \sum_{\alpha=1}^m w_\alpha = \sum_{\alpha>m}^{M_S} w_\alpha.$$

To conclude, the findings are the same as in Sect. 2.1.4. When the superblock is assumed to be in a pure state $|\Psi\rangle$, the optimal m states to keep to represent $|\Psi\rangle$ are the m most significant eigenstates of the reduced density-matrix of the system block. They are obtained from the wavefunction via Eq. (2.5).

2.1.6 Multiple target states

So far, we optimized the reduced basis to represent a specific state $|\Psi\rangle$, the target state. One can also consider the superblock to be in a *mixed state*. This would be a natural assumption for finite temperatures, but it is also necessary if we want to target multiple states simultaneously: e. g. if one wants to find several of the lowest lying eigenstates or

¹For a more detailed discussion see Sect. 2.2 of Ref. [Sch99] or Sect. 3.2.1 and App. A of Ref. [Mar99].

if one wants to target for different physical quantities (such as the ground state energy and a dynamic quantity, cf. [Sect. 2.2](#)). One represents the mixed case by defining that the superblock has probability W^k to be in state $|\Psi^k\rangle$. The appropriate definition for the error corresponding to the one-target-state formula (2.18) is then given by [[Noa99](#)]

$$\mathcal{S} = \sum_k W^k \sum_{i,j} \left(\Psi_{ij}^k - \sum_{\alpha=1}^m a_{\alpha}^k u_{\alpha,i} v_{\alpha,j}^k \right)^2. \quad (2.21)$$

The goal is determine a single set of optimal u_{α} for the system block, whereas the environmental part of the system is allowed to choose a different $|v_{\alpha}^k\rangle$ for each state $|\Psi^k\rangle$. Minimizing over the u_{α} , v_{α}^k , and a_{α}^k , the result can again be written in the form of an eigenvalue equation,

$$\hat{\rho}|u_{\alpha}\rangle = w_{\alpha}|u_{\alpha}\rangle, \quad (2.22)$$

with the $|u_{\alpha}\rangle$ being the eigenstates of $\hat{\rho}$. For this case of the superblock being in a mixed state the reduced density-matrix is given by

$$\rho_{i'i} = \langle i|\hat{\rho}|i'\rangle = \left\langle i \left| \left(\sum_k W^k \text{Tr}_{\text{env}} |\Psi^k\rangle\langle\Psi^k| \right) \right| i' \right\rangle = \sum_k W^k \sum_j \left(\Psi_{ij}^k \right)^* \Psi_{i'j}^k \quad (2.23)$$

and the weights w_{α} are given by

$$w_{\alpha} = \sum_k W^k \left(a_{\alpha}^k \right)^2. \quad (2.24)$$

The conclusion for the mixed case scenario is the same as for the pure state case: the optimal states to keep are the eigenvectors of the reduced density-matrix with the largest eigenvalues.

2.1.7 Infinite size algorithm

The simplest implementation of a numerical scheme based on a density-matrix truncation and a superblock procedure is the so-called *infinite size DMRG algorithm* [[Whi92a](#)].

- ❶ Choose a lattice of some small size L_S , forming the initial system block S . At initialization, the system block normally contains L_{\min} sites, i. e. the basis is complete for this block and of dimension $M_S \leq m$. Thus, the Hamiltonian $\mathcal{H}_S^{L_S}$ and all operators acting on the block are known exactly.
- ❷ Add a single lattice site \bullet with f degrees of freedom to the system block S yielding a new system block S' with $L_{S'} = L_S + 1$ sites represented by $M_{S'} = fM_S > m$ states.

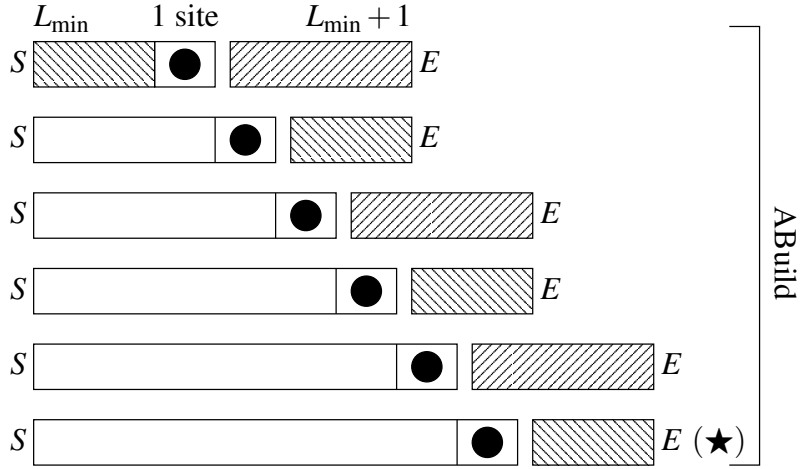


Figure 2.5: Scheme of our implementation of the infinite size DMRG algorithm (routine `ABuild` of the C++ program). Shaded rectangles are exact blocks of length L_{\min} or $L_{\min} + 1$, solid circles are single sites. The system (S) block is enlarged by one site \bullet and the small environment (E) block is chosen such that the total chain length stays even during the build-up procedure. The last configuration marked with \star is not mandatory as the resulting projected system block cannot be used as new environment block in the finite size algorithm, cf. [Sect. 2.1.8](#).

The Hamiltonian $\mathcal{H}_{S'}^{L_{S'}}$ acting on S' can now be expressed in this new enlarged basis. The same has to be done for all boundary operators or operators of interest.

- ③ Form an environment block E . In symmetric problems this could be a mirrored version of the system block. For our asymmetric situation we choose a small block of L_{\min} or $L_{\min} + 1$ sites which can be represented exactly with m or fm states, respectively: $M_E \leq fm$. The size of E is chosen in such a way that the superblock size remains even.
- ④ Form the superblock of length $L = L_{S'} + L_E$ from S' and E . In principle the superblock Hamiltonian could be constructed explicitly on the Hilbert space product basis of size $M_{S'}M_E$. This would lead to matrix-vector multiplications scaling with $M_{S'}^2M_E^2 \propto m^4$. A more efficient implementation provides routines for applying $\mathcal{H}_{S'} \otimes \mathbf{1}_E$, $\mathbf{1}_{S'} \otimes \mathcal{H}_E$ and $\mathcal{H}_{S'E}$ containing the *interblock* terms (involving sites of block S' and E). This leads to an DMRG algorithm of order $\mathcal{O}(m^3)$.
- ⑤ By using large sparse matrix algorithms find all target states $|\Psi^k\rangle$ in the superblock, i. e. the ground state, excited states, and in the dynamic DMRG a frequency dependent correction vector (see [Sect. 2.2](#)). Calculating all target states is the most time-consuming part of the algorithm.

- ⑥ Form the reduced density-matrix (2.23) of the system block: $\hat{\rho} = \sum_k W^k \text{Tr}_E |\Psi^k\rangle\langle\Psi^k|$. Determine its eigenbasis $|u_\alpha\rangle$ ordered by descending eigenvalues (density-matrix weights) w_α . Construct a rectangular ($M_{S'} \times m$) matrix \mathcal{O} where the columns of \mathcal{O} are the m eigenstates of $\hat{\rho}$ with the largest weights.
- ⑦ Now apply a density-matrix projection: form a new (reduced) basis for S' by carrying out the reduced basis transformation $\tilde{\mathcal{H}}_{S'} = \mathcal{O}^\dagger \mathcal{H}_{S'} \mathcal{O}$ onto the new m basis states.
All operators \mathcal{A} of interest (observables which shall be evaluated finally) or operators at the block boundaries (needed to glue the new block S' to another one) have also to be transformed to the new basis: $\tilde{\mathcal{A}} = \mathcal{O}^\dagger \mathcal{A} \mathcal{O}$.
- ⑧ Replace system block S with S' (and L_S with $L_{S'}$) and continue with step ② until the desired final length is reached.
- ⑨ Calculate desired properties (energies and correlations) for the final length. This step is normally also carried out at each intermediate length. This allows to do a finite size scaling for the desired properties and to extrapolate the results to infinite system size.

Some additional notes to this version of the infinite size algorithm, cf. Fig. 2.5, are necessary.

The system block S is enlarged by one site \bullet and the environment block E is chosen such that the total chain length stays even while building up the system. This prohibits the superblock ground state from switching the total spin- z sector ($\mathbf{S}_{\text{tot}}^z + \mathbf{T}_{\text{tot}}^z$) in the build-up procedure. As the final length of the spin chain is of size $L_{\text{spin}} = 2L_{\text{ferm}}$, and thus always even, the ground state of the final system has always zero total spin- z component. It has turned out to be useful not to allow for configurations differing from this prescription, i. e. we do not construct Jordan-Wigner spin chains of odd length. In the fermionic language these considerations reflect the fact that our calculations are done at half-filling.

In translationally invariant chains the environment block can be handled in the same way as the system block: enlarge E by one site $E' \rightarrow \bullet E$, use the superblock target states to find the reduced density-matrix of the block E' (by tracing out the system S' this time), project it onto a reduced basis of size m , and replace E with E' . For the spin chain version of the SIAM (where the hopping constants γ_i differ in principle from bond to bond for a general bath function) this build-up procedure would assume wrong couplings for the environment. Thus, we use the somewhat slower but model-independent version described above and depicted in Fig. 2.5. Additionally, for reflection-symmetric Hamiltonians, one may consider system and environment to be identical. This again is not useful here as the

targeting itself is asymmetric in our D-DMRG program. We will address the reason for the asymmetry in the target states in [Sect. 2.2.3](#).

Another aspect addresses the efficiency of the large sparse matrix operations. The separate bookkeeping of system and environment basis can be used to formulate a well-performing scheme for matrix-vector operations. In step ② the product basis of the system block S' (*not* the superblock) is built explicitly. Alternatively, the basis sets of the system block S and the single site \bullet can be handled separately. Thus, a routine which performs the application of $\mathcal{H}_{S'}^{L_{S'}} = \mathcal{H}_{S\bullet}^{L_{S'}+1}$ in terms of a basis of product states is needed. Let us collect the orders of all involved multiplications for both schemes assuming for simplicity that we have fm states in the system block $S' = S\bullet$ and in the environment block $E' = \bullet E$ as well as only nearest-neighbor interactions. Let s denote system and e environment block states. Applying $\mathcal{H}_{S'} \otimes \mathbf{1}_{E'}$ to a superblock vector $|\Psi\rangle$ gives

$$\begin{aligned} |\Phi\rangle &= (\mathcal{H}_{S'} \otimes \mathbf{1}_{E'}) |\Psi\rangle \\ \langle se|\Phi\rangle &= \sum_{\tilde{s}, \tilde{e}}^{fm} \langle se|\mathcal{H}_{S'} \otimes \mathbf{1}_{E'}|\tilde{s}\tilde{e}\rangle \langle \tilde{s}\tilde{e}|\Psi\rangle. \end{aligned}$$

Applying the Hamiltonian this way would result in a $\mathcal{O}([fm]^4)$ algorithm with very poor performance. By decomposing the products in system and environment contributions we end up with a well performing $\mathcal{O}(m^3)$ algorithm.

$$\begin{aligned} \text{decomposition: } \quad \langle se|\mathcal{H}_{S'} \otimes \mathbf{1}_{E'}|\tilde{s}\tilde{e}\rangle &= \langle s|\mathcal{H}_{S'}|\tilde{s}\rangle \langle e|\mathbf{1}_{E'}|\tilde{e}\rangle \\ \langle \tilde{s}e|\varphi\rangle &= \sum_{\tilde{e}}^{fm} \langle e|\mathbf{1}_{E'}|\tilde{e}\rangle \langle \tilde{s}\tilde{e}|\Psi\rangle \quad \text{and} \quad \langle se|\Phi\rangle = \sum_{\tilde{s}}^{fm} \langle s|\mathcal{H}_{S'}|\tilde{s}\rangle \langle \tilde{s}e|\varphi\rangle \\ &\Rightarrow \quad \mathcal{O}(fm \cdot [fm]^2) = \mathcal{O}(f^3 m^3), \end{aligned}$$

while for a typical interaction $\mathcal{H}_{S'E'} = \mathbf{S}_\ell^+ \mathbf{S}_{\ell+1}^-$, where ℓ is the last site of S' and $\ell+1$ the first site of E' ,

$$\begin{aligned} |\Phi\rangle &= (\mathbf{S}_\ell^+ \otimes \mathbf{S}_{\ell+1}^-) |\Psi\rangle \\ \langle se|\Phi\rangle &= \sum_{\tilde{s}, \tilde{e}}^{fm} \langle se|\mathbf{S}_\ell^+ \otimes \mathbf{S}_{\ell+1}^-|\tilde{s}\tilde{e}\rangle \langle \tilde{s}\tilde{e}|\Psi\rangle \quad \Rightarrow \quad \mathcal{O}([fm]^4)? \\ \text{decomposition: } \quad \langle se|\mathbf{S}_\ell^+ \otimes \mathbf{S}_{\ell+1}^-|\tilde{s}\tilde{e}\rangle &= \langle s|\mathbf{S}_\ell^+|\tilde{s}\rangle \langle e|\mathbf{S}_{\ell+1}^-|\tilde{e}\rangle \\ \langle \tilde{s}e|\varphi\rangle &= \sum_{\tilde{e}}^{fm} \langle e|\mathbf{S}_{\ell+1}^-|\tilde{e}\rangle \langle \tilde{s}\tilde{e}|\Psi\rangle \quad \text{and} \quad \langle se|\Phi\rangle = \sum_{\tilde{s}}^{fm} \langle s|\mathbf{S}_\ell^+|\tilde{s}\rangle \langle \tilde{s}e|\varphi\rangle \\ &\Rightarrow \quad \mathcal{O}([fm]^3 + [fm]^3) = 2\mathcal{O}(f^3 m^3). \end{aligned}$$

Summarizing the orders of this decomposition scheme we find

$$\mathcal{H} = \underbrace{\mathcal{H}_{S'} \otimes \mathbf{1}_{E'}}_{\mathcal{O}(f^3 m^3)} + \underbrace{\mathcal{H}_{S'E'}}_{2\mathcal{O}(f^3 m^3)} + \underbrace{\mathbf{1}_{S'} \otimes \mathcal{H}_{E'}}_{\mathcal{O}(f^3 m^3)} \Rightarrow 4\mathcal{O}(f^3 m^3). \quad (2.25)$$

If the single sites are not incorporated into the blocks, the decomposition can be taken one step further, leading to

$$\begin{aligned} \mathcal{H} &= \underbrace{\mathcal{H}_S \otimes \mathbf{1}_{\bullet\bullet E}}_{\mathcal{O}(f^2 m^3)} + \underbrace{\mathcal{H}_{S\bullet} \otimes \mathbf{1}_{\bullet E}}_{\mathcal{O}(f^3 m^2 + f^2 m^3)} + \underbrace{\mathbf{1}_S \otimes \mathcal{H}_{\bullet\bullet}}_{2\mathcal{O}(f^3 m^2)} + \underbrace{\mathbf{1}_{S\bullet} \otimes \mathcal{H}_{\bullet E}}_{\mathcal{O}(f^3 m^2 + f^2 m^3)} + \underbrace{\mathbf{1}_{S\bullet\bullet} \otimes \mathcal{H}_E}_{\mathcal{O}(f^2 m^3)} \\ &\Rightarrow 4\mathcal{O}(f^3 m^2 + f^2 m^3). \end{aligned} \quad (2.26)$$

Both schemes are of order $\mathcal{O}(m^3)$ which is essential for the algorithm's performance. Scheme (2.25) is easier to implement as only two basis sets have to be managed. Furthermore, an efficient preconditioner based on diagonalization of the block Hamiltonians $\mathcal{H}_{S'}$ and $\mathcal{H}_{E'}$ can be used, cf. Sect. 2.2.4. Nevertheless, if the number of degrees of freedom per site f is large, scheme (2.26) can be more efficient [Sch05a]. As in our case $f = 2$, we use the simpler deconstruction scheme not managing the single sites separately.²

The infinite size algorithm is intended to describe the properties of low-dimensional quantum systems in the thermodynamic limit $L \rightarrow \infty$. Systems of growing size ($L \rightarrow L + 1$ or $L \rightarrow L + 2$ in each step) are investigated, identifying converging properties (ground state energies, energies of excited states, correlation functions, etc.) and taking their limits as an approximation for the values at infinite system size. With system size growing but keeping fixed the number of states m kept in the reduced basis, truncation errors accumulate. This causes rather significant errors especially for approximate correlation functions when very large system sizes are treated. Another reason for the failure of the infinite size DMRG is the fact that the idea of simulating the final system size by small environment blocks in the early DMRG steps cannot be implemented very well. As DMRG is usually formulated in the canonical ensemble, the number of particles is kept fixed for a given system size L . In electronic systems where the particle number is growing during system growth (step ② in the infinite size DMRG algorithm) to maintain the particle density approximately constant, a lack of “thermalization” of the particles injected during system growth is observed [Sch05a]. Hubbard models far from half-filling or with complicated filling factors and models with the strong physical effects of impurities or randomness

²We kept track of the number of operations arising in a specific order of f and m . This is of course not a rigorous counting as implementation-dependent overhead might come into play in either of the schemes. Nevertheless, for small f and moderate m the prefactors might be of interest and thus we kept them in the formulas.

in the Hamiltonian are affected by this problem. They cannot be accounted for properly by the infinite-size algorithm as the total Hamiltonian is not yet known at intermediate steps. This can be overcome by optimizing for a given system size L using the *finite size algorithm* described in the [next chapter](#).

2.1.8 Finite size algorithm

The finite size DMRG manages to eliminate the problems of the infinite size algorithm to a very large degree and to reduce the error almost to the truncation error. The idea is to carry out the infinite size algorithm until the superblock reaches some preselected size L which is kept *fixed* in all subsequent steps. These steps are similar to the prescription used in the infinite size DMRG, but instead of growing the system block S while keeping the size of the environment block E constant (or simultaneous growing both blocks S and E in the case of reflection symmetry), growing one block is accompanied by shrinking the other block. The system block S is enlarged by one site and the environment block E is chosen such that the total chain length stays constant during building up the system. The reduced basis transformations (projections) are carried out only for the growing block. We refer to the growing block which undergoes the projections always as the *system* block. As *environment* block a previously stored system block is taken. Thus, system blocks of all sizes and operators acting on this block (expressed in the actual block's basis) must have been stored in preceding steps. They might result from the build-up via the infinite size algorithm or from previous applications of the finite size DMRG. The growth direction is reversed if one block (in our nomenclature always the environment block E) reaches some minimum size L_{\min} , which is normally chosen via [Eq. \(2.2\)](#) such that a block of size L_{\min} can be represented exactly. Reversing the growth direction implies interchanging the role of the two blocks: The former system blocks are now the environment blocks for the opposite growth direction; the former environment blocks are the new system blocks which are enlarged by one site prior to projection. In case of a system which is symmetric under reflection, blocks can be mirrored at equal size. In the asymmetric case studied in this thesis the environment block is shrunk to the minimum size for both directions. A complete sequence of growth and shrinkage for both blocks is called a *finite size sweep*.

Let us collect all necessary steps of our implementation of the finite size algorithm.

① *Build-up*

Build a superblock of size L_S using the infinite size algorithm described in [Sect. 2.1.7](#). End up with a configuration shown in the last line of [Fig. 2.5](#) or the first line of [Fig. 2.6](#). All system blocks constructed during the infinite size build-up have to be stored after the density-matrix projection (cf. [Sect. 2.1.3](#)). This includes the block Hamilton operators, all other operators of interest (observables which

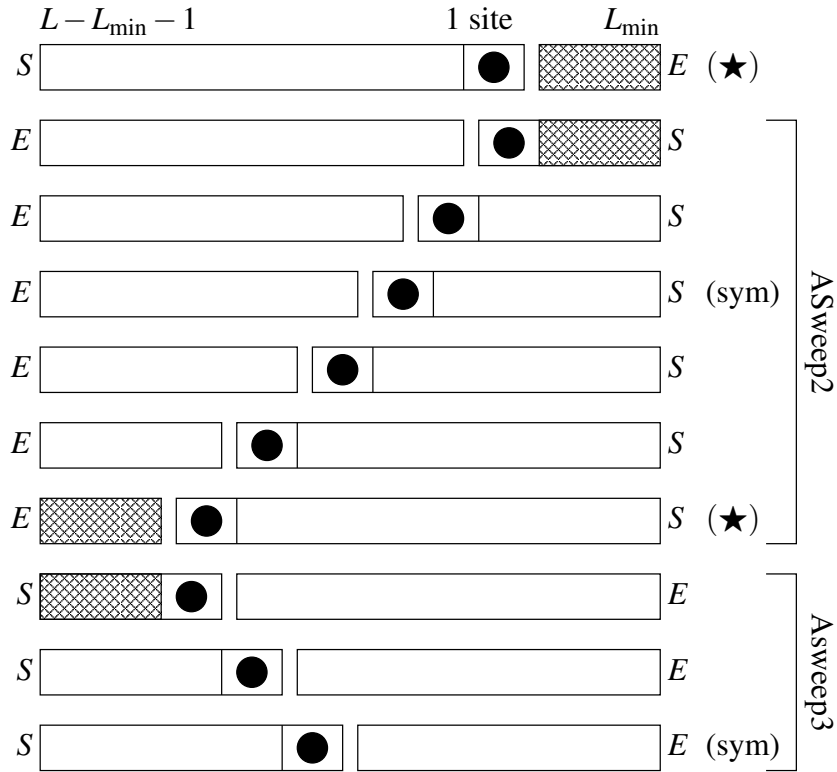


Figure 2.6: Scheme of our implementation of the finite size DMRG prescription done just after a infinite size build-up. Shaded rectangles are exact blocks of length L_{\min} , solid circles are single sites. The final block configuration is symmetric [marked with (sym) in the figure] and is the starting point for a finite-size sweep, cf. Fig. 2.7.

shall be evaluated finally), and operators at the block edges (needed to glue the saved block to another one).

② Warm-up

Continue with the procedure illustrated in Fig. 2.6. Interchange the role of system block S and environment E . Let the new small system block (shaded block in the second line of Fig. 2.6) grow until the environmental block reaches a minimal size of L_{\min} ending up with the configuration marked with \star . The blocks stored in step ① serve as environment blocks for this *right-to-left sweep*. This part is handled by the routine ASweep2 of the C++ program.

The steps to add a single site to block S and the adjacent density-matrix projection are nearly the same as in steps ② to ⑧ of the infinite size scheme. The only difference is that the total chain length $L = L_S + L_E$ is kept at a fixed value while $L_S \rightarrow L_S + 1$ and $L_E \rightarrow L_E - 1$.

- ③ Now the sweep direction is switched and the role of system and environment blocks is interchanged again. The system configuration is brought back to a symmetric situation [marked with (sym) in Fig. 2.6]. This half of the *left-to-right sweep* is done by the `ASweep3` routine.

This and the preceding step are the *warm-up* procedure. They are only performed just after a new build-up via step ①. They ensure that most of the stored blocks have been optimized once using the full system size L and restores a symmetric configuration before the real sweeping procedure starts in the next step.

④ *Full Sweep*

Starting from a symmetric configuration perform a full finite size sweep with fixed chain length L , i. e. do in a row a middle-to-right sweep (`ASweep1`), a right-to-left sweep (`ASweep2`), and a left-to-middle sweep (`ASweep3`). This part is visualized in Fig. 2.7.

Continue sweeping ④ until the desired accuracy in the calculated properties is reached or no further improvement (keeping the number m of states in the reduced basis fixed) is observed.

Again we note that the environmental blocks E are the projected system blocks of the previous steps. After the warm-up $3/4$ of the environment blocks and after the first middle-to-right sweep of step ④ *all* blocks E are optimized for the final chain length L . So all calculations after this stage of the algorithm are performed under knowledge of the full Hamiltonian and optimized environmental blocks. The superblock Hamiltonian is given for chains with nearest-neighbor couplings only as a sum of the system Hamiltonian, the environment Hamiltonian, and the contribution connecting the two blocks [cf. i. e. Eq. (2.25)],

$$\mathcal{H} = \mathcal{H}_S \otimes \mathbf{1}_E + \mathcal{H}_{SE} + \mathbf{1}_S \otimes \mathcal{H}_E . \quad (2.27)$$

The importance of using large *sparse* matrix operations to evaluate an application of \mathcal{H} to a superblock vector $|\Psi\rangle$ has been discussed in Sect. 2.1.8.

Configurations marked with \star are not mandatory as the resulting projected blocks can not be used as new environment blocks, so they could be dropped from the scheme introducing $L_{\min} + 1$ as new minimal block length. But these configurations are special in the sense that the environmental blocks of length L_{\min} are exact. Thus, we use these boundary configuration to analyze the numerical configuration dependence of physical quantities during a finite size sweep. For large L the inclusion of the \star configurations does not slow the algorithm significantly, so we prefer to keep them in the sweeping process.

The finite size algorithm mostly gives substantially more accurate results than the infi-

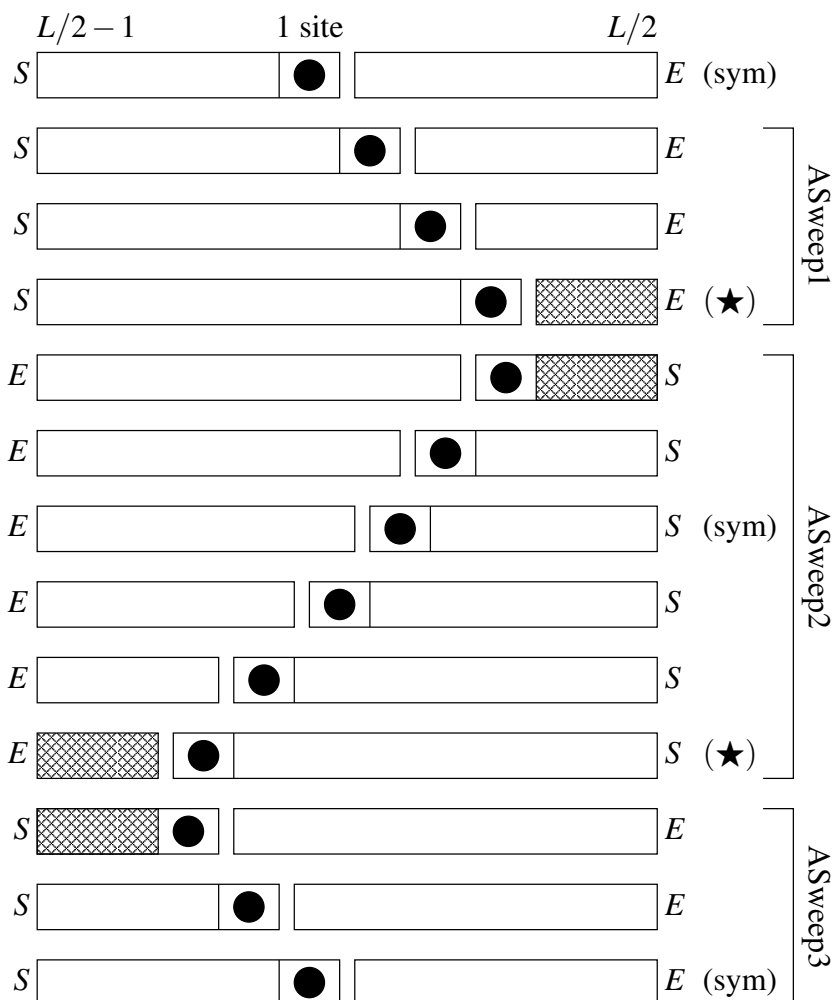


Figure 2.7: Scheme of our implementation of a full finite size DMRG sweep. Shaded rectangles are exact blocks of length L_{\min} or $L_{\min} + 1$, solid circles are single sites. Starting point is the last configuration reached in Fig. 2.6.

nite size algorithm for a given system size L . Therefore the finite size algorithm is usually preferred unless there is a specific reason to go to the thermodynamic limit.

2.1.9 Checks via conventional DMRG

Before we calculate dynamic properties with DMRG in Sect. 2.2, the “conventional” DMRG part of the C++ program has to be checked. This is most easily done by comparing the ground state energies obtained by DMRG with analytical results.

L	20	40	60
DMRG	-6.190 744 999 827 379e+00	-1.255 389 855 581 186e+01	-1.891 904 911 985 461e+01
exact	-6.190 744 999 827 377e+00	-1.255 389 855 581 189e+01	-1.891 904 911 985 469e+01
L	80	100	120
DMRG	-2.528 471 689 739 627e+01	-3.165 059 457 770 153e+01	-3.801 657 806 512 475e+01
exact	-2.528 471 689 739 745e+01	-3.165 059 457 771 009e+01	-3.801 657 806 516 119e+01
L	140	180	220
DMRG	-4.438 262 233 186 449e+01	-5.711 481 260 771 376e+01	-6.984 707 715 424 186e+01
exact	-4.438 262 233 198 018e+01	-5.711 481 260 834 951e+01	-6.984 707 715 641 598e+01

Table 2.1: Ground state energy $E_0(L)$ of an XY chain (2.28) of even length L . The exact results are obtained using Eq. (2.30). The DMRG values were calculated with $m = 256$ states and five sweeps.

fit order	e_0	\tilde{b}_0	\tilde{b}_{-1}	\tilde{b}_{-2}
L^1	-0.317132			
L^0	-0.31829	+0.177503		
L^{-1}	-0.318309	+0.181568	-0.12266	
L^{-2}	-0.31831	+0.181687	-0.13056	+0.1174
L^{-2}	fixed exact	+0.181689	-0.130684	+0.119118
L^{-2}	fixed exact	fixed exact	-0.13079	+0.120927
L^{-2}	fixed exact	fixed exact	fixed exact	+0.123356
exact	-0.318310	+0.181690	-0.130900	+0.130900

Table 2.2: Fit parameters obtained by least-square fits of DMRG results for the ground state energy of free fermions using $m = 256$ states and 5 finite size sweeps for system sizes between 20 and 220 in steps of 20 sites. The exact coefficients, cf. (2.30), are given for comparison.

XY chain

In the Hamilton operator (1.67) the case of spinless fermions corresponding to an XY spin $S=1/2$ chain is included. If we choose a vanishing Coulomb interaction $U = 0$, the \mathbf{S} spins in (1.67) decouple from the \mathbf{T} spins. Hence only the \mathbf{S} part of the chain has to be included in the DMRG calculations. By further specializing to constant couplings $V = \gamma_i := J/2$ introducing the energy scale J , the Hamiltonian is simply given by³

$$\mathcal{H}_{XY} = J/2 \sum_{i=1}^L (\mathbf{S}_i^+ \mathbf{S}_{i+1}^- + \text{h.c.}) = J \sum_{i=1}^L (\mathbf{S}_i^x \mathbf{S}_{i+1}^x + \mathbf{S}_i^y \mathbf{S}_{i+1}^y) . \quad (2.28)$$

We discussed the Jordan-Wigner mapping which relates this model to free fermions in Sect. 1.6.2. This allows us to use the dispersion relation $\varepsilon(k) = -\cos(k)$ for free spinless

³In a more strict nomenclature the term XX model is more appropriate as the coupling constants for the $\mathbf{S}_i^x \mathbf{S}_{i+1}^x$ and $\mathbf{S}_i^y \mathbf{S}_{i+1}^y$ terms are chosen to be equal here.

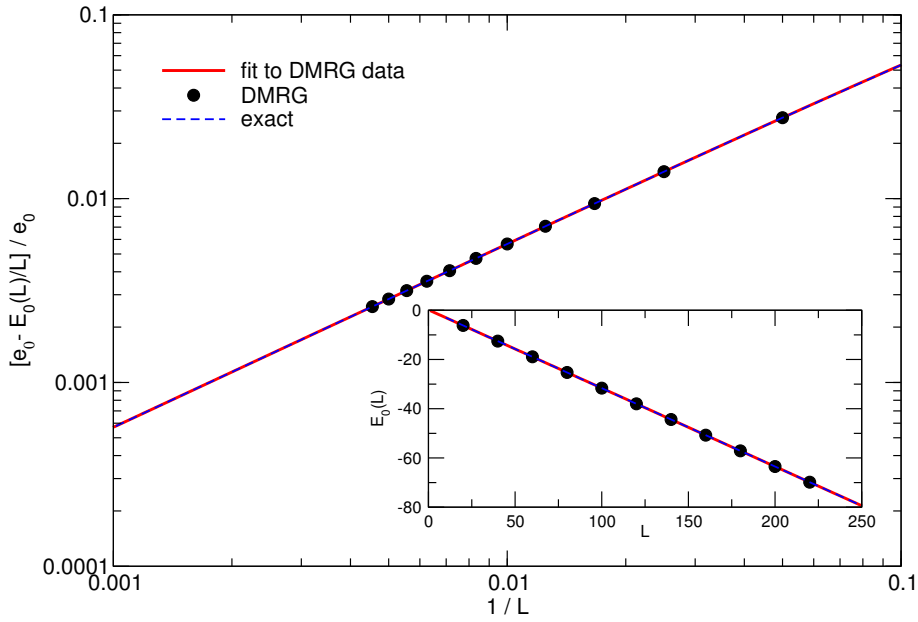


Figure 2.8: Ground state energy of an isotropic XY chain of length L calculated by finite size DMRG with $m = 256$ states and five sweeps (dots). *Larger plot:* relative finite size deviation vs. $1/L$ on double-log scale. *Inset:* $E_0(L)$ on linear scale. The straight line corresponds to a fit including powers in L from L^1 to L^{-2} . The fit parameters are given in the fourth line of [Tab. 2.2](#). The exact curve (dashed line) is nearly indistinguishable from the fit.

fermions, where we have chosen $J = 1$ and measure all energies in units of J for the remaining part of this section. For open boundary conditions—which are used in all our calculations—no particle creation at sites with indices ‘0’ and ‘ $L + 1$ ’ is possible. This restricts the possible momenta, $k(L + 1) = m\pi$ with $m = 1, \dots, L$. Summing up the negative contributions from the full set of energy eigenvalues E_m^L for a chain of length L ,

$$E_m^L = -\cos \frac{m\pi}{L+1} \quad , \quad m \in \{1, 2, \dots, L\} \quad , \quad (2.29)$$

we find the exact finite size energy $E_0(L)$. The result for chains of even length L is given by

$$E_0(L) = \sum_{m=1}^{L/2} E_m^L = \frac{1}{2} \left[1 - \frac{1}{\sin \left(\frac{\pi}{2(L+1)} \right)} \right] =: e_0 L + \sum_{i=0}^{\infty} \tilde{b}_{-i} L^{-i} \quad (2.30)$$

$$\simeq -\frac{L}{\pi} + \left(\frac{1}{2} - \frac{1}{\pi} \right) - \frac{\pi}{24} L^{-1} + \frac{\pi}{24} L^{-2} + \mathcal{O}(L^{-3}) \quad (2.31)$$

and for odd L by

$$E_0(L) = \sum_{m=1}^{L/2-1} E_m^L = \frac{1}{2} \left[1 - \frac{\sin\left(\frac{\pi L}{2(L+1)}\right)}{\sin\left(\frac{\pi}{2(L+1)}\right)} \right] \quad (2.32)$$

$$\simeq -\frac{L}{\pi} + \left(\frac{1}{2} - \frac{1}{\pi}\right) + \frac{\pi}{12}L^{-1} - \frac{\pi}{12}L^{-2} + \mathcal{O}(L^{-3}) \quad (2.33)$$

Tab. 2.1 compares the ground state energies obtained with finite size DMRG using $m = 256$ states and five sweeps with the exact values. As the number of decimal digits of precision in a double floating point number is 15 and the difference between 1.0 and the minimum double greater than 1.0 is $2.2204460492503131e-16^4$, agreement in 15 digits is the maximum one can achieve. For 20, 40, and 60 this maximum accuracy was obtained with the before-mentioned DMRG parameters, cf. **Tab. 2.1**. Enlarging the chain length up to 220 sites, the precision is only reduced to 10 digits.

Fig. 2.8 shows the data of **Tab. 2.1** as relative deviation of the finite size energy per site $E_0(L)/L$ from the bulk energy per site versus $1/L$ on a double-log scale and the energy $E_0(L)$ on a linear scale in the inset. The data is nearly indistinguishable from the exact results shown as dashed line. Thus, we extracted the prefactors in the leading contributions of an $1/L$ expansion of the exact solution. The analytical values can be read off from **Eq. (2.31)** and are given for comparison in the last line of **Tab. 2.2**. This table summarizes the results from the fits using a fit function with an $1/L^2$ term as highest power in $1/L$, i. e. $E_0(L) = e_0L + \tilde{b}_0 + \tilde{b}_{-1}L^{-1} + \tilde{b}_{-2}L^{-2}$. To test the stability of the least-square fits, we checked various orders of the polynomial—sometimes fixing one or more of the coefficients to the exact value. The agreement is excellent for e_0 (the bulk value for the ground state per site) and \tilde{b}_0 (a surface term which would vanish for periodic boundary conditions). For the $1/L$ coefficient the relative error is about 0.25%, if the fourth line (“unbiased” four parameter fit) was used. For a stable determination of the $1/L^2$ coefficient, the data is not precise enough. Nevertheless, the series of fits shows a clear tendency to reach the correct value from below. A series of values calculated for small chains would help to fit the higher order coefficients. But here we concentrated on the accuracy aspect of the energies obtained via DMRG. With only 11 system sizes the leading three coefficients of the scaling law for the energies of the XY chain could be extracted in a quantitative fashion.

To find the ground state energy $E_0(L)$ **(2.30)** we have summed up the energy eigenvalues E_m^L **(2.29)**. During the exact build-up phase **1** of the DMRG algorithm no projections are made as long as the Hilbert space size of the represented block does not exceed the

⁴Cf. DBL_DIG and DBL_EPSILON from float.h.

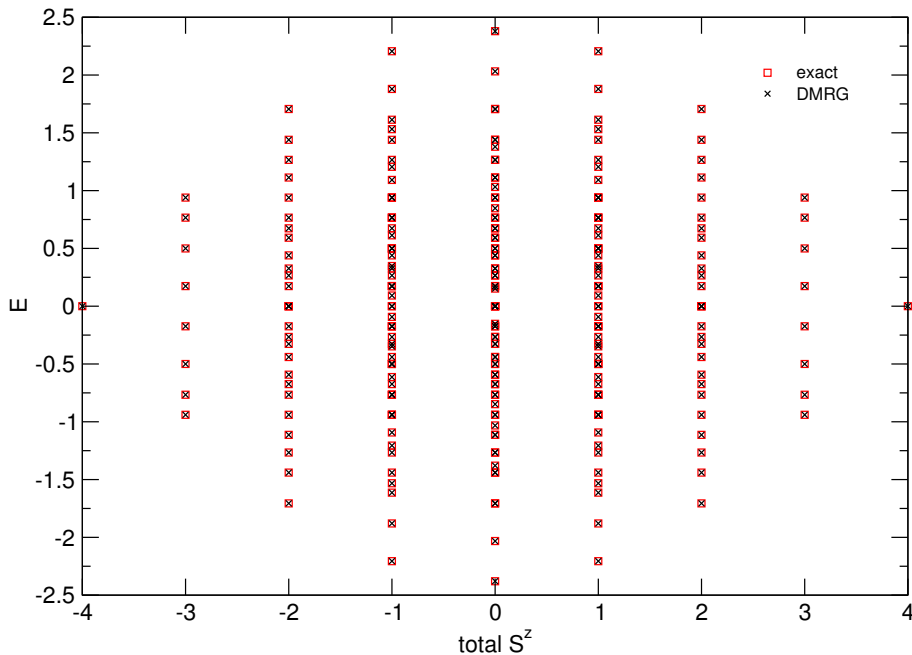


Figure 2.9: All energy eigenvalues of an isotropic XY chain of length $L = 8$ calculated during the exact stage of the build-up compared to the exact result.

number of states in the reduced DMRG basis. We can use this to compare *all* energy eigenvalues of the still exactly represented system block to the exact eigenvalues E_m^L . The diagonalization of a block Hamiltonian is easy as the Hamilton matrix is a sparse block-diagonal matrix. The total magnetization $\mathbf{S}_{\text{tot}}^z$ (or $\mathbf{S}_{\text{tot}}^z + \mathbf{T}_{\text{tot}}^z$ if also \mathbf{T} operators are involved) is due to $U(1)$ symmetry of the model a good (conserved) quantum number. Thus, all operators including the Hamilton operators of system and environment block can be expressed in matrix form as dense blocks of non-zero matrix elements with all other matrix elements zero. These dense blocks can be labelled by the good quantum number. [Fig. 2.9](#) shows all 256 energy eigenvalues of an XY chain with $L = 8$ sites labelled by $\mathbf{S}_{\text{tot}}^z$. The numerically determined eigenvalues agree perfectly with the E_m^L from [Eq. \(2.29\)](#). We performed similar check for larger chains, where DMRG projections have already been performed. Here the low-lying eigenvalues of the different $\mathbf{S}_{\text{tot}}^z$ sectors can be compared. Furthermore, we checked the correct implementation for even and odd length of the block and for the first stages of a sweep.

Up to this stage, we have only checked the correct implementation of the $\mathbf{S}^+\mathbf{S}^-$ or $\mathbf{T}^+\mathbf{T}^-$ operators, i. e. the hopping terms of the SIAM. To check in our C++ program the $\mathbf{S}^z\mathbf{T}^z$ term included in the SIAM Hamiltonian, i. e. the Coulomb repulsion, an additional analysis is needed.

L	10	20	22
exact	-0.425 803 520 728 288		
ED	-0.425 803 520 728 286	-0.434 123 666 719 945	-0.434 912 539 817 420
iDMRG	-0.425 803 520 728 288	-0.434 123 666 719 692	-0.434 912 539 816 51
L	24	26	28
ED	-0.435 574 406 683 723	-0.4361 376 789 521 105	-0.436 622 876 735 809
iDMRG	-0.435 574 406 681 765	-0.4361 376 789 489 03	-0.436 622 876 731 205
fDMRG			-0.436 622 876 735 817

Table 2.3: Ground state energy per site of Heisenberg chains of length L . The results obtained exactly (using a computer algebra tool), via exact Lanczos diagonalization, and via infinite (iDMRG) or finite (fDMRG) size density-matrix renormalization group are compared. For the DMRG calculations up to $m = 256$ states and five sweeps for the fDMRG value have been used.

fit order	e_0	E_{surf}	b_{conf}	b_{-2}
L^1	-0.442 876			
L^0	-0.443 142	+0.184717		
L^{-1}	-0.443 147	+0.188 607	-0.166 862	
L^{-2}	-0.443 147	+0.188 742	-0.181 25	+0.319
L^{-2}	fixed exact	+0.188 845	-0.190 5	+0.505
L^{-2}	fixed exact	fixed exact	-0.188 249	+0.457 753
L^{-2}	fixed exact	fixed exact	fixed exact	+1.004 07
exact	-0.443 147	+0.188 825	-0.205 617	

Table 2.4: Fit parameters for the finite size scaling behavior of ground state energy of a Heisenberg chain obtained by least-square fits of DMRG results using the data set presented in Fig. 2.10.

Heisenberg chain

In the language of the SIAM the on-site Coulomb repulsion was mapped onto a $US_0^z T_0^z$ term on the impurity Jordan-Wigner spins. Keeping the hopping constants fixed to $V = \gamma_i := J/2$ but allowing for $\mathbf{S}_i^z \mathbf{S}_{i+1}^z$ contributions on every bond instead of a single one—which is not included the Hamiltonian (1.67)—a full isotropic Heisenberg Hamiltonian

$$\mathcal{H}_{\text{Heis}} = J \sum_{i=1}^L \mathbf{S}_i \mathbf{S}_{i+1} \quad (2.34)$$

can be investigated. No additional programming had to be done for this, simply an if clause has to be changed. The analytical results available for the ground state energy of the Heisenberg chain (or the XXX Hamiltonian) are highly non-trivial compared to the

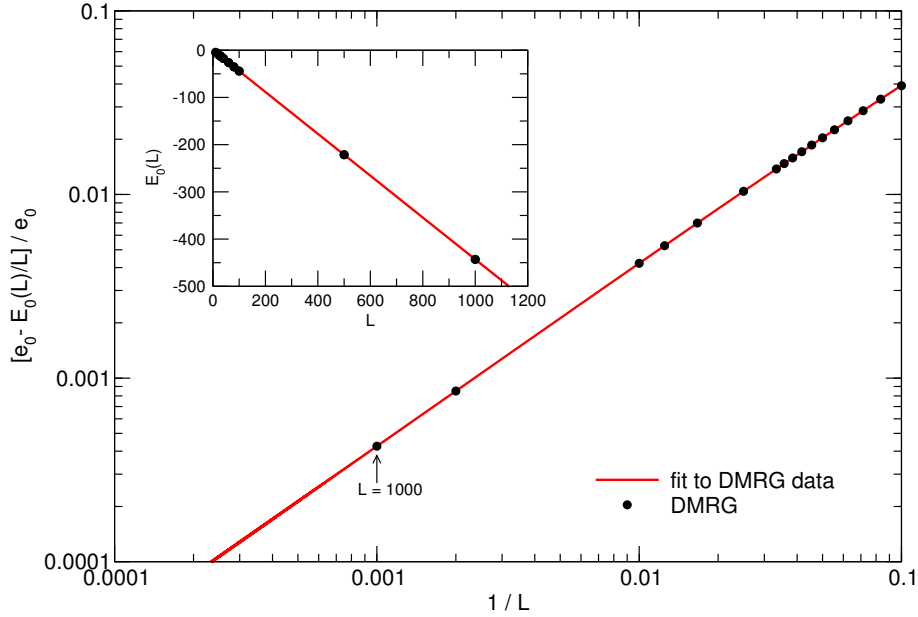


Figure 2.10: Ground state energy of an isotropic Heisenberg chain of length $L \in \{10, \dots, 100, 500, 1000\}$ calculated by finite size DMRG with $m \in \{128, 256, 512\}$ states and five sweeps (dots). $e_0 = 1/4 - \ln 2$ denotes the exact value for the ground state energy per site for a chain of infinite length. *Larger plot:* relative finite size deviation vs. $1/L$ on double-log scale. *Inset:* $E_0(L)$ on linear scale. From this data set the leading finite size scaling behavior was extracted and the resulting fit parameters, cf. [Tab. 2.4](#), can be compared to the analytical values.

XX case and are summarized in the following formula (again the energy unit is $J = 1$):⁵

$$E_0(L) = e_0 L + E_{\text{surf}} + b_{\text{conf}} L^{-1} + b_{-2} L^{-2} + \mathcal{O}(L^{-3}) \quad (2.35)$$

$$e_0 = \frac{1 - 4 \ln 2}{4} \approx -0.443147 \quad (2.36)$$

$$E_{\text{surf}} = \frac{\pi - 1 - 2 \ln 2}{4} \approx 0.188825 \quad (2.37)$$

$$b_{\text{conf}} = -\frac{\pi \nu c}{24} = -\pi^2/48 \approx -0.205617. \quad (2.38)$$

The contribution e_0 is the exact ground state energy per site of the isotropic Heisenberg chain [[Bet31](#), [Hul38](#)]. The surface term E_{surf} vanishes for periodic boundary conditions. The exact value for open boundary conditions was determined by *Batchelor* and *Hamer* [[Bat90](#)]. The L^{-1} contribution was calculated by conformal field theory [[Blö86](#)]⁶. The

⁵For a comment on the $b_{-2} L^{-2}$ term used in [Eq. \(2.35\)](#) cf. [footnote 7](#).

⁶For the exact result in the case of periodic boundary conditions see also Ref. [[Aff86](#)].

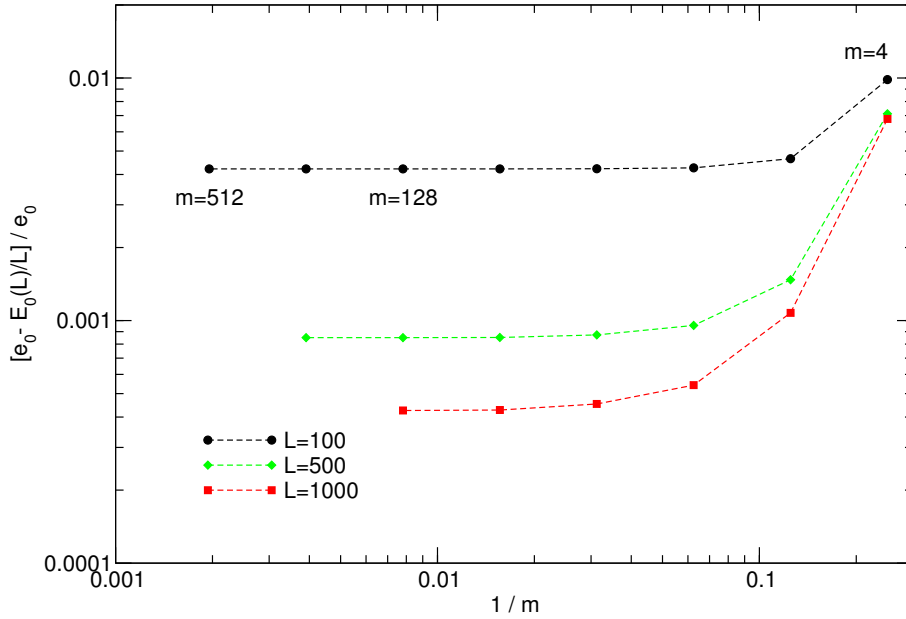


Figure 2.11: DMRG convergence for growing m . The relative finite size deviation in the ground state energy per site of an isotropic Heisenberg chain of length L is shown vs. $1/m$ on a double-log scale. The sizes of the truncated Hilbert space m used for this figure are $\{4, 8, 16, 32, 64, 128, 256, 512\}$.

conformal anomaly (or conformal charge) c for the Heisenberg model is $c = 1$ [Tak73, Tak74, Avd86] and the “sound velocity” is $v = \pi/2$ [Clo62].

For the Heisenberg chain no simple explicit formula for the finite size ground state $E_0(L)$ energy is available. To check the DMRG numerics for small systems, we used exact (Lanczos) diagonalization to produce numerically exact results for $E_0(L)$. The Lanczos routines themselves were checked for very small systems by solving the problem exactly with computer algebra tools. The results are summarized in Tab. 2.3. When finite size DMRG starts to loose accuracy for moderate system sizes, doing finite size sweeps regains the full floating point precision of 15 digits, cf. $L = 28$ in Tab. 2.3.

Fig. 2.10 shows the ground state energy obtained via DMRG for system sizes up to $L = 1000$. Repeating the analysis done for the XY chain, the finite size scaling behavior can be extracted. The exactly known values e_0 , E_{surf} , and b_{conf} [cf. (2.36–2.38)] are compared to the results obtained by least-square fitting the DMRG values. The findings are presented in Tab. 2.4. The bulk value of the ground state energy per site e_0 and the surface energy E_{surf} can be determined accurately and in a robust fashion. For the coefficient b_{conf} reflecting the conformal invariance of the underlying model the relative error is about 12%, if the fourth line (“unbiased” four parameter fit) is used. Here—and especially for the higher order $1/L$ contributions or logarithmic corrections—more

values for $E_0(L)$ would be very useful. The fit procedure for b_{-2} already turns out to be unstable.⁷

Nevertheless, it is obvious from the preceding analysis that the operators needed for the construction of the full SIAM Hamiltonian are correctly implemented. Furthermore, the modified build-up and sweeping scheme described in Sect. 2.1.7 and used in our program is capable of correctly approaching the thermodynamic limit of the models investigated. We complete the analysis using the conventional DMRG by investigating the convergence behavior with growing m or additional sweeping.

Fig. 2.11 shows the convergence of DMRG calculations for the finite size ground state energy of Heisenberg chains of length $L \in \{100, 500, 1000\}$ by increasing the number of states m kept in the reduced basis set. Up to $m = 512$ states for $L = 100$, $m = 256$ for $L = 500$, and $m = 128$ for $L = 1000$ were used for this calculation. Note, that typical chains investigated by D-DMRG will be of length $L_s = 240$ ($N_f = 120$) and at maximum $L_s = 800$ ($N_f = 400$). The plot clearly shows that enlarging the number of states beyond $m = 128$ is only necessary for very large chains. For the D-DMRG this means—as we need additional target states there—that $m = 128$ is a reasonable value for intermediate chains of $L_s = 240$ and $m = 256$ can be used to enhance accuracy for larger L_s .

Another aspect of optimizing the DMRG efficiency is the number of finite size sweeps. Fig. 2.12 shows the convergence behavior of the ground state energy of a Heisenberg chain of length $L = 500$ for fixed values of m between 8 and 256. When keeping only a small number of states in the reduced basis additional sweeping enhances the accuracy significantly. If m is already fairly large, cf. Fig. 2.13, the accuracy gain is only moderate. Clearly visible in Fig. 2.13 is that for $m = 128$ additional sweeping increases the accuracy in the ground state energy. Doubling the size of the reduced Hilbert space to $m = 256$ states, we gain an order of magnitude in the accuracy without additional sweeping. Thus, the number of sweeps and m have to be chosen in a reasonable fashion to obtain accurate results in an efficient way. For the application in the dynamic density-matrix renormalization using a second sweep turned out to be not very useful. As a second sweep doubles the computing time compared to one-sweep calculations we preferred to increase m when additional accuracy is needed. It is easier to find good a trade-off between computation time and accuracy by optimizing m than by doing additional very time-consuming finite size sweeps.

⁷ For periodic boundary conditions Lukyanov [Luk98] has shown that the correction beyond the L^{-1} contribution is proportional to $(L \ln^3 L)^{-1}$, cf. also Refs. [Med91, Klü98, Klü00]. It is a plausible assumption that this logarithmic correction also appears for open boundary conditions. Replacing the L^{-2} term in the fit function by the logarithmic term does not improve the results significantly, i. e. b_{conf} obtained from the fitting still deviates from the exact value.

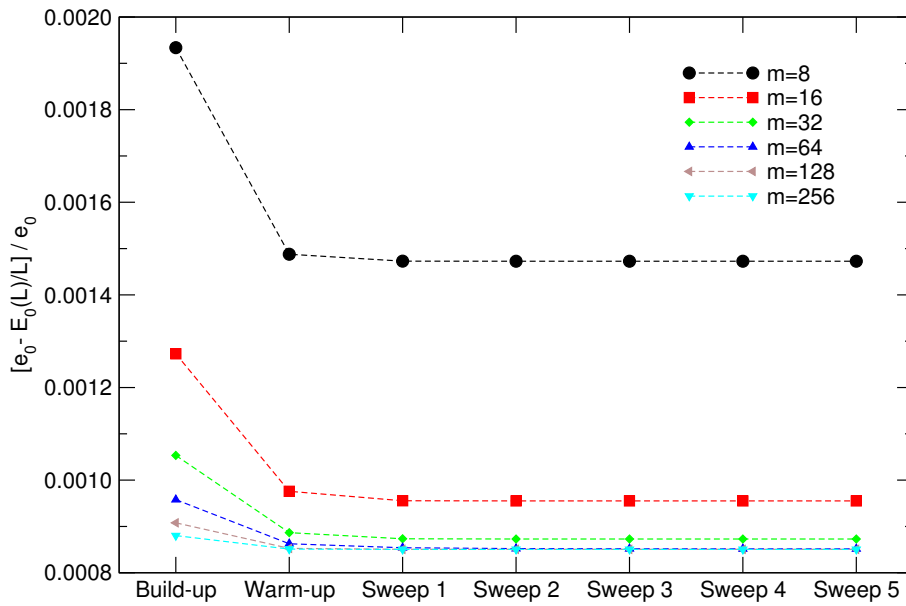


Figure 2.12: Sweep convergence for fixed $L = 500$ and various m . The DMRG results for the relative finite size deviation in the ground state energy per site of an isotropic Heisenberg chain are shown after the build-up ①, the warm-up ②+③ (equivalent to a $3/4$ sweep), and after one to five full finite size sweeps ④. A zoomed plot for $m = 128$ and $m = 256$ is given by Fig. 2.13.

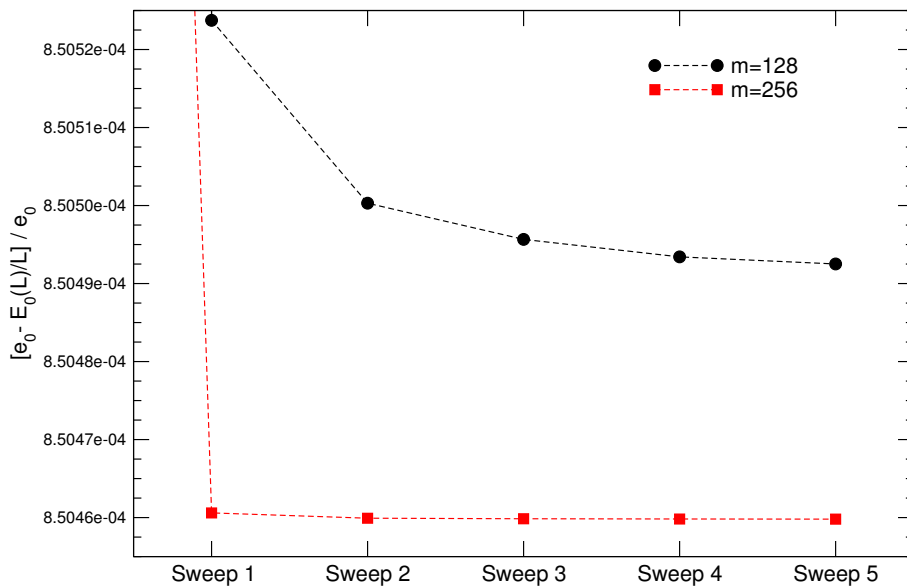


Figure 2.13: The same parameters as in Fig. 2.12 but on a zoomed scale for $m = 128$ and $m = 256$ states.

2.2 Dynamic DMRG

2.2.1 Introduction

In the [previous section 2.1](#) we introduced the DMRG as an excellent method to calculate ground states. Targeting also selected excited states they can be obtained at almost machine precision. The fact that for an accurate calculation of e. g. an excitation energy the corresponding excited state has to be included in the set of target states might lead us to the conclusion that even at zero temperature DMRG is not suitable to calculate dynamic properties as the time evolution of general excited states will explore large parts of the Hilbert space [[Sch05a](#)]. Nevertheless, it has turned out [[Hal95](#), [Ram97](#), [Küh99b](#)] that the relevant part of the Hilbert space can be properly addressed by DMRG.

Let \mathcal{A} be some operator and $\mathcal{A}(t)$ its representation in the Heisenberg picture. Then we can define the time dependent correlation function

$$C_{\mathcal{A}}(t-t') = \langle 0 | \mathcal{A}^\dagger(t') \mathcal{A}(t) | 0 \rangle \quad \text{with } t' \geq t \quad (2.39)$$

where $|0\rangle$ denotes the ground state of the system. Fourier transforming $C_{\mathcal{A}}(t-t')$ we can express the correlation function in spectral or Lehmann representation using the eigenstates $|n\rangle$ of the Hamiltonian \mathcal{H} with energy E_n

$$C_{\mathcal{A}}(\omega) = \sum_n |\langle n | \mathcal{A} | 0 \rangle|^2 \delta(\omega - (E_n - E_0)) . \quad (2.40)$$

This frequency-dependent correlation function is related to the Green function⁸

$$G_{\mathcal{A}}(\omega + i\eta) = \left\langle 0 \left| \mathcal{A}^\dagger \frac{1}{\omega + i\eta - (\mathcal{H} - E_0)} \mathcal{A} \right| 0 \right\rangle \quad (2.41)$$

via

$$C_{\mathcal{A}}(\omega) = -\frac{1}{\pi} \Im \lim_{\eta \rightarrow 0^+} G_{\mathcal{A}}(\omega + i\eta) . \quad (2.42)$$

The parameter η ensures causality in [Eq. \(2.41\)](#) and provides a Lorentzian broadening of $C_{\mathcal{A}}(\omega)$. The broadened correlation function can be written in terms of a convolution integral

$$C_{\mathcal{A}}(\omega + i\eta) = \int d\omega' C_{\mathcal{A}}(\omega') \rho_L^{(\eta)}(\omega - \omega') \quad (2.43)$$

⁸ For the definition of the full retarded Green function see Eqs. (1.35, 1.36, 1.37, 1.38) in [Sect. 1.5](#).

where $\rho_L^{(\eta)}$ is a Lorentzian of width η

$$\rho_L^{(\eta)}(\omega) = \frac{\eta}{\pi(\omega^2 + \eta^2)} \quad (2.44)$$

introduced in (1.72). The broadening serves either to broaden numerically obtained spectra of *finite* systems into some “thermodynamic limit” ($L = \infty$) behavior or to broaden analytical results for $C_{\mathcal{A}}$ for comparison to numerical spectra where η is finite. The latter route implies that one is not interested in sharp features in the correlation function as they are washed out by the broadening. If resolving peaks corresponding to excitations with very long lifetimes is the objective then one should follow the “opposite” route: retrieve $C_{\mathcal{A}}(\omega)$ from the numerically calculated $C_{\mathcal{A}}(\omega + i\eta)$ by deconvolution. We present various deconvolution schemes in [Chapt. 3](#).

The one-particle Green function with $\mathcal{A} = d_{\sigma}^{\dagger}$ for the single impurity Anderson model has been introduced in [Sect. 1.5](#), cf. [Eq. \(1.35\)](#). Reformulating the SIAM in the language of Jordan-Wigner spins we wrote the Green function with $\mathcal{A} = \mathbf{S}_0^+$ via [Eq. \(1.68\)](#), cf. [Sect. 1.6.3](#). Switching from the direct calculation of the local propagator to a calculation of the “improper” self-energy $Q(\omega + i\eta)$, cf. [Sect. 1.6.4](#), we have to set $\mathcal{A} = d_{\uparrow}^{\dagger} (n_{d,\downarrow} - 1/2)$ in fermionic language, cf. [Eq. \(1.98\)](#), or $\mathcal{A} = \mathbf{S}_0^+ \mathbf{T}_0^z$ in terms of Jordan-Wigner spins, cf. [Eq. \(1.99\)](#).

The calculation of the $T = 0$ one-particle dynamics for symmetric single impurity Anderson models is the objective of this thesis. In the next sections the various ways how this can be achieved by the means of the density-matrix renormalization are presented.

2.2.2 Lanczos method

The function $G_{\mathcal{A}}(\omega)$ can be written in the form of a continued fraction, cf. [Sect. 1.4](#):

$$G_{\mathcal{A}}(z) = \frac{\langle 0 | \mathcal{A}^{\dagger} \mathcal{A} | 0 \rangle}{z - a_0 - \frac{b_0^2}{z - a_1 - \frac{b_1^2}{z - a_2 - \dots}}} . \quad (2.45)$$

to choose the stopping criterion see Refs. [Küh99b, Sch05a]. In our implementation the building of the continued fraction is stopped when $|\langle f_0 | f_n \rangle| > 10^{-12}$.

To see whether the Lanczos DMRG fulfills our requirements we did calculations for the non-interacting case $U = 0$ of the SIAM using a semi-elliptic free DOS (1.54). The one-particle-propagator (1.35) was calculated for systems with 40 and 100 fermions by means of finite size DMRG using 5 sweeps, $m = 256$ states and targeting the ground state and 8 Lanczos vectors. The continued fraction was then evaluated numerically for the symmetric configuration where system and environment block have equal size and truncation errors are expected to be smallest. For this first check, the non-interacting case has the advantage that we can compare directly to exact results also for finite system sizes. Fig. 2.14 summarizes our findings. The first row shows the exact results for systems with 40 and 100 fermions compared to the limit of infinite system size. Note, that only the contribution for positive frequencies is shown. The full propagator is recovered by Eq. (1.37).

The finite size spectral density shows $L/2$ δ -peaks for positive frequencies. For graphical rendering they have to be broadened. For comparison, the result for the thermodynamic limit, the positive frequency part of a rescaled semi-circle, is also shown. The second row shows the Lanczos DMRG results rendered using a broadening $\eta = 0.1D$. Note that the exact *finite* size result broadened with $\eta = 0.1D$ would be indistinguishable from the broadened exact *infinite* size curve (on the shown scale). The Lanczos DMRG is capable to reproduce the overall shape qualitatively. The agreement is excellent for small and high frequencies but only moderate for intermediate ones. Here the Lanczos DMRG produces additional structures on the DOS where the exact result is a smooth curve. What happened becomes clearer if we render the spectral densities with a smaller broadening $\eta = 0.01D$, cf. third row of Fig. 2.14. The finite size peaks are clearly visible in the exact curve. The Lanczos DMRG results reproduce for $L = 40$ the first low-frequency peak quantitatively and the two next peaks qualitatively. All peaks at intermediate and high frequencies are missed. Of course, by targeting approximately $L/2$ Lanczos vectors $|f_n\rangle$ and enlarging m significantly the agreement is expected to be better. But as we are interested mainly in the thermodynamic limit the $L = 100$ results already show that Lanczos DMRG is not the appropriate tool to resolve the spectrum adequately. The $L/2$ finite size peaks distributed in a regular pattern in the bandwidth interval “collapse” to a small number of peaks carrying much weight. These spurious peaks induce the substructures on the $\eta = 0.1D$ curves. The overall shape is captured by the Lanczos vector method, but with no additional knowledge on the expected result the curves could be misinterpreted easily. It is a priori not clear whether additional peaks in the broadened spectra are physical or an effect of the spurious “peak clustering” visible in the last row of Fig. 2.14.

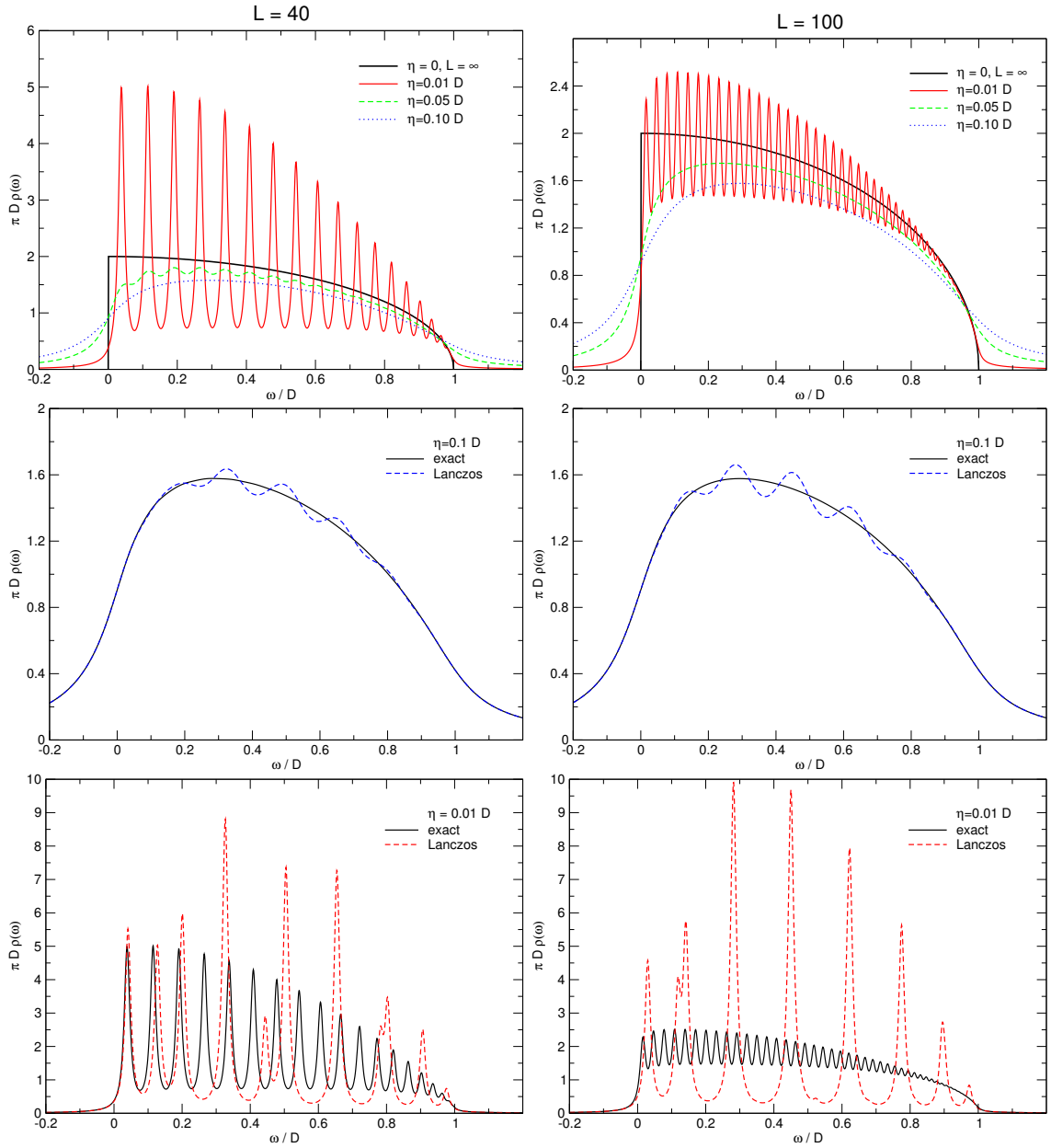


Figure 2.14: Lanczos DMRG results for the non-interacting case ($U = 0$) for $L = 40$ (left column) and $L = 100$ (right column). Only the particle propagator (1.35) has been evaluated. *Upper row:* exact finite size results with broadenings $\eta = 0.01D$, $\eta = 0.05D$, and $\eta = 0.1D$ and exact unbrodened result in the thermodynamic limit ($L = \infty$). *Middle row:* comparison of Lanczos DMRG and exact results for broadening $\eta = 0.1D$. *Lower row:* $\eta = 0.01D$. The Lanczos DMRG was performed with $m = 256$ states in the reduced basis and targeting the ground state and 8 Lanczos vectors.

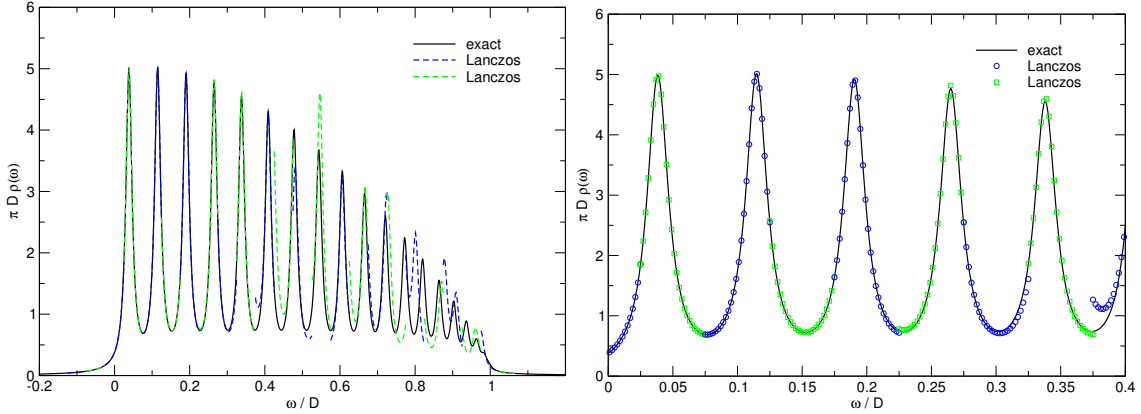


Figure 2.15: Lanczos DMRG results with frequency-optimized basis. The Lanczos algorithm was used in steps of $\delta\omega = 0.05D$ for $L = 40$ fermions with $m = 256$ states and targeting 8 Lanczos vectors. Lanczos results for adjacent intervals are shown in different shades or symbols.

We conclude that the Lanczos DMRG is a fast tool to get a quick overview of spectra, but it is not suited for detailed quantitative calculations for excitation continua. For excitation bands where no significant substructures are expected the broadened spectra provide a valuable insight, nevertheless they should be interpreted with care. Another field of application for the Lanczos method are dominant single modes. Isolated prominent structures in the spectrum can be described with continued fractions fairly low in depth and thus are in the regime where Lanczos DMRG works reliably.

By combining the Lanczos method with the method described in the [next section 2.2.3](#) the results obtained from the continued fractions (2.45) can be improved. The price one has to pay is a much slower algorithm.

The key idea is to optimize the DMRG basis for a given frequency ω_i by targeting an ω -dependent correction vector. The Lanczos algorithm is performed for each frequency ω_i yielding continued fractions which are optimized for a specific frequency interval. We chose for $L = 40$ sites a frequency stepsize of $\delta\omega = 0.05D$: $\omega_{i+1} = \omega_i + \delta\omega$. The spectrum is scanned in the interval $[-0.2D, 1.2D]$. It is worthwhile mentioning that this does not mean that the frequency-optimized Lanczos DMRG is slower by a factor of the number of frequencies ω_i compared to the standard Lanczos (where the whole spectrum is rendered using *one* continued fraction). The calculation of the ω -dependent “correction vector” is numerically extremely demanding and this slows down the performance by an additional order of magnitude. We postpone the details to the [next section](#).

[Fig. 2.15](#) shows the results of the frequency-optimized Lanczos procedure. The continued fractions are plotted for the intervals $[\omega_i - \delta\omega/2, \omega_i + \delta\omega/2]$. To render curves belonging to adjacent intervals distinguishably, we use two different shades (left) or symbols

(right). The first five finite size peaks are described excellently by the Lanczos results. For $0.4 \leq \omega/D \leq 0.75$ the agreement is good but the spectral weight at the minima or maxima of the peaks is over- or underestimated. The high-frequency part below the band edge D is only a poor approximation to the true spectrum. A problem of this way of calculating and presenting the findings is that the curves for adjacent intervals need not be connected continuously. It depends on the way the data is used whether the discontinuities are a severe drawback or a minor problem. For the implementation in the self-consistency cycle of the dynamic mean-field theory the jumps must be taken seriously. We note here that this approach can be improved further by targeting two correction vectors for frequencies ω_1 and ω_2 and obtaining the spectrum via continued fraction expansion in the interval $[\omega_1, \omega_2]$ (slowing down the performance by a factor of two), for details see Ref. [Küh99b].

Instead of using Lanczos vector DMRG and trying to eliminate the problem of discontinuities we use a different scheme, nowadays known as “correction vector DMRG” in the literature.

2.2.3 Correction vector method

The key idea of the dynamic DMRG is to include a frequency dependent correction vector $|\xi\rangle$ in the target states of a standard DMRG algorithm [Ram97, Küh99b, Küh99a, Höv00].⁹ The natural choice is

$$|\xi\rangle = \frac{1}{\omega + i\eta - \Delta\mathcal{H}} \mathcal{A}|0\rangle \quad (2.52)$$

where we introduced $\Delta\mathcal{H} := \mathcal{H} - E_0$. The computation of $|\xi\rangle$ is numerically the most demanding step due to the inversion of an almost singular non-hermitian matrix \mathbf{A} :

$$\underbrace{[\omega + i\eta - \Delta\mathcal{H}]}_{\mathbf{A}} |\xi\rangle = \underbrace{\mathcal{A}|0\rangle}_{|\mathcal{A}\rangle}. \quad (2.53)$$

We can split the correction vector into real and imaginary part, $|\xi\rangle =: |\xi^{\Re}\rangle + i|\xi^{\Im}\rangle$. The non-hermitian equation system (2.53) can then be reformulated as hermitian equation for $|\xi^{\Im}\rangle$

$$\underbrace{[(\omega - \Delta\mathcal{H})^2 + \eta^2]}_{\mathbf{B}} |\xi^{\Im}\rangle = -\eta|\mathcal{A}\rangle \quad (2.54)$$

⁹For other applications of the correction vector D-DMRG see for example Refs. [Pat99, Küh00, Nun02, Jec03, Mat04, Mat05].

and the real part $|\xi^{\Re}\rangle$ is obtained via the relationship

$$|\xi^{\Re}\rangle = -\frac{1}{\eta}[\omega - \Delta\mathcal{H}]|\xi^{\Im}\rangle. \quad (2.55)$$

The standard tool to solve either of the equations (2.53) or (2.54) is an appropriate iterative Krylov subspace method. We address the inversion problem in the [next section](#). Let us assume we have successfully inverted \mathbf{A} or \mathbf{B} , i. e. we have calculated the complex correction vector $|\xi\rangle$. The target states of the correction vector scheme are given by the ground state, the excitation vector $|\mathcal{A}\rangle$, and the real and the imaginary part of $|\xi\rangle$:

$$\begin{array}{l|l} |0\rangle & 40\% \\ |\mathcal{A}\rangle & 20\% \end{array} \quad \left| \quad \begin{array}{l} |\xi^{\Im}\rangle & 20\% \\ |\xi^{\Re}\rangle & 20\% \end{array} \right.$$

The weights W^k ($k = 1, 2, 3, 4$) given above to construct the reduced density-matrix (2.23) are experience values. For accurate calculations the real part of the correction vector $|\xi^{\Re}\rangle$ has to be included in the set of target states, cf. e. g. [[Küh99b](#), [Sch05a](#)], though it is not always needed to derive the spectral function. For example, we can evaluate the Green function (2.41) by

$$G_{\mathcal{A}}(\omega + i\eta) = \langle \mathcal{A} | \xi^{\Im} \rangle \quad (2.56)$$

and the spectral density is given by

$$-\pi\rho_{\mathcal{A}} = \langle \mathcal{A} | \xi^{\Im} \rangle \quad (\#1). \quad (2.57)$$

These are the relations used by *Kühner* and *White* [[Küh99b](#)].

A different approach was proposed by *Jeckelmann* [[Jec02](#)]. He reformulated the correction vector scheme in terms of a minimization principle.¹⁰ The functional

$$W_{\mathcal{A},\eta}(\omega, \Psi) = \langle \Psi | (\omega - \Delta\mathcal{H})^2 + \eta^2 | \Psi \rangle + \eta \langle \mathcal{A} | \Psi \rangle + \eta \langle \Psi | \mathcal{A} \rangle \quad (2.58)$$

¹⁰Jeckelmann calls his approach the “dynamical DMRG” (D-DMRG). We use a different nomenclature here: “dynamic DMRG” (D-DMRG) is the calculation of dynamic properties in the frequency domain by the means of DMRG. This can be done with Lanczos DMRG, cf. [Sect. 2.2.2](#), or with correction vector DMRG, cf. [this section](#), or with Jeckelmann’s variational correction vector DMRG. All variants belong to the family of D-DMRG algorithms.

A new approach to calculate time-dependent correlation functions (in the time domain) is the real-time DMRG [[Whi04](#), [Dal04](#), [Fei04](#), [Sch05b](#)] implementing Vidal’s TEBD algorithm [[Vid03](#), [Vid04](#)] in the DMRG framework. For applications see Refs. [[Sch04](#), [Gob05](#), [Kol05](#), [Man05](#)].

A path-integral variant of the DMRG method to calculate real-time correlation functions at arbitrary finite temperatures has been introduced recently [[Sir05](#)].

is minimized with respect to a state $|\Psi\rangle$. At the minimum, the minimizing state is

$$|\Psi_{\min}\rangle = |\xi^{\mathfrak{Jm}}\rangle. \quad (2.59)$$

The value of the functional itself is

$$W_{\mathcal{A},\eta}(\omega, \Psi_{\min}) = -\pi\eta C_{\mathcal{A}}(\omega + i\eta) \quad (2.60)$$

so that we find

$$-\pi\rho_{\mathcal{A}} = \frac{1}{\eta} W_{\mathcal{A},\eta}(\omega, \xi^{\mathfrak{Jm}}) \quad (\#2). \quad (2.61)$$

The variational approach is equivalent the original scheme if $|\xi^{\mathfrak{Jm}}\rangle$ could be calculated exactly. Let us assume we have an approximate solution $|\Psi\rangle = |\xi^{\mathfrak{Jm}}\rangle + \varepsilon|\Phi\rangle$ with $\langle\Phi|\Phi\rangle = 1$ and $\varepsilon \ll 1$. Using $|\Psi\rangle$ in Eq. (2.57) the error in the correlation function is also of the order of ε . By general properties of variational methods the error for Eq. (2.61) is only of the order of ε^2 . Thus, using (2.61) instead of (2.57) is a good idea. But this does not mean one is obliged to perform the minimization of the functional (2.58). Solving the equation system (2.53) or (2.54) for the correction vector and using (2.61) instead of (2.57) is also possible.

We can follow a third approach to calculate $\rho_{\mathcal{A}}(\omega + i\eta)$ from the correction vector $|\xi\rangle$. Using

$$\langle\xi|\xi\rangle = \langle\mathcal{A}|\frac{1}{[\omega + i\eta - \Delta\mathcal{H}]} \frac{1}{[\omega + i\eta - \Delta\mathcal{H}]}|\mathcal{A}\rangle \quad (2.62)$$

$$= \langle\mathcal{A}|\frac{1}{[(\omega - \Delta\mathcal{H})^2 + \eta^2]}|\mathcal{A}\rangle \quad (2.63)$$

we find with Eqs. (2.57, 2.54)

$$-\pi\rho_{\mathcal{A}} = -\eta\langle\xi|\xi\rangle \quad (\#3). \quad (2.64)$$

We compare the three methods to use the correction vector to calculate the imaginary part of the Green function in Fig. 2.16. Here the matrix \mathbf{A} has been inverted using preconditioned complex symmetric QMR as iterative solver (for details cf. Sect. 2.2.4). The shown convergence behavior is generic and does not depend very much on which system (hermitian or non-hermitian) is solved with which Krylov subspace algorithm. For every iteration we calculate the spectral density $\rho_{\mathcal{A}}$. The iterative solver is stopped when for the residuum vector

$$|\text{res}\rangle := [\omega + i\eta - \Delta\mathcal{H}]|\xi\rangle - |\mathcal{A}\rangle \quad (2.65)$$

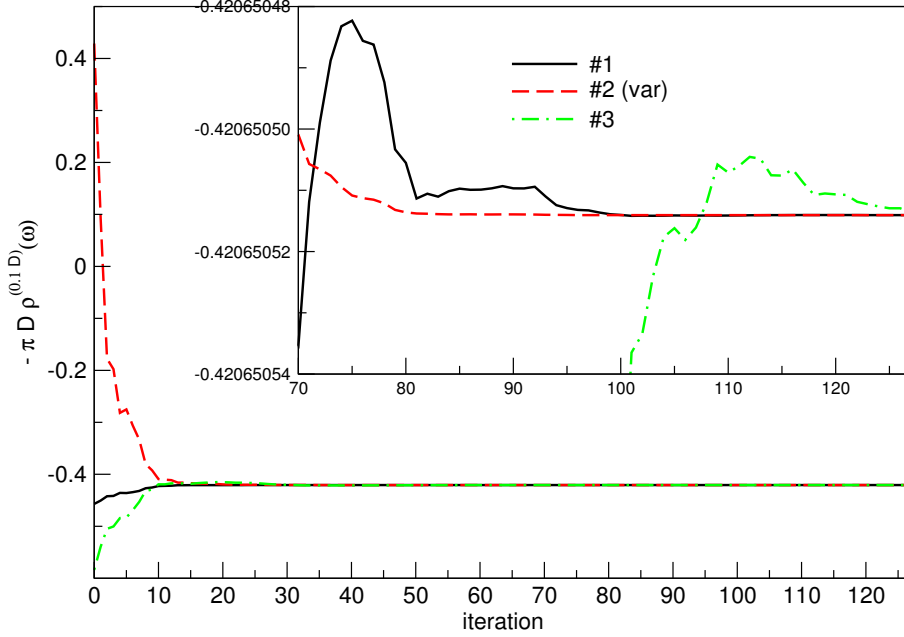


Figure 2.16: Comparison of the convergence behavior of the three different methods to evaluate the spectral density by correction vector DMRG, cf. Eqs. (2.57, 2.61, 2.64). The spectral density is shown via the iteration depth in an iterative solver. The SIAM and D-DMRG parameters used here are $U = 2D$, $V = D/2$, $N_f = 120$, $m = 128$, $\omega = 1D$, $\eta = 0.1D$. The operator \mathcal{A} is given by \mathbf{S}_0^+ , cf. Sect. 1.6.3.

the condition

$$\langle \text{res} | \text{res} \rangle \leq 10^{-15} \quad (2.66)$$

is fulfilled. Clearly visible, all three methods converge towards the same value, as expected. But variant #3 (2.64) performs worst, as can be seen from the inset in Fig. 2.16. The values for $\rho_{\mathcal{A}}$ obtained via the functional (2.61) shows the smoothest convergence behavior.

To make things more transparent, we plot the relative errors in Fig. 2.17 on a logarithmic scale. All methods are compared with the converged results of the variational approach #2 (2.61). The relative error for the variational result is over the full iteration range approximately proportional to the residuum vector squared,

$$\frac{\#2_{\text{conv}} - \#2_i}{\#2_{\text{conv}}} \bigg/ \langle \text{res} | \text{res} \rangle \approx \text{const.}, \quad (2.67)$$

where the constant fluctuates between 1.5 and 5 only, indicating that the ε^2 property of the functional $W_{\mathcal{A},\eta}$ (see above) is fulfilled. Things are not so obvious for the method #1 as

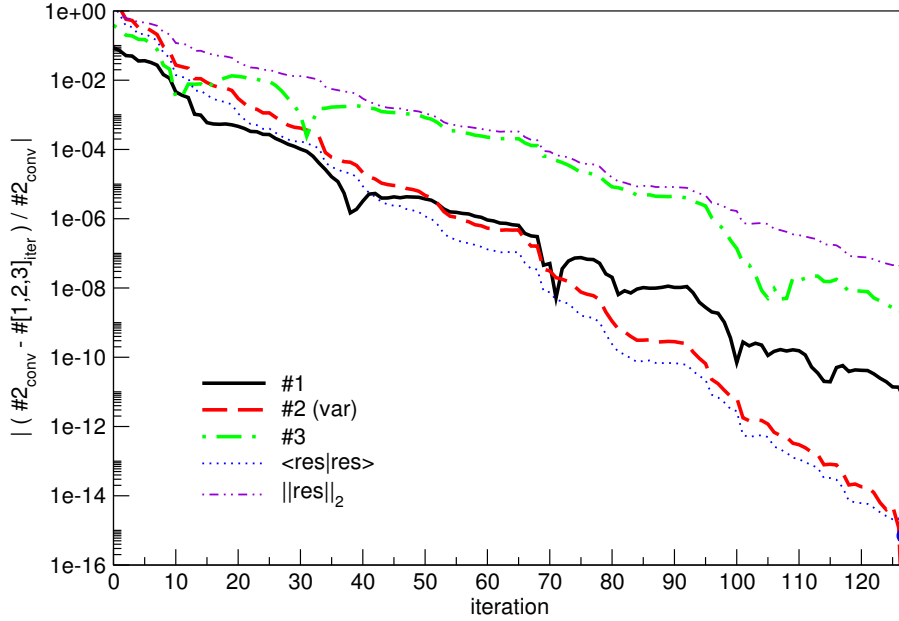


Figure 2.17: For the same parameters as in Fig. 2.16 the absolute value of the relative deviation from the converged variational result **#2** obtained via Eq. (2.61) is shown versus the iteration number. The dotted line is the square of the residuum vector (2.65). The iterative solver is stopped when the squared residuum is less than $1e-15$ (marked with a filled dot here).

the the curve shows big kinks. Nevertheless, the tendency that the convergence behavior of (2.57) is approximately proportional to ε is visible for iteration number > 40 . From this analysis we advocate using Jeckelmann’s functional $W_{\mathcal{A},\eta}$ to evaluate the imaginary part of the Green function.

The error in the real part (2.55) is of order $\mathcal{O}(\varepsilon)$ for all three methods. Whether this is a drawback or not depends on how the data is used. If we are only interested in the spectral function then knowing the imaginary part accurately is sufficient. Deconvolving $\Im G(\omega + i\eta)$ and subsequent Kramers-Kronig-transformation of $\Im G(\omega)$ gives $\Re G(\omega)$. If we do not calculate G directly but the Q -function introduced in Sect. 1.6.4 then we might need the real part of $Q(\omega + i\eta)$, i. e., when translating Q into the self-energy Σ using Eq. (1.91). This spoils the ε^2 property of the functional to some extent.

We make a last remark on the three methods to calculate $\rho_{\mathcal{A}}$. In Fig. 2.17 we compared the approaches by assuming implicitly that the converged result of method **#2** is the true one. A more rigorous study of the errors of the three approaches should compare to an exactly solvable case where the exact finite-size spectral functions are available, i. e. the XY model setting $U = 0$ in the SIAM. This analysis would also allow to investigate the error caused by the fact, that neither the ground state $|0\rangle$ nor the excited state $|\mathcal{A}\rangle$ are

known exactly. Using a frequency ω equal to the exact frequency of a finite-size pole in $\Im m G$ and a fairly small broadening η would make the analysis extremely sensible to all kind of errors. We postpone this study to future work.

Asymmetric targeting

In most of our calculations the operator \mathcal{A} is given by \mathbf{S}_0^+ (or in the fermionic language by d_\uparrow^\dagger). Since we focus on a spin-disordered solution the propagator for this operator has no dependence on σ ,

$$G_\uparrow(\omega + i\eta) = G_\downarrow(\omega + i\eta) = G(\omega + i\eta), \quad (2.68)$$

and we don't account for the operator \mathbf{T}_0^+ (d_\downarrow^\dagger) when defining the target states. Note that with $\mathbf{T}_0^+|0\rangle$ and the real and imaginary parts of the correction vector for \mathbf{T}_0^+ we would have to include three additional vectors in our set of target states. As both operators would—in our model—give exactly the same results we prefer to focus on one of the d^\dagger operators. The price we have to pay for this is that the targeting itself is asymmetric. This has to be taken into account when something like “mirroring” blocks shall be done. As soon as the sweeping procedure starts, system and environment blocks start to differ in geometry (except for the one symmetric configuration). Thenceforward both operators would have to be handled separately, irrespective of the fact that the spectral functions will be the same. This also means that two correction vectors have to be determined which will slow down the algorithm by a factor of two. The loss of accuracy for fixed m due to the enlarged number of target states is difficult to guess. Targeting both, $\mathbf{S}_0^+|0\rangle$ and $\mathbf{T}_0^+|0\rangle$ could enhance the accuracy in expectation values like

$$\begin{aligned} \langle 0 | \mathbf{S}_0^- \mathbf{S}_0^+ | 0 \rangle &= \langle 0 | d_\uparrow d_\uparrow^\dagger | 0 \rangle \stackrel{!}{=} 1/2 \\ \langle 0 | \mathbf{T}_0^- \mathbf{T}_0^+ | 0 \rangle &= \langle 0 | d_\downarrow d_\downarrow^\dagger | 0 \rangle \stackrel{!}{=} 1/2. \end{aligned}$$

This might be of interest for special cases where two almost degenerate ground states (spin \uparrow or \downarrow at the interacting site) are observed, cf. [Eq. \(5.2\)](#) and the discussion above.

2.2.4 Inversion performance

In the [previous section](#) we analyzed the accuracy of three schemes to calculate a correlation function provided the correction vector $|\xi\rangle$ is known. The calculation of the ω -dependent correction vector is numerically extremely demanding. Approximately 80% of the run-time of the D-DMRG algorithm is used for calculating the correction vectors.

Thus, the inversion problem is the most important part of the program when efficiency is concerned.

The correction vector is the solution of either of the equation systems, cf. Eqs. (2.54, 2.55)

$$\begin{aligned} \mathbf{x} &\hat{=} |\xi\rangle & \mathbf{a} &\hat{=} |\mathcal{A}\rangle \\ \mathbf{A} &\hat{=} \omega + i\eta - \Delta \mathcal{H} & \mathbf{A}\mathbf{x} &= \mathbf{a} \end{aligned} \quad (2.69)$$

$$\mathbf{B} \hat{=} (\omega - \Delta \mathcal{H})^2 + \eta^2 \quad \mathbf{B}\mathbf{x}^{\text{Im}} = -\eta \mathbf{a}^{\text{Im}}. \quad (2.70)$$

The equation system defined via the non-hermitian matrix \mathbf{A} is linear in the Hamiltonian \mathcal{H} but is solved for the complex correction vector $|\xi\rangle$. In the matrix \mathbf{B} the Hamiltonian enters squared but the equation system is only solved for the imaginary part of $|\xi\rangle$. Thus, (2.70) is supplemented by (2.55) to obtain $|\xi^{\text{Re}}\rangle$. A standard method to solve large sparse linear systems like (2.69, 2.70) are iterative Krylov subspace methods [Saa96, Mei99, Saa00, Vor02, Vor03, Bar94]. To decide whether it is more efficient to solve the linear complex problem (\mathbf{A}) or the squared real system (\mathbf{B}) we performed tests with a variety of iterative solvers.

We prefer to stabilize these inversion problems by optimized algorithms instead of using the variational approach proposed by *Jeckelmann* [Jec02] which requires a minimization in a high-dimensional Hilbert space, cf. (2.58). The minimization is normally performed by using an iterative minimization algorithm which is again a Krylov subspace method. Solving the equation systems instead of minimizing $W_{\mathcal{A},\eta}$ does not hinder us from using (2.61).

We compared the performance of various iterative solvers. The standard tool is the conjugate gradients method (CG) by *Hestenes* and *Stiefel* [Hes52]. We also tried BiCGSTAB by *van der Vorst* [Vor92], Bi-CGSTAB2 [Gut91, Gut93], Bi-CGSTAB(ℓ) [Sle93, Sle94] [especially Bi-CGSTAB(2)], and an algorithm proposed by *Ramasesha* [Ram90]. These algorithms are applied to the hermitian equation system to invert \mathbf{B} .

The linear system (2.69) is a shifted real symmetric system that is also complex symmetric, $\mathbf{A} = \mathbf{A}^T$. The shifted real symmetric structure can be exploited when special Krylov subspace methods are used [Fre90, Fre93a]. Thus, we used a special algorithm, complex symmetric QMR (quasi-minimal residual) by *Freund* [Fre92a]¹¹, to invert \mathbf{A} . All before-mentioned methods like CG or BiCGSTAB(2) applied to (2.70) do not exploit complex symmetry.

Another very important issue in the efficient solution of linear systems is the concept of preconditioning. A preconditioning matrix \mathbf{P} is used to transform the linear system and

¹¹See also Refs. [Fre92b, Fre93b].

solve the transformed system instead of the original one:

$$\mathbf{M}\mathbf{x} = \mathbf{a} \quad \Longrightarrow \quad \underbrace{\mathbf{P}\mathbf{M}}_{\tilde{\mathbf{M}}}\mathbf{x} = \underbrace{\mathbf{P}\mathbf{a}}_{\tilde{\mathbf{a}}} . \quad (2.71)$$

A standard preconditioning method is incomplete LU factorization (ILU). But this is difficult here as the matrix elements of \mathbf{M} are not known. Of course, they could be constructed for both cases, $\mathbf{M} = \mathbf{A}$ or $\mathbf{M} = \mathbf{B}$, but this would be extremely inefficient, as this corresponds to explicit construction of the full superblock Hamiltonian,

$$\mathcal{H} = \underbrace{\mathcal{H}_S \otimes \mathbf{1}_E + \mathbf{1}_S \otimes \mathcal{H}_E}_{\mathcal{H}_0} + \mathcal{H}_{SE} . \quad (2.72)$$

This is not within the spirit of the DMRG concept. Thus, we decided to use a DMRG-inspired preconditioner which takes the splitting in system and environment block into account. The Hamilton operators of system and environment block can be diagonalized easily due to their sparse block matrix structure. After “prediagonalization” of \mathcal{H}_S and \mathcal{H}_E we can construct the inverse of \mathcal{H}_0 . This operator does not include the \mathcal{H}_{SE} part connecting system and environment block but can serve as pseudo-inverse of the full Hamiltonian \mathcal{H} . The same can be done for the shifted operator

$$\mathbf{A}_0 \hat{=} \tilde{\omega} + i\eta - \mathcal{H}_0 := \omega + i\eta - (\mathcal{H}_0 - E_0) . \quad (2.73)$$

Thus we can transform

$$(\tilde{\omega} + i\eta - \mathcal{H}_0 - \mathcal{H}_{SE})|\xi\rangle = |\mathcal{A}\rangle \quad \Longrightarrow \quad (\mathbf{A}_0 + \mathbf{A}_1)\mathbf{x} = \mathbf{a}$$

into

$$\underbrace{(\mathbf{1} + \mathbf{A}_0^{-1}\mathbf{A}_1)}_{\tilde{\mathbf{A}}}\mathbf{x} = \underbrace{\mathbf{A}_0^{-1}\mathbf{a}}_{\tilde{\mathbf{a}}} \quad (2.74)$$

or

$$\begin{aligned} & \left(\mathbf{A}_0^{-1/2} \mathbf{A}_0^{1/2} \mathbf{A}_0^{1/2} + \mathbf{A}_0^{-1/2} \mathbf{A}_1 \mathbf{A}_0^{-1/2} \mathbf{A}_0^{1/2} \right) \mathbf{x} = \mathbf{A}_0^{-1/2} \mathbf{a} \\ \Longrightarrow & \underbrace{\left(\mathbf{1} + \mathbf{A}_0^{-1/2} \mathbf{A}_1 \mathbf{A}_0^{-1/2} \right)}_{\tilde{\mathbf{A}}}\underbrace{\mathbf{A}_0^{1/2}}_{\tilde{\mathbf{x}}}\mathbf{x} = \underbrace{\mathbf{A}_0^{-1/2}\mathbf{a}}_{\tilde{\mathbf{a}}} . \end{aligned} \quad (2.75)$$

Introducing bold symbols for matrices, the Hamilton matrix \mathbf{H} can be written as $\mathbf{H}_0 + \mathbf{H}_{SE}$

where the inverse of \mathbf{H}_0 is known. Splitting in real and imaginary parts we find

$$(\mathbf{A}_0 + \mathbf{A}_1) \mathbf{x} = \mathbf{a} \implies \left[\left(\begin{array}{c|c} \tilde{\omega} \mathbf{1} - \mathbf{H}_0 & -\eta \mathbf{1} \\ \hline \eta \mathbf{1} & \tilde{\omega} \mathbf{1} - \mathbf{H}_0 \end{array} \right) + \left(\begin{array}{c|c} -\mathbf{H}_{SE} & \mathbf{0} \\ \hline \mathbf{0} & -\mathbf{H}_{SE} \end{array} \right) \right] \begin{pmatrix} \mathbf{x}^{\Re} \\ \mathbf{x}^{\Im} \end{pmatrix} = \begin{pmatrix} \mathbf{a}^{\Re} \\ \mathbf{a}^{\Im} \end{pmatrix}.$$

As the constituents of \mathbf{H}_0 have been prediagonalized all four blocks of the matrix \mathbf{A}_0 are diagonal and constructing \mathbf{A}_0^{-1} , $\mathbf{A}_0^{-1/2}$, and $\mathbf{A}_0^{1/2}$ is trivial. We preferred the preconditioning (2.75) as it can be implemented efficiently in a QMR solver. The catch is that the matrices $\mathbf{A}_0^{\pm 1/2}$ can be redistributed in the steps of the algorithm so as to minimize the necessary matrix operations. We don't include excessive detail here and refer the reader to algorithm 3.2 of Ref. [Fre92a] and shortly note that the vectors \tilde{v}_{k+1} (in the notation of [Fre92a]) should be replaced by two set of vectors $\tilde{v}_{k+1}^< = \mathbf{A}_0^{+1/2} \tilde{v}_{k+1}$ and $\tilde{v}_{k+1}^> = \mathbf{A}_0^{-1/2} \tilde{v}_{k+1}$.

Let us make a last remark on preconditioning. The shifted real symmetric structure of (2.69) is lost when preconditioning is used, except for polynomial preconditioners, which, however, are not very powerful. The complex symmetric structure, on the other hand, is preserved when preconditioning is used, as long as the preconditioner is complex symmetric. Any reasonable preconditioner of a complex symmetric system will indeed be complex symmetric. This is obviously the case for \mathbf{A}_0^{-1} and $\mathbf{A}_0^{-1/2}$.

Fig. 2.18 shows the performance of various iterative solvers. We plot the integrated time used for all correction vector calculations performed within a finite size sweep for frequencies $\omega \in [-3, 3]D$ in steps of $\delta\omega = 0.1D$. Using the operator $\mathcal{A} = \mathbf{S}_0^+$ gives us $G^>(\omega + i\eta)$ and thus the positive frequency part of the spectrum. Nevertheless, the negative frequencies have to be evaluated also because we want to use (1.37) in the particle-hole symmetric version (1.47). The first observation is that the inversion time is *strongly* frequency dependent. For low and intermediate ω the preconditioned QMR (PreQMR) outperforms all other iterative solvers. The performance gain by preconditioning is not immense but definitely worth the effort. PreQMR run-time is about 50% to 75% of the unpreconditioned QMR. For $\omega = 0$ the inversion time for PreQMR is about 12% of the CG time. At $\omega \approx 1.3D$ the CG and the PreQMR curves intersect. For high frequencies the standard CG algorithm turned out to perform best. We did not encounter an example where BiCGSTAB in all its variants cited above performed better than CG. The reason for the subtle convergence differences for high frequencies are somewhat obscure to us. Nevertheless, the tactics is obvious: Choose in a frequency-dependent fashion the iterative solver which performs best. In our model PreQMR and CG turned out to be the optimum choice. Keeping track of the inversion times, it is possible to find an algorithm that switches from PreQMR to CG when PreQMR starts to perform worse than CG for high frequencies. This ‘‘switching recipe’’ turned out to be stable when gauged by benchmark

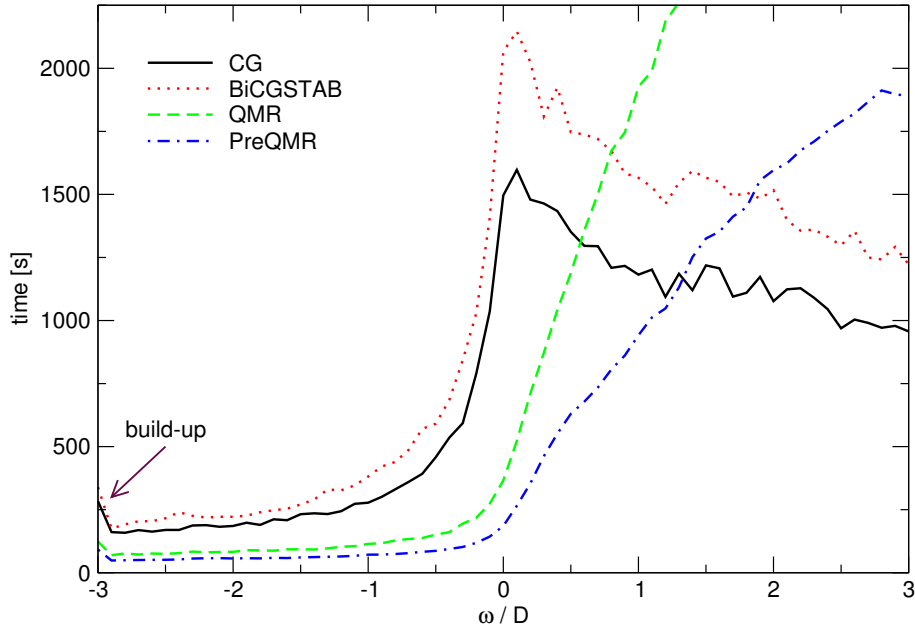


Figure 2.18: Performance of iterative solvers. The SIAM and D-DMRG parameters used here are $U = 2D$, $V = D/2$, $N_f = 120$, $m = 128$, $\eta = 0.1D$. The operator \mathcal{A} is given by \mathbf{S}_0^+ , cf. Sect. 1.6.3.

results and some practical experience is used. Summarizing, we can follow the lowest line in Fig. 2.18.

To construct the preconditioner for the QMR algorithm we prediagonalized the system and environment block Hamiltonians. This can be used at a different stage of the DMRG algorithm, the determination of the ground state. An initial guess for the ground state can be constructed from the product state of the system and the environment ground state, which are trivially known as both Hamiltonians are diagonal. This initial guess is used as starting vector in a Lanczos or Davidson algorithm to find iteratively the ground state of the full Hamiltonian. This turned out to perform as well as the concept of “transformation of the wave function” described in Refs. [Whi93, Noa99].

2.2.5 Projective D-DMRG

The basic idea behind the correction vector method is based on optimizing the DMRG basis to represent a correlation function for a given frequency. The correlation function has to be determined for frequency ω using a finite broadening: $\omega \rightarrow \omega + i\eta$. Thus, $C_{\mathcal{A}}(\omega + i\eta)$ carries information on the full frequency range due to the Lorentzian broadening.

We can go one step further and concentrate solely on a finite frequency interval

$[\omega_{\min}, \omega_{\max}]$. Assume we can construct a projection operator

$$\begin{aligned} \hat{P}(\mathcal{H}) &= \Theta(\Delta\mathcal{H} - \omega_{\min}) \Theta(\omega_{\max} - \Delta\mathcal{H}) \\ &= \sum_n \Theta((E_n - E_0) - \omega_{\min}) \Theta(\omega_{\max} - (E_n - E_0)) |n\rangle\langle n| \\ &= \sum_{\omega_{\min} \leq E_n \leq \omega_{\max}} |n\rangle\langle n| \end{aligned} \quad (2.76)$$

where again $\Delta\mathcal{H} = \mathcal{H} - E_0$ was used. With the correction vector $|\xi_P\rangle$ for the finite interval

$$|\xi_P\rangle = \hat{P}|\mathcal{A}\rangle. \quad (2.77)$$

we find

$$\begin{aligned} \langle \xi_P | \xi_P \rangle &= \langle \mathcal{A} | \hat{P}^\dagger \hat{P} | \mathcal{A} \rangle = \langle \mathcal{A} | \hat{P} | \mathcal{A} \rangle = ||\hat{P}|\mathcal{A}\rangle||^2 \\ &= \int_{\omega_{\min}}^{\omega_{\max}} d\omega \rho_{\mathcal{A}}(\omega) =: W_{\mathcal{A}}^{[\omega_{\min}, \omega_{\max}]} \end{aligned} \quad (2.78)$$

using $\hat{P}^\dagger = \hat{P} = \hat{P}^2$. $W_{\mathcal{A}}^{[\omega_{\min}, \omega_{\max}]}$ is the spectral weight for the interval $[\omega_{\min}, \omega_{\max}]$.

$$W_{\mathcal{A}}^{[\omega_{\min}, \omega_{\max}]} = \langle \mathcal{A} | \xi_P \rangle \quad (2.79)$$

can be used as additional check. Note that no finite broadening η enters here compared to standard correction vector DMRG, cf. [Eq. \(2.57\)](#),

$$\rho^{(\eta)}(\omega) = -\frac{1}{\pi} \left\langle \mathcal{A} \left| \xi \Im(\omega + i\eta) \right. \right\rangle.$$

The task is now to construct a projection operator that has finite density of states only in a given frequency interval. In this way we gain *frequency selectivity by filtering*. As we do not know all eigenvalues and eigenstates of \mathcal{H} precisely the projection operator cannot be evaluated via [Eq. \(2.76\)](#) directly. But we can calculate an approximation to the “box operator” of [\(2.76\)](#) by Gaussian numerical integration using a finite number of node points [[Sto83](#)].

We illustrate the procedure for a simple example of a box function

$$P(\omega) = \Theta(\omega + 1) \Theta(1 - \omega). \quad (2.80)$$

The function is shown in [Fig. 2.19](#) as P_∞ . Using the Cauchy formula

$$f(z_0) = \frac{1}{2\pi i} \oint \frac{f(z) dz}{z - z_0}$$

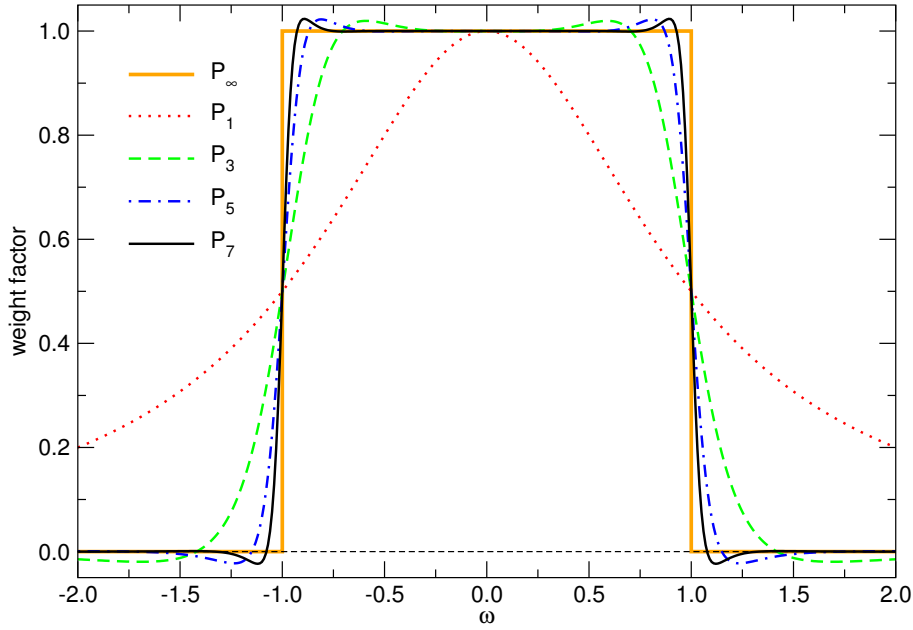
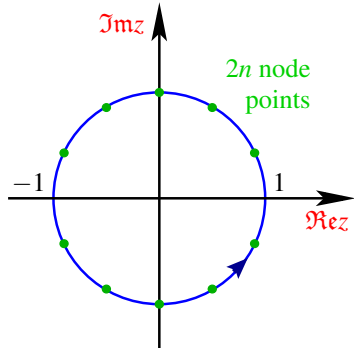


Figure 2.19: Schematic example: approximation of a frequency filter. The P_∞ is the exact sharp filter function, the P_m are approximations using a finite number of $2n$ node points in a Gaussian numerical integration scheme.

we can simplify P

$$\begin{aligned}
 P(\omega) &= \Theta(\omega + 1)\Theta(1 - \omega) = \frac{1}{2\pi} \Im \oint \frac{dz}{z - \omega} = \frac{1}{2\pi} \Re \int_0^{2\pi} \frac{e^{i\varphi} d\varphi}{e^{i\varphi} - \omega} \\
 &= \frac{1}{2\pi} \int_{-\pi}^{\pi} d\varphi \frac{1 - \omega \cos \varphi}{(\cos \varphi - \omega)^2 + \sin^2 \varphi} = \int_{-1}^1 d\zeta \underbrace{\frac{1}{2} \frac{1 + \omega \sin\left(\frac{\pi\zeta}{2}\right)}{1 + 2\omega \sin\left(\frac{\pi\zeta}{2}\right) + \omega^2}}_{=: f_\omega(\zeta)}.
 \end{aligned}$$

The integration can be approximated by a Gaussian numerical integration



$$\begin{aligned}
 P(\omega) &= \int_{-1}^1 f_\omega(\zeta) d\zeta \\
 &\approx \sum_{i=1}^n f_\omega(\zeta_i) w_i.
 \end{aligned} \tag{2.81}$$

The weights w_i and the abscissas ζ_i can be derived using Legendre polynomials, cf.

[Sto83], or can be looked up in tables for generic values for the number of node points [Abr64]. The results for the box function are summarized in Fig. 2.19. The approximated functions using $n \in \{1, 3, 5, 7\}$ are compared to the exact P_∞ . We see that already for a fairly low numbers of node points the approximation is accurate except for the overshooting and undershooting at the box edges.

Now let us use this scheme to find an approximation for

$$\hat{P}(\mathcal{H}) = \frac{1}{2\pi} \Im \oint \frac{dz}{z - \Delta \mathcal{H}}. \quad (2.82)$$

Assume we want to construct a projection operator for the interval $[\omega_{\min}, \omega_{\max}] =: [\omega_0 - r, \omega_0 + r]$ centered about ω_0 and of width $2r$ ($r > 0$). Introducing

$$z(\varphi) = \omega_0 + E_0 + \underbrace{\omega + i\eta}_{re^{i\varphi}} \quad (2.83)$$

we can write

$$\hat{P} = \frac{1}{2\pi} \Im \oint \frac{ird\varphi}{z(\varphi) - \mathcal{H}} = \frac{r}{2\pi} \Re \int_0^{2\pi} \frac{e^{i\varphi} d\varphi}{z(\varphi) - \mathcal{H}} = \frac{r}{\pi} \Re \int_0^\pi \frac{e^{i\varphi} d\varphi}{z(\varphi) - \mathcal{H}}.$$

Substituting $\varphi(\zeta) = \frac{\pi}{2}(\zeta + 1)$ we end up with

$$\hat{P} = \frac{r}{2} \Re \int_{-1}^1 \frac{e^{i\varphi} d\zeta}{z(\zeta) - \mathcal{H}} \approx \frac{r}{2} \Re \sum_{i=1}^n w_i \frac{e^{i\varphi(\zeta_i)} d\zeta}{z(\zeta_i) - \mathcal{H}} \quad (2.84)$$

where the integral was approximated with Gaussian numerical integration (n node points ζ_i and weights w_i). Now we have to solve

$$|\xi_i\rangle = \frac{1}{z_i - \mathcal{H}} |\mathcal{A}\rangle \quad (2.85)$$

for n vectors $|\xi_i\rangle$ where

$$z_i := z(\zeta_i) = \omega_0 + E_0 + r \underbrace{\cos \varphi(\zeta_i)}_{\varphi_i} + i r \underbrace{\sin \varphi(\zeta_i)}_{\eta_i}. \quad (2.86)$$

We have discussed in Sect. 2.2.3 and Sect. 2.2.4 how these equations can be solved. Note that the η_i can get very small for a large number of node points. This makes the inversions at the interval boundaries very time-consuming. If all n vectors $|\xi_i\rangle$ are calculated we have

to take care of the $e^{i\varphi_i}$ factors in the denominator of (2.84)

$$\begin{aligned}\mathfrak{Im}|\tilde{\xi}_i\rangle &:= \mathfrak{Im}[(\cos \varphi_i + i \sin \varphi_i)(\Re|\xi_i\rangle + i\mathfrak{Im}|\xi_i\rangle)] \\ &= \sin \varphi_i \Re|\xi_i\rangle + \cos \varphi_i \mathfrak{Im}|\xi_i\rangle \\ \Re|\tilde{\xi}_i\rangle &:= \cos \varphi_i \Re|\xi_i\rangle - \sin \varphi_i \mathfrak{Im}|\xi_i\rangle.\end{aligned}\tag{2.87}$$

We finally get the projected correction vector

$$|\xi_P\rangle = \hat{P}|\mathcal{A}\rangle \approx \frac{r}{2} \sum_{i=1}^n w_i |\tilde{\xi}_i\rangle.\tag{2.88}$$

The interval weight is then given by (2.79)

$$W_{\mathcal{A}}^{[\omega_0-r, \omega_0+r]} \approx \langle \xi^{\Re} | \xi^{\Re} \rangle \quad \text{or} \tag{2.89}$$

$$W_{\mathcal{A}}^{[\omega_0-r, \omega_0+r]} \approx \langle \mathcal{A} | \xi^{\Re} \rangle.\tag{2.90}$$

For small r and a large number of node points $W_{\mathcal{A}}^{[\omega_0-r, \omega_0+r]} \approx 2r\rho_{\mathcal{A}}(\omega_0)$.

The projective D-DMRG algorithm is useful to calculate the total weight of isolated structures in spectral densities which are very sharp and thus hard to deconvolve. But in the self-consistency cycle of the DMFT it is not very helpful. It is hardly possible to extract the new hybridization function for the next DMFT iteration from a discrete set of weights. Furthermore, the projective D-DMRG is very slow when applied to the full frequency range due to the large number of necessary inversions (n times the number of intervals compared to the number of frequencies in standard correction vector DMRG). On the level of the SIAM we were more interested in resolving sharp structures and analyzing their lineshapes than in calculating the integrated weight for given intervals. Thus, we did not use the projection scheme extensively. We present a brief ‘‘proof of concept’’ calculation for the XY chain where we can compare directly to the analytical values.

Fig. 2.20 shows the results for a small chain of free fermions. For $N_f = 10$ the spectral density has 10 poles for $\omega \geq 0$. The exact pole positions and their corresponding weights are shown with filled dots. The frequency range $[0, 1]D$ is subdivided into ten intervals of width $0.1D$. The bars depict the exact interval weights. For the dot at $\omega = 0.5$ the pole frequency is located exactly at an interval boundary. So we attributed the weight W of this pole to both adjacent intervals with $W/2$. The pluses and crosses are the projective D-DMRG results with $n = 4$ and $n = 11$. The results are satisfactory for $n = 11$. But we can analyze some principle problems which can come up. The $n = 4$ result for the interval centered about $\omega = 0.25D$ predicts a negative weight. This is due to the fact (2.79) was used which is not positive-definite. The approximate projector itself is expected to show

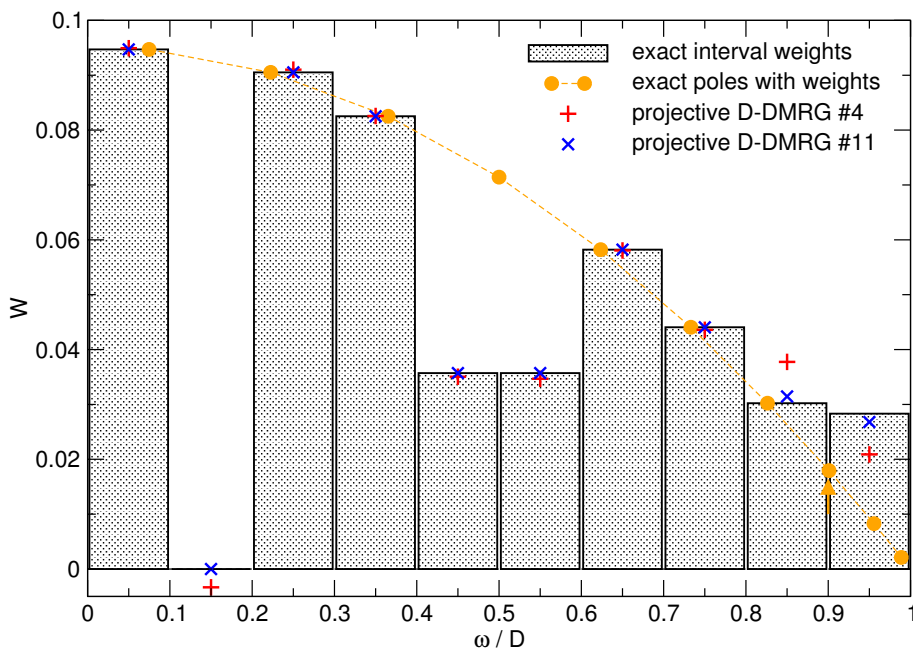


Figure 2.20: Comparison of the interval weights obtained from projective D-DMRG for the positive frequency part of an XY chain with the exact result. The SIAM and D-DMRG parameters used here are $U = 0$, $V = D/2$, $N_f = 10$, $m = 128$, $\delta\omega = 2r = 0.1D$. The operator \mathcal{A} is given by \mathbf{S}_0^+ , cf. Sect. 1.6.3.

features akin to the undershootings visible in Fig. 2.19 close to the box edges. Using (2.78) would help here. But in our limited amount of tests with this algorithm $W \approx \langle \mathcal{A} | \xi_P \rangle$ performed better. Another typical source of error are frequencies very close to an interval boundary. The pole at $\omega \simeq 0.901D$ is marked with an arrow in Fig. 2.20. Apparently a fraction of the weight of this pole was assigned to the neighboring interval. This can partly be healed by “sharpening” the projection operator, i. e. taking a larger number of node points. But even for $n = 11$ we observe a tiny mismatch between the interval weight for $[0.8, 0.9]D$ and $[0.9, 1.0]D$. Further tests and improvements of the projective D-DMRG are called for.

3 Deconvolution

3.1 Introduction

The computation of spectral properties is a central issue in theoretical physics. Many spectroscopic probes provide experimental information about the investigated systems. In order to understand the meaning of such data it is indispensable to be able to compute the corresponding quantities theoretically. This task is particularly demanding if the system under study is characterized by strong correlations. Then standard approaches like diagrammatic perturbation theory have difficulties to provide quantitative results.

An archetypal class of strongly correlated systems are impurity models where a small subsystem, the impurity, is coupled to a bath of degrees of freedom. The discrete levels of the impurity are broadened due to the interaction with the bath. The most fundamental fermionic representative of this class of models is the single impurity Anderson model (SIAM), cf. Ref. [Hew93] and [Chapt. 1](#).

The SIAM describes a plethora of physical problems. Historically it was used for diluted magnetic impurities in metals, see e. g. Ref. [Hew93]. But it also describes the electronic transmission through quantum dots, see e. g. Ref. [Pus04]. The smallness of the quantum dot implies a small capacitance, hence a large charging energy which represents the interaction energy U . The bath is given by the external leads. The dynamic mean-field theory (DMFT) [Pru95, Geo96] represents another broad and very active field where the SIAM occurs. In this approach, as in all mean-field approaches, the lattice problem of strongly interacting fermions is mapped onto an effective single-site problem, namely a SIAM. This SIAM is linked to the original lattice problem by a self-consistency condition. The clue is that the mean-field, the Green function of the bath, is a dynamic quantity depending on frequency.

The above examples illustrate that it is very important to be able to compute the dynamics of a SIAM in a reliable fashion. There are several numerical approaches which can be applied. Among the most prominent ones are quantum Monte Carlo (QMC) [Hir86] and the numerical renormalization group (NRG) [Sak89, Cos90]. Both approaches are powerful but do not have a high resolution away from the Fermi level. For QMC this is so since the dynamics is computed in imaginary time and the analytic continuation to real frequencies represents an ill-conditioned problem. Moreover, care must be taken to reach

low temperatures. The NRG can be used directly at zero temperature. But it is set up to focus on the limit $\omega \rightarrow 0$. The energy levels kept are broadened by a broadening which is proportional to the frequency which implies that features at higher energies tend to be smeared out [Raa04].

We investigate in this thesis a third complementary numerical approach given by the dynamic density-matrix renormalization (D-DMRG), cf. Refs. [Hal95, Ram97, Küh99b, Höv00, Jec02, Raa04, Nis04b] and Sect. 2.2. Dynamic density-matrix renormalization provides valuable numerical information on dynamic correlations by computing convolutions of the corresponding spectral densities. The dynamics at zero temperature is determined by computing the expectation values in the local propagator, cf. Sect. 2.2.3. This can be realized by targeting not only at the ground state and the excited state, but also at the resolvent applied to the excited state. This additional targeted state is called the correction vector. The main limitation of the D-DMRG is that one cannot obtain data for purely real frequencies but only for frequencies with a certain imaginary part. Hence the extraction of the behavior at purely real frequencies is one of the main problems to be solved in using the D-DMRG [Geb03, Raa04, Nis04b]. Here we illustrate how and to which extent such data can be deconvolved to retrieve the wanted spectral densities. It is the main aim of this chapter to discuss and to compare various algorithms to achieve this extraction. In particular, we will present a non-linear approach from the family of maximum entropy methods. This approach provides a *continuous, positive* ansatz for the wanted spectral density with the *least bias* (LB).

In Chapt. 4 we apply the D-DMRG to the the symmetric single impurity Anderson model and compute the $T = 0$ dynamics of the fermionic single-particle propagator of the d electron, cf. Sect. 1.5 and Eqs. (1.35, 1.36, 1.37):

$$G(\omega + i\eta) = \left\langle 0 \left| d_{\sigma} \frac{1}{\omega + i\eta - (\mathcal{H} - E_0)} d_{\sigma}^{\dagger} \right| 0 \right\rangle + \left\langle 0 \left| d_{\sigma}^{\dagger} \frac{1}{\omega + i\eta + (\mathcal{H} - E_0)} d_{\sigma} \right| 0 \right\rangle .$$

The frequencies ω and η are real. The standard retarded Green function is obtained for $\eta \rightarrow 0^+$, cf. Eq. (1.38),

$$G_{\text{R}}(\omega) = \lim_{\eta \rightarrow 0^+} G(\omega + i\eta) .$$

The quantity we are looking for is the spectral density

$$\rho(\omega) := -\frac{1}{\pi} \Im G_{\text{R}}(\omega) .$$

The D-DMRG provides data points at given values of $\omega = \xi_i$ for finite values of η_i

$$g_i = -\frac{1}{\pi} \Im G(\xi_i + i\eta_i) = \frac{1}{\pi} \int_{-\infty}^{\infty} \frac{\eta_i \rho(\omega) d\omega}{(\xi_i - \omega)^2 + \eta_i^2}, \quad (3.1)$$

where we used the Hilbert representation in the second equation. No data can be obtained directly at $\eta = 0$ since the inversion of the Hamiltonian is singular and cannot be achieved numerically in a stable way. Henceforth, we will call data at finite values of η *raw data*. One way to extract the physically relevant data on the real axis is to look at a sequence of decreasing values of η in order to extrapolate the result [Nis04b] to $\eta = 0$. This approach, however, is time-consuming and requires many resources, in particular, if one is interested in the whole spectral density. So the line followed in [this chapter](#) is to use the raw data as input of a generalized scheme to extract the information on the spectral density $\rho(\omega)$.

The features of these schemes will be illustrated by some toy spectral densities for which the broadened and the unbroadened data is analytically available. Results by the LB algorithm for the Kondo peak and the Hubbard satellites of the SIAM will be presented in the [next chapter](#) in Sects. 4.4 and 4.5.2, respectively.

If the unavoidable imaginary part η is constant for all frequencies [Eq. \(3.1\)](#) becomes

$$g_i = -\frac{1}{\pi} \Im G(\xi_i + i\eta) = \frac{1}{\pi} \int_{-\infty}^{\infty} \frac{\eta \rho(\omega) d\omega}{(\xi_i - \omega)^2 + \eta^2} \quad (3.2)$$

so that the raw data is the convolution of the true spectral density $\rho(\omega)$ with the Lorentzian

$$L_\eta(\omega) = \frac{1}{\pi} \frac{\eta}{\omega^2 + \eta^2} \quad (3.3)$$

of width η . Hence the necessary step for retrieving $\rho(\omega)$ is a deconvolution. It can be achieved in various ways. We consider two classes of extraction schemes, linear ones ([Sect. 3.2](#)) and non-linear ones ([Sect. 3.3](#)). Linearity means that there is a linear relation between the raw data and the wanted spectral density. We will give a short summary of our findings in [Sect. 3.4](#).

3.2 Linear Extraction Schemes

3.2.1 FFT

One standard way is to deconvolve the raw data. This is done in the time domain reached by Fourier transform because the convolution in [Eq. \(3.2\)](#) becomes a product in the time

domain

$$\rho(\tau)_{\text{raw}} = \exp(-\eta|\tau|)\rho(\tau), \quad (3.4)$$

where we use $\rho(\tau)$ for the Fourier transform of $\rho(\omega)$ and $\rho(\tau)_{\text{raw}}$ for the Fourier transform of the raw data. The raw data $\{g_i\}$ is obtained in the first place as a discrete set. In order to obtain a quasi continuous distribution we interpolate the discrete set $\{g_i\}$ by splines [Pre92] which leads to $\rho(\omega)_{\text{raw}}$. The Fourier transforms are most efficiently done by Fast Fourier algorithms [Pre92]. The actual deconvolution is done by dividing by $\exp(-\eta|\tau|)$ which inverts Eq. (3.4). Then one transforms back to the frequency domain. So this procedure is very efficient and straightforward [Raa04].

The restriction to be kept in mind is that splining and deconvolution cannot create information where no information was present before. If the input data is not precise enough or if the spline does not approximate the true continuous function $\rho(\omega)_{\text{raw}}$ well enough the deconvolution will fail to produce reasonable results. In practice this is seen in unreasonable values of $\rho(\tau)$ after the division by $\exp(-\eta|\tau|)$ because this division amplifies any inaccuracy for large values of $|\tau|$. This problem is circumvented by a suitable low-pass filter $p_{\tau_0, \Delta\tau}(\tau)$ which suppresses inaccurate values

$$\rho(\tau)_{\text{raw}} \exp(\eta|\tau|) \rightarrow \rho(\tau)_{\text{raw}} \exp(\eta|\tau|) p_{\tau_0, \Delta\tau}(\tau) \quad (3.5)$$

at large values of $|\tau|$ beyond τ_0 on the scale $\Delta\tau$. Of course, this implies that only a certain resolution in frequency can be achieved. In view of the inevitable inaccuracies of any numerical calculation one has to accept such a bound to the enhancement of the resolution. Nevertheless, the deconvolution enhances the resolution considerably and the final curve obtained is continuous for all practical purposes since the interpolation allows to make the grid as fine as needed.

The procedure is illustrated in Fig. 3.1 where we display a power law singularity $s(\omega) = \omega^{-\alpha}\Theta(\omega)$ exactly and convolved by a Lorentzian $L_\gamma(\omega)$ of width $\gamma = 0.05$

$$s(\omega; \gamma) = \frac{\cos[\pi(1-\alpha)/2 - \alpha \arctan(\omega/\gamma)]}{\sin(\pi\alpha) (\omega^2 + \gamma^2)^{\alpha/2}}. \quad (3.6)$$

This line shape is well known in photoelectron spectroscopy [Hüf03], named the Doniach-Šunjić line shape [Don70]. Note that we changed the normalization so that (3.6) represents exactly the convolution of $\omega^{-\alpha}\Theta(\omega)$ with $L_\gamma(\omega)$. The raw data $g_i = s(\xi_i; \gamma = \eta)$ that we use for these curves is obtained analytically at $\xi_i = i * 0.05$ in the interval $\xi_i \in [-3, 5]$, see the curve with the circle symbols. We do not use real D-DMRG here since we want first to illustrate the extraction schemes under ideal circumstances. The effect of inaccuracies will be discussed below.

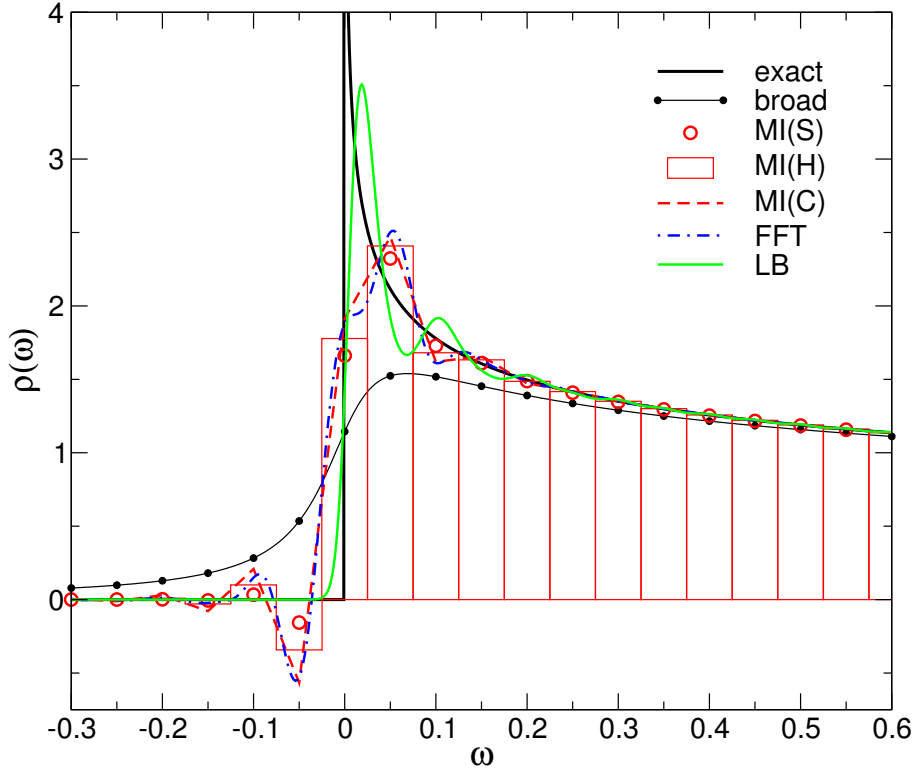


Figure 3.1: Doniach-Šunjić line shape [Eq. (3.6)] for $\alpha = 1/4$ with (thin black solid line with circles representing the raw data at $\xi_i = 0.05i$) and without broadening (thick black solid line) $\gamma = \eta = 0.05$. The results of various schemes to retrieve the unbroadened line are shown: by deconvolution via fast Fourier transform [FFT], by matrix inversion assuming spikes [MI(S)] or histograms [MI(H)] or a piecewise linear continuous function [MI(C)], by the non-linear least-bias algorithm [LB]. All schemes are described in the main text.

In judging the effect of the deconvolution one must keep in mind that the reconstruction of a diverging singular line is the worst case for any algorithm. We have chosen the Doniach-Šunjić line shape for illustration in order to highlight the differences in the various schemes. Below (Fig. 3.3) we will present results also for a smoother curve to show that such a curve can be reconstructed in a quantitatively reliable way.

The dashed-dotted line is the result of the above described deconvolution using the low-pass filter

$$p_{\tau_0, \Delta\tau}(\tau) := \begin{cases} 1 & \text{for } |\tau| < \tau_0 - \Delta\tau \\ 0 & \text{for } |\tau| > \tau_0 + \Delta\tau \\ \left\{ 1 + \exp \left[\tan \left(\frac{\pi(|\tau| - \tau_0)}{2\Delta\tau} \right) \right] \right\}^{-1} & \text{otherwise} \end{cases} \quad (3.7)$$

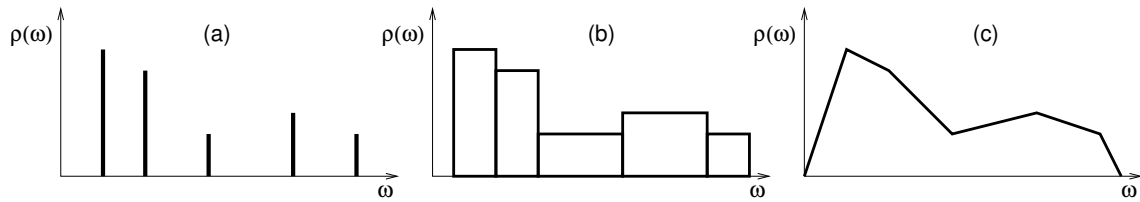


Figure 3.2: Illustration of various assumptions on the behavior of the spectral density $\rho(\omega)$. (a) *Spikes*: $\rho(\omega)$ consists of a set of δ -functions with given positions, but unknown weights. (b) *Histogram*: $\rho(\omega)$ is piecewise constant with given positions of the jumps, but unknown heights ρ_i . (c) *Continuous*: $\rho(\omega)$ is piecewise linear and continuous with given positions of the cusps, but unknown values $\rho(\omega_i)$.

which was also used to achieve the deconvolutions shown in Fig. 2 of Ref. [Raa04] and Fig. 4.1. The parameter τ_0 determines where the low-pass cutoff is done; the parameter $\Delta\tau$ determines on which time-scale the cutoff function switches from 1 to 0. We used $\tau_0 \approx 10.7$ and $\Delta\tau \approx 0.763$. In practice, it turns out that it is fairly obvious in the τ -domain which values one has to choose for the low-pass filter. The data for too large values of $|\tau|$ scatter very much.

3.2.2 Matrix inversion

A robust alternative to the deconvolution by Fourier transform is the explicit matrix inversion of the convolution procedure. This procedure shares the linearity with the Fourier transform and it may also lead to negative spectral weight close to abrupt changes of $\rho(\omega)$, for instance at singularities. An advantage over the Fourier deconvolution is that one may also consider variable widths η_i . In principle, this allows to adapt the grid $\{\xi_i\}$ to the expected behavior of $\rho(\omega)$. A denser grid can be taken where the spectral density varies more rapidly.

The raw data $\{g_i\}$ provided by D-DMRG for a set of $\{\xi_i\}$ are taken as the components of the vector \mathbf{g} . Then the process of convolution can be described by a linear mapping \mathbf{M} of a set of linear parameters $\{l_i\}$ characterizing $\rho(\omega)$ onto the raw data $\{g_i\}$. Let us take the $\{l_i\}$ also as components of a vector \mathbf{l} . Then the convolution reads

$$\mathbf{g} = \mathbf{M}\mathbf{l}. \quad (3.8)$$

Clearly, the deconvolution implies the inversion of this equation. To this end, we have to choose the matrix \mathbf{M} to be square which means that there must be as many data values g_i as there are parameters l_i to be determined. It is obvious that this analysis is linear. The

precise form of the matrix \mathbf{M} depends on further assumptions. Three generic scenarios are studied; they are illustrated in [Fig. 3.2](#).

Spikes

Assuming that $\rho(\omega)$ is given as set of δ -functions (cf. [Fig. 3.2a](#)) with weights $\{w_i\}$ at given frequencies $\{\omega_i\}$. Then the weights constitute the linear parameters defining the spectral density. The matrix \mathbf{M} is derived from [Eq. \(3.1\)](#); it has simple matrix elements given by Lorentzians

$$M_{n,i} = L_{\eta_n}(\omega_i - \xi_n). \quad (3.9)$$

This approach has been proposed and used by Jeckelmann and coworkers [[Geb03](#), [Nis04b](#)]. To have a square matrix problem the number of spikes has to equal the number of g_i determined by D-DMRG.

The rendering of the results is subtle. Since one cannot plot δ -functions they have to be broadened which adds another free parameter. Which broadening one has to choose is not *a priori* clear. For equidistant grids ω_i the distance between two consecutive peaks is a natural choice [[Geb03](#), [Nis04b](#)], cf. [Fig. 3.1](#). The values plotted in [Fig. 3.1](#) are $2w_i/(\xi_{i+1} - \xi_{i-1})$, i.e. for rendering the spectral density $\rho(\omega)$ it is treated as if it were piecewise constant. We stress again that this is not completely consistent with the way the weights are determined because there δ -spikes are assumed. Nevertheless, for equidistant grids $\{\omega_i\}$ the procedure appears to be plain sailing.

Histogram

One assumes that $\rho(\omega)$ is piecewise constant $\rho(\omega) = \rho_i$ for $\omega_i < \omega \leq \omega_{i+1}$ (cf. [Fig. 3.2b](#)) where the frequencies ω_i are given beforehand. The set of linear parameters defining the spectral density are the values $l_i = \rho_i$. Again, [Eq. \(3.8\)](#) has to be solved. The matrix elements of \mathbf{M} are found from the integration of the right hand side of [Eq. \(3.1\)](#)

$$M_{n,i} = \frac{1}{\pi} \arctan \left(\frac{\omega - \xi_n}{\eta_n} \right) \Big|_{\omega=\omega_i}^{\omega_{i+1}}. \quad (3.10)$$

The number of values ρ_i (not the number of ω_i) must be equal to the number of ξ_i to ensure that \mathbf{M} is square. The rendering is straightforward since the values ρ_i represent densities which can be plotted directly, cf. the histograms in [Fig. 3.1](#).

Continuous

One assumes that $\rho(\omega)$ is continuous and piecewise linear (cf. Fig. 3.2c) with $\rho(\omega_j) = \rho_j$, $j \in \{1, 2, 3, \dots, p\}$ at given frequencies ω_j . The obvious ansatz is given by

$$A(\xi)|_{[\omega_j, \omega_{j+1}]} = \rho_{j+1} \frac{\xi - \omega_j}{\omega_{j+1} - \omega_j} + \rho_j \frac{\omega_{j+1} - \xi}{\omega_{j+1} - \omega_j} = a_j \xi + b_j \quad (3.11)$$

introducing the abbreviations

$$\begin{aligned} a_j &:= \frac{\rho_{j+1} - \rho_j}{\omega_{j+1} - \omega_j} \\ b_j &:= \frac{\omega_{j+1} \rho_j - \omega_j \rho_{j+1}}{\omega_{j+1} - \omega_j}. \end{aligned} \quad (3.12)$$

The values ρ_i represent the linear parameters $l_i = \rho_i$ which are determined by Eq. (3.8). The matrix elements $M_{n,i}$ result from the integration in Eq. (3.1),

$$A_n^{(j)}(\xi) := \frac{1}{\pi} \int_{\omega_j}^{\omega_{j+1}} \frac{\eta_n A(\omega)|_{[\omega_j, \omega_{j+1}]}}{(\xi - \omega)^2 + \eta_n^2} d\omega. \quad (3.13)$$

They are given by

$$M_{n,i} = \partial_{\rho_i} A_n(\xi_n) \quad (3.14)$$

with

$$\begin{aligned} A_n(\xi) &:= \sum_{j=1}^{p-1} A_n^{(j)}(\xi) \\ &= \frac{1}{2\pi} \sum_{j=1}^{p-1} \left\{ \eta_n a_j \ln \left[1 + \left(\frac{\omega - \xi}{\eta_n} \right)^2 \right] + 2(\xi a_j + b_j) \arctan \left(\frac{\omega - \xi}{\eta_n} \right) \right\} \Bigg|_{\omega=\omega_j}^{\omega_{j+1}}. \end{aligned} \quad (3.15)$$

Using

$$\zeta_{n,j} := \frac{\omega_j - \xi_n}{\eta_n} \quad (3.16)$$

the matrix elements $M_{n,i}$ evaluate to

$$\begin{aligned}
M_{n,1} &= \partial_{\rho_1} \sum_{j=1}^{p-1} A_n^{(j)}(\xi_n) = \partial_{\rho_1} A_n^{(1)}(\xi_n) \\
&= - \frac{\eta_n \ln \left(\frac{1+\zeta_{n,2}^2}{1+\zeta_{n,1}^2} \right) - 2(\omega_2 - \xi_n) [\arctan(\zeta_{n,2}) - \arctan(\zeta_{n,1})]}{2\pi(\omega_2 - \omega_1)} \\
M_{n,p} &= \partial_{\rho_p} \sum_{j=1}^{p-1} A_n^{(j)}(\xi_n) = \partial_{\rho_p} A_n^{(p-1)}(\xi_n) \\
&= \frac{\eta_n \ln \left(\frac{1+\zeta_{n,p}^2}{1+\zeta_{n,p-1}^2} \right) - 2(\omega_{p-1} - \xi_n) [\arctan(\zeta_{n,p}) - \arctan(\zeta_{n,p-1})]}{2\pi(\omega_p - \omega_{p-1})} \\
M_{n,i} &= \partial_{\rho_i} \sum_{j=1}^{p-1} A_n^{(j)}(\xi_n) = \partial_{\rho_i} [A_n^{(i-1)}(\xi_n) + A_n^{(i)}(\xi_n)] \\
&= \frac{\eta_n \ln \left(\frac{1+\zeta_{n,i}^2}{1+\zeta_{n,i-1}^2} \right) - 2(\omega_{i-1} - \xi_n) [\arctan(\zeta_{n,i}) - \arctan(\zeta_{n,i-1})]}{2\pi(\omega_i - \omega_{i-1})} \\
&\quad - \frac{\eta_n \ln \left(\frac{1+\zeta_{n,i+1}^2}{1+\zeta_{n,i}^2} \right) - 2(\omega_{i+1} - \xi_n) [\arctan(\zeta_{n,i+1}) - \arctan(\zeta_{n,i})]}{2\pi(\omega_{i+1} - \omega_i)} \quad \text{for } 1 < i < p.
\end{aligned}$$

The number p must be equal to the number of raw data points. An example is depicted by the piecewise linear dashed curve in Fig. 3.1.

In all schemes, the numbers must be chosen such that \mathbf{M} is a square matrix. This is a necessary but not a sufficient condition for the existence of a unique solution \mathbf{I} in (3.8). In practice, we did not encounter problems in the inversion of Eq. (3.8) as long as the raw data points were distributed rather evenly along the real axis. Only if there are data points accumulating in certain regions, for instance several data points at the same frequency, the inversion can be problematic. Loosely speaking this may occur since the raw data is slightly contradictory due to numerical inaccuracies. The broadening by the $\{\eta_n\}$ reduces the differences between the spectral densities. Hence small deviations in the raw data have large effects on the extracted spectral densities.

All linear extraction schemes do not guarantee that the extracted spectral density is non-negative, see Fig. 3.1. Whether this must be considered a serious drawback depends on the extent to which negative values occur and on the context in which the result is used. If the spectral density is the final result small regions of overshooting are unproblematic. If, however, the overshooting is considerable and if the spectral density shall be used in a

subsequent step, e. g. in the self-consistency of a DMFT calculation, then negative values pose a severe problem. An important example is the determination of the coefficients of the continued fraction of the spectral density. This determination is only possible if the spectral density is really non-negative.

Another problem is the smoothness of the extracted density. Spurious discontinuities like the ones assumed in the spike ansatz or in the histogram ansatz (see Figs. 3.1 and 3.2) imply singularities in the real part of the propagator which is determined by the Kramers-Kronig relation. This in turn leads to unwanted features like slowly decaying oscillations in coefficients of the continued fraction. Of course, various schemes can be used to interpolate the discrete data provided by the matrix inversion approaches. But the interpolation represents an additional approximation which can be difficult to control.

3.3 Non-Linear Extraction Schemes

3.3.1 Basic Algorithm

In view of the drawbacks of the linear extraction schemes it is worthwhile to think about alternatives. The objective is to devise an ansatz for a continuous, non-negative spectral density $\rho(\omega)$ which is consistent with the numerically determined values of the raw data $\{g_i\}$ in Eq. (3.1). The ideal ansatz is completely unbiased. That means it does not use *any* information *other* than the one provided by the raw data. The information content of a density $\rho(\omega)$ is measured up to a constant by its negative entropy

$$-S = \int_{-\infty}^{\infty} \rho(\omega) \ln(\rho(\omega)) d\omega . \quad (3.17)$$

The least biased ansatz is the one with the least information content which is still compatible with the raw data. Hence we have to look for the density $\rho(\omega)$ which minimizes $-S$ (maximizes S) under the conditions Eq. (3.1) given by the raw data $\{g_i\}$ and by the known normalization

$$1 = \int_{-\infty}^{\infty} \rho(\omega) d\omega . \quad (3.18)$$

To find this least biased (LB) ansatz is a straightforward task. Using the Lagrange multipliers $\{\lambda_i\}$ for the p conditions set by the raw data $\{g_i\}$ and the Lagrange multiplier $\tilde{\mu}$ for the normalization (3.18) the least biased ansatz is characterized by $\delta S = 0$, i. e.

$$0 = -1 - \ln(\rho(\omega)) + \sum_{i=1}^p \lambda_i L_{\eta_i}(\omega - \xi_i) + \tilde{\mu} . \quad (3.19)$$

This equation implies that the LB ansatz reads

$$\rho(\omega) = \exp \left[\mu + \sum_{i=1}^p \lambda_i L_{\eta_i}(\omega - \xi_i) \right], \quad (3.20)$$

where we defined $\mu = \tilde{\mu} - 1$. The Lagrange multipliers are determined by the non-linear equations (3.18) and (3.1). They can be determined by any standard algorithm for a set of non-linear equations. Via the ansatz (3.20), the $p + 1$ Lagrange multipliers determine the most unbiased spectral density $\rho(\omega)$ which is still compatible with the numerically measured information on $\rho(\omega)$.

The LB ansatz (3.20) is positive and continuous. Hence it avoids two major drawbacks of the linear extraction schemes. In spite of its continuity the LB ansatz is governed by a restricted number of parameters. Despite its positivity, the LB ansatz is able to reproduce rather abrupt changes in the spectral density, see Fig. 3.1. If arbitrarily accurate data at a fixed value of η were available on an arbitrarily dense grid, the LB algorithm were able to provide the correct result with arbitrary resolution (see also the discussion of Fig. 3.4 below). But the accuracy of the raw data required to achieve a certain resolution in the deconvolved result grows exponentially. So in practice this route cannot be followed very far and the broadening η sets the scale for the achievable resolution.

The least bias approach belongs to the class of maximum entropy methods (MaxEnt) [Pre92]. The main difference to standard MaxEnt is that we do not use a χ -functional in addition to the entropy function (3.17). The χ -functionals are bilinear in the density. They are introduced to account for possible deviations of the g_i from their true values. Such deviations occur for instance in quantum Monte Carlo calculations due to the inevitable statistical error. The D-DMRG data is free from statistical errors. Hence we can use the entropy functional alone as described above. The correction of numerical inaccuracies is discussed in more detail below.

We emphasize a major difference between the extraction of the spectral density $\rho(\omega)$ from D-DMRG data and from QMC. In the former case the task to be solved is to remove a small imaginary part $\omega + i\eta \rightarrow \omega$. This means that in the D-DMRG the raw data is situated slightly above the real axis and has to be continued down to it. In the latter case the task to be solved is to continue QMC data from the imaginary axis (no real part) to the real axis $i\zeta \rightarrow \omega$. So the challenge in the QMC data analysis is much greater than in the D-DMRG data analysis. This explains why the D-DMRG approach is suited to investigate sharp features also at high energies [Raa04] while this is not a straightforward task by QMC.

The solution of the non-linear equations (3.18) and (3.1) is done by a standard algorithm. There is no mathematical argument to show that there is only one unique solution.

For instance, we found that the normalization of the spectral density need not be ensured by the parameter μ . This parameter can be fixed to almost any value. The remaining Lagrange parameters suffice to determine good approximations to $\rho(\omega)$ which fulfill the normalization condition (3.18) well. This implies that iterative numerical solutions have difficulties to fix μ independently. The root-finder algorithms run much more stable if the normalization is not included in the set of equations. Yet the resulting densities are normalized if the raw data provides a reasonable scan of the spectral density, i. e. if there is raw data at all frequencies ω where the density is non-negligible.

For other sum rules, for instance the second moment $\langle \omega^2 \rangle$, the same conclusion holds. If the raw data scans all relevant frequencies the sum rules do not provide useful additional information. But if raw data is only available for restricted frequency intervals, the sum rules help to improve the LB ansatz.

Furthermore, the iterative numerical solutions depend sometimes on the initial values. But the resulting $\rho(\omega)$ are in general (almost) identical. This remains true if the iterative algorithm does not find a true solution of the set of non-linear equations but only a set of parameters which makes the deviations

$$\Delta g_i := g_i - \frac{1}{\pi} \int_{-\infty}^{\infty} \frac{\eta_i \rho(\omega) d\omega}{(\xi_i - \omega)^2 + \eta_i^2} \quad (3.21)$$

small but fails to make them zero. In summary, the iterative determination of the Lagrange multipliers does not represent a major problem.

In Fig. 3.1 we display a comparison of all data extraction schemes introduced so far. The line shape to be found is a singular power law divergence. This line shape constitutes an unsolvable task since a divergence cannot be reproduced by the algorithms discussed. But this example illustrates well to which extent the algorithms manage to render the true distribution of spectral weight. All the linear schemes lead to regions of negative spectral densities which is a severe drawback. The divergence is approximated by a broad peak located at 0.05 away from the position of the divergence. There are some spurious oscillations in the approximated spectral density.

The LB scheme avoids negative spectral weight by construction. The divergence is approximated by a sharper peak at about 0.02 away from the position of the divergence. The algorithm implies spurious oscillations in the approximated spectral density. So we conclude that the LB analysis represents a very efficient reconstruction of the unbroadened data even though the spurious oscillations can be a nuisance.

On the other hand it is, of course, possible to improve the analysis. An additional data point at $\omega \approx 0.02$ will certainly help all algorithms to reproduce the unbroadened density more faithfully. The same is trivially true for a denser mesh of raw data points.

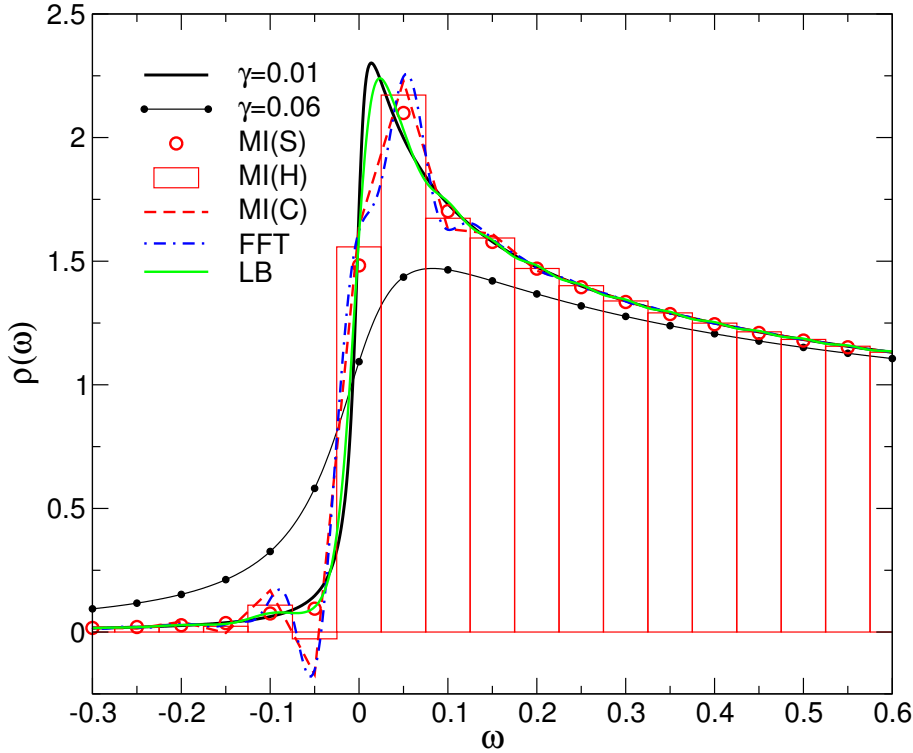


Figure 3.3: Exact (thick black solid line) and broadened (by $\eta = 0.05$, thin black solid line with circles representing the raw data at $\xi_i = 0.05i$) lines derived from the Doniach-Šunjić line shape in Eq. (3.6), see also main text. The results of various schemes to retrieve the unbroadened line are shown: by deconvolution via fast Fourier transform [FFT], by matrix inversion assuming spikes [MI(S)] or histograms [MI(H)] or a piecewise linear continuous function [MI(C)], by the non-linear least-bias algorithm [LB].

The former solution, however, requires either to intervene manually in the data analysis or to know beforehand where the peaks will be located. The latter requires much more numerical effort on the D-DMRG level so that this is not the most efficient approach.

In Fig. 3.3 we present the analysis of a smooth exact curve, namely the line shape in (3.6) at $\gamma = 0.01$. The curve broadened by $\eta = 0.05$ is the one at $\gamma = 0.06$ since the widths of Lorentzians is additive under convolution, in contrast to the root-mean-square of narrower distribution functions. Clearly, the extraction schemes do a better job for this non-singular case. The regions of negative spectral density in the linear schemes has shrunk. The LB scheme manages to reproduce the true density almost perfectly. The spurious oscillations are negligible. If we had chosen $\gamma = 0.02$ for the exact curve the LB density would be hardly distinguishable from the exact curve.

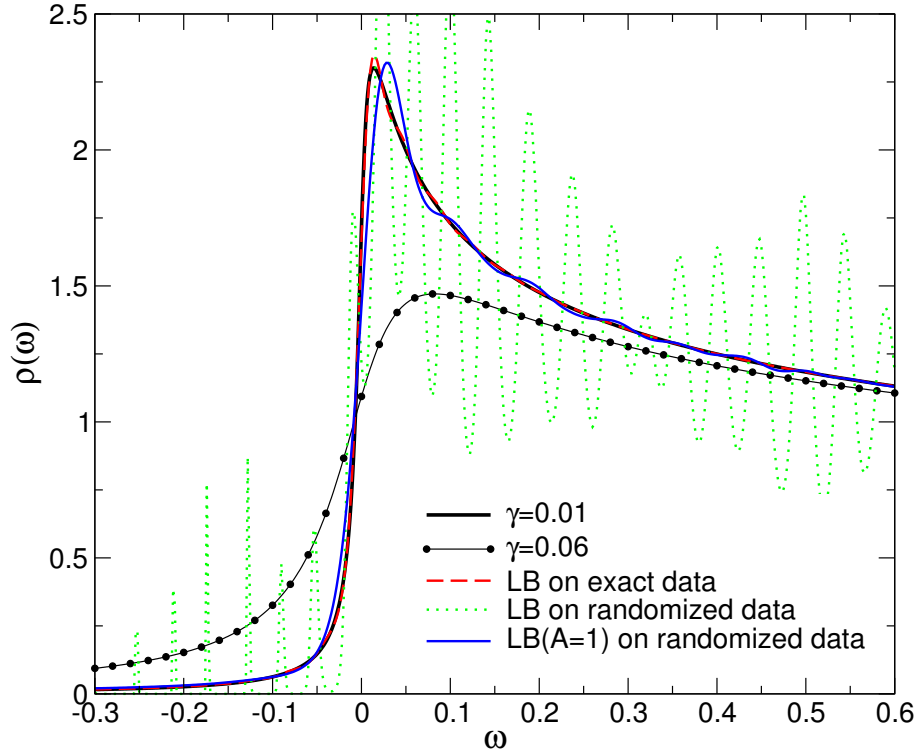


Figure 3.4: Exact (thick black solid line) and broadened (by $\eta = 0.05$, thin black solid line with circles representing the raw data at $\xi_i = 0.02i$) lines derived from the Doniach-Šunjić line shape in Eq. (3.6). The dashed line depicts the density extracted from exact raw data by the LB scheme (the curve lies on top of the thick black line except at the maximum). The dotted oscillations are the LB result from data contaminated by a random error, see main text. The thin solid line represents the density derived from the contaminated data by the robust LB scheme with $A = 1$ using Eqs. (3.23, 3.24).

3.3.2 Robustness towards inaccuracies

So far we analyzed ideal raw data, i. e. no errors were considered. Statistical errors do not occur in the D-DMRG approach but systematic errors occur. There are two main sources for such errors. The first is the inaccuracy of the algorithm due to the truncation of the Hilbert space. This is an unavoidable error; but it can be controlled by comparing the results for different numbers of states kept in the density-matrix renormalization. We perform our calculations for $m = 128$ and for 256 states using the representation of spinful fermions as two kinds of spins via a double Jordan-Wigner transformation (cf. [Raa04] and Sect. 1.6.2). The relative *truncation error* in the spectral densities is estimated to be of the order of 10^{-5} to 10^{-3} depending on the frequency where it is computed. For low

values of the frequency ($|\omega| \lesssim D$ in our model) the lower error applies; for frequencies beyond D the larger value applies.

The second important source of inaccuracy are *finite-size effects*. In principle, we wish to compute the spectral density for the infinite system. But this is not feasible numerically. So the system—the infinite chain—is approximated by finite chains of $L = 120$ to 400 sites. In a rigorous sense, the spectral density of the finite system consists of δ -functions, i. e. it is not a continuous function. But we do not intend to resolve all the fine details of the finite system. Rather we interpret our numerical raw data obtained for the finite chain as an approximate description of the infinite system. The deviation of the raw data for the finite chain from the desired raw data of the infinite chain is considered the source of a systematic error, the finite-size effect. There are two conceivable ways to deal with this error. One way is to perform an extrapolation in system size L for each raw data point g_i before the deconvolution is done. The other way is to deconvolve the raw data for various chain lengths and to check whether the results still depend on the length L .

In our work, we have chosen the second approach because the first is hampered by an unsystematic behavior of g_i on L . Depending on details a particular δ -peak of the finite systems contributes more or less to the g_i under study. This makes a controlled extrapolation for all $\{g_i\}$ difficult, if not impossible.

In the second approach, care must be taken that the length L is so large that the raw data is sufficiently close to the raw data of the infinite system. In practice, this puts a restriction on η and L , see [Sect. 4.4](#) and Ref. [[Jec02](#)]. Of course, the use of finite chains restricts the extent to which we may extract information on the exact infinite system from the broadened data obtained for the finite system.

Another sort of errors are *rounding errors*. But they are of minor importance compared to the two other sources discussed above.

In [Fig. 3.4](#) we display the LB analysis of raw data for the exact curve at $\gamma = 0.01$. In contrast to the procedure in [Fig. 3.3](#) we use a finer grid of $\xi_i = i * 0.02$ for the raw data (curve with circles). The extracted curve represents the exact one very well, see the dashed line in [Fig. 3.4](#). The agreement is significantly better than the one reached in [Fig. 3.3](#). This illustrates that sufficiently accurate broadened data at fixed η can be used to resolve features of widths below η .

As explained above, there are in practice restrictions to better resolutions due to the systematic errors, namely the truncation of the basis and the finite-size effect. To examine the effect of systematic errors on the LB deconvolution we deliberately contaminated the raw data by an error of the order of 10^{-3} according to

$$g_i \rightarrow g_i * (1 + 10^{-3}x) \quad (3.22)$$

where x is a random number between -1 and 1 . The randomness is just used to mimic a systematic error which is uncorrelated from frequency to frequency. We obtained qualitatively very much the same results for a non-random error $g_i \rightarrow g_i * [1 + 10^{-3} \cos(\sqrt{5}i)]$.

If the data is slightly inaccurate the deconvolution indeed fails as illustrated by the wild oscillations of the dotted line. We conclude that the occurrence of strong oscillations can be taken as criterion that the used raw data is not accurate enough for the LB analysis, i. e. the systematic errors are too large.

The thinner solid line depicts a successful deconvolution of the contaminated raw data. It is achieved by a modification of the LB algorithm which makes it a standard maximum entropy approach. The negative entropy functional (3.17) is supplemented as shown

$$\begin{aligned} F[\rho(\omega)] &:= -S[\rho(\omega)] + A\chi[\rho(\omega)] \\ &= \int_{-\infty}^{\infty} \rho(\omega) \ln(\rho(\omega)) d\omega + A \sum_i (\Delta g_i)^2 \end{aligned} \quad (3.23)$$

by a quadratic functional χ which measures the distance from the perfect fulfillment of the conditions (3.1). The differences Δg_i are defined in Eq. (3.21). The minimization of the functional F leads to the same ansatz (3.20) as before except that the parameters λ_i are now given by

$$\lambda_i = 2A\Delta g_i. \quad (3.24)$$

The set of these non-linear equations (instead of $\Delta g_i = 0$ as for the pure LB approach) is used to determine the parameters λ_i . It is obvious that the robust modification of the LB ansatz becomes the pure LB ansatz in the limit of $A \rightarrow \infty$ since in this limit the deviations Δg_i vanish for given values of the Lagrange parameters λ_i . If the data is only weakly contaminated by inaccuracies, large values of A can be used to extract the spectral densities. Our example in Fig. 3.4 shows fairly strongly perturbed data. Still the robust LB can make sense out of them and retrieves a good approximation to the underlying curve.

The modified LB ansatz (3.23) is more robust since it can deal with some inaccuracies or inconsistencies of the raw data. Imagine that we deal with raw data on a fine grid where the distance between the data points is significantly smaller than the Lorentzian width $\eta_i \gg (\xi_{i+1} - \xi_i)$. Then g_{i+1} and g_i may differ only slightly if they are derived from a smooth continuous density $\rho(\omega)$. Any inaccuracy spoils this relation and may introduce significant spurious oscillations, see Fig. 3.4. As we stressed already previously the broadening makes different data more alike. Hence, the inverse process enhances slight differences like the ones between exact and inaccurate raw data greatly. The robust LB ansatz (3.23) helps to make the data extraction less sensitive to such effects without losing much resolution. Thereby, spurious oscillations can be suppressed.

The robust LB scheme opens the possibility to resolve features of widths below a given

value of the broadening η by using a finer grid with $\Delta\xi < \eta$ since slightly inaccurate data can still be deconvolved. In this way, one may avoid the explicit use of small values of η . We emphasize, however, that the data must be accurate enough to contain the information on the relevant physics. Of course, the robust LB approach is no means to extract information which is not given by the raw data. For instance, one may stick to short chain lengths *only* if the underlying physical problem does not demand to describe long-range spatial fluctuations.

3.4 Summary

In [this chapter](#), we discussed a variety of schemes to extract the spectral density $\rho(\omega)$ from the results of dynamic density-matrix renormalization data. All these schemes have the aim to remove the unavoidable broadening which has to be included in a D-DMRG calculation. The linear schemes use either Fourier transform to deconvolve the raw data or they implement an explicit matrix inversion. These schemes are linear because there is a linear relationship between the raw data and the extracted spectral density. If the structures to be resolved are not too sharp the linear schemes work well. If there are sharp structures the linear schemes are prone to lead to negative spectral densities which result from spurious oscillations. Furthermore, they can resolve the positions of sharp peaks only with the accuracy of the grid on which the raw data has been computed.

The non-linear scheme introduced belongs to the family of maximum entropy methods. If the raw data is sufficiently accurate the least-bias approach works very well. It provides a positive and continuous ansatz for the spectral density with the least possible bias. Even relative abrupt changes of the spectral density can be reproduced satisfactorily. In the vicinity of singularities spurious oscillations occur. But they do not violate the positivity of the ansatz. The least-bias ansatz can be made more robust towards small numerical inaccuracies and finite-size effects by including besides the entropy functional a χ -functional in the functional to be minimized. Thereby, one can allow for small deviations from the raw data.

The properties of the above mentioned schemes are illustrated by calculations for a singular toy spectral density of the Doniach-Šunjić type.

In the [next chapter](#) we present results for the single impurity Anderson model. D-DMRG calculations were carried out for the symmetric SIAM in the Schrieffer-Wolff limit of $U > W$ where U is the interaction and W the band width. We present the results for the Kondo energy scale [Sect. 4.4](#) and for the Hubbard satellites in [Sect. 4.5.2](#). Here the LB deconvolution will turn out to be a very useful tool for the analysis of D-DMRG raw data.

4 Results for the SIAM

4.1 Introduction

In [Chapt. 1](#) and [Sect. 3.1](#) we introduced and motivated the single impurity Anderson model. The SIAM at half-filling is a very good and interesting testing ground. We will focus on [Eq. \(1.45\)](#),

$$\mathcal{H} = U (n_{d,\uparrow} - 1/2) (n_{d,\downarrow} - 1/2) + \sum_{\sigma} V \left(d_{\sigma}^{\dagger} c_{1,\sigma} + \text{h.c.} \right) + \sum_{i=1, \sigma}^{N_c-1} \gamma_i \left(c_{i,\sigma}^{\dagger} c_{i+1,\sigma} + \text{h.c.} \right),$$

with arbitrary symmetric density of states (DOS) $\rho_0(\omega)$ of the free ($U = 0$) one-particle Green function $G_0(\omega)$ of the d electron. The d electron represents the impurity which is correlated due to the interaction $U > 0$. The bath is represented by the coefficients $\gamma_i \geq 0$ in [\(1.45\)](#). They are the coefficients of the continued fraction of the hybridization function $\Gamma(\omega)$, see [Sect. 1.4](#). Any hybridization function with symmetric imaginary part $\rho_0(\omega) := -\pi^{-1} \Im G_0(\omega + i0^+)$ can be represented by an appropriate choice of the γ_i . Hence the representation of the bath as semi-infinite chain does not restrict the generality of the model. For details see [Chapt. 1](#), especially [Sect. 1.5](#).

We set up an algorithm in [Chapt. 2](#), the dynamic density-matrix renormalization, to calculate the single-particle dynamics of the SIAM. Now let us apply the D-DMRG to compute the $T = 0$ dynamics of the fermionic single-particle propagator of the d electron, see [Sect. 1.5](#) and [Eqs. \(1.35, 1.36, 1.37\)](#):

$$G(\omega + i\eta) = \left\langle 0 \left| d_{\sigma} \frac{1}{\omega + i\eta - (\mathcal{H} - E_0)} d_{\sigma}^{\dagger} \right| 0 \right\rangle + \left\langle 0 \left| d_{\sigma}^{\dagger} \frac{1}{\omega + i\eta + (\mathcal{H} - E_0)} d_{\sigma} \right| 0 \right\rangle.$$

Here the ground state is denoted by $|0\rangle$ and its energy by E_0 . Since we focus at a spin-disordered solution the propagator has no dependence on the spin index σ . Hence, it is not denoted as argument of G . The frequencies ω and η are real. The standard retarded

Green function is obtained for $\eta \rightarrow 0^+$, see [Eq. \(1.38\)](#),

$$G_{\text{R}}(\omega) = \lim_{\eta \rightarrow 0^+} G(\omega + i\eta).$$

The quantity we are looking for is the spectral density

$$\rho(\omega) := -\frac{1}{\pi} \Im G_{\text{R}}(\omega).$$

If necessary the real part can be obtained from the Kramers-Kronig relation.

The deconvolution schemes introduced in [Chapt. 3](#) are illustrated for the line shape and width of the Kondo peak (low energy feature, [Sect. 4.4](#)) and for the line shape of the Hubbard satellites (high energy feature, [Sect. 4.5.2](#)) of the SIAM. It is found that the Hubbard satellites are strongly asymmetric. The non-linear least-bias deconvolution, see [Sect. 3.3](#), turns out to be a useful tool to analyze DMRG raw data.

4.2 Overview

In [Fig. 4.1a](#), generic broadened spectral densities are plotted as they are computed by D-DMRG. Obviously, the value $\rho^{(\eta)}(0)$ is not independent of U . Increasing the chain length N_{f} does not lead to any significant change in the data (not shown). [Fig. 4.1b](#) displays the FFT deconvolved data, see [Sect. 3.2.1](#). The FFT deconvolution works very well except for some slight overshooting in regions where the spectral density changes rather abruptly. In particular, the value $\rho(0)$ is pinned to $D/(2\pi V^2)$ independent of U [cf. [Eq. \(1.59\)](#)] as required by Friedel's sum rule and the density of states rule [[Lut60](#), [Lut61](#), [And91](#), [Hew93](#)]. We take this fact as convincing evidence for the reliability of the numerical algorithm.

The central peak at $\omega = 0$ is the Abrikosov-Suhl resonance (ASR). For larger U (smaller V) its width decreases rapidly so that the ASR is very difficult to resolve [[Nis04b](#)] unless more elaborate deconvolution schemes are used. So a quantitative analysis of the ASR is postponed [Sect. 4.4](#), where we use the non-linear least-bias (LB) deconvolution on D-DMRG raw data obtained for larger chains.

For comparison, the thin dashed lines in [Fig. 4.1b](#) depict standard NRG data [[Bul98](#), [Bul00a](#)]. For small frequencies NRG is well-controlled. Indeed, for $|\omega| \lesssim D/3$, NRG and D-DMRG data agree excellently lending further support to the D-DMRG approach. Outside the band, the NRG spectra appear to be too wide due to the chosen constant broadening on a logarithmic mesh. This broadening does not account for the absence of states outside the bare band. The NRG does not possess intrinsic information about

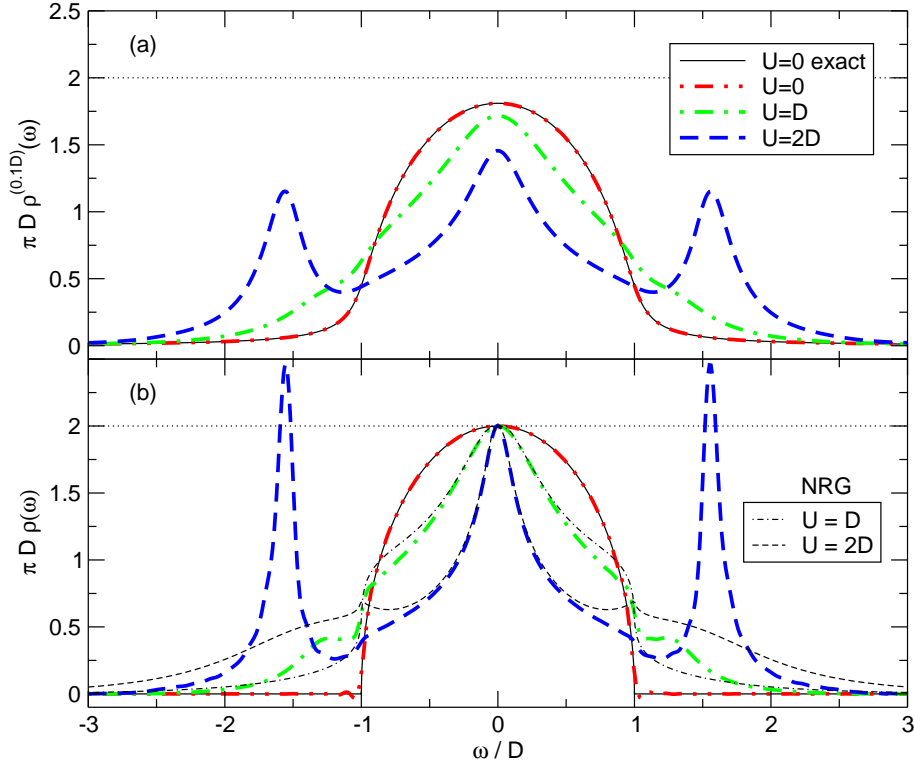


Figure 4.1: (a) Spectral densities for $V = D/2$ broadened by $\eta = 0.1D$. Chain length $N_f = 80$ fermionic sites; $m = 128$ DMRG states kept. (b) Spectral densities from (a) deconvolved in the time domain by FFT. NRG data ($\Lambda = 1.8$, 1500 states) depicted by thin dashed lines. The exact curves represent the analytic $N_f = \infty$ results.

the peak widths. The position of the high energy peak in the raw NRG data, however, coincides with the D-DMRG result.

An increase in U leads to the formation of Hubbard satellites below and above the free band (Fig. 4.1). They are situated at energies $\omega_{\text{up/low}} = \pm(U/2 + \delta_{\text{shift}})$, $\delta_{\text{shift}} > 0$ and become more pronounced on increasing U in two ways. They capture more weight and they become sharper. For $T_K \rightarrow 0$ the weight reaches $1/2$, see Ref. [And91]. The sharpening has not been discussed quantitatively before although the extended non-crossing approximation [Pru89] provides sharp satellites if they lie outside the bare bands, see e. g. Fig. 1 in Ref. [And91]. Recently, indications have occurred [Geb03] that other standard algorithms overestimate the width of the Hubbard satellites. The exaggerated width of the NRG data at high energies results from the Gaussian broadening of the order of the energy range [Sak89].

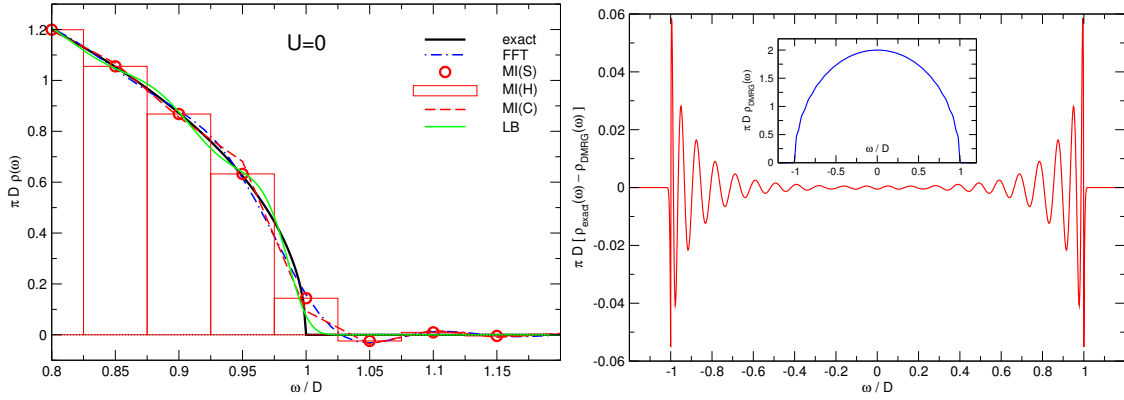


Figure 4.2: Non-interacting half-elliptic spectral density $\rho(\omega)$ as obtained from D-DMRG. *Left:* comparison of various deconvolution schemes. Chain length $N_f = 80$ fermionic sites; $m = 128$ DMRG states kept. *Right:* results from LB deconvolution (shown in the inset) compared to the exact curve. $N_f = 200$; $m = 256$; $\eta = 0.1D$ prior to deconvolution.

4.3 Non-interacting case

Fig. 4.2 shows the non-interacting half-elliptic spectral density $\rho(\omega)$ as obtained from D-DMRG in the vicinity of the upper band edge. The left graph compares the deconvolutions from the various schemes introduced in [Chapt. 3](#). The findings agree with the observations made for the singular toy spectral density of the Doniach-Šunjić type. In the vicinity of sharp edges the linear extraction schemes can produce negative spectral densities. The LB curve remains positive-definite by construction and shows some negligible oscillations. The sharp band edge is reproduced excellently by the LB data. We plot the deviation from the exact curve in the right plot of [Fig. 4.2](#). The LB extraction of the D-DMRG raw data is shown on a larger scale in the inset.

The right plot showing the deviation between exact and LB data points up the spurious oscillations that can occur in the vicinity of singularities. The regular pattern might suggest to apply a filter function that filters out the oscillations. We prefer not to manipulate the LB results this way. Often it is clear by intuition whether the oscillations are due to the deconvolution of data with systematic errors, see [Sect. 3.3.2](#), or have physical reasons. Furthermore, the appearance of oscillations can be taken as a hint that the D-DMRG calculation for the quantity of interest has to be redone with higher accuracy. If the DMRG raw data is available on a relatively fine mesh of frequencies, it is advisable to thin out the data set, e. g. to drop every second point of the raw data. Comparing the deconvolutions of the reduced data set and of the original data delivers valuable insight in the quality of the DMRG data. From our experience, excellent numerical data is very robust against this

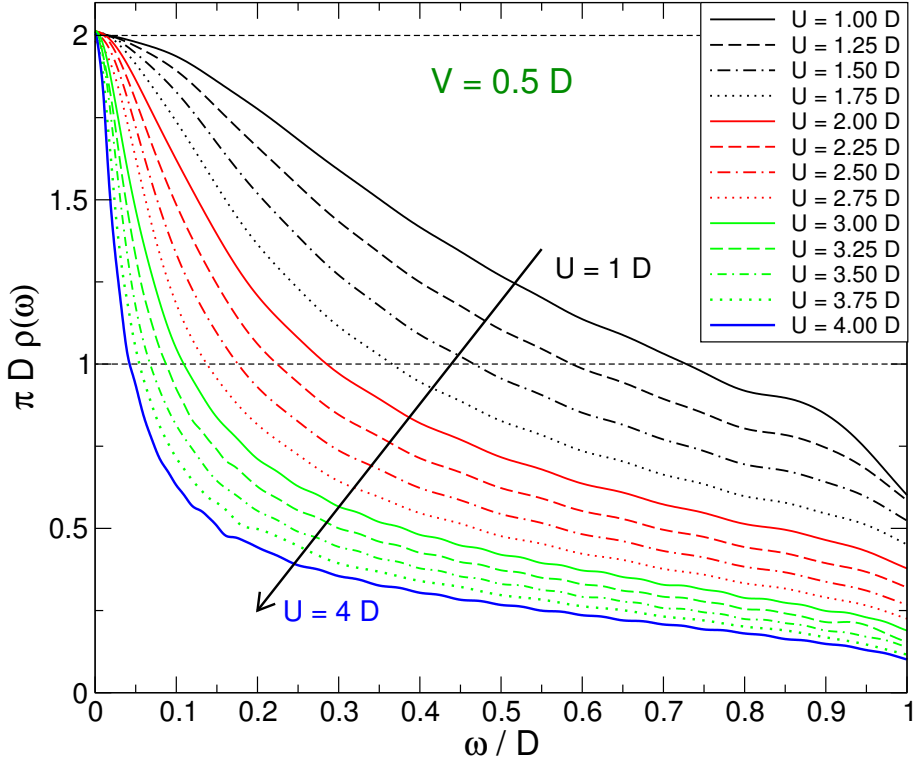


Figure 4.3: Kondo peaks for the single impurity Anderson model (1.45) for a hybridization function with semi-elliptic spectral density and $V = D/2$. On increasing interaction the Kondo peak becomes rapidly narrower.

manipulation. The less accurate the data is the more probable are spurious oscillations for small stepsizes in the DMRG raw data, i. e. $\Delta\xi = \xi_{i+1} - \xi_i < \eta/2$.

4.4 Kondo resonance

In the [present section](#) we focus on the behavior at low energies where $\rho(\omega)$ is dominated by the Kondo peak, see e. g. Ref. [[Hew93](#)]. This peak can be computed by NRG in a very efficient way [[Sak89](#), [Cos90](#), [Hew93](#)]. So the idea of the present calculation is not to provide novel data, but to gauge the D-DMRG and to demonstrate that features at low energies can be resolved. We use the least-bias (LB) scheme to extract the real spectral density from the raw data as explained in [Sect. 3.3](#). This is one of the differences to the investigation by Nishimoto and Jeckelmann [[Nis04b](#)]. For details of the numerical realizations we refer to [Sect. 2.2.3](#) and Ref. [[Nis04b](#)]. Another difference concerns the parameter regime. We consider here interaction values U beyond the bare band width $W = 2D$, i. e. $U > 2D$, while Nishimoto and Jeckelmann look at Lorentzian bare spectral

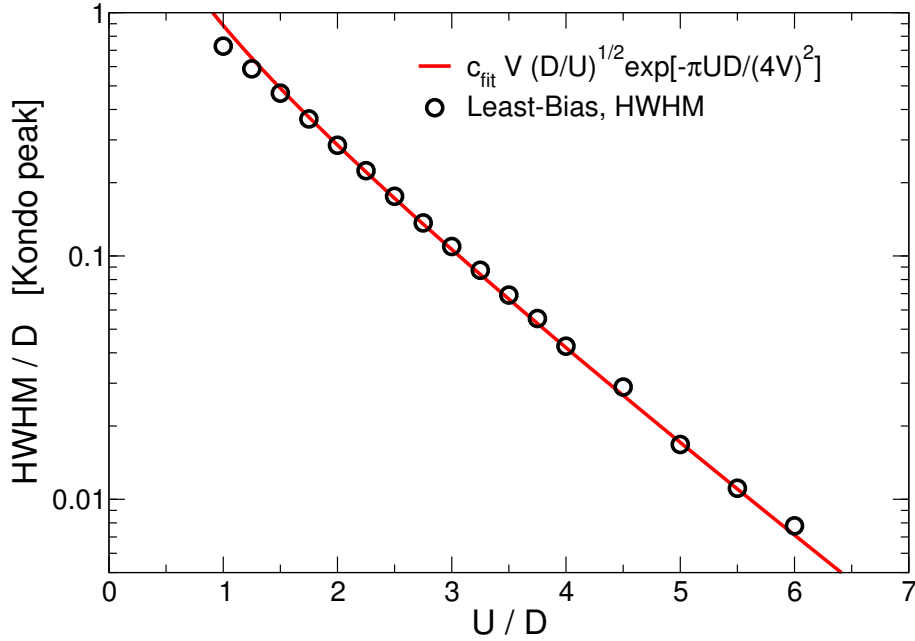


Figure 4.4: Kondo energy scale (Kondo temperature) for the single impurity Anderson model (1.45) for a hybridization function with semi-elliptic spectral density and $V = D/2$ in the Schrieffer-Wolff limit $U > 2D$. *Symbols:* half-width-half-maximum (HWHM) read off from $\rho(\omega)$ as found by the LB analysis of D-DMRG raw data. *Solid line:* analytic result in Eq. (4.3). The proportionality factor of the fit is $c_{\text{fit}} = 3.887$.

function whose band width is very large. But for the low energy region this difference is only a quantitative one.

Our results are depicted in Fig. 4.3. We have chosen the parameters such that the hybridization function has a semi-elliptic spectral density. The hybridization is taken to be $V = D/2$ so that the spectral density of the d site without interaction is semi-elliptic, too. Clearly visible is the rapid narrowing of the Kondo peak on increasing interaction. Note that the density at zero energy $\rho(0)$ is pinned to its non-interacting value $2/(\pi D)$ [cf. Eq. (1.60)] as required by the sum rules [Lut60, Lut61, And91, Hew93]. This exact result is fulfilled to numerical accuracy which ranges from 0.1% for smaller interactions to 1% at larger interactions, see Fig. 4.3 and the following table (calculated for $V = D/2$, $N_f = 120\text{--}400$, $m = 256$, $\eta = 0.1\text{--}0.05D$):

U/D	$\pi D \rho(0)$	U/D	$\pi D \rho(0)$
1.0	2.00015	3.0	2.00331
1.5	2.00094	3.5	2.00398
2.0	2.00384	4.0	2.00422
2.5	2.00711	5.0	2.04662

The data in Fig. 4.3 is obtained on various grids in frequency, for various chain lengths and for varying widths η . All calculations are done with $m = 128$ sites kept in the truncations of the DMRG. The chain lengths N_f vary between 120 and 400 fermionic sites which translates to 240 (e. g. at $U = 1.25D$) to 800 (e. g. at $U = 4.00D$) spin sites after the double Jordan-Wigner transformation. The smaller the widths η are chosen the longer the chains have to be taken [Höv00, Jec02]. A chain of N_f fermionic sites implies N_f main peaks distributed over the band width $W = 2D$. Assuming a roughly equidistant distribution the distance between two main peaks is W/N_f which should be significantly smaller than η

$$2W/N_f \leq \eta \quad (4.1)$$

in order to ensure that the discrete structure of the finite system is sufficiently smeared out. Then the data provided can be interpreted reasonably well as data of the infinite system.

Since the calculations are less costly at low energies than at higher energies we used mixed raw data coming from various chain lengths. The width η is varied correspondingly; we always used $\Delta\xi = \xi_{i+1} - \xi_i = \eta$. For instance at $U = 4D$, we used $N_f = 400$ with $\eta = 0.01D$ between $\omega = 0.00D$ and $0.05D$; $N_f = 200$ with $\eta = 0.02D$ between $\omega = 0.06D$ and $0.18D$; $N_f = 200$ with $\eta = 0.05D$ between $\omega = 0.20D$ and $2.95D$; $N_f = 120$ with $\eta = 0.10D$ between $\omega = 3.00D$ and $4.00D$. The analysis of the raw data was done in all cases by the pure LB ansatz (3.20) with the conditions $\Delta g_i = 0$. There was no need to use the robust LB with $\lambda_i = 2A\Delta g_i$.

The rapidly narrowing peaks in Fig. 4.3 are characterized by the Kondo energy scale T_K . This scale can be read off from the spectral densities, for instance as half the width at half the maximum, i. e. at $\pi D\rho(\omega = T_K) = 1$. From analytic considerations (Sect. 3.4 in Ref. [Hew93]), it is known that the Kondo energy scale is exponentially small in the interaction (cf. Eq. (3.54) in Ref. [Hew93])

$$k_B T_K \propto D \sqrt{\frac{\Delta U}{|\epsilon_d||\epsilon_d + U|}} \exp\left(-\pi \frac{|\epsilon_d||\epsilon_d + U|}{2\Delta U}\right). \quad (4.2)$$

Using $\epsilon_d = -U/2$ and $\Delta = 2V^2/D$ one finds

$$T_K \propto V \sqrt{\frac{D}{U}} \exp\left(-\pi \frac{UD}{(4V)^2}\right). \quad (4.3)$$

This formulas apply in the limit of $U \gtrsim W = 2D$ which is called the Schrieffer-Wolff limit of the SIAM. It holds for $U \rightarrow \infty$.

The numerical results for the Kondo scale and the analytical prediction (4.3) agree very well in Fig. 4.4. Only for $U < W$ deviations occur as was to be expected. The widths at

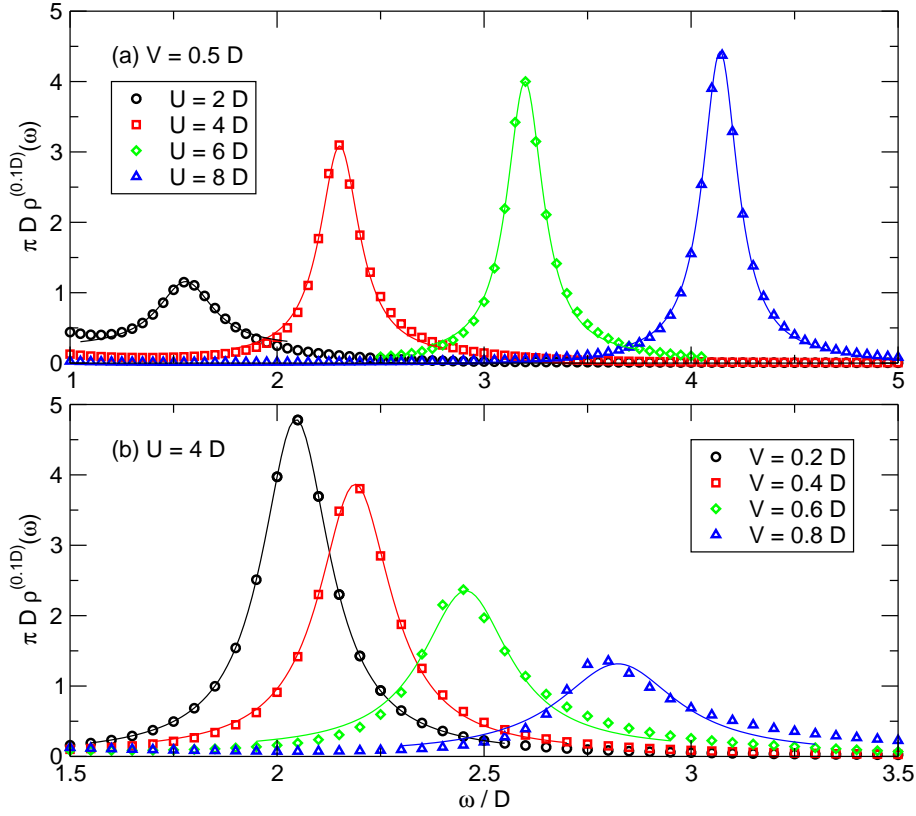


Figure 4.5: D-DMRG data of the upper Hubbard satellite at $\eta = 0.1D$. Thin lines are fits with Lorentzians and an offset $\propto \eta_{\text{eff}}/(\eta_{\text{eff}}^2 + (\omega - \omega_{\text{up}})^2) + C$. The fits were done for the intervals shown. (a) dependence on U at constant V ($N_f = 80$); (b) dependence on V at constant U ($N_f = 40$).

large values of U ($U > 4D$) are found from results for $\rho(\omega)$ where we extracted only the behavior at low energies. To determine the HWHM it is not necessary to know the whole line shape. It is an asset of the LB extraction scheme that it allows also to determine only a part of the whole curve. In conclusion, Fig. 4.4 demonstrates that the dynamic DMRG is able to reproduce the low energy scale of the SIAM over two orders of magnitude.

4.5 Hubbard satellites

4.5.1 Broadened data

To investigate the line shapes of the satellites we plot them for various values of U and V in Fig. 4.5. The ASR at $\omega = 0$ is not displayed since it is too much smeared out at $\eta = 0.1D$ for larger values of the interaction. The shifts δ_{shift} increase on increasing V ; they decrease

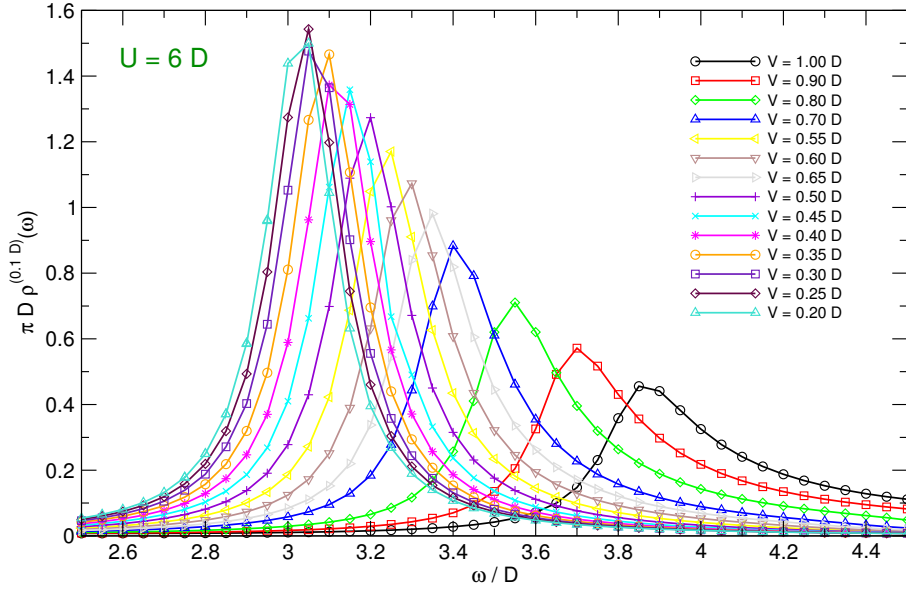


Figure 4.6: D-DMRG data of the upper Hubbard satellite at $\eta = 0.1D$ for $U = 6D$, cf. Fig. 4.5b.

on growing interaction U . The widths behave qualitatively similar. A complete FFT deconvolution suffers unfortunately from severe overshooting due to the sharpness of the resonance. To make the analysis nonetheless quantitative we fit the broadened data by Lorentzians plus an offset (Fig. 4.5 and Fig. 4.6). These fits work very well for large values of U and not too large values of V . To deduce the true width of the Hubbard satellite we assume that it is well described by a Lorentzian. The width η_{eff} of the convolution of two Lorentzians of widths η_1 and η_2 is $\eta_{\text{eff}} = \eta_1 + \eta_2$. From the effective widths η_{eff} we deduce the true half-widths at half-maximum (HWHM) of the Hubbard satellite by subtracting the artificial broadening η , i. e., $\text{HWHM} = \eta_{\text{eff}} - \eta$. In Fig. 4.7, the widths are depicted as function of U and of V . The results show that the HWHM are proportional to V^4/U^2 . The deviations for smaller widths must be attributed to the numerical constraints, e. g., finite η and finite chain length N_f . The deviations for larger widths, mainly for larger values of V and smaller values of U result from the vicinity of the bare bands. Fig. 4.8 displays the analogous analysis for the shifts δ_{shift} of the satellite positions. Again, strong evidence for power law behavior is found, namely $\delta_{\text{shift}} \propto V^2/U$.

How can the above findings be understood? Let us start by the positions. The energy levels of isolated impurities, i. e., $V = 0$ are at $\pm U/2$ [Sch66]. Switching on V mixes the impurity levels with the bath states which lie in the interval $[-D, D]$. If U is large compared to D second order perturbation in V implies that the impurity levels are repelled from the bath states. The shift should be of the order of J , see Eq. (11) in

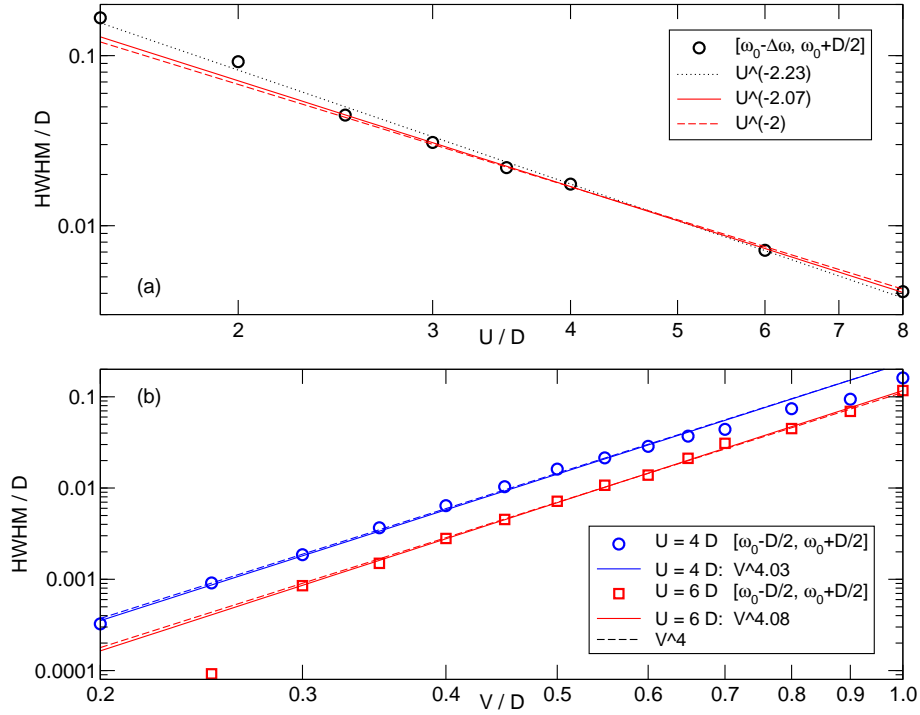


Figure 4.7: Widths (symbols) of the Hubbard satellites as found from the fits in Fig. 4.5. The fit intervals are given in the legend. The lines show various power law fits. (a) dependence on U at $V = D/2$; (b) dependence on V .

Ref. [Sch66]. The coupling constant J of the antiferromagnetic s-d exchange interaction in the Schrieffer-Wolff limit of the SIAM is given by

$$J = -V^2 \frac{U}{-U/2(-U/2+U)} = \frac{4V^2}{U} \quad (4.4)$$

which is gained by inserting $\varepsilon_d = -U/2$ in Eq. (1.12). The shift dependence $\delta_{\text{shift}} \propto V^2/U$ agrees nicely with the power laws in Fig. 4.8.

The widths of the satellites have been discussed quantitatively when they lie within the bare band [Log98]. If the satellites lie outside, perturbation theory in U , to second order or the random phase approximation, implies that a finite width is to be expected at least for $U < 6D$. But the reasoning in powers of U is not helpful for $U > 6D$ and it does not explain the power laws found. So we return to perturbing in powers of V . The impurity levels mix with particle-hole excitations in the bands, see Eq. (10a) in Ref. [Sch66]. In the *symmetric* case the doubly occupied electron and hole state are degenerate so that mixing with particle-particle (or hole-hole) states matters also, see Eq. (12) in Ref. [Sch66]. The mixing is of order $J = 4V^2/U$. So Fermi's golden rule implies a lifetime of $J^2 N_0$ where N_0

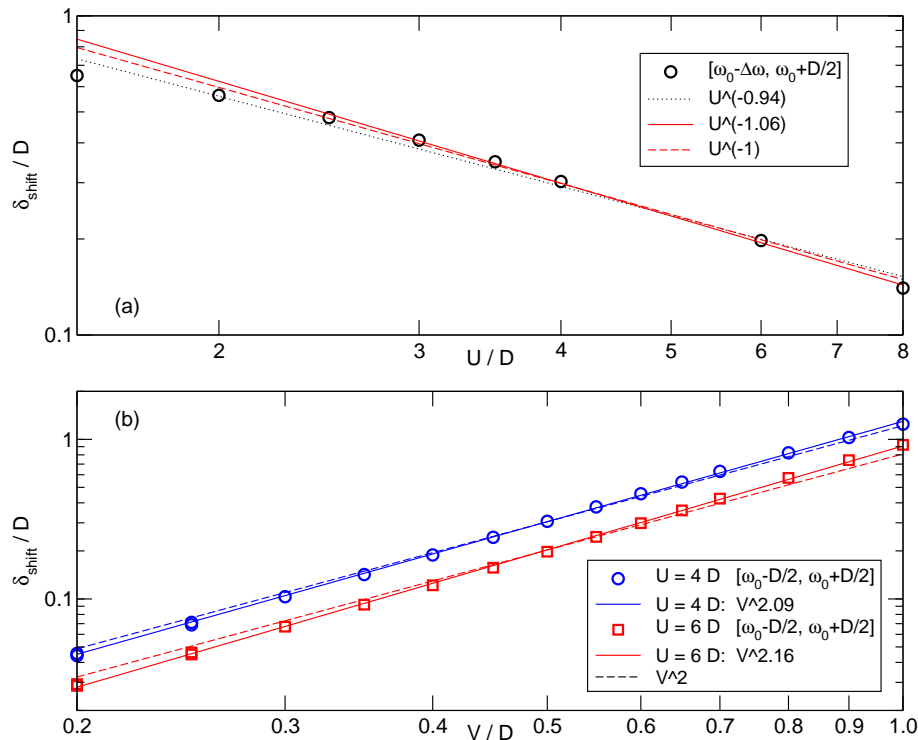


Figure 4.8: Position shifts of the Hubbard satellites analyzed like the widths in Fig. 4.7; (a) $V = D/2$; (b) see legend.

measures the density of states with which the impurity level mixes; N_0 is of the order of D^{-1} . Indeed, $\text{HWHM} \propto J^2$ explains conclusively the data of Fig. 4.7.

In summary, we have investigated the dynamic propagator of the SIAM by D-DMRG. This powerful large-scale algorithm provides information with a constant energy resolution. Up to moderate interactions $U \approx 2D$, FFT deconvolution yields the explicit spectral densities. For larger interactions, the width of sharp resonances can be extracted by fitting Lorentzians. In particular, we analyzed the positions and widths of the Hubbard satellites. The shifts are of order V^2/U due to level repulsion; the line widths are of order V^4/U^2 .

So far, the width of the Hubbard satellites for $U > 2D$ was extracted under the assumption that the satellites are Lorentzians. We present a further investigation of the line shape in the next section. Numerically, improvements of the resolution are necessary to determine the line shape of the satellites explicitly and an improved deconvolution scheme has to be used. Analytically, the quantitative argument for the widths must be supplemented by an explicit calculation of the line shapes for $V^2/U \rightarrow 0$.

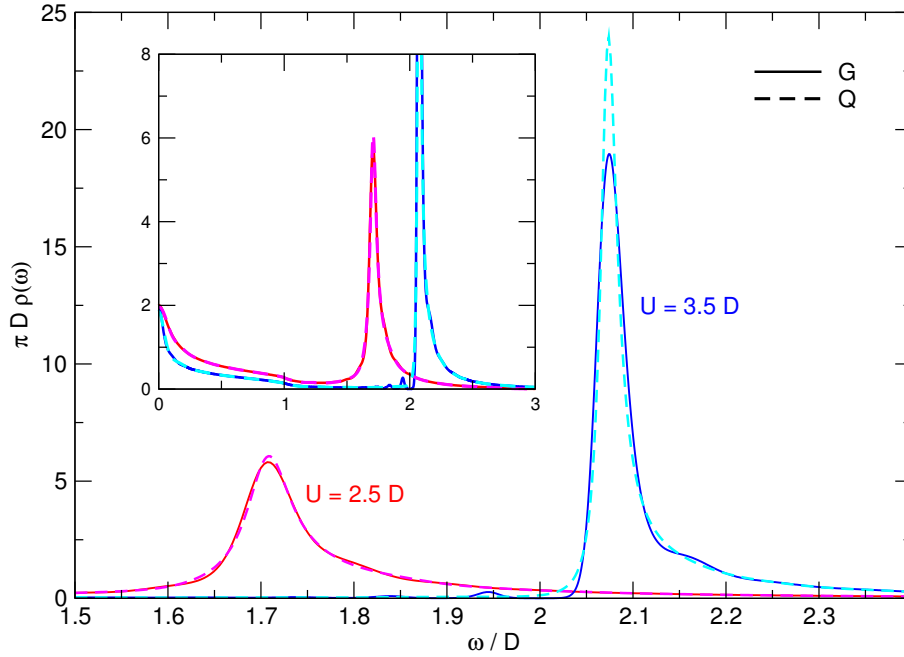


Figure 4.9: Upper Hubbard satellite for two values of the interaction U obtained from D-DMRG raw data ($V = D/2$, $\eta = 0.1D$, $m = 256$; G calculation shown as straight lines: $\Delta\xi = 0.05D$, $N_f = 120$; Q calculation shown as dashed lines: $\Delta\xi = 0.1D$, $N_f = 200$) processed by the LB scheme. The inset shows the spectrum on a larger scale. At larger U a strongly asymmetric line shape occurs.

4.5.2 Deconvolved data

In this section we show that the D-DMRG combined with the powerful LB scheme allows to resolve features at high energies which so far eluded a quantitative determination. The calculation of the line shapes of energy levels at high energies represents a new field of applications since previous methods are not suited to perform such computations. An exception are features at high energies which can be understood and described as shifted low energy features [Hel05]. We emphasize that the progress in the manipulation of quantum dots by optical means has brought the measurements of high energy features within reach, see e. g. Refs. [War00] and [Kar04a].

In the [previous section](#), we have shown that the Hubbard satellites at about $\omega = \pm U/2$ become increasingly sharp once the interaction U is larger than the bandwidth $W = 2D$. We were, however, not able to resolve the sharp Hubbard satellites since the deconvolution by Fourier transform was not powerful enough to do so, see [Chapt. 3](#). By means of the LB extraction we are now able to address the line shape. In [Fig. 4.9](#) the results for a moderate value of U ($2.5D$) and for a larger value of U ($3.5D$) are shown. While the

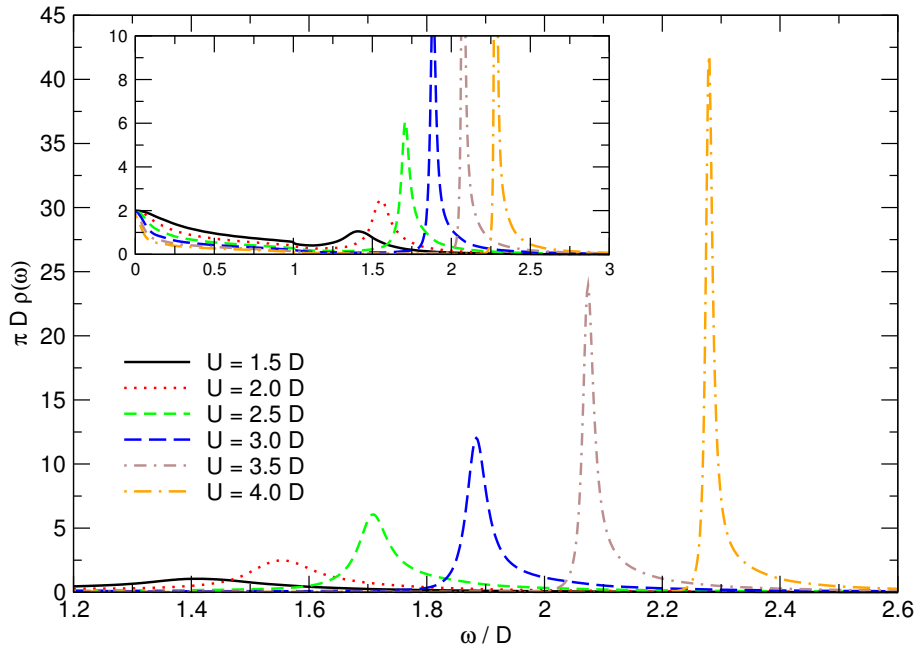


Figure 4.10: Upper Hubbard satellite for various values of the interaction U obtained from D-DMRG raw data (Q calculation, $V = D/2$, $\eta = 0.1D$, $m = 256$, $\Delta\xi = 0.1D$, $N_f = 200$) processed by the LB scheme. The inset shows the spectrum on a larger scale.

line at $U = 2.5D$ is still fairly symmetric (cf. also the line for $U = 2D$ in Fig. 4.1) the line at $U = 3.5D$ has a clear asymmetric shape. The rise at the low energy side is rather abrupt and steep while the decrease at the high energy side is much more gentle and slow. The peak is very pronounced and the maximum value very high. We performed our calculations using a direct calculation of the local propagator (G) and by means of the “improper” self-energy (Q), see Sect. 1.6.4.

Let us first look at the results obtained via the Green function. The small bumps left of the peak are artefacts of the data extraction similar to the small dip in front of the uprise in Fig. 3.3. We also consider the shoulder on the right side of the peak in Fig. 4.9 to be an artefact of the data analysis in analogy to the spurious oscillations in Fig. 3.1.

The curve obtained for $U = 3.5D$ using the Q function does neither show the bumps left of the peak nor the shoulder right side of the peak. The spurious oscillations which can occur in the vicinity of sharp features in the DOS are attenuated by this alternative calculation. We used the scheme (1.100) to derive the spectral density from the Q function. This has turned out to be the optimum procedure to translate $Q(\omega + i\eta)$ into $G(\omega)$, see Ref. [Fas05]. Fig. 4.10 gives an overview of the Hubbard satellites developing for increasing U . For $U > 4D$ the D-DMRG calculations become very difficult also when using

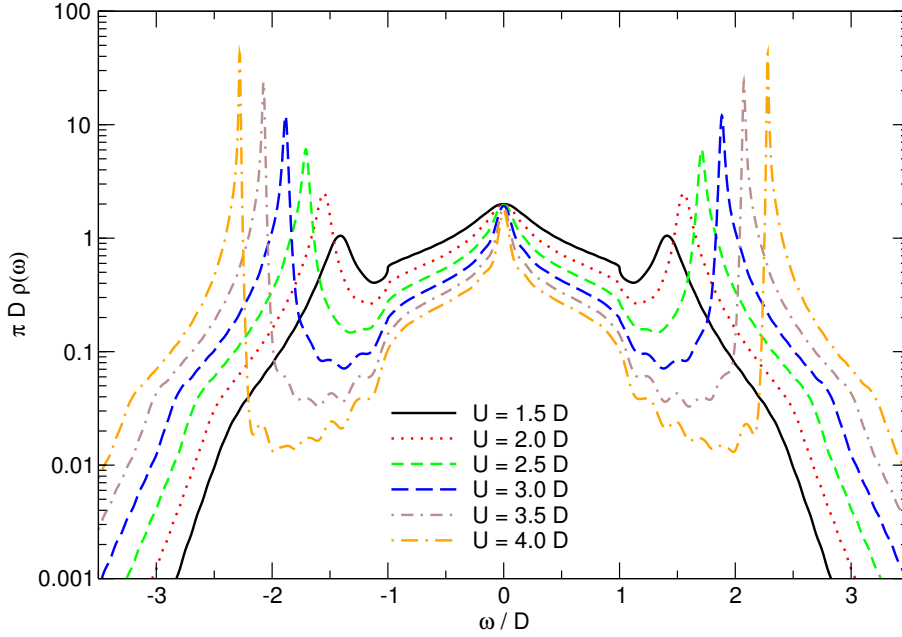


Figure 4.11: Same data set as Fig. 4.10, shown on a semi-logarithmic scale.

the Q function. Here the D-DMRG raw data lacks the accuracy necessary to deconvolve in a robust fashion. As the Hubbard satellites are already very sharp and high for $U = 4D$, we plot the data of Fig. 4.10 on a semi-logarithmic scale in Fig. 4.11. Two features are eye-catching. The typical LB oscillations are visible on the semi-logarithmic scale in the region between Kondo peak and the Hubbard satellites. The LB deconvolution has problems in reproducing the very small spectral weight in this region. This can be regarded as a minor drawback. When comparing the heights of the Hubbard satellites with the values for $\rho(\omega)$ in these intermediate regions, the relative error is negligible. The second prominent feature is the appearance of kinks at the outer side of the Hubbard satellites.

At present, we do not have an analytical description of the line shape in Figs. 4.9 and 4.10. Qualitatively, however, the following description holds. The doubly occupied level has the energy $U/2$ in the atomic limit for $V = 0$. This level is shifted to higher energies by a finite hybridization $V > 0$ [Sch66] and it is broadened (see Sect. 4.5.1). The shift $\propto V^2/U$ is due to level repulsion between the doubly occupied level and modes where the doubly occupied level excites additional particle-hole pairs. A rough, averaged description of the broadening is provided by Fermi's golden rule implying that the width is proportional to V^4/U^2 .

In view of the asymmetric line shape and of the very narrow peak this averaged picture can be improved. The narrow peak itself has a certain intrinsic width which is small. Note that the general understanding of the SIAM as a local Fermi liquid implies that there are

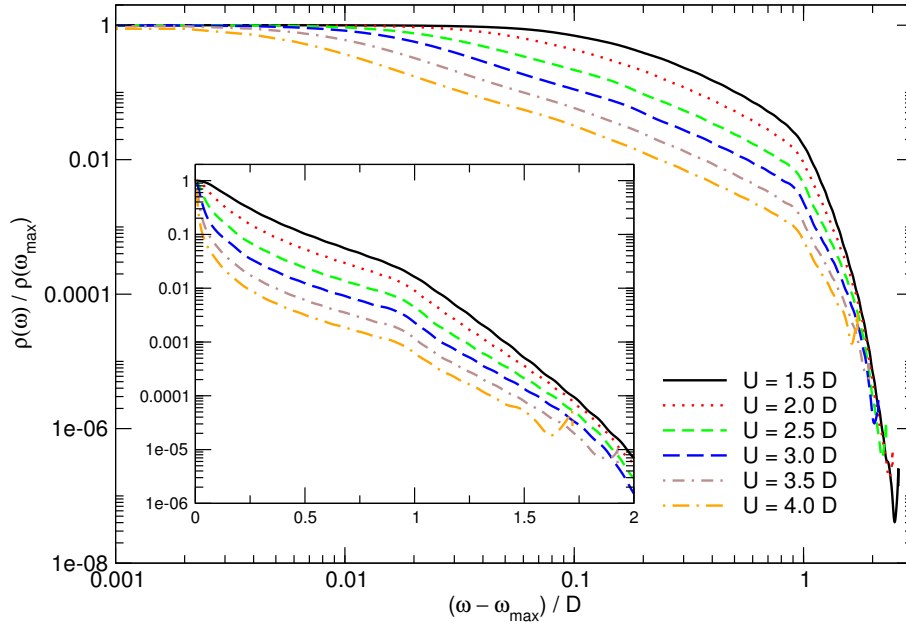


Figure 4.12: Same data set as Fig. 4.10 shown on a double-logarithmic scale in the main plot and on a semi-logarithmic scale in the inset. Frequencies shifted by the position of the Hubbard peak maximum ω_{\max} and ordinates rescaled $\rho(\omega)/\rho(\omega_{\max})$.

no singularities in the propagator. The spectral density is a smooth function though it may display very narrow features. This is in contrast to the X-ray edge problem where the added fermion is completely immobile (no recoil).

The intrinsic width of the narrow peak results from the decay of the doubly occupied level into particle-hole pairs of the local Fermi liquid. According to Fermi's golden rule such a decay can take place only if the energy of the initial and the final state is equal which means that many particle-hole pairs have to be excited in order to make up for the relatively large energy $\approx U/2$ of the double occupancy. Very many particle-hole pairs are needed in view of the reduced effective band width of the order of the Kondo energy scale T_K . This argument accounts for a finite, though very large, lifetime of the doubly occupied level as seen in Fig. 4.9.

The high energy tail of the line in Fig. 4.9 can be understood as an effect of particle-hole pairs which are generated by the double occupancy. This is *not* the same as the decay of the double occupancy described above. In the decay the double occupancy disappears in the process while it remains on generating additional particle-hole pairs. This explains why the contribution of this process is found at the high energy side of the peak in Fig. 4.9. The additional particle-hole pairs require an additional amount of energy to be created. The physics of this process is similar to the physics of the X-ray edge problem where

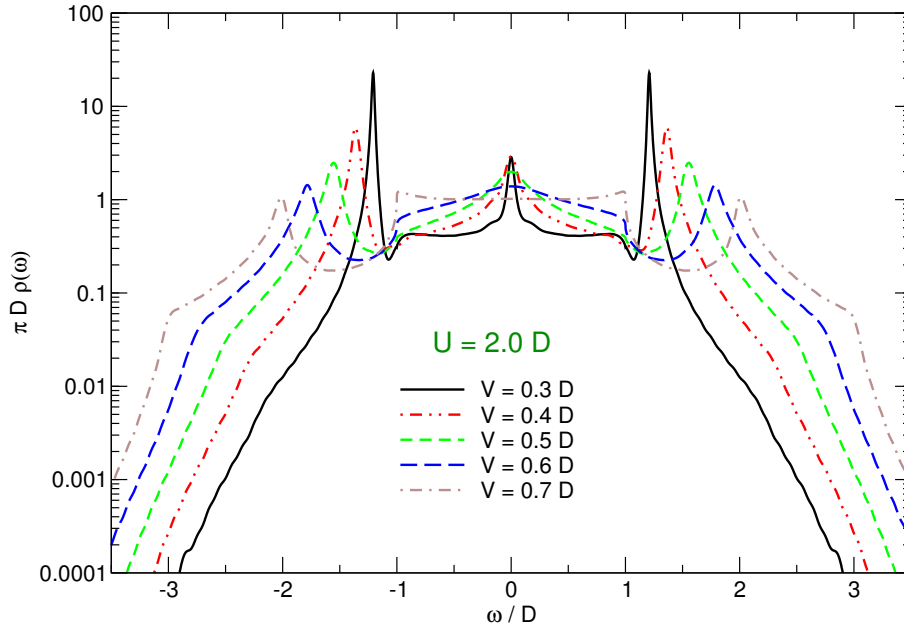


Figure 4.13: Spectral densities obtained from D-DMRG raw data ($N_f = 120$, $\eta = 0.1D$, $\Delta\xi = 0.1D$, $m = 128$) for $U = 2.0D$ and various values of the hybridization V processed by the LB scheme.

the change of a local potential induces infinitely many particle-hole pairs thus leading to slowly decreasing tails in the spectra, see for instance Ref. [Sch69] and references therein. The main difference to the X-ray edge problem is that there is no true singularity here so that the line shape is smoother.

At present, the accuracy of the data in the high energy tails is not sufficient to search for approximate power laws which possibly describe the tails of the Hubbard satellites in Figs. 4.9 and 4.10. This becomes apparent from Fig. 4.12. The figure shows the data of Fig. 4.10 shifted in frequencies by the position of the Hubbard satellites maximum ω_{\max} . We also rescaled the ordinates by plotting $\rho(\omega)/\rho(\omega_{\max})$ rather than $\pi D\rho(\omega)$ which makes the curves for the various U values easier to distinguish. The possible approximate power laws describing the tails of the satellites cannot be identified from the figure. Further investigations are called for, regarding as well the accuracy of the D-DMRG data as theoretical predictions for the expected behavior of the tails. It is apparent from Fig. 4.12 that the kinks at the outer side of the Hubbard peaks are located approximately at $\omega_{\max}(U) + D$ (for the upper Hubbard peak, $\omega > 0$).

Let us have a close look at these kinks. By using hybridizations V differing from $D/2$ we can change the shape of the free Green function, see Sect. 1.5. By enlarging V from $D/2$ to nearly $D/\sqrt{2} \approx 0.707D$, we can make the band edges more and more singular, see Fig. 1.5. Fig. 4.13 shows for $U = 2D$ the D-DMRG results for hybridizations between

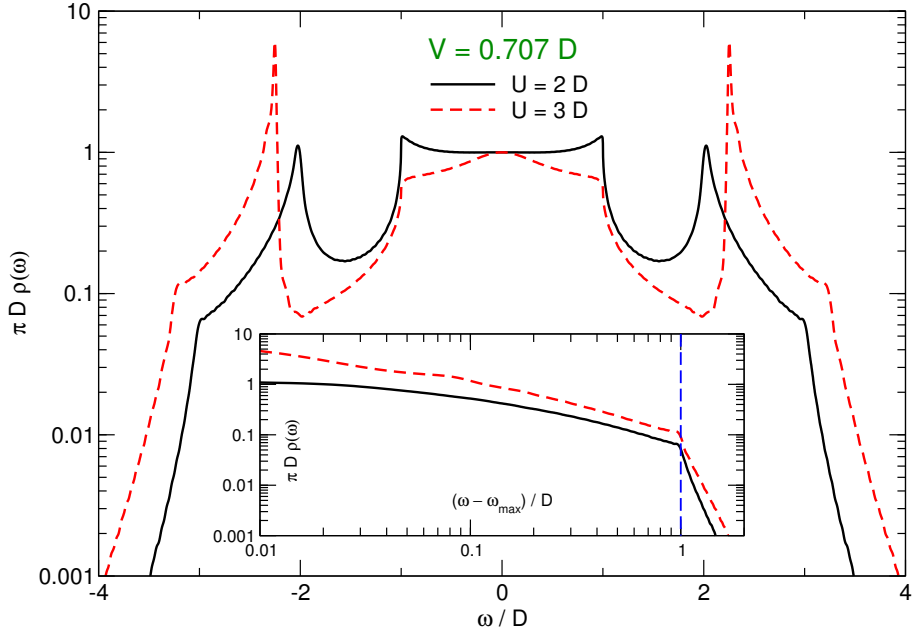


Figure 4.14: Spectral densities obtained from D-DMRG raw data ($N_f = 120$, $\eta = 0.1D$, $\Delta\xi = 0.1D$, $m = 256$) for $U = 2D$ and $U = 3D$ and hybridization $V = 0.707D$ processed by the LB scheme. The inset shows the spectral densities shifted by ω_{\max} on a double-logarithmic scale.

$V = 0.3D$ and $V = 0.7D$. Indeed, the kink at $\omega_{\max}(U) + D$ is intensified by enlarging V . Using the extreme value of $V = 0.707D \lesssim D/\sqrt{2}$, we show in **Fig. 4.14** the D-DMRG results for $U = 2D$ and $U = 3D$. From the inset (frequencies shifted by ω_{\max} , see above) we find again that the kinks are at frequencies $\omega_{\max} + D$. They are much more prominent for $V = 0.707D$ than for $V = 0.5D$, see **Fig. 4.12**. Also **Fig. 4.14** does not provide a clear indication for a possible power law in the region $\omega_{\max} < \omega < \omega_{\max} + D$ for $\omega > 0$. We have to leave this aspect open for future work.

To our knowledge, numerically exact results like those obtained for the line shape of the Hubbard satellites at $\omega = \pm U/2$ beyond the region of the bare band $\omega \in [-D, D]$ are not available in the literature. Especially the sharpness of Hubbard peaks is missed by other zero temperature algorithms for the SIAM. By these line shapes we extended our analysis of the Hubbard satellites based on broadened D-DMRG raw data, cf. **Sect. 4.5.1**. Furthermore, these line shapes illustrate that the dynamic density-matrix renormalization is suited to provide high resolution data at high energies, i. e. away from the Fermi level. It is to be expected that such information will become more and more important as the experimental techniques are improving. Hence the D-DMRG is a very valuable complementary tool. Position and width of the Hubbard satellites are important for several widely used applications, e. g., in the self-consistency cycle of the DMFT.

5 Results for the $d = \infty$ Hubbard model on a Bethe lattice

A high-resolution investigation of the electron spectra close to the metal-to-insulator transition in dynamic mean-field theory is presented [Kar04b, Kar05]. The all-numerical, consistent confirmation of a smooth transition at zero temperature is provided. In particular, the separation of energy scales is verified. Unexpectedly, sharp peaks at the inner Hubbard band edges occur in the metallic regime. They are signatures of the important interaction between single-particle excitations and collective modes.

5.1 Introduction

The interplay of electronic degrees of freedom with collective modes is one of the central issues in current condensed matter physics. It is particularly intriguing when the collective modes are formed by the electrons themselves due to strong interactions. Famous examples for the complexity of such systems are the high-temperature superconductors, see e. g. Refs. [Nor03, Dem04], and materials displaying colossal magnetoresistance, see e. g. Refs. [Ima98, Tok00].

We focus on charge and spin degrees of freedom by considering a narrow single-band model with nearest-neighbor hopping t where the interaction U stems from the Coulomb repulsion. For simplicity, we study the half-filled case with one electron per site. Thus the minimal model is the Hubbard model

$$\mathcal{H} = -t \sum_{\langle i,j \rangle; \sigma} c_{i,\sigma}^\dagger c_{j,\sigma} + U \sum_i (n_{i,\uparrow} - 1/2) (n_{i,\downarrow} - 1/2) \quad (5.1)$$

where i, j denote sites on a lattice with $\langle i, j \rangle$ being nearest neighbors, $\sigma \in \{\uparrow, \downarrow\}$ the spin and $c_{i,\sigma}^{(\dagger)}$ the electron annihilation (creation) and $n_{i,\sigma}$ their density.

Leaving aside all effects of long-range order like charge or spin density waves the system is metallic for weak interaction and insulating for strong interaction. The weakly interacting system does not have significant effects of collective modes because they are overdamped by Landau damping. The strongly interacting system is a paramagnetic insu-

lator governed at low energies by the collective modes which are the magnetic excitations. The charge modes display a large gap of the order of U . Thus charge and collective modes are well separated in energy so that no significant interplay is to be expected. Hence, the regime *close* to the transition between the metal and the insulator is the most likely to be influenced by the interplay of single-particle and collective excitations.

An estimate shows that the two-dimensional (2D) superconducting cuprates are indeed close to the metal-insulator transition. The magnetic coupling J is approximately given by $4t^2/U$; empirically, one has $J \approx t/3$ so that $U/W \approx 1.5$ where $W = 8t$ is the band width in 2D. This can be compared to the value of about $U/W \approx 1.2$ where the paramagnetic insulating phase becomes unstable due to closing of the charge gap [Rei04].

It is the aim of the present work to provide evidence that a generic paramagnetic system with values of U/W in the range 1 to 1.5 constitutes a highly correlated metal with significant interplay between single-particle and collective modes. Since a controlled treatment of finite dimensional systems other than the one-dimensional chain is not possible we study the Hubbard model on the Bethe lattice with infinite coordination number $z \rightarrow \infty$.

At low, but finite, temperatures T the phase transition between metal and insulator is of first order [Geo96] and takes place at $U_c(T)$ [Ton02, Blü03] between $U_{c,1}(T)$ (instability of the insulator against infinitesimal changes in amplitude) and $U_{c,2}(T)$ (instability of the metal). At $T = 0$, the transition has peculiar properties [Zha93, Kot99, Bul99, Pot03]. It bears features from first order transitions: a jump in the entropy and a finite hysteresis between $U_{c,1} := U_{c,1}(T = 0)$ and $U_{c,2} := U_{c,2}(T = 0)$. But there are also second order features because $U_c := U_c(T = 0) = U_{c,2}$ where the quasi-particle weight vanishes continuously and the ground state energy $E(U)$ changes differentiably. The behavior of $E(U)$ is derived from a projective DMFT [Mö195] which is based on the hypothesis that the energetically high-lying spectral features do not change at the transition from the metallic to the insulating solution (separation of energy scales).

There are many determinations of $U_{c,1}$ and $U_{c,2}$. They (almost) agree on $(2.39 \pm 0.02)D$ for $U_{c,1}$ [Bul01, Blü05b, Gar04] with the outlier of $(2.225 \pm 0.025)D$ [Nis04a]. For $U_{c,2}$ the values range from $2.92D$ to $3.0D$ [Mö195, Bul99, Bul00b, Bul01, Gar04, Blü05a]. The spectral densities $\rho(\omega) := -\pi^{-1} \Im G(\omega)$ (DOS) display a quasi-particle peak at $\omega = 0$ in the metallic solution which is pinned to its non-interacting value $\rho_0(0)$. But its width decreases on $U \rightarrow U_{c,2}$ [Zha93, Mö195, Bul99, Gar04]. The insulating solutions display the lower and the upper Hubbard bands which merge for $U \rightarrow U_{c,1}$ when the single-particle gap Δ closes [Zha93, Bul01, Nis04a, Gar04].

5.2 D-DMRG as impurity solver in a DMFT framework

Recent progress in the numerical calculation of dynamic quantities for quantum impurity models, cf. [Geb03, Raa04, Nis04b, Raa05] and [Chapt. 4](#), by dynamic density-matrix renormalization (D-DMRG, cf. [Hal95, Ram97, Küh99b] and [Sect. 2.2](#)) make calculations possible with well-controlled resolution at all energies. Thereby, spectral functions and ground state energies become accessible which so far eluded a quantitative determination. With the correction vector method, cf. [Sect. 2.2.3](#), we compute $\rho(\omega)$ broadened (convolved) by Lorentzians of width $\eta \in [0.01, 0.1]D$. The unbroadened $\rho(\omega)$ is retrieved by least-bias (LB) deconvolution, cf. [Raa05] and [Sect. 3.3](#). It is used to determine the continued fraction of the bath function in the next iteration of the DMFT self-consistency cycle [Geo96]. The LB deconvolution provides a positive and continuous ansatz for the spectral density with the least possible bias. Positivity is important in the robust implementation of the DMFT self-consistency conditions as non-causal artefacts in $\Im G(\omega)$ are absent. For all U about 20 iterations were performed till two subsequent $\rho(\omega)$ differ less than $\approx 10^{-3}/D$ everywhere *and* the ground state energy and the double occupancy differ less than $10^{-2}\%$. For the insulator, it is required in addition that the static gap, derived from energy differences of the finite bath representation, differs less than 1%.

The D-DMRG is performed with 128 or 256 states in the projected DMRG basis. We use 120, 160, or 240 fermionic sites in the metallic regime (one for the impurity site, the rest representing the bath). An odd number of sites implies a pole at $\omega = 0$ in $\rho_0(\omega)$. This pole is split by the interaction. The splitting results from a pole in $\Sigma(\omega)$ at $\omega = 0$. Such a solution is insulating. Hence an odd number of sites is slightly biased towards an insulator. Vice versa an even number of sites leads to a $\Im \Sigma(0) = 0$ implying a small bias towards the metallic solution. The relative bias is estimated by the inverse number of sites: 4 to $8 \cdot 10^{-3}$. In odd chains, we observe two almost degenerate ground states (spin \uparrow or \downarrow at the interacting site) which must be considered both. Otherwise a spurious magnetic moment is generated. If we find a ground state $|1\rangle$ with energy E_1 using a standard Lanczos or Davidson algorithm starting from an initial guess $|I_1\rangle$, the degenerate counterpart $|2\rangle$ with $E_2 = E_1$ is easily calculated starting from a new initial vector $|I_2\rangle = |I_1\rangle - \langle I_2|1\rangle|1\rangle$. The state $|0\rangle = \alpha_1|1\rangle + \alpha_2|2\rangle$ with appropriate α_1 and α_2 is again normalized $\langle 0|0\rangle = 1$, has energy $E_0 = E_1 = E_2$ and restores

$$\langle 0 | d_\sigma d_\sigma^\dagger | 0 \rangle = 1/2 \quad (5.2)$$

for $\sigma = \{\uparrow, \downarrow\}$.

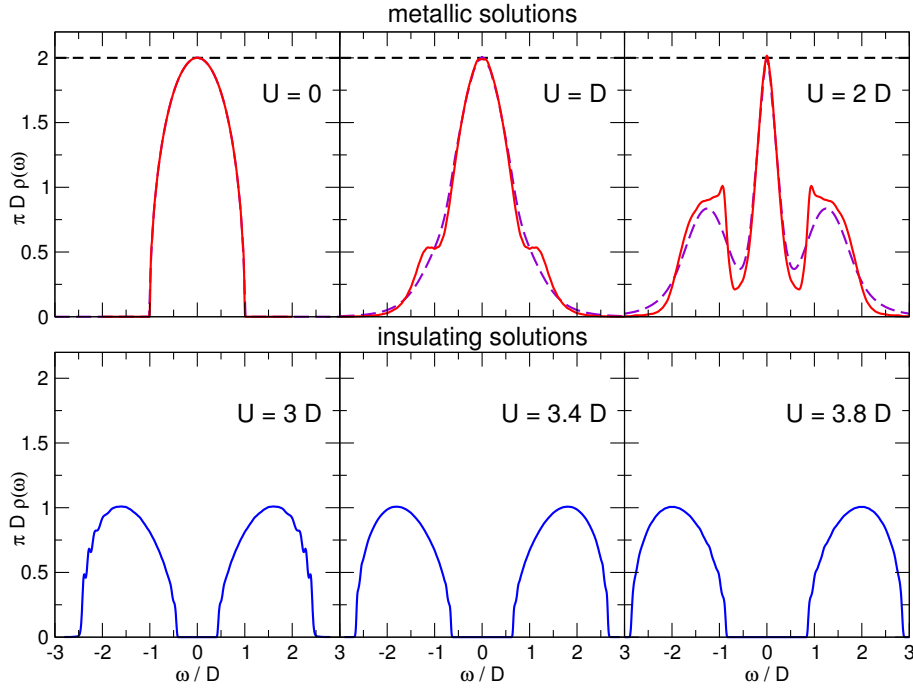


Figure 5.1: Spectral densities $\rho(\omega)$ deep in the metallic (upper row) and deep in the insulating regime (lower row) in DMFT for the Bethe lattice at $T = 0$; dashed lines: NRG data [Bul04a].

5.3 Results

In Figs. 5.1 and 5.2, our results for metallic and insulating $\rho(\omega)$ are shown. In the metallic solutions, the narrowing of the quasi-particle band around $\omega = 0$ is clearly visible. From $U \approx D$ on, the DOS displays side features which develop into the lower and upper Hubbard band. At $U \approx 2D$ the Hubbard bands are well separated from the quasi-particle peak at $\omega = 0$ by a precursor of the gap Δ in the insulator: a pseudo-gap. The comparison with the NRG data from Ref. [Bul99] shows good agreement in the quasi-particle peak but deviations in the Hubbard bands. There the DMRG data is much sharper and does not have significant tails at higher energies. This difference stems from the broadening proportional to the frequency which is inherent to the NRG algorithm [Geb03, Raa04].

The insulating solutions display the lower and the upper Hubbard bands clearly. They agree excellently with the perturbative result (not shown) [Eas03] for $U \gtrsim 3D$. At $U = U_{c,1} = (2.38 \pm 0.02)D$ both bands touch each other. No upturn in $\rho(\omega)$ as in Ref. [Nis04a] is found when we consider the deconvolved $\rho(\omega)$ for all ω . An upturn occurs only if the *static* gap is used. But such a procedure did not lead to stable self-consistent solutions.

In Fig. 5.3 the quasi-particle weight Z in the metal and the single-particle gap Δ in the

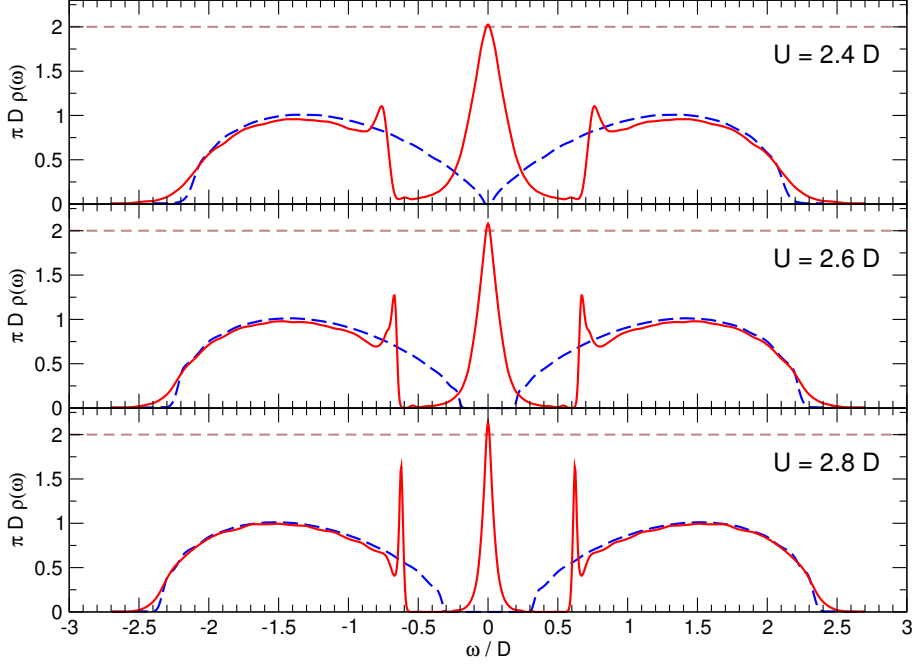


Figure 5.2: Spectral densities $\rho(\omega)$ of the metallic (solid) and the insulating solution (dashed) between $U_{c,1}$ and $U_{c,2}$.

insulator are shown. The weight

$$Z = \frac{1}{1 - \partial_{\omega} \Re \Sigma(0)} \quad (5.3)$$

is found from fitting the derivative of the Dyson equation

$$G(\omega) = G_0(\omega - \Sigma(\omega)) \quad (5.4)$$

implying

$$\frac{1}{Z} = \frac{D^2 \partial_{\omega} G(0)}{2} \quad (5.5)$$

where $G_0(\omega)$ is the bare local Green function of the lattice. The gap Δ is found from a fit $\propto \sqrt{\omega - \Delta}$ to the sharp uprise of the DOS at the inner band edges. The DMRG data agrees excellently with the perturbative results where the respective perturbation holds. The comparison to the NRG data shows that the broader high energy features reduce Z to some extent so that the NRG weight stays below the DMRG data.

From the power law fit

$$\Delta = (U - U_{c,1})^{\zeta} [a_1 + a_2 (U - U_{c,1})] \quad (5.6)$$

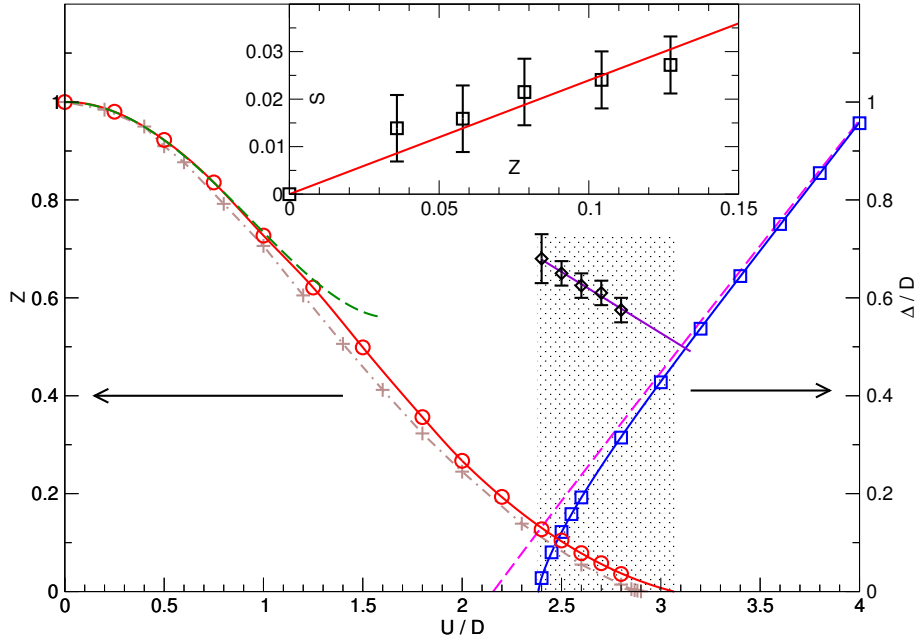


Figure 5.3: *Dotted area:* region of two solutions. *Left curves:* metallic quasi-particle weight Z ; line with circles: interpolated DMRG, line with pluses: NRG [Bul99]; dashed line: perturbation up to U^4 [Geb03]. *Right curves:* insulating gap Δ or pseudo-gap in the metal (line with diamonds); line with squares: DMRG; dashed line: perturbation up to $1/U^2$ [Eas03]. *Inset:* weight S of the peaks at inner Hubbard band edges.

shown in Fig. 5.3 we find $U_{c,1} = (2.38 \pm 0.02)D$ in perfect agreement with most of the previous results [Bul01, Blü05b, Gar04]. The exponent is found to be $\zeta = 0.72 \pm 0.05$. The value for $U_{c,2} = (3.07 \pm 0.1)D$ is determined reliably from a second order extrapolation shown in Fig. 5.3. The value of $U_{c,2}$ agrees well with the previous results [Möl95, Bul99, Bul00b, Bul01, Gar04, Blü05a]. We attribute the small deviation to the enhanced accuracy of our D-DMRG algorithm.

Fig. 5.2 nicely shows the evolution of the metallic and the insulating $\rho(\omega)$ between $U_{c,1}$ and $U_{c,2}$. It represents the first all-numerical high-precision confirmation of the hypothesis of the separation of energy scales. Clearly, the metallic Hubbard bands at higher energies approach the insulating ones for $U \rightarrow U_{c,2}$. Differences remain at the inner band edges and around $\omega = 0$ as long as $U < U_{c,2}$. The frequency of the sharp uprise in $\rho(\omega)$ at the inner edges in the metallic solutions defines the pseudo-gap. Its evolution (Fig. 5.2) shows that it tends to the insulating gap at $U = U_{c,2}$. This corroborates strongly that the metallic $\rho(\omega)$ approaches the insulating $\rho(\omega)$ for $U \rightarrow U_{c,2}$. Remarkably, the metal and the insulator have the same single-particle correlations at $U = U_{c,2}$, which is again a feature of a second order phase transition.

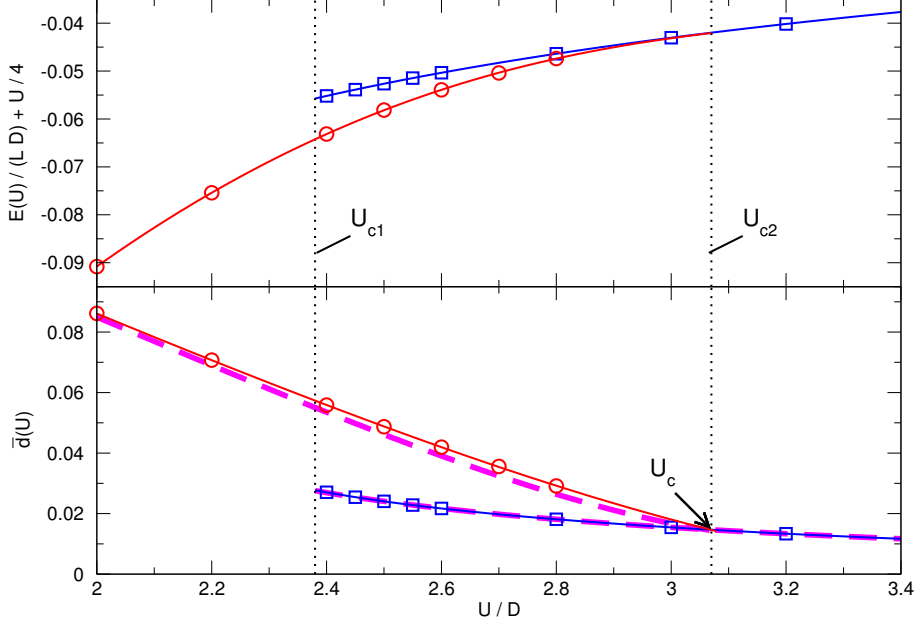


Figure 5.4: *Upper panel:* ground state energy $E(U)$ in the insulator (squares) and in the metal (circles). *Lower panel:* corresponding double occupancy $\bar{d}(U)$. At $U_c = (3.07 \pm 0.04)D$ the double occupancies intersect. The dashed lines depict the derivative of the interpolations for $E(U)$.

From equations of motion [Nis04a] one obtains the ground state energy per site

$$\frac{E(U)}{L} = \sum_{\sigma} \left\langle c_{i,\sigma}^{\dagger} \left[c_{i,\sigma}, \mathcal{H} \right] \right\rangle - U (\bar{d}(U) - 1/4) \quad (5.7)$$

where $\bar{d}(U)$ is the double occupancy $\langle n_{i,\uparrow} n_{i,\downarrow} \rangle$. All the local expectation values are computed directly at the interaction site of the SIAM at self-consistency. Then they equal the local expectation values on the lattice. In Fig. 5.4, $E(U)$ and $\bar{d}(U)$ are depicted. The equality of $\bar{d}(U)$ in the SIAM [data points and interpolations (solid lines)] and in the lattice, obtained from $\bar{d}(U) = \partial_U E + 1/4$ (dashed lines), is a very sensitive check of the data quality. It is perfectly fulfilled in the insulator (difference $\lesssim 2 \cdot 10^{-4}$). The comparison of energies after integrating $\bar{d}(U)$ for $U \in [2.4, 4.0]D$ as in Ref. [Nis04a] shows agreement within $8 \cdot 10^{-6}D$. In the metal, our check for $\bar{d}(U)$ works very well, but not perfectly (difference $\lesssim 3 \cdot 10^{-3}$). The remaining deviation is a finite-size effect of the bath because the deviation decreases on increasing the number of fermionic sites.

Assuming a differentiable behavior of $E(U)$ we deduce the critical interaction $U_c = (3.07 \pm 0.04)D$ from the intersection of the double occupancies. The corresponding metallic and insulating energies differ less than $10^{-4}D$. This justifies the assumption

of differentiability *a posteriori*. The agreement of U_c and $U_{c,2}$ in our numerical treatment proves the consistency of our data. Thereby, the previously proposed scenario [Zha93, Möl95, Kot99] for the metal-insulator transition is numerically confirmed.

An unexpected feature in our metallic solution are the sharp peaks at the inner edges of the Hubbard bands, see Fig. 5.2 and Fig. 5.1 for $U = 2D$. The only previous evidence for similar features were weak shoulders in NRG [Bul99] and QMC data [Blü03]. Based on the following arguments we interpret it as the signature of a collective mode.

Since the sharp peaks occur only in the metal the heavy quasi-particles must be involved. But the peaks are located at relatively high energies compared to the quasi-particle band. So a binding or antibinding phenomenon with something else must take place. Since the peaks are very sharp (to numerical accuracy for $U \gtrsim 2.6D$) we conclude that an immobile, local mode is involved. Spin excitations like spin waves are the best-known collective excitations in Hubbard systems. In infinite dimensions, they are indeed dispersionless [Kle95]. In absence of any magnetic order they are located at zero energy in the insulator because the Hartree term vanishes [MH89a]. By continuity, we deduce that their energy is very low also in the metal with an estimated upper bound of $0.2D$ deduced from the energy of a spin wave in the long-range ordered Néel state which is $zJ/2 \approx D^2/(2U) \approx 0.2D$ at $U = 2.5D$. Hence, we conclude from the energy of the sharp features that it signals the *antibound* state or resonance of a heavy quasi-particle with a collective spin excitation. We refer to this state as antipolaron.

In the inset of Fig. 5.3 we plot the weight S of the antipolaron peak as function of Z . The error bars result from the numerical difficulty to resolve this sharp feature and from the analytical difficulty to separate it from the background of the Hubbard bands. For the separation, we fitted an approximate square root onset starting at the pseudo-gap, multiplied with a quadratic polynomial, to the Hubbard bands. The excess weight S is attributed to the antipolaron peak. From the inset in Fig. 5.3 we conclude that S vanishes linearly with Z , rather than quadratically or cubically. Thus the antipolaron peak vanishes proportional to the matrix element of a *single* quasi-particle. If S had vanished quadratically (cubically) one would have concluded that two (three) quasi-particles would be involved. The linear dependence of S on Z corroborates the scenario of an antibound state formed from one quasi-particle and one collective mode. Surely, further investigations are called for.

We point out that the antibinding between the heavy quasi-particles and the collective magnetic modes suggests an interesting answer to the so far open question why the metal forms Hubbard bands and eventually becomes insulating. The weight close to the Fermi level is pushed away to higher energies by a strong repulsive interaction between the low-lying quasi-particles and magnetic modes. Note that this scenario is also applicable in finite dimensions if the finite dispersion of the collective modes is accounted for.

In summary, we provided the all-numerical confirmation of the metal-insulator transi-

tion proposed earlier [Zha93, Möl95, Kot99] on the basis of the hypothesis of the separation of energy scales. We found that the spectral density of the metal approaches the one of the insulator for $U \rightarrow U_{c,2}$. The critical interactions $U_{c,1} = (2.38 \pm 0.02)D$ and $U_{c,2} = (3.07 \pm 0.1)D$ were found; the latter value coincides with $U_c = (3.07 \pm 0.04)D$ where the ground state energies $E(U)$ intersect differentiably. Hence, a consistent picture of a differentiable $E(U)$ emerged.

The unprecedented resolution of the spectral densities enabled us to detect sharp peaks at the inner Hubbard band edges. We interpreted them as antibound states or resonances formed from a heavy quasi-particle and a collective magnetic mode. The occurrence of such signatures in electron spectra opens up the interesting route to investigate the interplay of single-particle and collective excitations in photoelectron spectroscopy.

6 Summary

The computation of spectral properties is a central issue in theoretical physics. Many spectroscopic probes provide experimental information about the investigated systems. In order to understand the meaning of such data it is indispensable to be able to compute the corresponding quantities theoretically. This task is particularly demanding if the system under study is characterized by strong correlations. Then standard approaches like diagrammatic perturbation theory have difficulties to provide quantitative results.

An archetypal class of strongly correlated systems are impurity models where a small subsystem, the impurity, is coupled to a bath of degrees of freedom. The discrete levels of the impurity are broadened due to the interaction with the bath. The most fundamental fermionic representative of this class of models is the single impurity Anderson model (SIAM).

The SIAM describes a plethora of physical problems. Historically it was used for diluted magnetic impurities in metals. But it also describes the electronic transmission through quantum dots. The smallness of the quantum dot implies a small capacitance, hence a large charging energy which represents the interaction energy U . The bath is given by the external leads. The dynamic mean-field theory (DMFT) represents another broad and very active field where the SIAM occurs. In this approach, as in all mean-field approaches, the lattice problem of strongly interacting fermions is mapped onto an effective single-site problem, namely a SIAM. This SIAM is linked to the original lattice problem by a self-consistency condition. The clue is that the mean-field, the Green function of the bath, is a dynamic quantity depending on frequency.

The above examples illustrate that it is very important to be able to compute the dynamics of a SIAM in a reliable fashion. There are several numerical approaches which can be applied. Among the most prominent ones are quantum Monte Carlo (QMC) and the numerical renormalization group (NRG). Both approaches are powerful but do not have a high resolution away from the Fermi level. For QMC this is so since the dynamics is computed in imaginary time and the analytic continuation to real frequencies represents an ill-conditioned problem. Moreover, care must be taken to reach low temperatures. The NRG can be used directly at zero temperature. But it is set up to focus on the limit $\omega \rightarrow 0$. The energy levels kept are broadened by a broadening which is proportional to the frequency which implies that features at higher energies tend to be smeared out.

Method

We investigated in this thesis a third complementary numerical approach given by the dynamic density-matrix renormalization (D-DMRG). Dynamic density-matrix renormalization provides valuable numerical information on dynamic correlations by computing convolutions of the corresponding spectral densities. The dynamics at zero temperature is determined by computing the expectation values in the local propagator. This can be realized by targeting not only at the ground state and the excited state, but also at the resolvent applied to the excited state. This additional targeted state is called the correction vector. Three schemes how the correction vector can be used to determine the spectral density were discussed. The calculation of the ω -dependent correction vector is numerically extremely demanding due to the inversion of an almost singular non-hermitian matrix. We compared the performance of several iterative solvers for linear equation systems and managed to stabilize the inversion problem of the D-DMRG by using optimized algorithms. For low and intermediate frequencies complex symmetric QMR (quasi-minimal residual) with a DMRG-inspired preconditioning scheme turned out to perform best. The preconditioner is based on a pseudo-inverse of the superblock Hamilton operator gained by diagonalizing the system and environment block Hamiltonians. For high frequencies the performance of the standard conjugate gradients method (CG) was best.

Calculating the “improper” self-energy (Q -function) via DMRG and subsequent extraction of the Green function instead of directly calculating G is advantageous. Finite size effects due the rendering of the bath with finite instead of semi-infinite chains are reduced.

The main limitation of the correction vector D-DMRG is that one cannot obtain data for purely real frequencies but only for frequencies with a certain imaginary part. Hence the extraction of the behavior at purely real frequencies is one of the main problems to be solved in using the D-DMRG. We illustrated how and to which extent such data can be deconvolved to retrieve the wanted spectral densities. We discussed and compared various algorithms to achieve this extraction. The linear schemes use either Fourier transform to deconvolve the raw data or they implement an explicit matrix inversion. These schemes are linear because there is a linear relationship between the raw data and the extracted spectral density. If the structures to be resolved are not too sharp the linear schemes work well. If there are sharp structures the linear schemes are prone to lead to negative spectral densities which result from spurious oscillations. Furthermore, they can resolve the positions of sharp peaks only with the accuracy of the grid on which the raw data was computed. We presented a non-linear approach from the family of maximum entropy methods. This approach provides a continuous, positive ansatz for the wanted spectral density with the least bias (LB). Even relative abrupt changes of the spectral density can

be reproduced satisfactorily. In the vicinity of singularities spurious oscillations occur. But they do not violate the positivity of the ansatz. The least-bias ansatz can be made more robust towards small numerical inaccuracies and finite-size effects by including besides the entropy functional a χ -functional in the functional to be minimized. Thereby, one can allow for small deviations from the raw data.

Applications

We investigated the dynamic propagator of the symmetric single impurity Anderson model by D-DMRG. This powerful large-scale algorithm provides information with a constant or adaptive energy resolution.

The central peak at $\omega = 0$ is the Abrikosov-Suhl resonance (ASR). For larger U (smaller V) its width decreases rapidly so that the ASR is very difficult to resolve. We calculated the ASR to gauge the D-DMRG and to demonstrate that features at low energies can be resolved. The least-bias (LB) scheme was used to extract the real spectral density from the raw data. We were able to reproduce the low energy scale of the SIAM over two orders of magnitude.

An increase in U leads to the formation of Hubbard satellites below and above the free band. They are situated at energies $\omega_{\text{up/low}} = \pm(U/2 + \delta_{\text{shift}})$, $\delta_{\text{shift}} > 0$ and become more pronounced on increasing U in two ways. They capture more weight and they become sharper. The width of sharp resonances can be extracted by fitting Lorentzians to the broadened D-DMRG raw data. In particular, we analyzed the positions and widths of the Hubbard satellites. The shifts are of order V^2/U due to level repulsion; the line widths are of order V^4/U^2 .

By means of the LB extraction we were now able to address the line shape of the Hubbard satellites. It is found that the Hubbard satellites are strongly asymmetric. We illustrated this for the upper Hubbard satellite: the rise at the low energy side is rather abrupt and steep while the decrease at the high energy side is much more gentle and slow. The peak is very pronounced and the maximum value very high. At present, the accuracy of the data in the high energy tails is not sufficient to search for approximate power laws which possibly describe the tails of the Hubbard satellites. But we were able to resolve a generic feature in the asymmetric tails of the satellites. A kink is observed at $\pm|\omega_{\text{max}}| \pm D$ where $\pm|\omega_{\text{max}}|$ are the positions of the satellite maxima and $W = 2D$ is the bandwidth. We showed that the D-DMRG combined with the powerful LB scheme allows to resolve features at high energies which so far eluded a quantitative determination. Especially the sharpness of Hubbard peaks is missed by other zero temperature algorithms for the SIAM. The calculation of the line shapes of energy levels at high energies represents a new field of applications since previous methods are not suited to perform such computations.

We investigated the Hubbard model on the Bethe lattice with infinite coordination number by means of the dynamic mean-field theory (DMFT) using the D-DMRG as impurity solver. A high-resolution investigation of the electron spectra close to the metal-to-insulator transition in dynamic mean-field theory was presented. The all-numerical, consistent confirmation of a smooth transition at zero temperature is provided. In particular, the separation of energy scales is verified. We found that the spectral density of the metal approaches the one of the insulator for $U \rightarrow U_{c,2}$. The critical interactions $U_{c,1} = (2.38 \pm 0.02)D$ and $U_{c,2} = (3.07 \pm 0.1)D$ were found; the latter value coincides with $U_c = (3.07 \pm 0.04)D$ where the ground state energies $E(U)$ intersect differentiably. Hence, a consistent picture of a differentiable $E(U)$ emerged. The unprecedented resolution of the spectral densities enabled us to detect sharp peaks at the inner Hubbard band edges in the metallic regime. We interpreted them as antibound states or resonances formed from a heavy quasi-particle and a collective magnetic mode. The occurrence of such signatures in electron spectra opens up the interesting route to investigate the interplay of single-particle and collective excitations in photoelectron spectroscopy.

Bibliography

- [Abr64] M. ABRAMOWITZ and I. A. STEGUN. *Handbook of Mathematical Functions* (Dover Publisher, New York, 1964). [2.2.5](#)
- [Aff86] I. AFFLECK. *Universal term in the free energy at a critical point and the conformal anomaly*. *Phys. Rev. Lett.* **56**, 746 (1986). [6](#)
- [All05] J. W. ALLEN. *The Kondo Resonance in Electron Spectroscopy*. *J. Phys. Soc. Jpn.* **74**, 34–48 (2005). [1.5](#)
- [And61] P. W. ANDERSON. *Localized Magnetic States in Metals*. *Phys. Rev.* **124**(1), 41–53 (1961). [1.1](#), [1.3](#), [6](#)
- [And80] N. ANDREI. *Diagonalization of the Kondo Hamiltonian*. *Phys. Rev. Lett.* **45**, 379–382 (1980). [1.1](#)
- [And83] N. ANDREI, K. FURUYA, and J. H. LOWENSTEIN. *Solution of the Kondo Problem*. *Rev. Mod. Phys.* **55**(2), 331 (1983). [1](#)
- [And91] F. B. ANDERS, N. GREWE, and A. LOREK. *On the validity of sum rules and Fermi-liquid properties in calculations for strongly correlated electrons*. *Z. Phys. B* **83**, 75 (1991). [1.5](#), [4.2](#), [4.4](#)
- [Ani97] V. I. ANISIMOV, A. I. POTERYAEVY, M. A. KOROTINY, A. O. ANOKHINY, and G. KOTLIAR. *First-principles calculations of the electronic structure and spectra of strongly correlated systems: dynamical mean-field theory*. *J. Phys.: Condens. Matter* **9**, 7359–7367 (1997). [1.7](#)
- [Ash76] N. W. ASHCROFT and N. D. MERMIN. *Solid State Physics* (Holt-Saunders, Philadelphia, 1976). [1.1](#)
- [Avd86] L. V. AVDEEV and B.-D. DORFEL. *Finite-size corrections for the XXX anti-ferromagnet*. *J. Phys. A: Math. Gen.* **19**(1), L13 (1986). [2.1.9](#)

- [Bar94] R. BARRETT, M. BERRY, T. F. CHAN, J. DEMMEL, J. DONATO, J. DONGARRA, V. EIJKHOUT, R. POZO, C. ROMINE, and H. V. DER VORST. *Templates for the Solution of Linear Systems: Building Blocks for Iterative Methods* (SIAM, Philadelphia, PA, 1994), 2nd edn. [2.2.4](#)
- [Bat90] M. T. BATCHELOR and C. J. HAMER. *Surface energy of integrable quantum spin chains*. *J. Phys. A: Math. Gen.* **23**, 761 (1990). [2.1.9](#)
- [Bet31] H. BETHE. *Zur Theorie der Metalle. I. Eigenwerte und Eigenfunktionen der linearen Atomkette*. *Z. Phys.* **71**, 205 (1931). [2.1.9](#)
- [Bla59] A. BLANDIN and J. FRIEDEL. *Propriétés magnétiques des alliages dilués – interactions magnétiques et antiferromagnétisme dans les alliages du type métal noble-métal de transition*. *J. Phys. Radium* **20**(2-3), 160–168 (1959). [1.3](#)
- [Blö86] H. W. J. BLÖTE, J. L. CARDY, and M. P. NIGHTINGALE. *Conformal invariance, the central charge, and universal finite-size amplitudes at criticality*. *Phys. Rev. Lett.* **56**, 742 (1986). [2.1.9](#)
- [Blü02] N. BLÜMER, K. HELD, G. KELLER, and D. VOLLHARDT. *Metal-Insulator Transition and Realistic Modelling of Correlated Electron Systems*. In H. ROLLNIK and D. WOLF (Eds.), *NIC Symposium 2001*, vol. 9 of *John von Neumann Institute of Computing (NIC) series*, p. 347 (Forschungszentrum, Jülich, 2002). [1.7](#)
- [Blü03] N. BLÜMER. *Mott-Hubbard Metal-Insulator Transition and Optical Conductivity in High Dimensions*. Ph.D. thesis, Universität Augsburg (2002), Shaker Verlag, Aachen (2003). [5.1](#), [5.3](#)
- [Blü05a] N. BLÜMER and E. KALINOWSKI. *Ground state of the frustrated Hubbard model within DMFT: energetics of Mott insulator and metal from ePT and QMC*. *Physica B* **359**, 648 (2005). [5.1](#), [5.3](#)
- [Blü05b] N. BLÜMER and E. KALINOWSKI. *The Mott insulator - 10th order perturbation theory extended to infinite order using QMC*. *Phys. Rev. B* **71**, 195102 (2005). [5.1](#), [5.3](#)
- [Bul98] R. BULLA, A. C. HEWSON, and T. PRUSCHKE. *Numerical renormalization group calculations for the self-energy of the impurity Anderson model*. *J. Phys.: Condens. Matter* **10**(37), 8365–8380 (1998). [1.6.4](#), [1.6.4](#), [13](#), [4.2](#)

- [Bul99] R. BULLA. *Zero temperature metal-insulator transition in the infinite-dimensional Hubbard model*. Phys. Rev. Lett. **83**, 136 (1999). [5.1](#), [5.3](#), [5.3](#), [5.3](#), [5.3](#)
- [Bul00a] R. BULLA. *The Numerical Renormalization Group Method for correlated electrons*. In B. KRAMER (Ed.), *Advances in Solid State Physics*, vol. 40, p. 169 (Vieweg, Braunschweig, 2000). [1.6.1](#), [4.2](#)
- [Bul00b] R. BULLA and M. POTTHOFF. “*Linearized*” *Dynamical Mean-Field Theory for the Mott-Hubbard transition*. Eur. Phys. J. B **13**, 257 (2000). [5.1](#), [5.3](#)
- [Bul01] R. BULLA, T. A. COSTI, and D. VOLLHARDT. *Finite temperature numerical renormalization group study of the Mott-transition*. Phys. Rev. B **64**, 045103 (2001). [5.1](#), [5.3](#)
- [Bul04a] R. BULLA. private communication (2004). [5.1](#)
- [Bul04b] R. BULLA. *Dynamical Mean-Field Theory - from Quantum Impurity Physics to Lattice Problems*. [cond-mat/0412314](#) (2004). [1.7](#)
- [Clo62] J. DES CLOIZEAUX and J. J. PEARSON. *Spin-Wave Spectrum of the Antiferromagnetic Linear Chain*. Phys. Rev. **128**, 2131 (1962). [2.1.9](#)
- [Cos90] T. A. COSTI and A. C. HEWSON. *A New Approach to the Calculation of Spectra for Strongly Correlated Systems*. Physica B **163**, 179 (1990). [3.1](#), [4.4](#)
- [Cos94] T. A. COSTI, A. C. HEWSON, and V. ZLATIĆ. *Transport coefficients of the Anderson model via the numerical renormalization group*. J. Phys.: Condens. Matter **6**(13), 2519–2558 (1994). [1.6.1](#)
- [Cos99] T. A. COSTI. *Wilson’s Numerical Renormalization Group*. In I. PESCHEL, X. WANG, M. KAULKE, and K. HALLBERG (Eds.), *Density-Matrix Renormalization – A New Numerical Method in Physics*, vol. 528 of *Lecture Notes in Physics*, chap. I.1 (Springer, Berlin, 1999). [2.1](#)
- [Czy96] G. CZYCHOLL, A. L. KUZEMSKY, and S. WERMBTER. *New interpolative treatment of the single-impurity Anderson model*. Europhys. Lett. **34**(2), 133–138 (1996). [1.6.4](#)
- [Dal04] A. J. DALEY, C. KOLLATH, U. SCHOLLWÖCK, and G. VIDAL. *Time-dependent density-matrix renormalization-group using adaptive effective Hilbert spaces*. J. Stat. Mech.: Theor. Exp. **P04005** (2004). [10](#)

- [Dem04] E. DEMLER, W. HANKE, and S.-C. ZHANG. *SO(5) theory of antiferromagnetism and superconductivity*. Rev. Mod. Phys. **76**, 909 (2004). 5.1
- [Don70] S. DONIACH and M. ŠUNJIĆ. *Many-electron singularity in X-ray photoemission and X-ray line spectra from metals*. J. Phys. C **3**, 285–291 (1970). 3.2.1
- [Duk99] J. DUKELSKY and G. SIERRA. *A Density Matrix Renormalization Group Study of Ultrasmall Superconducting Grains*. Phys. Rev. Lett. **83**, 172 (1999). 2
- [Duk00] J. DUKELSKY and G. SIERRA. *The Crossover from the Bulk to the Few-Electron limit in Ultrasmall Metallic Grains*. Phys. Rev. B **61**, 12302 (2000). 2
- [Duk04] J. DUKELSKY and S. PITTEL. *The density matrix renormalization group for finite fermi systems*. Rep. Prog. Phys. pp. 513–552 (2004). 2
- [Eas03] M. P. EASTWOOD, F. GEBHARD, E. KALINOWSKI, S. NISHIMOTO, and R. M. NOACK. *Analytical and Numerical Treatment of the Mott-Hubbard Insulator in Infinite Dimensions*. Eur. Phys. J. B **35**, 155 (2003). 5.3, 5.3
- [Fas05] R. FASSBENDER. *Spektraldichten und Selbstenergie des Einstörstellen-Anderson-Modells mittels dynamischer Dichtematrixrenormierung* (Diplomarbeit, Universität zu Köln, 2005). 1.6.4, 4.5.2
- [Fei04] A. E. FEIGUIN and S. R. WHITE. *Time-step targetting methods for real-time dynamics using DMRG*. Phys. Rev. Lett. **93**, 076401 (2004). 10
- [Fil82] V. M. FILYOV, A. M. TSVELIK, and P. B. WIEGMANN. *Low-temperature properties of the asymmetric Anderson model. I. Symmetric case*. Phys. Lett. A **89**(3), 157–162 (1982). 4
- [Fre90] R. W. FREUND. *On Conjugate Gradient Type Methods and Polynomial Preconditioners for a Class of Complex Non-Hermitian Matrices*. Numerische Mathematik **57**, 285–312 (1990). 2.2.4
- [Fre92a] R. W. FREUND. *Conjugate Gradient-Type Methods for Linear Systems with Complex Symmetric Coefficient Matrices*. SIAM Journal on Scientific and Statistical Computing **13**, 425–448 (1992). 1.6.3, 2.2.4, 2.2.4
- [Fre92b] R. W. FREUND. *Quasi-Kernel Polynomials and Their Use in Non-Hermitian Matrix Iterations*. Journal of Computational and Applied Mathematics **43**, 135–158 (1992). 11

- [Fre93a] R. W. FREUND. *Solution of Shifted Linear Systems by Quasi-Minimal Residual Iterations*. In L. REICHEL, A. RUTTAN, and R. S. VARGA (Eds.), *Numerical Linear Algebra*, pp. 101–121 (W. de Gruyter, 1993). [2.2.4](#)
- [Fre93b] R. W. FREUND. *A Transpose-Free Quasi-Minimal Residual Algorithm for Non-Hermitian Linear Systems*. *SIAM Journal on Scientific Computing* **14**, 470–482 (1993). [11](#)
- [Fri58] J. FRIEDEL. *Metallic alloys*. *Nuovo Cimento (Suppl)* **7**, 287–311 (1958). [1.3](#)
- [Ful93] P. FULDE. *Electron Correlations in Molecules and Solids*, vol. 100 of *Solid State Sciences* (Springer, Berlin, 1993). [1.6.4](#)
- [Gai01] J. GAITE. *Angular quantization and the density matrix renormalization group*. *Mod. Phys. Lett. A* **16**(17), 1109–1116 (2001). [3](#)
- [Gai04] J. GAITE. *Entanglement Entropy and the Density Matrix Renormalization Group*. In D. IAGOLNITZER, V. RIVASSEAU, and J. ZINN-JUSTIN (Eds.), *Proceedings of the International Congress on Theoretical Physics (TH-2002, Paris, July 22-27, 2002)* (Birkhäuser, 2004). [3](#)
- [Gar04] D. J. GARCÍA, K. HALLBERG, and M. J. ROZENBERG. *Dynamical Mean Field Theory with the Density Matrix Renormalization Group*. *Phys. Rev. Lett.* **93**, 246403 (2004). [5.1](#), [5.3](#)
- [Geb03] F. GEBHARD, E. JECKELMANN, S. J.-S. MAHLERT, S. NISHIMOTO, and R. M. NOACK. *Fourth-Order Perturbation Theory for the Half-Filled Hubbard Model in Infinite Dimensions*. *Eur. Phys. J. B* **36**, 491 (2003). [1.6.3](#), [1.7](#), [3.1](#), [3.2.2](#), [4.2](#), [5.2](#), [5.3](#), [5.3](#)
- [Geo92] A. GEORGES and G. KOTLIAR. *Hubbard Model in Infinite Dimensions*. *Phys. Rev. B* **45**, 6479 (1992). [1.7](#)
- [Geo96] A. GEORGES, G. KOTLIAR, W. KRAUTH, and M. J. ROZENBERG. *Dynamical mean-field theory of strongly correlated fermion systems and the limit of infinite dimensions*. *Rev. Mod. Phys.* **68**(1), 13 (1996). [1.7](#), [3.1](#), [5.1](#), [5.2](#)
- [Geo04] A. GEORGES. *Strongly Correlated Electron Materials: Dynamical Mean-Field Theory and Electronic Structure*. In *Lectures on the Physics of Highly Correlated Electron Systems VIII: Eighth Training Course in the Physics of Correlated Electron Systems and High- T_c Superconductors*, vol. 715 of *American Institute of Physics (AIP) Conference Proceedings*, pp. 3–74 (2004). [1.7](#)

- [Gob05] D. GOBERT, C. KOLLATH, U. SCHOLLWÖCK, and G. SCHÜTZ. *Real-time dynamics in spin-1/2 chains with adaptive time-dependent DMRG*. Phys. Rev. E **71**, 036102 (2005). [10](#)
- [Gol96] G. H. GOLUB and C. F. V. LOAN. *Matrix Computations* (John Hopkins University Press, Baltimore and London, 1996). [2.1.5](#)
- [Gut91] M. H. GUTKNECHT. *Variants of Bi-CGSTAB for matrices with complex spectrum*. Tech. Rep. 90-16, IPS, ETH Zürich, Switzerland (1991). [2.2.4](#)
- [Gut93] M. H. GUTKNECHT. *Variants of Bi-CGSTAB for matrices with complex spectrum*. SIAM J. Sci Comput **14**, 1020–1033 (1993). [2.2.4](#)
- [Haa34] W. J. DE HAAS, J. H. DE BOER, and G. J. VAN DEN BERG. *The electrical resistance of gold, copper and lead at low temperatures*. Physica **1**, 1115–1124 (1934). [1.1](#)
- [Hal95] K. A. HALLBERG. *Density matrix algorithm for the calculation of dynamical properties of low dimensional systems*. Phys. Rev. B **52**(14), 9827–9830 (1995). [1.6.1](#), [1.7](#), [2.2.1](#), [2.2.2](#), [3.1](#), [5.2](#)
- [Hal99] K. A. HALLBERG. *Density Matrix Renormalization*. [cond-mat/9910082](#) (1999). [2](#)
- [Hal04] K. A. HALLBERG. *Density Matrix Renormalization: A Review of the Method and its Applications*. In D. SÉNÉCHAL, A.-M. TREMBLAY, and C. BOURBONNAIS (Eds.), *Theoretical Methods for Strongly Correlated Electrons*, CRM Series in Mathematical Physics, pp. 3–38 (Springer, New York, 2004). [2](#)
- [Hei28] W. HEISENBERG. *Zur Theorie des Ferromagnetismus*. Z. Phys. **40**, 619 (1928). [2.1](#)
- [Hel01a] K. HELD, I. A. NEKRASOV, N. BLÜMER, V. I. ANISIMOV, and D. VOLLHARDT. *Realistic modeling of strongly correlated electron systems: An introduction to the LDA+DMFT approach*. Int. J. Mod. Phys. C **15**, 2611 (2001). [1.7](#)
- [Hel01b] K. HELD, I. A. NEKRASOV, and D. VOLLHARDT. *Realistic modeling of strongly correlated electron systems: An introduction to the LDA+DMFT approach*. Int. J. Mod. Phys. B **15**, 2611 (2001). SCES-Y2K Conference Proceedings. [1.7](#)

- [Hel02] K. HELD, I. A. NEKRASOV, G. KELLER, V. EYERT, N. BLÜMER, A. K. MCMAHAN, R. T. SCALETTAR, T. PRUSCHKE, V. I. ANISIMOV, and D. VOLLHARDT. *The LDA+DMFT Approach to Materials with Strong Electronic Correlations*. In J. GROTENDORST, D. MARX, and A. MURAMATSU (Eds.), *Quantum Simulations of Complex Many-Body Systems: From Theory to Algorithms*, vol. 10 of *John von Neumann Institute of Computing (NIC) series*, pp. 175–209 (Rolduc Conference Centre, Kerkrade, The Netherlands, 2002). [1.7](#)
- [Hel03] K. HELD, I. A. NEKRASOV, G. KELLER, V. EYERT, N. BLÜMER, A. MCMAHAN, R. T. SCALETTAR, T. PRUSCHKE, V. I. ANISIMOV, and D. VOLLHARDT. *Realistic investigations of correlated electron systems with LDA+DMFT*. Ψ_k Newsletters **56**, 65–103 (April 2003). [1.7](#)
- [Hel05] R. W. HELMES, M. SINDEL, L. BORDA, and J. VON DELFT. *Absorption and Emission in quantum dots: Fermi surface effects of Anderson excitons*. [cond-mat/0502329](#) (2005). [4.5.2](#)
- [Hes52] M. R. HESTENES and E. STIEFEL. *Methods of Conjugate Gradients for Solving Linear Systems*. J. Res. Natl. Bur. Stand. **49**, 409 (1952). [2.2.4](#)
- [Hew93] A. C. HEWSON. *The Kondo Problem to Heavy Fermions* (Cambridge University Press, Cambridge, 1993). [1.1](#), [4](#), [1.2](#), [1.3](#), [1.5](#), [1.5](#), [1.6.1](#), [3.1](#), [4.2](#), [4.4](#), [4.4](#)
- [Hir86] J. E. HIRSCH and R. M. FYE. *Monte Carlo Method for Magnetic Impurities in Metals*. Phys. Rev. Lett. **56**(23), 2521–2524 (1986). [3.1](#)
- [Höv00] T. HÖVELBORN. *Boundary Dynamics of the XY-Chain with the Density Matrix Renormalization Group*. Master’s thesis, Universität zu Köln, Universität Bonn (2000). [1.6.1](#), [1.6.3](#), [2.2.3](#), [3.1](#), [4.4](#)
- [Hub63a] J. HUBBARD. *Electron Correlations in Narrow Energy Bands*. Proc. R. Soc. London, Ser. A **276**, 238–257 (1963). [2.1](#)
- [Hub63b] J. HUBBARD. *Electron Correlations in Narrow Energy Bands II: The Degenerate Band Case*. Proc. R. Soc. London, Ser. A **277**, 237–259 (1963). [2.1](#)
- [Hub64] J. HUBBARD. *Electron Correlations in Narrow Energy Bands III: An Improved Solution*. Proc. R. Soc. London, Ser. A **281**, 401–419 (1964). [2.1](#)
- [Hüf03] S. HÜFNER. *Photoelectron Spectroscopy* (Springer, Berlin, 2003). [3.2.1](#)

- [Hul38] L. HULTHÉN. *Über das Austauschproblem eines Kristalles*. Arkiv för Matematik, Astronomi och Fysik **26A**(11), 1–105 (1938). [2.1.9](#)
- [Ima98] M. IMADA, A. FUJIMORI, and Y. TOKURA. *Metal-insulator transitions*. Rev. Mod. Phys. **70**(4), 1039–1263 (1998). [5.1](#)
- [Jar92] M. JARRELL. *Hubbard Model in Infinite Dimensions: A Quantum Monte Carlo Study*. Phys. Rev. Lett. **69**, 168 (1992). [1.7](#)
- [Jec02] E. JECKELMANN. *Dynamical density-matrix renormalization-group method*. Phys. Rev. B **66**, 045114 (2002). [1.6.3](#), [2.2.3](#), [2.2.4](#), [3.1](#), [3.3.2](#), [4.4](#)
- [Jec03] E. JECKELMANN. *Optical excitations in a one-dimensional Mott insulator*. Phys. Rev. B **67**, 075106 (2003). [9](#)
- [Jon89] R. O. JONES and O. GUNNARSSON. *The density functional formalism, its applications and prospects*. Rev. Mod. Phys. **61**, 689 (1989). [1.2](#)
- [Jor28] P. JORDAN and E. WIGNER. *Über das Pauli sche Äquivalenzverbot*. Z. Phys. **47**, 42 (1928). [1.6.2](#), [1.6.2](#)
- [Kaj96] H. KAJUETER and G. KOTLIAR. *New Iterative Perturbation Scheme for Lattice Models with Arbitrary Filling*. Phys. Rev. Lett. **77**(1), 131–134 (1996). [1.6.4](#)
- [Kar04a] K. KARRAI, R. J. WARBURTON, C. SCHULHAUSER, A. HOGELE, B. URBASZEK, E. J. MCGHEE, A. O. GOVOROV, J. M. GARCIA, B. D. GERARDOT, and P. M. PETROFF. *Hybridization of electronic states in quantum dots through photon emission*. Nature **427**, 135 (2004). [1.6.1](#), [4.5.2](#)
- [Kar04b] M. KARSKI. *Dynamische Molekularfeldtheorie mittles dynamischer Dichtematrix-Renomierung* (Diplomarbeit, Universität zu Köln, 2004). [1.4](#), [1.7](#), [1.7](#), [5](#)
- [Kar05] M. KARSKI, C. RAAS, and G. S. UHRIG. *Electron Spectra close to a Metal-to-Insulator Transition*. [cond-mat/0507132](#) (2005). [1.7](#), [1.7](#), [5](#)
- [Kaw81] N. KAWAKAMI and A. OKIJI. *Exact expression of the ground-state energy for the symmetric Anderson model*. Phys. Lett. A **86**(9), 483–486 (1981). [4](#)
- [Kaw82] N. KAWAKAMI and A. OKIJI. *Electronic specific heat for the Anderson model*. Solid State Commun. **43**(6), 467–469 (1982). [4](#)

- [Kaw83] N. KAWAKAMI and A. OKIJI. *Temperature-dependent susceptibility for the asymmetric Anderson model*. Phys. Lett. A **98**(1-2), 54–56 (1983). [4](#)
- [Kle95] B. KLEINE, G. S. UHRIG, and E. MÜLLER-HARTMANN. *Spin Waves in Quantum Antiferromagnets*. Europhys. Lett. **31**, 37 (1995). [5.3](#)
- [Klü98] A. KLÜMPER. *The Spin- $\frac{1}{2}$ Heisenberg Chain: Thermodynamics, Quantum Criticality and Spin-Peierls Exponents*. Eur. Phys. J. B **5**, 677 (1998). [7](#)
- [Klü00] A. KLÜMPER and D. C. JOHNSTON. *Thermodynamics of the Spin $S = \frac{1}{2}$ Antiferromagnetic Uniform Heisenberg Chain*. Phys. Rev. Lett. **84**, 4701 (2000). [7](#)
- [Km80a] H. R. KRISHNA-MURTHY, J. W. WILKINS, and K. G. WILSON. *Renormalization-group approach to the Anderson model of dilute magnetic alloys. I. Static properties for the symmetric case*. Phys. Rev. B **21**(3), 1003–1043 (1980). [1.6.1](#), [2.1.1](#)
- [Km80b] H. R. KRISHNA-MURTHY, J. W. WILKINS, and K. G. WILSON. *Renormalization Group Approach to the Anderson Model of Dilute Magnetic Alloys. II. Static Properties for the Asymmetric Case*. Phys. Rev. B **21**(3), 1044–1083 (1980). [2.1.1](#)
- [Kol05] C. KOLLATH, U. SCHOLLWÖCK, J. VON DELFT, and W. ZWERGER. *One-dimensional density waves of ultracold bosons in an optical lattice*. Phys. Rev. A **71**, 053606 (2005). [10](#)
- [Kon64] J. KONDO. *Resistance Minimum in Dilute Magnetic Alloys*. Prog. Theor. Phys. **32**, 37 (1964). [1.1](#)
- [Kon65] J. KONDO. *Anomalous Density of States in Dilute Magnetic Alloys*. Prog. Theor. Phys. **33**, 575 (1965). [1.1](#)
- [Kot99] G. KOTLIAR. *Landau theory of the Mott transition in the fully frustrated Hubbard model in infinite dimensions*. Eur. Phys. J. B **11**, 27–39 (1999). [5.1](#), [5.3](#)
- [Kot01] G. KOTLIAR and S. Y. SAVRASOV. *Dynamical Mean Field Theory, Model Hamiltonians and First Principles Electronic Structure Calculations*. In A. M. TSVELIK (Ed.), *New Theoretical Approaches to Strongly Correlated Systems*, pp. 259–301 (Kluwer Academic Publishers, 2001). Invited talk at the Nato Advanced Study Institute on New Theoretical Approaches to Strongly Correlated Systems, Cambridge, UK, 10-20 April 1999. [1.7](#)

- [Kot04] G. KOTLIAR and D. VOLLHARDT. *Strongly Correlated Materials: Insights From Dynamical Mean-Field Theory*. *Physics Today* **30**, 53–59 (2004). 1.7
- [Kou01] L. KOUWENHOVEN and L. GLAZMAN. *Revival of the Kondo effect*. *Physics World* pp. 33–38 (2001). 1.1
- [Küh99a] T. D. KÜHNER. *Dynamics with the Density-Matrix Renormalization Group*. Ph.D. thesis, Universität Bonn (1999). 2.2.3
- [Küh99b] T. D. KÜHNER and S. R. WHITE. *Dynamical Correlation Functions using the Density Matrix Renormalization Group*. *Phys. Rev. B* **60**(1), 335–343 (1999). 1.6.1, 1.6.3, 1.7, 2.2.1, 2.2.2, 2.2.2, 2.2.3, 2.2.3, 2.2.3, 3.1, 5.2
- [Küh00] T. D. KÜHNER, S. R. WHITE, and H. MONIEN. *One-dimensional Bose-Hubbard model with nearest-neighbor interaction*. *Phys. Rev. B* **61**(18), 12474–12489 (2000). 9
- [Lan50] C. LANZOS. *An iterative method for the solution of the eigenvalue problem of linear differential and integral operators*. *J. Res. Natl. Bur. Stand.* **45**, 255 (1950). 1.4, 2.2.2
- [Lan79] J. K. LANG and Y. BAER. *Bremsstrahlung isochromat spectroscopy using a modified XPS apparatus*. *Rev. Sci. Instr.* **50**(2), 221–226 (1979). 12
- [Lat04] J. I. LATORRE, E. RICO, and G. VIDAL. *Ground state entanglement in quantum spin chains*. *Quantum Inf. Comput.* **4**(1), 048–092 (2004). 3
- [Lei04] *International Workshop on “Recent Progress and Prospects in Density-Matrix Renormalization”, Lorentz Center, Leiden University, The Netherlands*. <http://dmrg.info/workshop/> (2004). 2
- [Ley79] L. LEY and M. CARDONA (Eds.). *Photoemission in Solids I: General Principles*, vol. 26 of *Topics in Applied Physics* (Springer, Berlin, 1979). 1.5
- [Lic98] A. I. LICHTENSTEIN and M. I. KATSNELSON. *Ab initio calculations of quasiparticle band structure in correlated systems: LDA++ approach*. *Phys. Rev. B* **57**, 6884–6895 (1998). 1.7
- [Log98] D. E. LOGAN, M. P. EASTWOOD, and M. A. TUSCH. *A local moment approach to the Anderson model*. *J. Phys.: Condens. Matter* **10**(12), 2673–2700 (1998). 4.5.1

- [Luk98] S. LUKYANOV. *Low Energy Effective Hamiltonian for the XXZ Spin Chain*. Nucl. Phys. B **522**(3), 533–549 (1998). [7](#)
- [Lut60] J. M. LUTTINGER. *Fermi Surface and Some Simple Equilibrium Properties of a System of Interacting Fermions*. Phys. Rev. **119**, 1153 (1960). [1.5](#), [4.2](#), [4.4](#)
- [Lut61] J. M. LUTTINGER. *Analytic Properties of Single-Particle Propagators for Many-Fermion Systems*. Phys. Rev. **121**, 942 (1961). [1.5](#), [4.2](#), [4.4](#)
- [Mal03] A. L. MALVEZZI. *An Introduction to Numerical Methods in Low-Dimensional Quantum Systems*. Brazilian Journal of Physics **33**(1), 55–72 (2003). [2](#)
- [Man05] S. R. MANMANA, A. MURAMATSU, and R. M. NOACK. *Time evolution of one-dimensional Quantum Many Body Systems*. [cond-mat/0502396](#) (2005). [10](#)
- [Mar99] B. MARIĆ. *Untersuchung von Solitonen in Spin-Peierls-Systemen mit Hilfe der Dichtematrix-Renormierungsgruppe* (Diplomarbeit, Universität zu Köln, 1999). [1](#)
- [Mat04] H. MATSUEDA, T. TOHYAMA, and S. MAEKAWA. *Dynamical density matrix renormalization group study of photoexcited states in one-dimensional Mott insulators*. Phys. Rev. B **70**, 033102 (2004). [9](#)
- [Mat05] H. MATSUEDA, T. TOHYAMA, and S. MAEKAWA. *Excitonic effect on optical response in one-dimensional two-band Hubbard model*. Phys. Rev. B **71**, 153106 (2005). [9](#)
- [McC01] I. P. MCCULLOCH. *Collective Phenomena in Strongly Correlated Electron Systems*. Ph.D. thesis, Australian National University (2001). [2](#)
- [McC02] I. P. MCCULLOCH and M. GULÁCSI. *The non-Abelian density matrix renormalization group algorithm*. Europhys. Lett. **57**(6), 852–858 (2002). [2](#)
- [Med91] D. MEDEIROS and G. G. CABRERA. *Lanczos calculation for the $s = \frac{1}{2}$ antiferromagnetic Heisenberg chain up to $N = 28$ spins*. Phys. Rev. B **43**(4), 3703–3705 (1991). [7](#)
- [Mei99] A. MEISTER. *Numerik linearer Gleichungssysteme* (Vieweg, Braunschweig/Wiesbaden, 1999). [2.2.4](#)
- [Met89] W. METZNER and D. VOLLHARDT. *Correlated Lattice Fermions in $d = \infty$ Dimensions*. Phys. Rev. Lett. **62**, 324 (1989). [1.7](#)

- [MH89a] E. MÜLLER-HARTMANN. *Correlated Fermions on a Lattice in High Dimensions*. Z. Phys. B **74**, 507 (1989). 1.7, 5.3
- [MH89b] E. MÜLLER-HARTMANN. *The Hubbard Model at high dimensions: some exact results and weak coupling theory*. Z. Phys. B **76**, 211–217 (1989). 1.6.4, 1.6.4
- [Möl95] G. MÖLLER, Q. SI, G. KOTLIAR, M. J. ROZENBERG, and D. S. FISHER. *Critical Behavior near the Mott Transition in the Hubbard Model*. Phys. Rev. Lett. **74**, 2082 (1995). 5.1, 5.3, 5.3
- [Nis99] T. NISHINO. *Density Matrix Renormalization Group – Introduction from a variational point of view*. Int. J. Mod. Phys. B **13**, 1 (1999). 2
- [Nis02] S. NISHIMOTO, E. JECKELMANN, F. GEBHARD, and R. M. NOACK. *Application of the Density Matrix Renormalization Group in momentum space*. Phys. Rev. B **65**, 165114 (2002). 2
- [Nis04a] S. NISHIMOTO, F. GEBHARD, and E. JECKELMANN. *Dynamical density-matrix renormalization group for the Mott-Hubbard insulator in high dimensions*. J. Phys.: Condens. Matter **16**(39), 7063–7081 (2004). 5.1, 5.3, 5.3, 5.3
- [Nis04b] S. NISHIMOTO and E. JECKELMANN. *Density-matrix renormalisation group approach to quantum impurity problems*. J. Phys.: Condens. Matter **16**, 613–625 (2004). 1.5, 1.7, 3.1, 3.1, 3.2.2, 4.2, 4.4, 5.2
- [Noa99] R. M. NOACK and S. R. WHITE. *The Density Matrix Renormalization Group*. In I. PESCHEL, X. WANG, M. KAULKE, and K. HALLBERG (Eds.), *Density-Matrix Renormalization – A New Numerical Method in Physics*, vol. 528 of *Lecture Notes in Physics*, chap. I.2 (Springer, Berlin, 1999). 2, 2.1.6, 2.2.4
- [Nor03] M. R. NORMAN and C. PÉPIN. *The electronic nature of high temperature cuprate superconductors*. Prog. Theor. Phys. **66**(10), 1547 (2003). 5.1
- [Nun02] T. S. NUNNER, P. BRUNE, T. KOPP, M. WINDT, and M. GRÜNINGER. *Cyclic Spin Exchange in Cuprate Spin Ladders*. Phys. Rev. B **66**, 180404 (2002). 9
- [Ogi83] E. OGIEVETSKI, A. M. TSVELIK, and P. B. WIEGMANN. *Exact solution of the degenerate Anderson model*. J. Phys. C **16**(22), L797–L802 (1983). 4

- [Os02] T. J. OSBORNE and M. A. NIELSEN. *Entanglement, quantum phase transitions, and density matrix renormalization*. Quantum Inf. Process. **1**, 45 (2002). [3](#)
- [Pat99] S. K. PATI, S. RAMASESHA, Z. SHUAI, and J. L. BRÉDAS. *Dynamical nonlinear optical coefficients from the symmetrized density-matrix renormalization-group method*. Phys. Rev. B **59**(23), 14827–14830 (1999). [9](#)
- [Pat03] S. K. PATI, S. RAMASESHA, and D. SEN. *Exact and Approximate Theoretical Techniques for Quantum Magnetism in Low Dimensions*. In J. S. MILLER and M. DRILLON (Eds.), *Magnetism: Molecules to Materials*, vol. IV, pp. 119–171 (Wiley-VCH, Weinheim, 2003). [2](#)
- [Pes99] I. PESCHEL, X. WANG, M. KAULKE, and K. HALLBERG (Eds.). *Density-Matrix Renormalization – A New Numerical Method in Physics*, vol. 528 of *Lecture Notes in Physics* (Springer, Berlin, 1999). [1.6.1](#), [2](#)
- [Pet85] D. G. PETTIFOR and D. L. WEAIRE. *The Recursion Method and Its Applications*, vol. 58 of *Springer Series in Solid-State Sciences* (D. G. Pettifor and D. L. Weaire, Berlin, 1985). [1.4](#)
- [Pot97] M. POTTHOFF, T. WEGNER, and W. NOLTING. *Interpolating self-energy of the infinite-dimensional Hubbard model: Modifying the iterative perturbation theory*. Phys. Rev. B **55**(24), 16132 (1997). [1.6.4](#)
- [Pot03] M. POTTHOFF. *Self-energy-functional approach: Analytical results and the Mott-Hubbard transition*. Eur. Phys. J. B **36**, 335 (2003). [5.1](#)
- [Pre92] W. H. PRESS, S. A. TEUKOLSKY, W. T. VETTERLING, and B. P. FLANNERY. *Numerical Recipes* (Cambridge University Press, Cambridge, 1992). [2.1.5](#), [3.2.1](#), [3.3.1](#)
- [Pru89] T. PRUSCHKE and N. GREWE. *Magnetism and Electrical Transport in Kondo-Lattices*. Z. Phys. B **74**, 439 (1989). [4.2](#)
- [Pru95] T. PRUSCHKE, M. JARRELL, and J. K. FREERICKS. *Anomalous Normal-State Properties of High- T_c Superconductors – Intrinsic Properties of Strongly Correlated Electron Systems?* Adv. Phys. **44**, 187 (1995). [1.7](#), [3.1](#)
- [Pus04] M. PUSTILNIK and L. GLAZMAN. *Kondo effect in quantum dots*. J. Phys.: Condens. Matter **16**, R513–R537 (2004). [3.1](#)

- [Raa04] C. RAAS, G. S. UHRIG, and F. B. ANDERS. *High Energy Dynamics of the Single Impurity Anderson Model*. Phys. Rev. B **69**(4), 041102(R) (2004). [1.6.1](#), [1.6.3](#), [1.7](#), [3.1](#), [3.2.1](#), [3.2.1](#), [3.3.1](#), [3.3.2](#), [5.2](#), [5.3](#)
- [Raa05] C. RAAS and G. S. UHRIG. *Spectral Densities from Dynamic Density-Matrix Renormalization*. Eur. Phys. J. B **45**(3), 293–303 (2005). [1.7](#), [5.2](#)
- [Ram90] S. RAMASESHA. *A New Algorithm for Solving Large Inhomogeneous Linear System of Algebraic Equations*. Journal of Computational Chemistry **11**(5), 545–547 (1990). [2.2.4](#)
- [Ram97] S. RAMASESHA, S. K. PATI, H. R. KRISHNA-MURTHY, Z. SHUAI, and J. L. BRÉDAS. *Low-lying electronic excitations and nonlinear optic properties of polymers via symmetrized Density Matrix Renormalization Group Method*. Synthetic Metals **85**(1-3), 1019–1022 (1997). [1.6.1](#), [1.6.3](#), [1.7](#), [2.2.1](#), [2.2.3](#), [3.1](#), [5.2](#)
- [Rei04] A. REISCHL, G. S. UHRIG, and E. MÜLLER-HARTMANN. *Systematic mapping of the Hubbard model to the generalized $t - J$ model*. Phys. Rev. B **70**, 245124 (2004). [5.1](#)
- [Ric80] G. RICKAYZEN. *Green's Functions and Condensed Matter* (Academic Press, London, 1980). [1.6.4](#), [3](#)
- [Saa96] Y. SAAD. *Iterative methods for sparse linear systems* (PWS, 1996). [2.2.4](#)
- [Saa00] Y. SAAD and H. A. VAN DER VORST. *Iterative Solution of Linear Systems in the 20-th Century*. J. Comp. Appl. Math. **123**, 1–22 (2000). [2.2.4](#)
- [Sak89] O. SAKAI, Y. SHIMIZU, and T. KASUYA. *Single-particle and magnetic excitation spectra of degenerate Anderson model with finite f - f Coulomb interaction*. J. Phys. Soc. Jpn. **58**(10), 3666–3678 (1989). [1.6.1](#), [3.1](#), [4.2](#), [4.4](#)
- [Sch66] J. R. SCHRIEFFER and P. A. WOLFF. *Relation between the Anderson and Kondo Hamiltonians*. Phys. Rev. **149**, 491 (1966). [1.1](#), [2](#), [1.3](#), [1.3](#), [7](#), [4.5.1](#), [4.5.1](#), [4.5.2](#)
- [Sch68] L. I. SCHIFF. *Quantum Mechanics* (McGraw-Hill, 1968), 3rd edn. [1.6.2](#)
- [Sch69] K. D. SCHOTTE and U. SCHOTTE. *Threshold Behavior of the X-Ray Spectra of Light Metals*. Phys. Rev. **185**, 509 (1969). [4.5.2](#)

- [Sch82] P. SCHLOTTMANN. *Bethe ansatz solution of the ground state of a model for mixed-valent cerium and ytterbium impurities in metals*. Z. Phys. B **49**, 109 (1982). [1.6.1](#)
- [Sch89] P. SCHLOTTMANN. *Some exact results for dilute mixed-valent and heavy-fermion systems*. Phys. Rep. **181**(1-2), 1–119 (1989). [1](#)
- [Sch99] F. SCHÖNFELD. *Untersuchung dimerisierter, frustrierter Heisenbergketten mittels DMRG-Methoden*. Ph.D. thesis, Universität zu Köln (1999). [1](#)
- [Sch04] P. SCHMITTECKERT. *Nonequilibrium electron transport using the density matrix renormalization group method*. Phys. Rev. B **70**, 121302(R) (2004). [10](#)
- [Sch05a] U. SCHOLLWÖCK. *Density-matrix renormalization group*. Rev. Mod. Phys. **77**, 259 (2005). [2](#), [2.1.3](#), [2.1.7](#), [2.2.1](#), [2.2.2](#), [2.2.3](#)
- [Sch05b] U. SCHOLLWÖCK. *Time-dependent Density-Matrix Renormalization-Group Methods*. J. Phys. Soc. Jpn. **74** (Suppl.), 246–255 (2005). [10](#)
- [Shi03] N. SHIBATA. *Application of the density matrix renormalization group method to finite temperatures and two-dimensional systems*. J. Phys. A: Math. Gen. **36**, R381 (2003). [2](#)
- [Sir05] J. SIRKER and A. KLÜMPER. *Real-time dynamics at finite temperature by DMRG: A path-integral approach*. Phys. Rev. B **71**, 241101(R) (2005). [10](#)
- [Sle93] G. L. G. SLEIJPEN and D. R. FOKKEMA. *BICGSTAB(ℓ) for linear equations involving unsymmetric matrices with complex spectrum*. ETNA **1**, 11–32 (1993). [2.2.4](#)
- [Sle94] G. L. G. SLEIJPEN, H. A. VAN DER HORST, and D. R. FOKKEMA. *Bi-CGSTAB(ℓ) and other hybrid Bi-CG methods*. Numerical Algorithms **7**, 75–109 (1994). [2.2.4](#)
- [Sto83] J. STOER and R. BULIRSCH. *Einführung in die Numerische Mathematik*, vol. I, chap. 3.5 (Springer, Berlin, 1983). [2.2.5](#), [2.2.5](#)
- [Tak73] M. TAKAHASHI. *Low temperature specific heat of a spin-1/2 anisotropic Heisenberg ring*. Prog. Theor. Phys. **50**(5), 1519–1536 (1973). [2.1.9](#)
- [Tak74] M. TAKAHASHI. *Numerical calculation of thermodynamic quantities of spin-1/2 anisotropic Heisenberg ring*. Prog. Theor. Phys. **51**, 1348 (1974). [2.1.9](#)

- [Tok00] Y. TOKURA and N. NAGAOSA. *Orbital Physics in Transition-Metal Oxides*. Science **288**(5465), 462–468 (2000). 5.1
- [Ton02] N.-H. TONG, S.-Q. SHEN, and F.-C. PU. *Mott-Hubbard transition in infinite dimensions*. Phys. Rev. B **64**(23), 235109 (2002). 5.1
- [Tsv82a] A. M. TSVELIK and P. B. WIEGMANN. *Exact solution of the degenerate exchange model (Kondo problem for alloys with rare earth impurities)*. J. Phys. C **15**(8), 1707–1712 (1982). 1
- [Tsv82b] A. M. TSVELIK and P. B. WIEGMANN. *Low-temperature properties of the asymmetric Anderson model (exact solution) II*. Phys. Lett. A **89**(7), 368–372 (1982). 4
- [Tsv83a] A. M. TSVELIK and P. B. WIEGMANN. *Exact results in the theory of magnetic alloys*. Adv. Phys. **32**(4), 453–713 (1983). 1
- [Tsv83b] A. M. TSVELIK and P. B. WIEGMANN. *Exact solution of the Anderson model. II. Thermodynamic properties at finite temperatures*. J. Phys. C **16**(12), 2321–2336 (1983). 4
- [Tsv84] A. M. TSVELIK. *Thermodynamics of the degenerate Anderson model*. J. Phys. C **17**(13), 2299–2311 (1984). 4
- [Uhr03] G. S. UHRIG. private communication (2003). 1.6.4, 1.6.4
- [Vid03] G. VIDAL. *Efficient Classical Simulation of Slightly Entangled Quantum Computations*. Phys. Rev. Lett. **91**, 147902 (2003). 10
- [Vid04] G. VIDAL. *Efficient Simulation of One-Dimensional Quantum Many-Body Systems*. Phys. Rev. Lett. **93**, 040502 (2004). 10
- [Vis94] V. S. VISWANATH and G. MÜLLER (Eds.). *The Recursion Method; Application to Many-Body Dynamics*, vol. m23 of *Lecture Notes in Physics* (Springer, Berlin, 1994). 1.4, 1.4, 1.4, 1.6.4
- [Vol05] D. VOLLHARDT, K. HELD, G. KELLER, R. BULLA, T. PRUSCHKE, I. A. NEKRASOV, and V. I. ANISIMOV. *Dynamical Mean-Field Theory and Its Applications to Real Materials*. J. Phys. Soc. Jpn. **74**, 136 (2005). 1.7
- [Vor92] H. A. VAN DER VORST. *Bi-CGSTAB: A fast and smoothly converging variant of Bi-CG for the solution of nonsymmetric linear systems*. SIAM J. Sci. Statist. Comput. **13**, 631–644 (1992). 2.2.4

- [Vor02] H. A. VAN DER VORST. *Lecture Notes on Iterative Methods*. <http://www.math.ruu.nl/people/vorst/lecture.html>, Mathematical Institute of Utrecht University (2002). 2.2.4
- [Vor03] H. A. VAN DER VORST. *Iterative Krylov Methods for Large Linear Systems* (Cambridge University Press, Cambridge, 2003). 2.2.4
- [War00] R. J. WARBURTON, C. SCHÄFLEIN, D. HAFT, F. BICKEL, A. LORKE, K. KARRAI, J. M. GARCIA, W. SCHOENFELD, and P. M. PETROFF. *Optical emission from a charge-tunable quantum ring*. *Nature* **405**, 926–929 (2000). 1.6.1, 4.5.2
- [Whi92a] S. R. WHITE. *Density Matrix Formulation for Quantum Renormalization Groups*. *Phys. Rev. Lett.* **69**, 2863 (1992). 1.6.1, 2, 2.1.3, 2, 2.1.5, 2.1.7
- [Whi92b] S. R. WHITE and R. M. NOACK. *Real-space quantum renormalization groups*. *Phys. Rev. Lett.* **68**(24), 3487 (1992). 2.1.2
- [Whi93] S. R. WHITE. *Density-Matrix Algorithms for Quantum Renormalisation Groups*. *Phys. Rev. B* **48**, 10345 (1993). 1.6.1, 2, 2.1.3, 2, 2.1.5, 2.2.4
- [Whi98] S. R. WHITE. *Strongly correlated electron systems and the density matrix renormalization group*. *Phys. Rep.* **301**(1-3), 187–204 (1998). 2, 1
- [Whi04] S. R. WHITE and A. E. FEIGUIN. *Real time evolution using the density matrix renormalization group*. *Phys. Rev. Lett.* **93**, 076401 (2004). 10
- [Wie80] P. B. WIEGMANN. *Exact solution of s-d exchange model at $T = 0$* . *JETP Lett.* **31**, 364–370 (1980). 1.1
- [Wie81a] P. B. WIEGMANN. *Exact solution of the s-d exchange model (Kondo problem)*. *J. Phys. C* **14**(10), 1463–1478 (1981). 1, 4
- [Wie81b] P. B. WIEGMANN and A. M. TSVELIK. *Exact solution of Kondo problem for alloys with rare-earth impurities*. *Physica B+C* **107**(1-3), 379–380 (1981). 1
- [Wie83a] P. B. WIEGMANN. *Exact solution of the Anderson model*. *Soviet Journal of Low Temperature Physics* **9**(7), 400–400 (1983). 4
- [Wie83b] P. B. WIEGMANN. *Towards an exact solution of the Anderson model*. *Phys. Lett. A* **80**(2-1), 163–167 (1983). 4

- [Wie83c] P. B. WIEGMANN and A. M. TSVELIK. *Exact solution of the Anderson model: I*. J. Phys. C **16**(12), 2281–2319 (1983). [4](#)
- [Wil75] K. G. WILSON. *The renormalisation group: Critical Phenomena and the Kondo problem*. Rev. Mod. Phys. **47**, 773–840 (1975). [1.1](#), [2](#), [2.1](#), [2.1.1](#)
- [Xia96] T. XIANG. *Density-matrix renormalization-group method in momentum space*. Phys. Rev. B **53**, 10445 (1996). [2](#)
- [Zen51] C. ZENER. *Interaction Between the d Shells in the Transition Metals*. Phys. Rev. **81**, 440 (1951). [1.1](#)
- [Zha93] X. Y. ZHANG, M. J. ROZENBERG, and G. KOTLIAR. *Mott Transition in the $d = \infty$ Hubbard Model at Zero Temperature*. Phys. Rev. Lett. **70**, 1666 (1993). [5.1](#), [5.3](#)

Appendix

Kurze Zusammenfassung

In dieser Arbeit wurde ein numerischer Zugang, die dynamische Dichte-Matrix-Renormierung (D-DMRG) untersucht, implementiert, geeicht, optimiert und angewendet. Die dynamische Dichte-Matrix-Renormierung ist die Erweiterung der Standard-DMRG auf die Berechnung dynamischer Größen. Die D-DMRG berechnet numerisch die Faltungen von Spektraldichten zu dynamischen Korrelationsfunktionen. Die Dynamik bei $T = 0$ wird durch Bestimmung der Erwartungswerte des lokalen Propagators gewonnen. Dies wird ermöglicht, indem neben dem Grundzustand und dem angeregten Zustand auch die Resolvente angewandt auf den Anregungszustand als DMRG-Zielzustand benutzt wird. Dieser frequenzabhängige zusätzliche Zielzustand wird Korrekturvektor genannt. Seine Berechnung ist der anspruchsvollste Teil in einem D-DMRG-Algorithmus, da ein beinahe singuläres nicht-hermitesches Gleichungssystem gelöst werden muss. Wir haben das Laufzeitverhalten mehrerer iterativer Gleichungssystem-Löser verglichen und so das Invertierungsproblem der D-DMRG unter Verwendung spezialisierter Algorithmen stabilisieren können.

Die Haupt-Einschränkung der Korrektur-Vektor-DMRG besteht darin, dass man nicht bei rein reellen Frequenzen sondern nur bei Frequenzen mit einem kleinem Imaginärteil rechnen kann. Daher ist die Extraktion des Verhaltens bei reellen Frequenzen ein essenzielles Problem bei der Verwendung der D-DMRG. Wir diskutieren und vergleichen verschiedene Algorithmen, die diese Entfaltung vornehmen. Ein nicht-linearer Zugang aus der Familie der Maximum-Entropie-Methoden, die Least-Bias-Entfaltung (LB), wurde vorgestellt. Das LB-Schema berechnet mit einem kontinuierlichen und positiv-definiten Ansatz die Entfaltung mit der geringsten Voreingenommenheit. Sogar sehr abrupte Änderungen in der Spektral-Dichte können zufriedenstellend reproduziert werden. In der Nähe von Singularitäten treten störende Oszillationen auf. Der Least-Bias-Ansatz kann bezüglich kleiner numerischer Ungenauigkeiten in den Rohdaten stabilisiert werden.

Wir haben den dynamischen Propagator des symmetrischen Einstörstellen-Anderson-Modells mittels D-DMRG untersucht. Die Abrikosov-Suhl-Resonanz (ASR) wurde zur Eichung der D-DMRG untersucht. Damit belegen wir, dass mit der D-DMRG die Niederenergie-Skala des Modells aufgelöst werden kann, was über zwei Größenordnungen hinweg reproduziert werden konnte. Weiterhin wurden die Hubbard-Satelliten untersucht. Aus verbreiterten Rohdaten konnten die Breiten und die Peak-Verschiebungen aus den atomaren Niveaus bestimmt werden. Mit Hilfe der LB-Entfaltung wurde die Linienform der Satelliten untersucht. Diese stellen sich als stark asymmetrisch heraus.

Das Hubbard-Modell auf dem Bethe-Gitter mit unendlicher Koordinationszahl wurde mit Hilfe der dynamischen Molekularfeldtheorie (DMFT) und der D-DMRG als Störstellenlöser untersucht. Eine Berechnung der Spektren nahe des Metall-Isolator-Übergangs wurde mit hoher Auflösung durchgeführt. Wir bieten mit dieser rein numerischen Untersuchung eine konsistente Bestätigung des Szenarios eines glatten Übergangs bei $T = 0$.

Abstract

In this thesis we investigated, implemented, gauged, optimized, and applied a numerical approach given by the dynamic density-matrix renormalization (D-DMRG). The dynamic density-matrix renormalization is the extension of standard DMRG to the calculation of dynamic quantities. D-DMRG provides valuable numerical information on dynamic correlations by computing convolutions of the corresponding spectral densities. The dynamics at zero temperature is determined by computing the expectation values in the local propagator. This can be realized by targeting not only at the ground state and the excited state, but also at the resolvent applied to the excited state. This additional targeted state is called the correction vector. The calculation of the frequency-dependent correction vector is numerically extremely demanding due to the inversion of an almost singular non-hermitian matrix. We compared the performance of several iterative solvers for linear equation systems and managed to stabilize the inversion problem of the D-DMRG by using optimized algorithms.

The main limitation of the correction vector D-DMRG is that one cannot obtain data for purely real frequencies but only for frequencies with a certain imaginary part. Hence the extraction of the behavior at purely real frequencies is one of the main problems to be solved in using the D-DMRG. We illustrated how and to which extent such data can be deconvolved to retrieve the wanted spectral densities. We discussed and compared various algorithms to achieve this extraction and presented a non-linear approach from the family of maximum entropy methods. This approach provides a continuous, positive ansatz for the wanted spectral density with the least bias (LB). Even relative abrupt changes of the spectral density can be reproduced satisfactorily. In the vicinity of singularities spurious oscillations occur. The least-bias ansatz can be made more robust towards small numerical inaccuracies and finite-size effects by including besides the entropy functional a χ -functional in the functional to be minimized.

We investigated the dynamic propagator of the symmetric single impurity Anderson model by D-DMRG. The Abrikosov-Suhl resonance (ASR) was calculated to gauge the D-DMRG and to demonstrate that features at low energies can be resolved. The low energy scale of the SIAM was reproduced over two orders of magnitude. The Hubbard satellites were investigated. From the broadened D-DMRG raw data we extracted the width and the shifts from the atomic positions. By means of the LB extraction we were able to address the line shape of the satellites. It was found that the Hubbard satellites are strongly asymmetric, the peak is very pronounced and the maximum value is very high.

The Hubbard model on the Bethe lattice with infinite coordination number was investigated by means of the dynamic mean-field theory (DMFT) using the D-DMRG as impurity solver. A high-resolution investigation of the electron spectra close to the metal-to-insulator transition in dynamic mean-field theory was presented. The all-numerical, consistent confirmation of a smooth transition at zero temperature is provided.

Danksagung

Ich möchte mich an dieser Stelle herzlich bei Prof. Dr. Götz S. Uhrig für die Vergabe und Betreuung dieser Arbeit bedanken. Seine tatkräftige Unterstützung kann nicht genug hervorgehoben werden.

Für die gute Zusammenarbeit danke ich auch Frithjof B. Anders und den Kölner Diplomanden Michał Karski und Rolf Fassbender.

Für die schöne Zeit in Köln und das angenehme Arbeitsklima bedanke ich mich bei Prof. Dr. E. Müller-Hartmann und allen Mitgliedern seiner Arbeitsgruppe.

Meiner Familie danke ich für die Unterstützung in jeglicher Hinsicht.

Erklärung

Ich versichere, dass ich die von mir vorgelegte Dissertation selbständig angefertigt, die benutzten Quellen und Hilfsmittel vollständig angegeben und die Stellen der Arbeit – einschließlich Tabellen, Karten und Abbildungen –, die anderen Werken im Wortlaut oder dem Sinn nach entnommen sind, in jedem Einzelfall als Entlehnung kenntlich gemacht habe; dass diese Dissertation noch keiner anderen Fakultät oder Universität zur Prüfung vorgelegen hat; dass sie – abgesehen von unten angegebenen Teilpublikationen – noch nicht veröffentlicht worden ist sowie, dass ich eine solche Veröffentlichung vor Abschluss des Promotionsverfahrens nicht vornehmen werde. Die Bestimmungen dieser Promotionsordnung sind mir bekannt. Die von mir vorgelegte Dissertation ist von Herrn Prof. Dr. Götz S. Uhrig betreut worden.

Saarbrücken, den 15. Mai 2005

Teilpublikationen

- Carsten Raas, Götz S. Uhrig, and Frithjof B. Anders:
High Energy Dynamics of the Single Impurity Anderson Model,
[Phys. Rev. B **69**\(4\), 041102\(R\) \(2004\), cond-mat/0309675](#)
- Carsten Raas and Götz S. Uhrig:
Spectral Densities from Dynamic Density-Matrix Renormalization,
[Eur. Phys. J. B **45**\(3\), 293-303 \(2005\), cond-mat/0412224](#)
- Michał Karski, Carsten Raas, and Götz S. Uhrig:
Electron Spectra close to a Metal-to-Insulator Transition,
[cond-mat/0507132](#)

Lebenslauf

Persönliche Daten

Name: Carsten Raas
Geburtsdatum: 29. August 1973
Geburtsort: Trier
Familienstand: ledig
Staatsangehörigkeit: deutsch

Schulbildung

1981–1985 Grundschole Bollendorf
1985–1993 Privates St. Josef Gymnasium Biesdorf
Juni 1993 Abitur

Hochschulstudium

Oktober 1994 Immatrikulation an der Universität zu Köln,
Studiengang: Physik, Diplom
November 1996 Vordiplom
Juli 2000 Abschluss der Diplomarbeit bei Prof. Dr. G. S. Uhrig und
Prof. Dr. E. Müller-Hartmann
seit März 2001 Anfertigung der vorliegenden Dissertation unter Anleitung
von Prof. Dr. G. S. Uhrig

Arbeitsverhältnisse

1997–1998 Studentische Hilfskraft beim Studentenwerk Köln
1999–2000 Studentische Hilfskraft am Institut für Theoretische Physik
der Universität zu Köln
2000 Wissenschaftliche Hilfskraft am Institut für Theoretische
Physik der Universität zu Köln
2001–März 2005 Wissenschaftlicher Mitarbeiter am Institut für Theoretische
Physik der Universität zu Köln
seit April 2005 Wissenschaftlicher Mitarbeiter am Institut für Theoretische
Physik der Universität des Saarlandes (Saarbrücken)

